STUDIES ON THE MAGNETIC AND ELECTRICAL PROPERTIES OF NANOSIZED TRANSITION METAL OXIDES AND FERRITES

thesis

submitted to the

UNIVERSITY OF PUNE

for the degree of

DOCTOR OF PHILOSOPHY

in Chemistry

By

Sasanka Deka

Physical and Materials Chemistry Division

National Chemical Laboratory

Pune 411008

India

August 2006

CERTIFICATE

Certified that the work incorporated in the thesis

Studies on the Magnetic and Electrical Properties of Nanosized Transition Metal Oxides and Ferrites

submitted by **Mr.** Sasanka Deka for the Degree of *Doctor of Philosophy* in Chemistry was carried out by the candidate under my supervision at the Physical & Materials Chemistry Division of National Chemical Laboratory, Pune. Such material as has been obtained from other sources has been duly acknowledged in the thesis.

Date: **Dr. P. A. Joy**

Place: Pune (Research Guide)

...Dedicated to my Parents...

DECLARATION BY RESEARCH SCHOLAR

I hereby declare that the thesis entitled "**STUDIES ON THE MAGNETIC AND ELECTRICAL PROPERTIES OF NANOSIZED TRANSITION METAL OXIDES AND FERRITES**", submitted for the Degree of Doctor of Philosophy in Chemistry to the University of Pune, has been carried out by me at the Physical & Materials Chemistry Division, National Chemical Laboratory, Pune 411 008, India, under the supervision of Dr. P. A. Joy. The work is original and has not been submitted in part or full by me for any other degree or diploma to this or any other University.

Sasanka Deka

Date:

Physical & Materials Chemistry Division

National Chemical Laboratory

Pune–411008

India

Acknowledgements

This thesis is the result of four and half years of research work. During this period I have been accompanied and supported by many people. It is the pleasant moment and opportunity for me to express my gratitude for all of them.

The first and foremost person I would like thank is my supervisor ***Dr. P. A. Joy****. I owe a debt of gratitude to Dr. Joy, from whom I have learned much about materials science, magnetism and magnetic nanomaterials. No thanks can be enough to acknowledge Dr. Joy, for the encouragement and support I received from him. I wish to acknowledge his support, encouragement, patience and guidance throughout the research period. The many hours of discussions we had and his enthusiasm and positive attitude towards science kept me on the right track. I am deeply indebted to him for his help, stimulating suggestions and the inspiring discussions during writing and completion of this thesis.*

I express my sincere thanks to Dr. S. K. Date and Dr. S. Pal, former and present Head of the Physical Chemistry Division, for their constant support and encouragement. I thank Dr. S. Sivaram, Director of NCL, Pune, for giving me the opportunity to work in this institute and making all the facilities available for my research work. Also, I am grateful to UGC, Govt. of India, for awarding me a research fellowship.

I would like to acknowledge all my former teachers, who guided me towards the right path to reach the present stage.

I would like to express my profound gratitude to Dr. K. Vijayamohanan, Dr. V. Ravi, Dr. M. Sastry, Dr. A. Kumar, Dr. S. B. Deshpande, Dr. K. Sreedhar, Dr. H. S. Potdar, Dr. B. L. V. Prasad and Dr. P. Ghosh, from Physical Chemistry Division, and Dr. C. S. Gopinath, Dr. P. Manikandan and Dr. C. V. Satyanarayana, from Catalysis Division for their timely help and also being kind and considerate throughout my doctoral studies.

I am sincerely thankful to Mrs. R. Pasricha, Dr. N. R. Pavaskar, Dr.(Mrs.) S. D. Kulkarni, Dr. P. P. Bakare and Mr. A. B. Gaikwad from the Center for Materials Characterization, NCL, for all the help in the characterizations required during my research work. I would also like to thank Dr. S. D. Pradhan, Mr. P. D. Godbole and Mr. Gholap for their timely help.

My sincere thanks are to my senior colleagues, Dr. Joly and Dr. S. Verma for their help, support, interest and valuable hints. A very special thanks to Shekhar, Raj Sankar and Sanjay for giving me the feeling of being home at work and being with me from the very first day of my life in NCL. At the same time I wish to acknowledge my fellow lab mates Ganga, Khaja, Vijay, Sreeja, Sudesh and Rubul for their help and cooperation. I am thankful to Harawade Kaka for his care and help.

My sincere gratitude goes to Jadab da, Manash da, Arindam da, Senapati da, Pranjal da, Diganta, Pranjal, Sanjeeb, Lakshi, Khirud, Gitali, Ankur, Maitri, Rahul, Sofia, Gupta and Prem for their support and love, especially during difficult times. I take this opportunity to thank Bidyut, Palash, Ankur, Rupam, Moumita, Manash, Mridu, Ajay and Jon who have helped me in all possible ways.

I would like to thank all my seniors and friends in NCL, Selvakannan, Shiv sanker, Govindaraju, Saikat, Yogesh, Kannan, Easwar, Dhananjoy da, Anamitra da, Hrushikesh, Nimu da, Bhalu, Mahima, Girish, Atul, Bhaiya, Baag, Mukulesh da, Dinesh, Venketesh, Mahesh, Nagendra, Sachin, Shanbag, Thiru, Sankar, Pratheep, Mukesh, Abhishek, Shweta, Suvarna and Shraddha for the wonderful time I had with them.

My sincere thanks to the staff of our divisional office, glass bowling center, workshop and all the other NCL staff members, who were somehow always connected with my research work.

No thanks can be enough to acknowledge for the endless encouragement, care and long-distance support, which I had from Bobu and Ma, my brothers Muna and Baba. Moreover, I would like to thank Dulal mama and all my family members, for their encouragement and affection to complete my research work. Finally, I would like to express my deepest gratitude for the constant support, understanding and care that I received from Smriti during the past years.

Sasanka Deka

Contents

List of Tables

List of Figures

Abstract

Nanosized magnetic materials have received great attention and importance during the last decade. Nanomagnetic material is one of the hottest subjects of present day research activities. The physical properties of nanosized magnetic materials differ considerably from that of their bulk counterparts and the magnetic characteristics of many materials can be tuned by reducing their size. The objectives of this research work are the synthesis and studies on the structural and magnetic properties of some selected transition metal oxides and ferrites in nanocrystalline form.

The present research work has been carried out on transition metal doped zinc oxide based diluted magnetic semiconductors (DMSs), some ferrites and magneto-polymer nanocomposite systems. The respective nanocrystalline oxides are synthesized by a simple solution combustion method and characterized using various techniques. The results from the studies on different materials are presented in this thesis, consisting of six chapters.

The first chapter is a brief introduction to magnetism, and a review of the structural and magnetic properties of the different magnetic oxides such as ZnO based diluted magnetic semiconductor materials, $ZnFe_2O_4$, $Ni_{0.5}Zn_{0.5}Fe_2O_4$, γ-Fe_2O_3, polymer/metal/ferrite nanocomposites and the $Co/CoO/Co_3O_4$ nanocomposites, studied in the present research work.

The second chapter describes the method employed for the synthesis of the nanocrystalline oxides. All the experimental methods and characterization techniques used are briefly discussed in the specific sections.

Synthesis procedures and the structural and magnetic properties of the transition metal (Co, Ni, Mn and Fe) doped nanocrystalline ZnO are discussed in the third chapter. The nanocrystalline materials having particle sizes in the range of 10–40 nm are synthesized by an autocombustion method. Optical and XPS studies showed that the Zn ions have been replaced by divalent transition metal ions in the tetrahedral site of the wurtzite structure of ZnO. Room temperature ferromagnetism is observed after doping Co, Ni and Fe in ZnO. However, the magnetic properties change drastically when the synthesize procedure is modified slightly. Mn doped ZnO samples are found to be always

paramagnetic down to 12 K. The origin of the observed ferromagnetism is found to be from metallic nanoclusters or secondary ferromagnetic phases depending on the synthesis conditions and metal ions used.

The detailed studies on the synthesis, characterization, and magnetic properties of nanocrystalline NiZn ferrite, $Ni_{0.5}Zn_{0.5}Fe_2O_4$, are discussed in the fourth chapter. Narrow particle size distribution with high rate of reproducibility is achieved by using a simple autocombustion method for the synthesis. The T_C of the nanocrystalline ferrite is increased to large values due to the unusual cation distribution in the nanosized ferrite. The nanosized ferrite sintered using Bi_2O_3 and Ag as additives showed good microstructure, high density at low sintering temperatures, very high magnetic permeability and dielectric constant values at room temperature.

The fifth chapter deals with synthesis and studies on the structural and magnetic properties of nanocrystalline $ZnFe_2O_4$ and γ-Fe_2O_3. Single phase of superparamagnetic $ZnFe_2O_4$ obtained when smaller amounts of glycine is used as the fuel in the autocombustion reaction. However, Fe_3O_4 is found to be formed as a secondary phase, when larger amounts of glycine is used. Zn-doped γ-Fe_2O_3 is synthesized by the same autocombustion method. Zn-doping is found to stabilize the maghemite phase and increases the transformation temperature to the hematite phase.

The sixth chapter deals with the synthesis, characterization and preliminary studies on some magnetic nanocomposites. $Ni/NiFe_2O_4$ and $Co/CoFe_2O_4$ nanocomposites are synthesized under *in situ* conditions by an autocombustion method. The composites are then blended with PVDF polymer matrix. Moderate values of initial permeability and dielectric constant are obtained for the polymer/metal/ferrite nanocomposites, comparable to that reported in the literature. $Co/CoO/Co_3O_4$ nanocomposite is synthesized using the same autocombustion method. This nanocomposite could be transformed to Co/CoO nanocomposite by proper reduction at elevated temperatures.

List of abbreviations

AFM: Antiferromagnetism

bcc: Body Centered Cubic

BE: Binding Energy

ac: Alternating current

$\mathbf{D}_c$: Critical Diameter

DMS: Diluted Magnetic Semiconductor

EDX: Energy Dispersive X-ray

emu: Electromagnetic Unit

eV: Electron Volt

FC: Field Cooled

fcc: Face Centered Cubic

FM: Ferromagnetism

GMR: Giant Magnetoresistance

GNP: Glycine-Nitrate-Process

$\mathbf{H}_c$: Coercivity

HMF: Hyperfine Magnetic Field

IS: Isomer Shift

JCPDS: Joint Committee on Powder Diffraction Standards

K: Kelvin

μ_B: Bohr Magneton

M: Magnetization

$\mathbf{M}_s$: Saturation magnetization

Oe: Oersted

PCW: Powder Cell for Windows

PDP: Powder Diffraction Package

PVA: Polyvinyl Alcohol

PVDF: Poly (Vinylidene Fluoride)

QS: Quadruple Splitting

rlf: Relative Loss Factor

SAED: Selected Area Electron Diffraction

SEM: Scanning Electron Microscopy

TEM: Transmission Electron Microscopy

TGA: Thermo-Gravimetric Analysis

T: Temperature

$\mathbf{T}_C$: Curie Temperature

TM: Transition Metal

TMA: Thermal Mechanical Analyzer

UV: Ultra Violet

VSM: Vibrating Sample Magnetometer

XPS: X-ray Photoelectron Spectroscopy

XRD: X-Ray Diffraction

ZFC: Zero Field Cooled

Chapter 1

Introduction

1.1 Materials Science

The index of human progress is valued by the use and development of materials. Materials science is the multidisciplinary field related to the studies on different aspects of materials. Materials science in a primitive form is one of the oldest forms of engineering and applied science. It is closely related to applied physics, chemistry and chemical engineering, biology and bioengineering, electrical engineering, civil engineering and mechanical engineering. In other terms, materials science is defined as the one which is concerned with the relation of composition, structure, and processing of materials to their properties and uses.

The emergence of materials science as an important area is the result of several converging developments that occurred during the last few decades. In the context of materials science, the term **materials** designates physical matter used by human beings in creating structure, machine, articles, vehicles, devices, and many other objects whose examples are beyond the limit of this thesis. Modern industrial society consume large amounts of materials in the production of durable consumer goods such as appliances. New technology for telecommunications, information generation and processing, storage and transmission of data, storage of energy, etc have stimulated the development and use of specialized materials. Photography, printing, medicine, etc. depend increasingly on advanced materials. Only solid substances are generally being classified as **materials**. But some liquids, especially those used because of their physical properties, are also considered as materials, e.g. magnetic fluid. Thus, materials science is one of the most multidisciplinary fields in science and engineering and it is one of the most applied and uti-

lizable science in day-to-day life. Among the different types of materials, transition metal oxides are known for their various kinds of applications on human life. These transition metal oxides play a very crucial role in the field of ceramics, electronic materials, magnetic materials, semiconductors, oxide-composites, etc., exhibiting interesting properties.

1.2 Magnetic Materials

Magnetism, the power of attracting iron by a material, was known to mankind for centuries before Christ. The oldest magnetic material or simply **the magnet**, the so called magnetite (Fe_3O_4), is a mineral which was initially found in the district of Magnesia of the modern Turkey. The word *magnet* is a Greek word, and thought to come from the name of the district. In general, a magnet is known for its attraction towards iron, nickel and cobalt and also known that a piece of iron can become magnetic if it were touched or rubbed with **the magnet**. Later on, it was found that a freely hanging magnetic needle automatically orients towards the north-south pole direction of the Earth.

In any material, the origin of magnetism lies in the orbital and spin motions of electrons and how the electrons are distributed in the orbitals and interact with one another. The interesting fact is that, all materials are magnetic. It's just that some materials are more 'magnetic' than others. The main distinction is that in some materials there is no collective interaction of atomic magnetic moments, whereas in other materials there are very strong interactions between atomic moments. The best way to introduce different types of magnetism is to describe how materials respond to magnetic fields. In general, preferably Fe, Co, Ni, Dy, Gd, CrO_2, MnAs, MnBi, ferrites, and some alloys are named as magnetic materials. Magnetic materials are used in various applications, eg. in power conversion from electrical to mechanical or vise versa (motors, generators, electromagnets), power adaption (power transformers), signal transfer (low and high frequency transformer), magnetic field screening, permanent magnets (loudspeaker, small generators, small motors, sensors), data storage analog (video tape, audio tape), data storage digital (ferrite core memory, drum hard disc, floppy disc, bubble memory), quan-

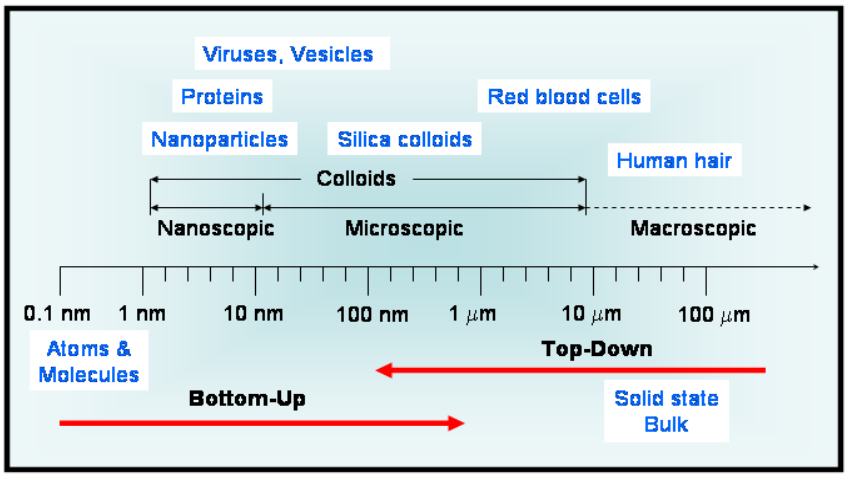

Figure 1.1: Approaches to nanoscale structure from reference [30].

tum devices (GMR read head, MRAM), unidirectional microwave devices (ferromagnetic resonance), memory loop, etc. Some of the widely used permanent magnetic materials are magnetite, magnetic carbon steel, alnico magnets (alloys based on Al, Co, and Ni), cobalt platinum magnets, hard ferrite magnets ($BaFe_{12}O_{19}$ or $SrFe_{12}O_{19}$), samarium cobalt, neodymium iron boron magnets, and samarium iron nitride. After the discovery of oxide ferrimagnetic materials (ferrites, garnets, etc) in the early 1940's, they occupy a key position among the technologically important magnetic materials. In simple words, without magnetic materials, we can not think about modern technological revolutions.

1.3 Magnetic Nanomaterials

The present trend in materials science is the studies on materials in the nanometer size. The main emphasis is on the synthesis, characterization, study the differences in the properties with respect to the corresponding bulk counter parts and on the application of nanomaterials for the benefit of human kind [1–5]. It is referred that 'small is beautiful' due the beautiful color, shape and properties of nanosized materials [6, 7]. Nanoscience

has become the focus of modern materials science because of the potential technological importance, which stems from the unique physical properties of nanomaterials [3, 5, 8, 9]. Fundamentally, all of nanoscience and nanotechnology is also a part of materials science. When the dimension (any) of a particle, when reached below 100 nm, is called a nanoparticle. The nanosized materials are distinguished from bulk polycrystalline materials by the size of the crystallite that compose it. A nanocrystalline material might be a ceramic, metallic, oxide, semiconducting material or an alloy. An overview of the typical dimensional ranges of various materials approaching the nanosize region are shown in Figure 1.1. When bulk materials are reduced to nanometer range, changes in several physical properties take place [10–17]. In general, nanoceramics and nanocomposites become better electrical conductors and nanosized metal particles become electrically more resistive. Blue-shift of the optical absorption is observed for quantum-confined crystallites. In the case of magnetic materials, at a particular critical particle diameter (D_c) the nanoparticles show highest coercivity and superparamagnetic behavior below this size. Nanoparticles have higher surface to volume ratio, hardness and strength as compared to that of the bulk. The interesting and sometimes unexpected properties of nanoparticles are partly due to the aspects of the surface of the material dominating the properties in lieu of the bulk properties. The percentage of atoms at the surface of a material becomes significant as the size of the material approaches the nanoscale. The nanomaterials can be shaped as nanospheres, nanorods, nanocups, nanowires, nanotubes, nanoribbons, nanoplates, nanocubes, and many more by specialized synthesis procedures. Depending on the enhanced properties of the nanomaterials compared to the bulk, several high quality applications have been predicted [18–30]. Some of the already applied and some predicted applications of nanoparticles are: information storage [31–33], refrigeration [34, 35], sensors [25, 36–40], targeted drug delivery [28, 41–45], tagging of DNA and DNA chips [46, 47], solar cells [48–50], water purification [51–54], catalysis [29, 55, 56], nanophotonics & optoelectronic [24, 57–60], etc.

Nanosized magnetic materials are of special interest [3, 5, 7] because the magnetic properties changes drastically when the size of a magnetic particle is reduced below 100

nm [13, 14, 61] and the modified properties are used (some are predicted) in some of the above mentioned applications and devices [62, 63]. The expansion of research in the area of magnetic nanomaterials is driven by the extensive technological applications of magnetic nanoparticles in high density magnetic data storage arrays, magneto-optical switches, and targeted drug delivery. Nanoparticles of magnetic metals are also finding applications as catalysis, nucleators for the growth of high-aspect-ratio nanomaterials, and toxic waste remediation. Efforts are being made to study nanoscale magnetic materials ranging from inorganic metal clusters to single molecular magnets [3, 5]. Thus, investigation on magnetic nanoparticles is a subject of intensive research from the viewpoint of probing their magnetic behavior (size and surface effects) and applications [64–73]. Some of the major applications of magnetic nanoparticles are: in information storage where single nanoparticle can act as an individual bit of information providing high density data storage [13,32,33,61]; in magneto-optical switches, sensors based on GMR, magnetically controllable single electron transistor device [74–76]; in magnetic resonance imaging (MRI), detection of biomolecular interactions, detection of DNA hybridization [77–80]; diluted magnetic semiconductors [81, 82]; toxic waste and water treatment [51, 52], etc. There are several methods classified for the synthesis of nanoparticles of magnetic metals or alloys or metal oxides [1, 3]. Some of the methods are commercially employed. Thus, developing new routes for the synthesis of the nanoparticles and the investigation of their properties are of great importance. The magnetism of fine particles is dominated by two factors:

- There is a size limit below which the specimen can no longer gain a favorable energy configuration by breaking into domains and hence it remains single domain.
- The thermal energy can decouple the magnetization from the particle itself to give rise to superparamagnetism.

1.4 Magnetism

In the history of scientific study on magnetism, several scholars made efforts and remarkable discoveries to understand magnetism in depth. In 1820, Hans Christian Oersted discovered that an electric current produces a magnetic field. Based on this discovery, the first electromagnet was made in 1825.

There are various phenomenons and terms related to magnetism. Magnetic moment is an important and fundamental quantity. It is defined as, in a uniform magnetic field H, if a magnetic pole of strength p is placed at an angle θ to another pole and separated by a distance l, then a couple acts on the magnet, called as magnetic moment (m), and is given by

$$m = (pHsin\theta)(l/2) + (pHsin\theta)(l/2) = (pHlsin\theta) \tag{1.1}$$

If $H = 1$ Oe and $\theta = 90°$,

$$m = pl \tag{1.2}$$

The magnetic moment per unit volume is called intensity of magnetization or simply magnetization and is given by

$$M = \frac{m}{V} \tag{1.3}$$

where V is the volume of the material. The specific magnetization is defined as

$$\sigma = \frac{m}{W} = \frac{m}{V\rho} = \frac{M}{\rho} emu/g \tag{1.4}$$

where W is the mass and ρ is the density of the material. The magnetic properties of a material are characterized not only by the magnitude and sign of M, but also the way in which M varies with H.

The magnetization per unit magnetic field is called the magnetic susceptibility (χ).

$$\chi = \frac{M}{H} emu/cm^3Oe \tag{1.5}$$

χ is also called volume susceptibility. Depending on the values and orders of susceptibility, substances are divided into certain categories. The most significant ones are paramagnetism, ferromagnetism, ferrimagnetism, antiferromagnetism and superparamagnetism [83, 84].

1.4.1 Paramagnetism

A paramagnetic substance consists of atoms or ions, each of which has a net magnetic moment μ. In the absence of an applied magnetic field, these atomic moments point at random and cancel each other, so that the net magnetization of the substance is zero. When a field is applied, there is a tendency for each atomic moment to turn toward the direction of the field. If there is no opposing force, complete alignment of the atomic moments would be produced and as a whole, the specimen would gain a very large magnetic moment in the direction of the field. But thermal agitation opposes this tendency and tends to keep the moments pointed at random. Therefore, only a partial alignment of the moments will be possible in the field direction, and as a result a small positive susceptibility could be seen. The effect of an increase in the temperature is to increase the randomizing effect of thermal agitation and therefore to decrease the susceptibility [83].

In 1895, the French Physicist Pierre Curie first reported about the variation of paramagnetic susceptibilities with temperature. He stated that, mass susceptibility of a paramagnetic substance varies inversely with the absolute temperature and this is mathematically given by

$$\chi = \frac{C}{T} \tag{1.6}$$

This equation is known as Curie's law, where C is the Curie constant. But Curie's law has some drawbacks. In this theory, it is assumed that individual magnetic moments do not interact with each other, but acted only by the applied magnetic field and thermal agitation. In 1907, Weiss modified this law by employing the idea of a molecular field 'H_m'. This term is the internal field inside a material and acted in addition to the applied field H. Thus

$$H_m = \gamma M \tag{1.7}$$

where γ is called the molecular field constant. Therefore, the total field in the material

$$H_t = H + H_m \tag{1.8}$$

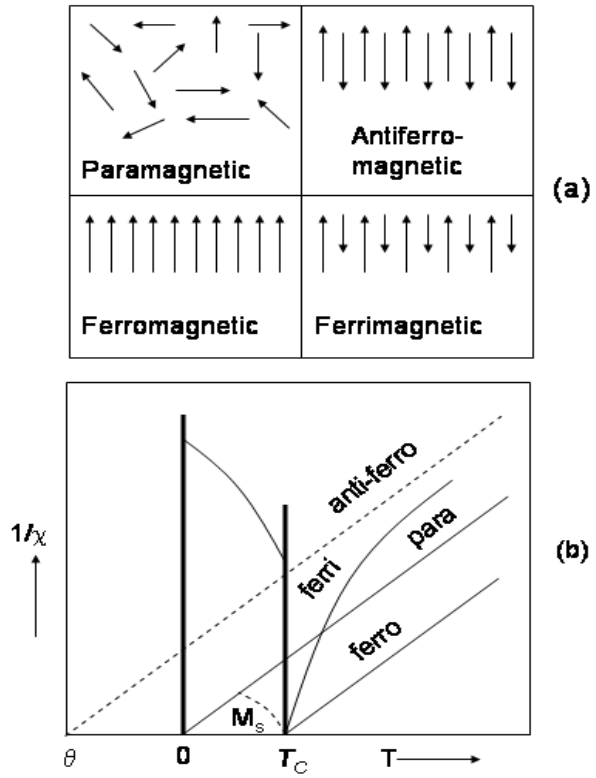

Figure 1.2: (a) Alignment of the magnetic moments in different magnetic materials and (b) variation of inverse susceptibility with tempertaure of para-, antiferro-, ferro- and ferri-magnetic materials.

Solving for these equations and Curie's law, Weiss postulated that

$$\chi = \frac{M}{\rho H} = \frac{C}{T - \rho C\gamma} = \frac{C}{T - \Theta} \tag{1.9}$$

This equation is known as the Curie-Weiss law, where Θ is a measure of the strength of the magnetic interactions. For substances obeying Curie's law, $\Theta = \gamma = 0$. The alignment of magnetic moments and the variation of the paramagnetic susceptibility with temperature is shown in Figure 1.2.

1.4.2 Ferromagnetism

Ferromagnetism is a property exhibited by certain metals, alloys, and compounds of the transition metal ions (iron group), rare-earth, and actinide elements in which, below a certain temperature called the Curie temperature, the atomic magnetic moments tend to line up in a common direction. In a ferromagnetic substance, within a region, all the atomic moments are essentially aligned giving a net magnetic moment even after the removal of the external magnetic field [84]. Ferromagnetic materials are like paramagnets above the T_C. The alignment of the magnetic moments and the temperature variation of the susceptibility of a ferromagnetic material is shown in Figure 1.2.

1.4.3 Antiferromagnetism

In the case of antiferromagnetic substances, the individual magnetic moments align in a regular pattern with neighboring moments pointing in opposite directions. Below the characteristic temperature, called the Neel temperature, T_N, the two sublattices of an antiferromagnet spontaneously magnetize in the same way as in a ferromagnet but the net magnetisation is zero due to the opposing orientation of the sublattice's magnetisation. If an external field, H, is applied, a small net magnetisation can be detected. The resultant magnetization depends upon the orientation of the field with respect to the magnetization axis. Antiferromagnetic materials are like paramagnets above the T_N. The alignment of the magnetic moments and the temperature variation of the susceptibility of an antiferromagnetic material is shown in Figure 1.2.

1.4.4 Ferrimagnetism

Ferrimagnetism is a phenomenon, where there can be incomplete cancelation of antiferromagnetically arranged moments giving a net magnetic moment. Or else, ferrimagnetism is called uncompensated antiferromagnetism [83, 85]. Ferrimagnetic materials are like paramagnets above the T_C, and are like ferromagnets in the sense that they can hold a spontaneous magnetization below T_C. Ferrimagnetism is exhibited by ferrites and mag-

netic garnets. The oldest-known magnetic substance, magnetite, is a ferrimagnet. The alignment of the magnetic moments and the temperature variation of the susceptibility of a ferrimagnetic material is shown in Figure 1.2.

1.4.5 Superparamagnetism

Superparamagnetism is a phenomenon observed in very fine magnetic particles, where the energy required to change the direction of the magnetic moment of a particle is comparable to the ambient thermal energy. At this point the rate becomes significant, at which the particles will randomly move in reverse direction. This is particularly important in the field of hard disk technology, where the superparamagnetic effect limits the minimum size of the particles that can be used [86]. Current hard disk technology with longitudinal recording has an estimated limit of 100 to 200 Gbit/sq. inch, though this estimate is constantly changing [87]. Some other commercialized applications of superparamagnetism or superparamagnetic particles are in magnetic resonance imaging (MRI); cell, DNA, and protein separation; RNA fishing; targeted drug delivery; magnetic hyperthermia; magnetofaction; tunable viscosity (ferro-fluid); high sensitivity sensors (GMR), etc [88–91].

Nanosized magnetic materials exhibit a behavior similar to paramagnetism at temperatures below the Curie or the Neel temperature. It is half-way between ferro and paramagnetism. In this case, below the Curie or Neel temperature, the thermal energy is not sufficient to overcome the coupling forces between neighboring atoms, where as the energy is sufficient to change the direction of the magnetization of the entire crystallite. The resulting fluctuations in the direction of magnetization cause the magnetic moments average to zero [92]. Thus, the material behaves in a manner similar to paramagnetism, except that instead of each individual atom being independently influenced by an external magnetic field, the magnetic moment of the entire particle tends to align with the magnetic field. Thus, these particles are called superparamagnetic particles. Superparamagnetism occurs when the material is composed of very small crystallites (1-10 nm). Magnetocrystalline (K_1) anisotropy is an intrinsic property of a magnetic material, which

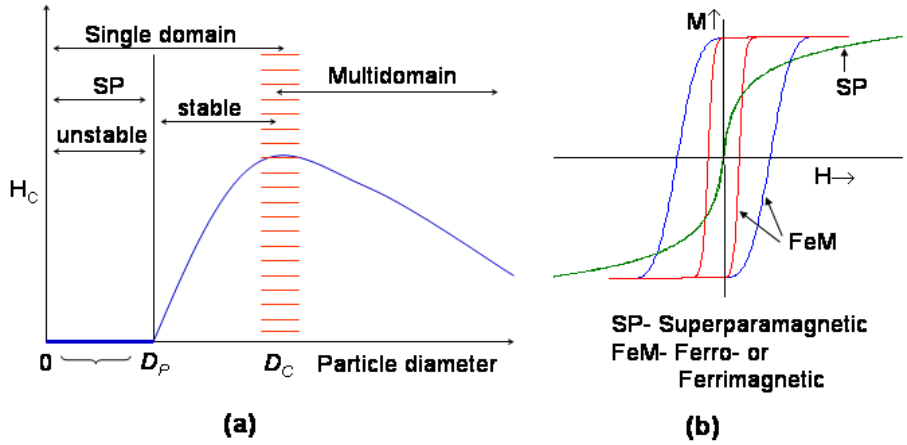

Figure 1.3: Variation of the coercivity of magnetic particles with particle diameter, and comparison of magnetization curves of typical ferro, ferri and superparamagnetic substances.

is caused by the spin-orbit interaction of the electrons. K_1 is expressed as

$$K_1 = 25kT/V_{sp} \tag{1.10}$$

where k is the Boltzmann constant and V_{sp} is the volume of a superparamagnetic particle. Above a particular temperature, kT is dominates and this temperature is called blocking temperature (T_B). Below a particular size (called critical particle diameter, D_c), the particles become single domains, and in this particle size range the coercivity reaches a maximum. Below a critical diameter the coercivity become zero, because of thermal effect, which are strong enough to spontaneously demagnetize the previously saturated assembly of particles [93]. The variation of the coercivity of magnetic particles with particle diameter, and comparison of magnetization curves of typical ferro-, ferri- and superparamagnetic substances are shown in Figure 1.3.

1.4.6 Magnetic exchange interactions

Ferromagnetic, ferrimagnetic and antiferromagnetic materials exhibit *long-range ordering* of the moments in the lattice. The long range ordering arises mainly due to three types of exchange interactions between the magnetic dipoles; direct exchange, indirect or superexchange and double exchange [94].

The direct exchange depends on the exchange integral between two neighboring dipoles as follows

$$E_{ex} = -2J_{ex}\mathbf{s}_1.\mathbf{s}_2 = -2J_{ex}s_1s_2cos\theta \tag{1.11}$$

where E_{ex} is the energy of exchange, J_{ex} is the exchange integral, s_1 and s_2 are neighboring spins and θ is the relative angle between them.

In transition metal compounds, the magnetic cations are intervened by the anions, and therefore direct exchanges are not possible. The two main indirect coupling of magnetic moments are the 180° and 90° *cation-anion-cation superexchange*. Depending on the nature of the t_{2g} and e_g orbitals (considering an octahedral crystal field) of cations, the coupling results in different types of magnetic ordering, e.g. if both e_g orbitals are half-filled, then antiferromagnetic alignment and if one is empty with the other half-filled, then ferromagnetic alignment results. The sign of the superexchange interactions can be predicted using the Goodenough-Kanamori rules [94].

In 1951 Zener proposed another exchange mechanism to explain the experimentally observed ferromagnetism in some doped perovskite manganites [95]. This double exchange mechanism is based on the electron transfer from Mn^{3+} to Mn^{4+} via oxygen atoms between neighboring Mn^{3+} and Mn^{4+} ions, but different from superexchange by the involvement of carriers.

1.5 Magnetic Materials Related to the Present Work

1.5.1 Diluted magnetic semiconductors

Semiconductors are materials whose electrical resistance is in between that of a metal and an insulator. The well known examples are the elemental semiconductors silicon and germanium as well as the compound semiconductors CdS, GaAs, etc. Semiconductor electronics is based on the manipulation of the charge of an electron. In semiconductors, the number of electrical charge carriers can be manipulated and controlled by doping with other suitable elements and depending on the applications. Semiconductors have been in use since the 1960s and the present age of technological advancement has made semiconductor research and development a huge market. The present day interest in semiconductors is in the development of smallest, fastest and cheapest microchips for use in computers, cellphones and other electronics components. They have become essential components for the developments in telecommunications, computers and military applications. Modern scientific research is aiming at improving and enhancing the capabilities of semiconductors in electronics.

Spintronics is the latest development in the area of electronics and diluted magnetic semiconductors are a remarkable class of materials where magnetic ions are incorporated into semiconductor host lattices [96–106]. Spintronics is the branch of science dealing with the active manipulation of spin degrees of freedom in solid state materials. In a conventional semiconductor, it is the charge of an electron which is relevant. However, an electron is associated with its own spin also, which is responsible for the magnetic properties of materials. In spintronics (spin+electronics) both the charge and the spin of an electron are made use off [107–111].

In general, most of the semiconductors commonly used are nonmagnetic, where no magnetic elements are present, such as the commonly used semiconductors Si, GaAs, GaN, ZnS, ZnO, etc. Semiconducting and magnetic properties are known to coexist in some antiferromagnetic and ferromagnetic substances. In a magnetic semiconductor, the electrical properties are greatly affected by the magnetic ordering. In fact, ferromagnetic

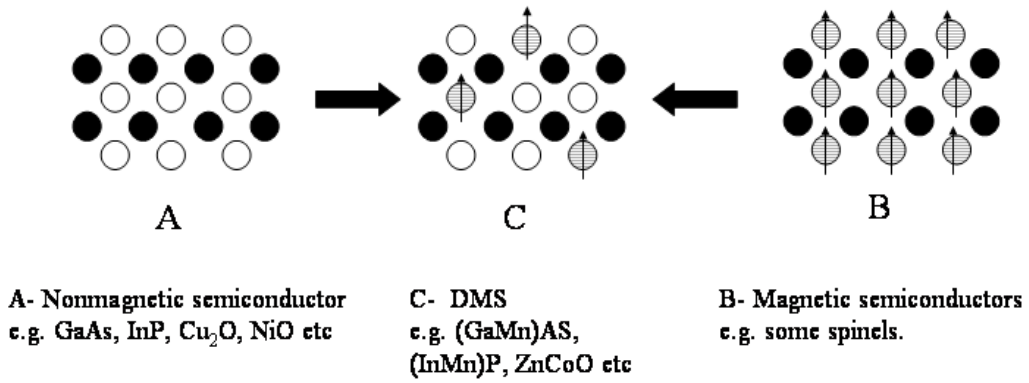

Figure 1.4: Schematic representation of (A) nonmagnetic semiconductor, (B) magnetic semiconductor, and (C) diluted magnetic semiconductor. The open circles are nonmagnetic element I, filled circles are nonmagnetic element II and arrowed circles are magnetic element III.

semiconductors were not known until 1960 and it was thought that ferromagnetic and semiconducting properties were incompatible. But extensive research made it possible that the nonmagnetic semiconductors used in electronics can be made magnetic by the incorporation of suitable magnetic impurities in their crystal lattice [112]. In such magnetic semiconductors, the amount of the magnetic component is in very small amounts and hence they are known as semimagnetic semiconductors (SMSC) or diluted magnetic semiconductors (DMS) [101, 113–115]. The wide variety of both host crystals and magnetic atoms provides materials which range from wide gap to zero gap semiconductors, and which reveal many different types of magnetic interactions. Several of the properties of these materials may be tuned by changing the concentration of the magnetic ions. In a DMS, the net electronic (spin plus orbital) angular momentum of the individual magnetic dopants are coupled ferromagnetically by free charge carriers. Such materials have spin polarized state in either the valence or the conduction bands. These mixed compounds contain two different types of interacting subsystems, the delocalized conduction and va-

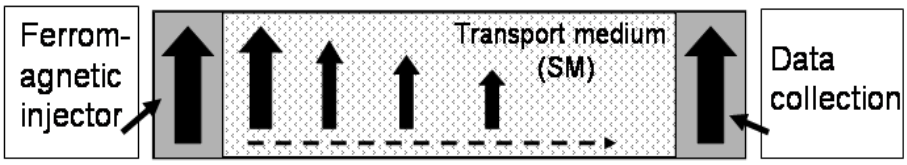

Figure 1.5: Schematic representation of the processes involved in spintronics devices.

lence band electrons, and the diluted system of localized magnetic moments associated with the magnetic atoms. These new functional materials exhibit inherent properties from the charge and spin of an electron in a single material and the ability of DMSs to combine their transport and optical properties with magnetism can be made use of in spintronics. The diluted magnetic semiconductor is an alternative to the magnetic semiconductors and the non-magnetic semiconductors, in which the non-magnetic semiconductor is made magnetic by doping with some magnetic impurities. All three categories of semiconducotrs are shown schematically in Figure 1.4 and the processes taking place in a DMS material are shown schematically in Figure 1.5.

A change in the concentration of the magnetic ions can alter the magnitude of several magneto-optical effects and influences the magnetic properties of the material. There are several reasons that DMS materials become so important; i) information is stored (written) into spins as a particular spin orientation (up or down), ii) the spins, being attached to mobile electrons, can carry the information along a wire, iii) the information is read at a terminal, and iv) spin orientation of conduction electrons survives for a relatively longer time and this makes spintronics devices particularly attractive for memory storage, magnetic sensor applications, etc. All these important issues can make the DMSs for some predicted potential applications like photonics plus spintronics, improved spin transistor, transistors spinning toward quantum computing, magnetic spins to store quantum information, microscope to view magnetism at atomic level, ballistic magnetoresistance,

missile guidance, fast and accurate position and motion sensing of mechanical components in precision engineering, in robotics, in automotive sensors and many more.

The field of DMS received a considerable attention when a few years ago Ohno *et al.* doped Mn ions into GaAs, and found Curie temperature above 100 K [112]. This temperature is far less than room temperature (∼300 K) and therefore is not sufficient for applications. However, the progress in this area is very rapid and room temperature ferromagnetism could be achieved with considerable amount of doping, in the near future. Apart from the reports on GaAs [97, 98, 100, 103, 107, 109], ferromagnetism above room temperature for the III-V system is reported for GaN [114, 116, 117], InAs [118, 119], InN [120, 121] etc. In 1999, Fiederling *et al.* [122] and Ohno *et al.* [123] successfully showed the controlling of polarization of light by using ZnSe and GaAs based DMSs, respectively, as the spin polarizer in a p-(i)-n junction.

(Ga,Mn)As and (Ga,Mn)N are the most widely studied magnetic semiconductors. Although the crystal structure and typical Mn concentrations studied are very similar, the magnetic mechanisms turn out to be different in the two systems. In both the materials Mn atoms are substituted for Ga which are tetrahedrally coordinated to four As or N atoms in the unit cell. The Mn atom provides a magnetic moment of 4 Bohr magnetons/ Mn atom. However, in (Ga,Mn)As the Mn atom is a shallow acceptor providing delocalized holes, whereas in (Ga,Mn)N the Mn atom behaves like a deep trap acceptor. Both the materials exhibit ferromagnetism: in (Ga,Mn)As ferromagnetism is hole mediated related to the delocalized Mn induced hole states, while in (Ga,Mn)N ferromagnetism is related to the strongly localized magnetic moments related to the Mn atoms. The electronic state of the Mn impurity in (Ga,Mn)As in the dilute limit has been shown to be $3d^5$ positive hole with antiferromagnetic *p-d* coupling [124, 125]. Matsukura *et al.* showed from the magnetoresistance and the concentration dependance of T_C that (Ga,Mn)As with higher Mn concentration is a metallic ferromagnet.

Figure 1.6 shows the predicted Curie temperature as a function of the band gap for some of the important semiconductors. As per the predictions, ZnO when doped with suitable magnetic impurities can attain Curie temperatures above room temperature.

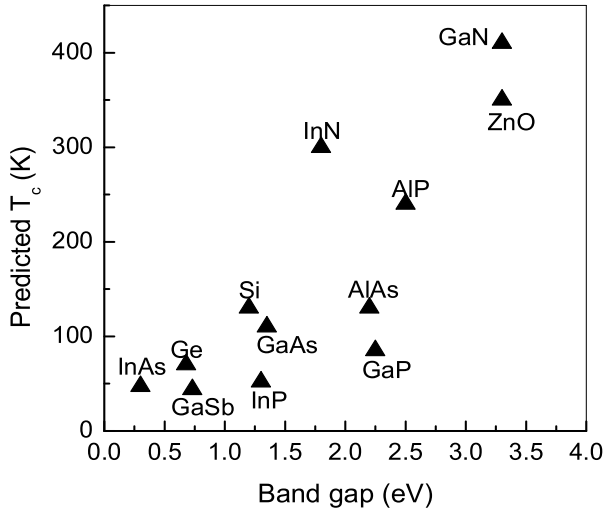

Figure 1.6: Predicted Curie temperature, as a function of the semiconductor band gap [128].

Therefore, apart from the III-V semiconductors based DMSs, considerable attention has also been focused on the studies on oxide based semiconductors such as ZnO, TiO_2, SnO_2 and Cu_2O. Among them doped ZnO is the widely studied DMS system. Oxide materials are very stable to different atmospheres and conditions. Also, oxide based semiconductors are transparent to visible light and therefore, if magnetic semiconductors based on these oxides are realizable, they will serve as transparent semiconductors which can be controlled by magnetic and electric fields and are potential candidates for magneto-optical applications.

From the *ab initio* calculations on ZnO based DMSs, it has been shown that when 3d transition metal atoms (V, Cr, Mn, Fe, Co and Ni) are doped in ZnO, ferromagnetism is possible without any additional carrier doping treatments [126, 127]. It was found that among the different transition metal doping, $Zn_{1-x}Mn_xO$ shows the highest magnetic moment per one transition metal atom [128]. The calculated total magnetic moment per one transition metal atom is shown in Figure 1.7 based on the generalized gradient approximation (GGA) [129]. Based on these theoretical calculations, several experimental

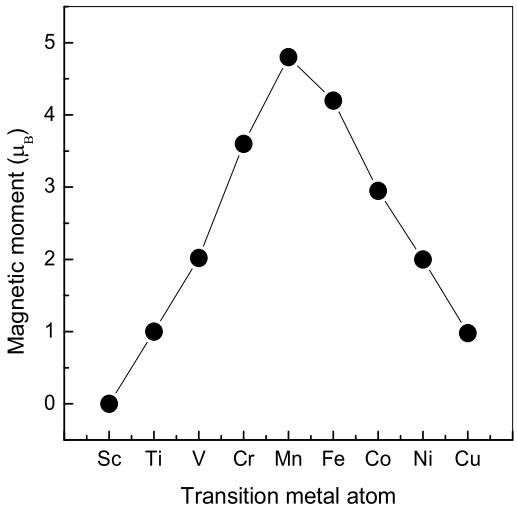

Figure 1.7: Calculated magnetic moment per one transition metal atom, in $Zn_{1-x}TM_xO$ [129].

investigations have been carried out by different researchers on this II-VI semiconductor [100–102, 105, 114]. The importance of ZnO is its identical crystal structure and almost identical band gap as that of GaN of the III-V system. The hexagonal wurtzite stucture of ZnO [130] is shown in Figure 1.8.

Most of the studies on ZnO based DMSs have been carried out on thin film samples, whereas very few experiments are performed on polycrystalline samples. The first experimental result on the doping of transition metal (TM) in n-type ZnO was reported in 2001 [131]. In this report 3d transition metal doped ZnO thin films were formed on sapphire substrates using a pulsed-laser deposition (PLD) technique. The concentration of doped transition metals, Co, Mn, Cr and Ni were within the range $0.05 \leq x \leq 0.25$ in $Zn_{1-x}Mn_xO$. Interestingly, it was found that few of the Co doped films were ferromagnetic with Curie temperature nearly 300 K, whereas Mn, Cr and Ni doped ZnO films were nonmagnetic. Moreover, reproducibility of magnetization in the ferromagnetic films were very less. After this report, several efforts have been made to obtain room temperature ferromagnetism in $Zn_{1-x}Mn_xO$ thin films. A T_C higher than 350 K is reported when Co

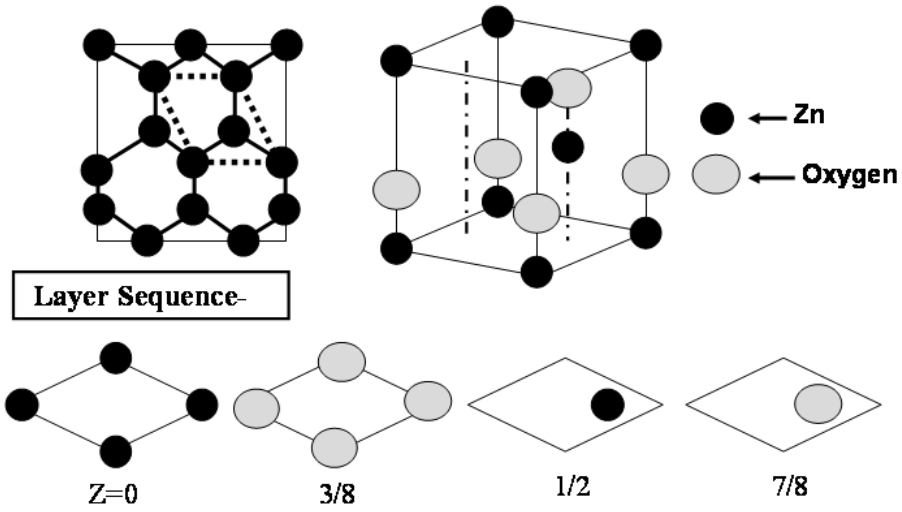

Figure 1.8: Crystal and layered structure of wurtzite ZnO [130].

is doped in ZnO [132]. Following these initial reports, thin films of $Zn_{1-x}TM_xO$ (TM = transition metal) were grown by various techniques, including PLD, radio frequency magnetron co-sputtering, sol-gel method and combinational laser molecular epitaxy methods. There are various reports on the observation of ferromagnetism near or above room temperature [81, 82, 132–142], as well as on the absence of ferromagnetism even at low temperatures [143–151] in the *TM* doped oxide semiconductors. At the same time, reports are available questioning the methods of sample preparation [152–154]. There are few reports where metal clusters or secondary phases have been shown as the origin of ferromagnetism [155–157]. Very recently, it has been shown that, hydrogen-induced ZnCoO thin films can be ferromagnetic at low temperatures [158]. A carrier-mediated double exchange mechanism is proposed for the observed ferromagnetism, where hydrogen in ZnO has been suggested to be a shallow donor impurity and therefore it is expected to provide extra conduction electrons.

Similarly, large numbers of studies has been made on the TiO_2 based diluted magnetic

semiconductors also [159–166]. Curie temperatures as high as 1000 K has been reported for transition metal doped TiO_2. However, as in the case of ZnO based DMSs, the reproducibility rate is very poor and in certain cases ferromagnetic impurities are observed, questioning the validity of many reports [167–172]. *TM* doped SnO_2 [173–175] and Cu_2O [176–178] have also been found to be ferromagnetic at room temperature, but still the origin of ferromagnetism in these systems is not clear.

Magnetic interactions in DMS

There are several models put forwarded to explain the origin of ferromagnetism in DMSs. The carrier-induced ferromagnetism, which originates from the Ruderman-Kittel-Kasuya-Yosida (RKKY) interaction is a prominent model used to explain the high Curie temperatures in (Ga,Mn)As DMS [108, 112]. This refers to a coupling mechanism of nuclear magnetic moments or localized inner d shell electron spins in a metal by means of an interaction through the conduction electrons [179]. Indirect exchange couples moments over relatively large distances. It is the dominant exchange interaction in metals where there is little or no direct overlap between neighboring magnetic electrons. It therefore acts through an intermediary which in metals are the conduction electrons. The RKKY interaction is characterized by a coupling coefficient, j, given by

$$j(R_l - R_{l'}) = 9\pi \frac{j^2}{\epsilon_F} F(2k_F \mid R_l - R_{l'} \mid) \tag{1.12}$$

where k_F is the radius of the conduction electron Fermi surface, R_l is the lattice position of the point moment and ϵ_F is the Fermi energy .

The near-field model (Zener model) in a DMS considers that ferromagnetism is mediated by delocalized or weakly localized holes in p-type materials [128]. This model takes into account the anisotropy of the carrier mediated exchange interaction related with the spin-orbit coupling in the host material and the Curie temperature is proportional to the density of the Mn ions and the hole density.

There are also other theoretical models put forwarded to explain the origin of ferro-

magnetism, such as the double resonance mechanism where the resonant states are formed at the top of the down spin valence band due to magnetic impurities and this gives rise to a strong and long-ranged ferromagnetic coupling between the Mn moments [180]. Positional disorder mechanism is also put forwarded to explain the origin of ferromagnetism in DMSs [181]. Furthermore, there are several other models reported based on theory and experiments [98, 107, 118, 182–184].

Optical and electrical properties

Apart from magnetic properties, optical and electrical properties are also very important for a DMS system. Optical properties give the evidence for incorporation of the transition metal ions inside the host lattice. Transition metal compounds are well known for their beautiful colors due various electronic transitions. The important one, which deals with DMSs is the d–d transition. On the substitution of *TM* ions in various environments (e.g. tetrahedral, octahedral, etc) of the host lattice, various spin allowed transitions will appear. These transitions correspond to characteristic optical absorption in the UV-Vis region [185]. Therefore, the optical absorption studies directly give information on the incorporation of *TM* ions and their oxidation states inside the semiconductor host. Moreover, optical band gap, which is of particular interest for a semiconductor, is also obtained from optical investigations. Electrical properties, mainly resistivity and magnetoresistance, are also topics of interest for DMS materials. On the other hand, Hall effect measurement is carried out to find out the nature and concentration of charge carriers.

1.5.2 Ferrites

Mixed metal oxides with iron (Fe) as their main component are known as ferrites. Ferrites are the crucial example of ferrimagnetic materials. Ferrites are the most important magnetic materials without which we can not think about technological revolution. These are very well established group of magnetic materials of the transition metal oxides [186]. Ferrites are used virtually in all application areas and in some cases, there are no other

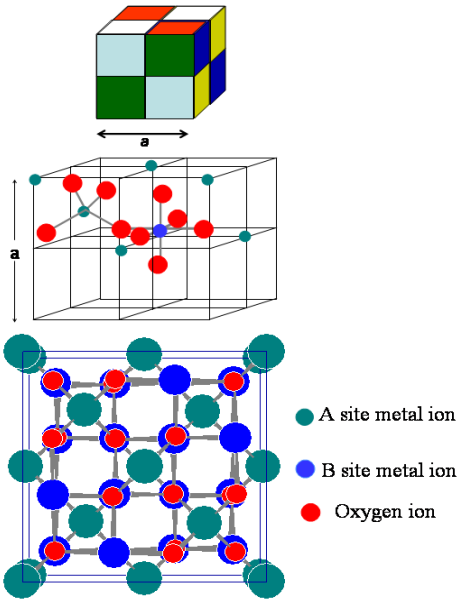

Figure 1.9: Cubic crystal structure of spinel-ferrite representing A- and B-sites.

practical alternative materials. The naturally abundant ferrites are magnetite (Fe_3O_4) and maghemite (γ-Fe_2O_3). Prof. Takeshi Takei is truly regarded as the 'father' of modern ferrites, whose pioneering efforts in the early 1930's gave ferrites a new dimension. Later, Dr. Alex Goldman involved in the field of ferrites and became responsible for various improvements on the properties of ferrites.

Bulk, ferrites are used in permanent magnets, inductors, power transformers, channel filters, magnetic recording heads, loading coils, loud speakers, electric motors, stepping motors, pulse transformers, flyback converters, push-pull converters, catalysis, surface chemistry, waveguide in microwave region, etc [85, 187–189]. Ferrites crystallize mainly in three different crystal types, namely, spinel, garnet and magnetoplumbite. In this thesis, the ferrites studied are having the spinel structure (from the mineral spinel, $MgAl_2O_4$) and will be called simply ferrites through out the thesis.

Structure

The crystal structure of spinel ferrite can be regarded as an interlocking network of positively charged metal ions and negatively charged divalent oxygen ions. Spinels belong to the AB_2O_4 family of oxides [190]. Spinel ferrites have the general chemical formula $A^{2+}Fe_2{}^{3+}O_4{}^{2-}$ or $A^{2+}O^{2-}.Fe_2{}^{3+}O_3{}^{2-}$ where A^{2+} is a divalent metal ion and Fe is trivalent. The spinel ferrite crystalizes in the cubic system and the structure was first determined by Bragg [191] and Nishikawa [192]. Spinel ferrites are very stable due to their stable crystal structure, and they are predominantly ionic. The crystal structure is best described by subdividing the unit cell into 8 octants, with edge $a/2$ (a is the lattice parameter) as shown in Figure 1.9. The unit cell contains 8 formula units or each octant contain 1 formula unit and may thus be written as $M_8Fe_{16}O_{32}$. The oxygen anions form an ideal face-centered cubic (fcc) lattice. Within this lattice two types of intersticial positions occurs viz. tetrahedral and octahedral, which are depicted pictorially in Figure 1.10. There are 64 tetrahedral sites and 32 octahedral sites available, and, out of these 8 tetrahedral and 16 octahedral sites are occupied by cations. Each cation in the tetrahedral position has 4 neighboring oxygen ions and is often called an A site, while each cation in the octahedral position has 6 neighboring oxygen ions and is called a B site, in the genral formula AB_2O_4. The oxygen (O) ions have a four-fold coordination, formed by three B cations and one A cation. The different coordination environments of A, B and O are shown in Figure 1.10. The spinel ferrite space group is $O_h{}^7$ ($Fd3m$) [130, 193] and the space group number is 227. The oxygen ions in the ferrite structure are not generally located at the exact position of the *fcc* sublattice. Their detailed positions are determined by a parameter, u, called the oxygen parameter. u reflects the adjustments of the structure to accommodate difference in the radius ratio of the cations in the tetrahedral and octahedral sites [186, 194]. Packing of the ions within the lattice is perfect when $u = 3/8$.

The different properties of ferrites are governed by the cation distribution i.e. the distribution of iron and the divalent metal ions among the tetrahedral and octahedral

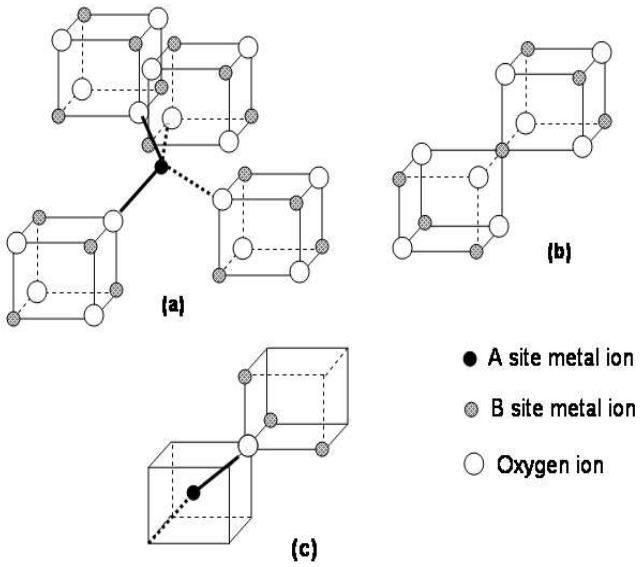

Figure 1.10: Corner sharing of A- and B-site metal ions and oxygen ions [194].

sites of the spinel lattice. The distribution of different cations can be generalized as $M_{1-x}{}^{2+}Fe_x{}^{3+}[M_x{}^{2+}Fe_{2-x}{}^{3+}]O_4$ where the ions inside the square brackets [ ] are located in the octahedral sites and the ions outside the brackets are in the tetrahedral sites. When $x = 0$, the spinel is called a normal spinel, eg. $ZnFe_2O_4$, $CdFe_2O_4$, etc. When $x = 1$, the spinel is called an inverse spinel, eg. Fe_3O_4, $CoFe_2O_4$, $NiFe_2O_4$, etc. On the other hand if $0 \leq x \leq 1$, it is called a mixed spinel, eg. $MgFe_2O_4$, $MnFe_2O_4$, etc. In most of the mixed ferrites, two or more types of divalent metal ions may be present, eg. NiZn ferrite, MnZn ferrite, NiCoZn ferrite, NiCuZn ferrite, etc. In some cases, the divalent ion may be replaced by monovalent+trivalent ions, while still retaining the spinel structure, eg. $Li^+_{0.5}Fe^{3+}_{0.5}[Fe^{3+}_2]O_4$. The cation distribution over the two different sites is dependent on the methods of synthesis and is variable with temperature. By changing the existing cation distribution one can change the interesting magnetic (eg. change in Curie temperature) and electrical (eg. change in resistivity) properties of spinel ferrites and can be used for some new applications. There are several factors which determine the cation distribution.

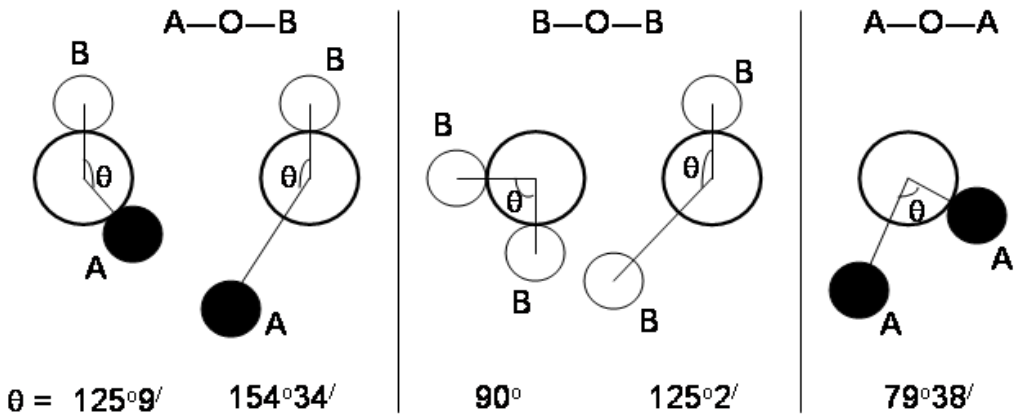

Figure 1.11: Different types of interactions for different types of lattice sites in ferrite [188].

These are i) ionic radius, ii) electronic configuration, iii) electrostatic energy (Madelung energy), iv) elastic energy, v) polarization effect, vi) covalent bonding effect, and the most important vii) crystal field stabilization energy.

Magnetism in ferrites

The exchange forces between the metal ions in a ferrimagnetic material will act through the oxygen ions by means of the indirect exchange mechanism, which is best known as the *superexchange* interaction. If there are n identical magnetic ions per unit volume, with a fraction x located on A site and a fraction y=(1-x) on B site with μ_A and μ_B as the average moments of A and B ions, respectively, in the the direction of the field at temperature T ($\mu_A \neq \mu_B$, being different sites), then the total magnetization on the two sublattices is

$$M = M_A + M_B = xM_a + yM_b \tag{1.13}$$

The molecular field acting on the sublattice A is

$$H_m A = -\gamma_{AB} M_B + \gamma_{AA} M_A \tag{1.14}$$

and molecular field acting on the sublattice B is

$$H_m B = -\gamma_{AB} M_A + \gamma_{BB} M_B \tag{1.15}$$

where M_A and M_B are the magnetization of the A and B sublattices, respectively. γ_{AA} and γ_{BB} define the strength of the A-A and B-B interactions and γ_{AB} defines that of the A-B interaction. In the equations 1.14 and 1.15, the molecular field coefficients γ are regarded as positive quantities and the negative sign corresponds to the antiparallel interaction between A and B ions, whereas the positive sign corresponds to the parallel interaction between the same site ions. The magnetization of each sublattice obeys the Curie law,

$$M_A = \frac{C_A}{T}(H + H_{mA}) \tag{1.16}$$

$$M_B = \frac{C_B}{T}(H + H_{mB}) \tag{1.17}$$

Since the Curie constants C_A and C_B are not identical for the two different sites, the above equations are modified by introducing the term density of ferrimagnetic materials on the right hand sides and now putting the values of H_{mA} and H_{mB} in equations 1.15 and 1.16, the magnetization on the two different sites are obtained as

$$M_A = \frac{\rho C_A}{T}(H + \gamma_{AA} M_A - \gamma_{AB} M_B) \tag{1.18}$$

and

$$M_B = \frac{\rho C_B}{T}(H + \gamma_{BB} M_B - \gamma_{AB} M_A) \tag{1.19}$$

After solving this two equations, the mass susceptibility, χ, of a ferrimagnetic material is obtained as

$$\chi = \frac{M}{\rho H} = \frac{T}{C} + \frac{1}{\chi_0} - \frac{K}{T - \Theta} \tag{1.20}$$

where $\mathrm{C} = \mathrm{C}_A + \mathrm{C}_B$ and K is a constant. Although θ has the dimension of temperature, it has no physical significance above the Curie temperature. Therefore,

$$\chi = \frac{C}{T - \Theta} \tag{1.21}$$

Thus, from equation 1.20, it is concluded that above the Curie temperature ferrimagnetic materials obey the Curie-Weiss law [83, 85, 195].

Magnetization in ferrites occurs from the uncompensated antiferromagnetism, so the magnitude of magnetization depends on composition, cation distribution and the relative strength of the possible interactions. Since cation–cation distances are large in ferrites due to their crystal structure, direct exchange interactions are negligible. The major interaction occurs in ferrites is the superexchange interaction between octahedral and tetrahedral cations or A–O–B interactions [85, 186, 188]. The next acceptable interaction is B–O–B superexchange. However A–O–A interaction is not coming into picture, as it is very weak [194]. The types of interactions in ferrite and the angle between them are shown in Figure 1.11 schematically. The strength of exchange interactions control the saturation magnetization and the Curie temperature of the ferrites and this exchange interaction is controlled by cation distribution. NiZn ferrite, $MnFe_2O_4$, $NiFe_2O_4$ and MnZn ferrites are extreme examples of interesting cation distributions.

NiZn ferrite: $Ni_{1-x}Zn_xFe_2O_4$ is the most versatile ferrite from the viewpoint of its large number of applications, due to its high value of magnetization, high permeability, low dielectric loss, high Curie temperature, high resistivity, simplicity and low cost in their preparation, etc [188]. The properties of these ferrites are highly sensitive to the cation distribution which in turn depends on the method of preparation and sintering conditions [196]. Recent interest in the study of several ferrites is in terms of their synthesis and sintering at low temperatures as well as in the study of nanosized ferrite materials for various applications [197–201]. Nanosized ferrites are useful with better performance in magnetic recording, catalysis, surface chemistry, biological applications, etc [202–204]. NiZn ferrite is a mixed spinel in which the tetrahedral (A) sites are occupied by Zn^{2+} and Fe^{3+} ions and the octahedral (B) sites are occupied by Ni^{2+} and Fe^{3+} ions in the spinel formula AB_2O_4. It is found that for x greater than 0.5 the tetrahedral and octahedral (B) site Fe moments have collinear arrangement, whereas for x less than 0.5 a noncollinear arrangement of B-site Fe moments exists. Upadhyay *et al.* have reported

unusual cation distribution for nanosized NiZn ferrite depending on the synthesis conditions [205]. Ponpandian *et al.* have reported large enhancement of the T_C of NiZn ferrite nanoparticles due to the unusual cation distributions [200]. There are several reports available on the unusual cation distribution and different magnetic properties for nanosized $MnFe_2O_4$ [206, 207], $NiFe_2O_4$ [208, 209] and MnZn ferrite [210].

Zinc ferrite: Zinc ferrite, $ZnFe_2O_4$, is a normal ferrite, with the Zn^{2+} ions occupying the tetrahedral A-sites and the Fe^{3+} ions occupying the octahedral B-sites in the spinel structure of AB_2O_4. The A-O-B magnetic superexchange interactions are very crucial in determining the ferrimagnetic properties of spinel-type ferrites and $ZnFe_2O_4$ does not exhibit any ferrimagnetism because the A-site ion here is non-magnetic [186]. In fact, zinc ferrite shows paramagnetic properties at room temperature and undergoes a transition to antiferromagnetic state below 10 K [211]. In the spinel structure, usually Zn^{2+} ions have strong preference to occupy the tetrahedral site (A-site). However, if it is possible to synthesize $ZnFe_2O_4$ with inverted or partially inverted structure, symbolized by $Zn_{1-x}Fe_x[Zn_xFe_{2-x}]O_4$ where $x = 1$ for inverted and $0 < x < 1$ for partially inverted structure, then $ZnFe_2O_4$ is also expected to show ferrimagnetic or superparamagnetic properties at or above room temperature [212–215]. This is similar to $MgFe_2O_4$, which shows ferrimagnetic properties at room temperature due to the partially inverted structure in which part of Mg^{2+} ions are in the octahedral sites and corresponding amounts of Fe^{3+} are moved to the tetrahedral sites [216]. However, it is not possible to make ferrimagnetic $ZnFe_2O_4$ by the usual solid state method of synthesis and the inversion parameter usually obtained is less than 0.05 [211]. One way to overcome this draw back is to make the material in nanocrystalline form, either by following low-temperature methods of synthesis or by reducing the size of the bulk samples to nanometer scales by mechanical milling. If a low temperature method of synthesis is used, it is possible to obtain materials with different degrees of distributions of Zn^{2+} and Fe^{3+} ions in the tetrahedral and octahedral sites [217–219]. Similarly, mechanical milling can also rearrange the distribution of the Zn^{2+} and Fe^{3+} ions in the two different sites of the spinel structure [213, 220, 221].

A third method is to quench the sample from high temperatures during the solid state method of synthesis, which also is expected to produce materials with different metal ion distributions [222, 223].

γ-Fe_2O_3: Maghemite (γ-Fe_2O_3) is a material of great technological importance for its use in magnetic recording systems and in catalysis. Moreover, some properties of maghemite are particularly enhanced when the size of the particles reaches the nanometer range [224–226]. Because of the small coercivity of γ-Fe_2O_3 nanoparticles, they can be used as magneto-optical devices. Magneto-optic media can be made by depositing magnetic and optically transparent materials, and maghemite particles satisfy the required condition, since they can be easily incorporated in to ultrathin polymer films [227]. Maghemite consists of unusual cation distribution over its A and B sites. It consists of Fe^{3+} ions and the B-site is not completely filled. The structural formula of maghemite is given as $Fe_8[Fe_{13.33}\square_{2.67}]O_{32}$, where $\square$ represents the vacancies in octahedral sites. Although nanosized γ-Fe_2O_3 transforms into α-Fe_2O_3 (hematite) at rather low temperatures ($\sim$623 K) [228, 229], it can be stabilized by doping transition metal ions (Mn^{3+}) [230] or through the incorporation of the nanoparticles into polymeric, glassy or ceramic matrices.

Some important parameters of ferrites

Initial permeability, μ_i

Initial permeability is one of the most important properties of soft magnetic materials, basically of soft ferrites. It depends on various factors, but the main factors are microstructure of the material, grain size (D), saturation magnetization (M_s), and anisotropy energy (K_1). μ_i is given by,

$$\mu_i = \frac{3\mu_0 M_S^2 D}{16\gamma_\omega} \tag{1.22}$$

where μ_0 is the permeability of free space (A/m) and γ_ω is the domain wall energy (J/m^2) [194]. Thus, the initial permeability is a linear function of grain size. Porosity and defects are also responsible for μ_i values. If the pores are confined to grain boundaries, μ_i is

not affected, otherwise μ_i is severely decreased if these are situated inside the grains. Thus, the main requirement to achieve higher μ_i is to get bigger grain with uniform size and high material density (low porosity). Moreover, μ_i varies inversely with crystalline anisotropy energy. So, ferrites having low K_i will give higher values of initial permeability. The thermal behavior of the initial permeability is very important for many applications. Getting a constant μ_i over a wide range of temperature is very important for many high quality applications. Anisotropy energy decreases on heating and it decreases faster than the magnetization, thus μ_i increases with temperature, tend to become infinity just below the Curie temperature and then drops to a very small value in the paramagnetic state. The measurement of permeability (as function of frequency and temperature) is a very important characterization technique for a ferrite. Although extensive research has been carried out in the past, the emphasis is to attain highest initial permeability and lowest permeability loss at different frequency ranges. Another new trend is the study of the permeability of the nanosized ferrites and nanocomposite materials. There are few reports where initial permeability of ferrite nanoparticles and polymer based nanocomposites have been studied.

Dielectric constant, $\epsilon^{'}$

Materials having high dielectric properties or dielectric constant are used as capacitors in electronic applications. The basic property is the dielectric polarization, which can be defined as the finite displacement of bound charges of a dielectric in response to an applied electric field, and the orientation of their molecular dipoles if the latter exists. The dielectric properties vary widely with the nature of the material and are a function of the applied field, humidity, crystal structure, etc. The value of $\epsilon^{'}$ of a dielectric material is calculated as follows

$$\epsilon_T^{'} = \frac{C_P h}{\epsilon_0 A} \tag{1.23}$$

where C_P is the capacitance of the sample at a given temperature, h is the sample thickness, A is the surface area of the conducting plate and ϵ_0 is the permittivity of air.

Electrical resistivity, ρ

Electrical resistivity is an important property of ferrites and other magnetic materials. The initial permeability is solely dependent on ρ. One of the factors controlling the permeability loss in ferrites is the eddy current and this loss (P_e) is inversely proportional to resistivity. As ρ increases, P_e will decrease and hence a higher value of μ_i. Therefore, higher electrical resistivity is always a desired parameter for ferrite materials, for high frequency applications.

Microstructure

Microstructure refers to the microscopic structure of solid materials. This is an important parameter for ferrites. For the better performance parameters and properties, uniform microstructure is an essential condition. It means all the grains should be of same size and minimum porosity. Microstructural aspects of ferrites have always some special interest, such as to attain proper saturation, to minimize anisotropy, to minimize magnetostriction and to avoid foreign ions that can strain the lattice [188]. There are several conditions maintained to get proper microstructure for better properties, some of them are variation of sintering conditions, additives, etc. In 1977 Igarashi *et al.* put forwarded the following relationship from his experimental findings [231].

$$\mu \propto D^{1/3} \tag{1.24}$$

where D is the diameter of a grain.

1.5.3 Magnetic nanocomposites

A composite is one or more distinctive components dispersed in a continuous matrix creating a compositional heterogeneity of the final solid structure. A typical conventional composite is glass-fibre-reinforced plastic (GFRP) that is widely used in aircrafts, large containers and automotive parts. Some other examples are; SiC in high strength ceramic materials, ZrO_2 in superplastic ceramics, magnetic metallic phases of Fe and Co in magnetic materials, etc. Composite materials are used in large number of multifunctional

applications, from cryogenic to corrosion resistance, from biomedical to engineering, from automotive to thermoplastics, from high density recording to GMR, etc [232–234]. A "nanocomposite" is defined as a composite in which the distinctive component(s) is/are in the nanometer range. The accepted length scale for the nanophase is less than 100 nm in at least one dimension. The continuous materials can be ceramic, metallic, organic or polymers, either in the bulk form or as a thin film. Nanocomposites are a special class of materials originating from suitable combinations of two or more nanoparticle samples or nanosized objects in some suitable medium, resulting in materials having unique physical properties and wide application potential in diverse areas. Novel properties for the nanocomposites can be derived from the successful combination of the characteristics of parent constituents into a single material. Moreover, these materials typically consist of an inorganic (host) solid containing an organic component or vice versa. Or they can consist of two or more inorganic/organic phases in some combinational form with the constraint that at least one of the phase of various features be in nanosize [2].

Composites are expected to exhibit superior properties or better performance than their elemental or monolithic counterpart. Most of the property changes can be estimated by some rule of mixtures. The simplest change of a composite property, P_c, is monotonic increases or decrease with the increase of volume fraction, V_i, of the added components; which is represented by the following equation

$$P_c = \sum_{i=1}^{N} (P_i)^n V_i \tag{1.25}$$

where P_i is the added component property and n is an experimental parameter ($-1 \leq n \leq 1$). Nanocomposites differ from their bulk components in terms of the strong interactions of grains around the grain boundaries. There are six properties of interest in nanocomposites. These are: mechanical, magnetic, electrical, optical, quantum dots and catalytic properties. Nanocomposites exhibit unique behavior due to three effects (i) the smaller size effect, (ii) the large grain boundary effect, and (iii) the quantum confinement effect. Moreover, they exhibit high reactiveness during synthesis and in processing situa-

tions. Thus, these conditions leads to increase in strength and hardness of ceramic matrix nanocomposites, lowering in melting point and increase in electrical resistivity of metallic matrix nanocomposites, increase in absorption of UV wavelength in polymer matrix nanocomposites, increase in shielding the electrostatic field for semiconducting matrix nanocomposites, etc. Nanocomposites find their applications in various areas, such as electromagnetic wave absorber, biocompatible magnetic nanofibre, conducting polymer nanocomposites, cheaper optoelectronic, photonic and electronic devices, integrated circuit (IC) products, etc [235–240].

Out of the application oriented nanocomposites, magnetic nanocomposites in which magnetic species are dispersed within nonmagnetic or magnetic matrices are practically very useful. Magnetic recording, GMR, magnetic refrigeration, etc., are some important areas in which magnetic nanocomposites have importance [2, 241–244].

One newly studied nanocomposite material is the polymer/metal/ferrite composite [245, 246]. The importance of such a system is that after little modification, these can be used as capacitors and inductors. Moreover, they have advantages over the current ferromagnetic-ferroelectric ceramic composites in various terms. The currently used multifuntional composites must be co-fired and sintered at high temperatures. Again, such processes are time consuming and requires much energy, and the mismatch between the components could cause some other problems, such as cracks and warps in the final product. But, as an alternative, polymer based magnetic nanocomposites with high initial permeability and high dielectric constant are interesting because of their flexibility, compatibility and easy fabrication nature. Polymer/metal/ferrite composites consist of a polymer, a magnetic metal and a ferrite material either on the coronal surface or in the interior core of the polymer microdomains as filler. This is a totally innovative composite material, where properties of both the matrix polymer and the nanocomposite components are synergized. In such polymer/metal/ferrite composites, high initial permeability can be obtained by dispersing ferrite particles with large initial permeability in the polymer matrix as filler, and in addition, dielectric constant can be enhanced over their polymer matrix. Thus, merging these two different properties in polymer based composites, it will

be easier to overcome the disadvantages of purely ceramic based composites.

The Co/CoO [91, 247] composite system is an important composite from the view point of GMR effect and FM/AFM interactions. The exchange coupling of ferromagnetic (FM) and antiferromagnetic (AFM) films across their common interface causes a shift in the hysteresis loop of the ferromagnet, called exchange bias. The shift can be useful in controlling the magnetization in devices, such as spin valves which sense changing magnetic fields through the giant magnetoresistance effect. Read heads based on this effect are used in magnetic disk storage. Studying exchange bias in nanostructured FM/AFM bilayers with nanoscopic feature has the unique advantage of probing the role of domain size and morphologies [91]. It is also technologically important as the exchange bias in FM/AFM nanostructures provide an additional, tunable source of anisotropy to stabilize the magnetization, thereby possibly reducing the length scale that determines the superparamagnetic limit in magnetic recording. The exchange bias phenomenon is of tremendous utility in magnetic recording, where it is used to pin the state of the readback heads of hard disk drives at exactly their point of maximum sensitivity; hence the term "bias". Almost all studied materials for this purpose are in the form of thin film bilayers, eg. Co/CoO thin film [248–252].

1.6 Scope of the Present Work

Oxide based diluted magnetic semiconductors: There are enormous scopes and challenges for the research on diluted magnetic semiconductors and especially on oxide based materials. In these compounds, what is required ultimately is ferromagnetism above room temperature. If ferromagnetism in the oxide based DMSs is an inherent property of the material, then processing techniques need to be optimized to fabricate high quality thin films or polycrystalline materials with high rate of reproducibility. These materials are then potential candidates for many new technological applications based on spintronics. We have investigated the synthesis, characterization and magnetic properties of polycrystalline $Zn_{1-x}TM_xO$, (TM = Co, Ni, Fe and Mn).

Ferrites: There are tremendous scope on the studies of ferrite systems, particularly ferrite nanoparticles. Research interest in nanocrystalline soft ferrites has dramatically increased in the recent past. This is due, in part, to the enhanced properties as compared to that of their bulk counterpart, e.g. increase or decrease in T_C, low temperature sintering, enhancement in permeability and dielectric constant, higher coercivity, evolution of magnetism in nonmagnetic ferrite, etc. The benefits found in the nanocrystalline ferrites stem from their chemical and structural variations on a nanoscale which are important for various applications. Therefore, the $Ni_{0.5}Zn_{0.5}Fe_2O_4$ and $ZnFe_2O_4$ compositions should be interesting for studying their magnetic properties, if it is possible to change the cation distribution. Again it will be interesting, if it is possible to synthesize γ-Fe_2O_3 nanoparticle with high stability.

Nanocomposites: As already stated, polymer/metal/ferrite type nanocomposites become very important from the view point of new technological applications, but in the available literature of polymer/metal/ferrite composite, the filler (metal and ferrite particles) are added separately to the polymer matrix and followed by hot molding. So the major disadvantage of this procedure is that nonuniform mixing of metal and ferrite particles may occurs giving rise to defective properties. However, it would be advantageous, if one can synthesize metal/ferrite nanoparticles under *in situ* conditions and use as a filler in a polymer matrix, where uniform distribution of the nanoparticles can be expected. In the current study, we have attempted to synthesize metal/ferrite nanocomposites under *in situ* conditions and further dispersed in poly(vinylidene fluoride) (PVDF) polymer and measured magnetic permeability and dielectric constant of these *three phase* nanocomposites. The magnetic composites synthesized in the present study are $Ni/NiFe_2O_4$ and $Co/CoFe_2O_4$. Moreover, Co/CoO system is an important composite system. Since most of the work performed are on thin films and bulk samples, it will be interesting to study different structural and magnetic phenomenon of Co/CoO nanocomposite system. We have tried to synthesize Co/CoO nanocomposite under an *in situ* condition and carried out some preliminary studies.

Chapter 2

Experimental Methods

2.1 Introduction

The experimental methods employed to synthesize the transition metal oxides and the techniques used for the characterizations the materials are discussed in this chapter. An autocombustion method, which is simple and time saving is used to synthesize various oxides. To compare the properties of the nanocrystalline materials obtained by this method, with that of their bulk counterpart, the corresponding bulk materials have been synthesized by the solid state method. Different instrumental techniques have been used for the characterization and evaluation of the properties of the materials.

2.2 Methods of Synthesis

2.2.1 Glycine-nitrate autocombustion method

The autocombustion method of synthesis of metal oxides using redox mixtures involves a mixture of oxidizing reagents such as nitrates of metals and a fuel such as glycine, urea, citric acid, hydrazine, glycerol, etc, which acts as a reducing reagent [253–261]. The method is actually self-sustainable after the reaction is initiated and owing to the exothermic nature of the reaction, high internal temperature ensures the crystallization and formation of the oxides [253, 262]. The advantages of the autocombustion process are that, one will get batches of yield (>96%) in a short time period. Some of the salient

features of the process are:

i) the oxides and their composites can be prepared at very low temperatures of < 673 K;

ii) the products are homogenous and crystalline; they are soft and fine with high surface area;

iii) narrow particle size distribution with nanosized particles;

iv) the materials prepared are of high purity;

v) the particles show less agglomeration; and

vi) large quantities can be prepared, relatively cheaply.

In the present work, the synthesis method used is the glycine-nitrate process (GNP) where glycine is used as the fuel [263]. In the case of GNP, the low molecular weight amino acid, glycine (H_2NCH_2COOH), which act as a 'zwitterion' or bi-dentate ligand, prevents selective precipitation of the metal ions from the solution. Glycine has a more negative heat of combustion (–3.24 kcal/g) as compared to some other combustion fuels such as urea (–2.98 kcal/g) or citric acid (–2.76 kcal/g) [264]. It serves as a fuel for the combustion reaction and oxidized by the nitrate ions easily [254]. In GNP, the glycine-to-nitrate ion (G/N) ratio can be adjusted to get good particle morphology and homogeneity, because G/N ratio affects the flame temperature and combustion velocity or reaction time. It is reported that a maximum flame temperature of ∼1773 K is observed for G/N ratio of ∼0.55 [263]. The complete combustion reactions for the divalent and the trivalent metal nitrates can be represented as shown in Eq. 2.1 and Eq. 2.2, respectively. In both cases, the G/N ratio is ∼0.55. However, usage of larger amounts of glycine per mole of metal ion (up to 3 moles of glycine) is found to be more favorable to reduce the rate of the reaction rate while the reaction remains spontaneous and self-sustaining. Another advantage of adding extra fuel is that the formation of intermediate nitrates of the metals can be avoided. Synthesis of many single and multi-component oxides, using the glycine nitrate process, has been reported in the literature [254, 256, 262–266].

$$M(NO_3)_2 + \frac{10}{9}C_2H_5O_2N = MO + \frac{20}{9}CO_2 + \frac{25}{9}H_2O + \frac{14}{9}N_2 \tag{2.1}$$

$$2M(NO_3)_3 + \frac{30}{9}C_2H_5O_2N = M_2O_3 + \frac{60}{9}CO_2 + \frac{75}{9}H_2O + \frac{42}{9}N_2 \quad (2.2)$$

For the synthesis of different oxides studied in this work, all the chemicals used were of AR grade. For the synthesis of different oxides containing Fe, Ni, Co, etc., stoichiometric quantities of the corresponding metal nitrates such as $Fe(NO_3)_3.9H_2O$ (Merck, India), $Ni(NO_3)_2.6H_2O$ (Merck, India), $Co(NO_3)_2.6H_2O$ (Merck, India) were dissolved in minimum amount of distilled water. Since zinc nitrate and manganese nitrate are highly hygroscopic, stoichiometric quantities of the corresponding metal powders [Zn (BDH, England), and Mn (Aldrich Chemical,USA)] were taken and dissolved in minimum amount of 4N HNO_3 to get the corresponding metal nitrates. The fuel, glycine H_2NCH_2COOH, (Merck, India), was taken according to various glycine/nitrate ratios (as indicated in the respective chapters) and dissolved in minimum amount of distilled water. According to the required metal oxides, the solutions of the respective metal nitrates and glycine were mixed together in a large crystallizing dish (150 x 75 mm, Schott Duran, Germany). The bottom of the crystallizing dish should be flat to provide uniform heating to the solution. The final mixed solution (in the crystallizing dish) was kept over a hot plate for evaporation and autocombustion, at a temperature of 473 K. A viscous gel formed at the bottom of the dish after the complete evaporation of water and subsequently underwent autocombustion producing the oxide product within few seconds (as-synthesized product). The optimized synthesis conditions and the G/N ratios for the synthesis of different oxides are discussed in the respective chapters.

It has been reported in certain cases that, when stoichiometric amounts of glycine is used for the autocombustion reaction, the final product contains impurities such as metal clusters and the individual metal oxides [263–265]. Also, when the (G/N) ratio is less than 0.44, non-homogeneous particle size distribution with lower reproducibility is obtained [266].

One way of overcoming the problem of impurity phases, particle size distribution and non-reproducibility is to slow down the rate of the combustion reaction in the GNP by the

use of a suitable additional fuel. We have considered dextrose ($C_6H_{12}O_6$), as an additional fuel for the synthesis of NiZn ferrite nanoparticles. The choice of dextrose is based on the fact that its heat of combustion is larger than that of glycine (-3.71 kcal/g for dextrose when compared to -3.24 kcal/g for glycine) and it contains only carbon and hydrogen so that the combustion products will be CO_2 and H_2O. Also, the combustion will be less vigorous due to the absence of the amino group. More over, the amount of gases produced in the combustion reaction is comparable to that from the glycine reaction,

$$M(NO_3)_2 + \frac{5}{12}C_6H_{12}O_6 = MO + \frac{5}{2}CO_2 + \frac{5}{2}H_2O + N_2 \tag{2.3}$$

$$2M(NO_3)_3 + \frac{5}{4}C_6H_{12}O_6 = M_2O_3 + \frac{15}{2}CO_2 + \frac{15}{2}H_2O + 3N_2 \tag{2.4}$$

If the combustion reaction rate is reduced, this will ensure the chemical homogeneity of the product and the low reaction temperature is expected to give rise to smaller crystallite sizes for the product. So, if dextrose is added along with glycine, it is expected that dextrose will help in the formation of single phase ferrite particles with a reduction in the particle size. The optimized synthesis conditions, the G/N ratios and the amount of dextrose for the synthesis of different oxides are discussed in the respective chapters.

2.2.2 Ceramic or solid state method

To compare various properties of the nanosized oxides with their bulk counterpart, standard ceramic method of synthesis was used to synthesize the bulk materials. In the ceramic or solid state process, the constituent oxides (all oxides from Aldrich Chemical, USA) in the stoichiometric ratio were taken and mixed thoroughly in an agate mortar with the help of an agate pestle and acetone was used as the grinding medium [267–269]. After thorough grinding, the ground dry powder was calcined at a high temperature ($\sim$1273 K). After the first calcination, the calcined powder was again thoroughly ground and processed at higher temperatures (1373 and 1473 K) after intermediate grindings.

2.3 Characterization and Measurement Techniques

2.3.1 Powder X-Ray Diffraction

Powder X-ray diffraction (XRD) is used for the basic characterization of the different materials. XRD pattern is the finger print of a crystalline material [84, 270] as this technique gives information on the structure, phase and purity of a material. The Bragg's law is used widely to treat diffraction from crystals. The Bragg's law is given as

$$n\lambda = 2dsin\theta \tag{2.5}$$

where d is the spacing between two adjacent lattice planes, λ is the wave length of the X-radiation, n is an integer and θ is known as the diffraction angle or Bragg's angle [270]. It is known that the width of a diffraction peak increases when the crystallite size is reduced below a certain limit ($<$ 100 nm). Therefore, XRD patterns can be used to estimate the average size of very small crystallites, from the measured width of the diffraction patterns. The commonly accepted formula for determination of crystallite size from XRD line broadening is the Scherrer formula [270],

$$t = \frac{0.9\lambda}{\beta cos\theta_B} \tag{2.6}$$

where t is the thickness of the crystallites (in Å), λ is the X-ray wavelength, θ_B is the diffraction angle and β is the width of the diffraction peak. Generally, there will be a contribution to line broadening from the instrument due to various factors and this natural width is corrected as

$$\beta^2 = \beta_M^2 - \beta_S^2 \tag{2.7}$$

where β_M is the measured peak width at half peak height and β_S is the contribution from the instrumental line broadening, in radians. β_S is obtained from the width of the XRD pattern of a standard bulk material. The thickness of the crystallite or the average crystallite size t is generalized as the average particle size in the following chapters.

In the present study, the phase analysis of the samples was carried out using a Philips PW 1830 diffractometer, and using Ni-filtered Cu Kα radiation. The wavelength of Cu Kα radiation is 1.5418 Å. The diffractometer was calibrated with reference to standard Si wafer. For the general phase analysis the scan rate used was 4°/minute. But for detailed phase analysis, a slow scan rate of 0.25°/minute was used. The lattice parameters and d-spacings were calculated using the computer programs, Powder Diffraction Package (PDP) [271] and PowderCell for Windows (PCW) [272].

2.3.2 Transmission Electron Microscopy (TEM)

Transmission electron microscopy (TEM) is an imaging technique whereby a beam of electrons is focused onto a specimen causing an enlarged version to appear on a fluorescent screen or a layer of photographic film, or to be detected by a CCD camera. TEM operates on the same basic principles as the light microscope but uses electrons instead of light. Virtually, TEM is useful for determining size, shape and arrangement of the particles which make up the specimen. Moreover, it is highly useful for determination of the lattice planes and the detection of atomic-scale defects in areas of few nanometers in diameter with the help of selected area electron diffraction (SAED) technique [273, 274]. The d-spacing between lattice planes of crystalline materials can be calculated from a SAED pattern using the relationship–

$$dr = \lambda L \tag{2.8}$$

where L is the distance between the specimen and the photographic plate, λL is known as the camera constant and r is the radius of diffracted rings. It is easy to measure r directly from the photographic plate, and λL can be established from the instrument by calibrating it with a standard material (usually Ag), and hence one can easily get d values. Since each d value corresponds to a specific lattice plane for a specific crystal structure, a minimum description of the crystal structure of a crystalline specimen can be obtained from a SAED pattern. In some cases SAED pattern is more helpful as compared to XRD, due to the limited detection limit of XRD instruments.

The TEM measurements were performed on a Jeol model 1200EX instrument operating at 120 kV, camera length of 80 cm and field limited aperture of 100 μm. Prior to TEM measurements, the samples were dispersed in a suitable organic solvent (isoamyl acetate, acetone, toluene, etc.) and a drop of the solution was poured on carbon-coated TEM grids. The film formed on the TEM grids was allowed to dry for 2 minutes following which the extra solvent was removed using a blotting paper and the TEM and SAED measurements were performed.

Simulation of SAED patterns: Experimental electron diffraction patterns of various samples were compared with the simulated electron diffraction patterns of the corresponding phases. Electron diffraction ring patterns were simulated using the computer program JECP/PCED [275].

2.3.3 Scanning Electron Microscopy (SEM)

The scanning electron microscope (SEM) is a very useful instrument to get information about topography, morphology, composition and microstructural information of materials. It is a type of electron microscope capable of producing high resolution images of a sample surface. Due to the manner in which the image is created, SEM images have a characteristic three-dimensional appearance and are useful for judging the surface structure of the sample. The SEM has compensating advantages, though, including the ability to image a comparatively large area of a specimen and the ability to image bulk materials [276]. SEM images are much easier to interpret than TEM images, and many SEM images, beyond their scientific value, are actually beautiful.

Particle topology of the powder samples and microstructure of the sintered samples in the present study were obtained using a Leica Stereoscan-440 scanning electron microscope. Energy dispersive X-ray (EDX) measurements were carried out using a Phoenix EDAX intrument, which is attached to the SEM. For the analysis of a powder sample's morphology and EDX, the sample powder was spread on an Al holder using isoamyl acetate. On the other hand, sintered pellets were fractured to expose the inner portion and

mounted on a specimen mounting stub. Silver paste was used to connect the sample to sample holder for electrical conduction. A thin layer of gold was coated on the surface of the sample to avoid charging of the specimen.

2.3.4 Thermogravimetric Analysis

Thermogravimetry (TG) is the branch of thermal analysis which examines the weight change of a sample as a function of temperature in the scanning mode or as a function of time in the isothermal mode. In the present study, dynamic thermogravimetry technique is used, in which the sample is heated in an environment whose temperature is changing in a predetermined manner, at a linear rate. There are many events considered in TG, such as desorption, absorption, sublimation, vaporization, oxidation, reduction and decomposition. Moreover, TG is used to characterize the decomposition and thermal stability of materials under a variety conditions [277, 278]. TG curves are usually recorded using a thermobalance.

A Seiko 32 thermal analyzer was used to perform the thermogravimetric analysis (TGA) of various precursors and samples. Thermal analysis was carried out up to 1073 K in flowing air, at a heating rate 10 K/min.

2.3.5 Thermo-Mechanical Analysis

Thermo mechanical analyzer (TMA) is an instrument used to measure thermo mechanical characteristics such as thermal expansion, thermal contraction, and softening of various materials. Moreover, this technique is highly useful to measure the stress and strain of polymers.

A Perkin Elmer Instrument, Pyris Diamond TMA (Thermal Mechanical Analyzer) was used to study the best sintering temperature for the ferrite samples in terms of rate of liner shrinkage as a function of temperature. The temperature range employed is 300-1773 K at a heating rate of 10 K/min. An alumina probe was used as the TMA probe. The sample pellet was kept inside the sample tube on an alumina plate and a constant

force, 100 mN, was applied to it. An independently connected linear voltage differential transformer (LVDT) and core detected the changes in sample length as a function of temperature.

2.3.6 UV-Visible Spectroscopy

UV-Visible spectroscopy is the measurement of the intensity of absorption of near-ultraviolet and visible light by a sample. Ultraviolet and visible light are energetic enough to promote outer electrons in an atom to higher energy levels. UV-Vis spectroscopy is usually applied to molecules and inorganic ions or complexes in solution or solid samples [185]. The UV-Vis spectra have broad features that are of limited use for sample identification but it is a very useful technique for quantitative measurements. Moreover, UV-Vis spectroscopy is used to determine the optical band gap transitions of semiconductors.

In the present study, UV-Vis spectroscopy measurements of the solid samples at room temperature were carried out on a Jasco UV-Vis spectrophotometer (V570 UV-VIS-NIR) operated at a resolution of 1 nm.

2.3.7 X-ray Photoelectron Spectroscopy

X-Ray Photoelectron Spectroscopy (XPS), also known as Electron Spectroscopy for Chemical Analysis (ESCA), is a surface analysis technique used for obtaining chemical information about the surfaces of solid materials. The method utilizes an X-ray beam to excite a solid sample resulting in the emission of photoelectrons. An energy analysis of these photoelectrons provides both elemental and chemical bonding information about the material comprising the sample surface. All elements, except hydrogen and helium, can be detected.

Photoemission spectra at room temperature were recorded on a VG Microtech Multilab ESCA 3000 spectrometer using non-monochromatized Mg Kα X-ray source (1253.6 eV). Extreme care has been taken to minimize the surface contamination problem by scraping the samples thoroughly and repeatedly over the surface with a stainless steel

blade *in situ* under high vacuum. The scraping was repeated until the higher binding energy shoulder in the O 1s XPS showed a minimum and no further decrease in the intensity [279, 280]. All binding energies are referred and corrected with respect to the O 1s peak at 530 eV [281].

2.3.8 Mössbauer Spectroscopy

The Mössbauer spectroscopy technique is being used in many analytical, biological, geological and engineering research areas [282, 283]. It is a branch of spectroscopic study, where resonant absoption of γ rays by the nuclei of atoms of a sample is studied. The Mössbauer spectroscopy is used as a fingerprint technique in mineralogy and geochemistry. Moreover, the existence of chemically, crystallographically or magnetically inequivalent sites are generally revealed by the appearance of distinct components arising from the different absorption peaks in a Mössbauer spectrum.

There are basically two types of informations that can be derived from a Mössbauer spectrum. The relative and absolute line energies are determined by electronic effects on the nuclear energy levels. These effects are generally lumped together as 'hyperfine parameters' and they are the isomer shift (or chemical shift, *IS*), electric quadruple hyperfine interaction (quadruple splitting, *QS*), and magnetic dipole hyperfine interaction (or magnetic hyperfine field, *HMF*) [283].

The room temperature Mössbauer spectra of the ferrite samples were obtained using an Austin Scientific Associates S-600 Mössbauer spectrometer coupled to a Canberra-95 multichannel analyzer. A Co^{57} in Rh matrix was used as the Mössbauer source. The spectrometer was calibrated with natural iron foil. The isomer shift is reported with respect to Fe metal and the data were analyzed using a standard computer program.

2.3.9 Magnetic measurements

The magnetic characteristics of the different materials as a function of the applied field at different temperatures and as a function of temperature at different applied field strengths

were measured on a Vibrating Sample Magnetometer (VSM). A VSM is a device in which a sample is vibrated in an uniform magnetic field, and the induced voltage in a properly positioned set of coils, which is proportional to the magnetization of the material, is detected. The instrument allows precise magnetization measurements to be made as a function of magnetic field strength, temperature, and crystallographic orientation [83,284].

An EG&G PAR 4500 vibrating sample magnetometer is used for the present work. The magnetometer was calibrated using a standard Ni sample. Field dependance of magnetization was measured out using a maximum field of ± 10 kOe. For high temperature measurements, an electrically heated oven was attached to the VSM to heat the sample (300-973 K). Here, a constant magnetic field is applied and the magnetization is measured by varying the temperature from 300 K to 973 K at a constant heating rate of 2 K/min.

A closed cycle helium cryostat was used for low temperature measurements (12-300 K). The sample holder used for room temperature and low temperature measurements is made of a non-magnetic polymer material, Kel-F (poly(cholorotriflouro)ethelene). For the zero field cooled (ZFC) measurements, the sample is first cooled to the lowest possible temperature (12 K) in zero magnetic field and magnetization is recorded while warming the sample. In the field cooled (FC) magnetization measurements, the sample is cooled under an applied field and the magnetization is measured while heating in the same field.

2.3.10 AC Susceptibility

A simple and versatile technique used for probing the actual susceptibility is the ac (alternating current) susceptibility (dM/dH) of different types of magnetic materials [285]. This technique is generally used to study superparamagnetic and spin glass materials and is very useful for the determination of the Curie temperature of ferromagnetic and ferrimagnetic materials. ac susceptibility can be measured as a change in the self inductance of a coil when a magnetic sample is inserted in the coil. More accurate measurements can be obtained by monitoring the changes in the mutual inductance of a pair of coils when a magnetic material is inserted in one of the coils. In the ac susceptibility measurements, a small ac field is applied in a primary coil and the sample is inserted in one of the sec-

ondary coils located inside the primary coil. The *emf* generated in the secondary coil is proportional to the susceptibility of the sample.

In the present study, the ac susceptibility measurements below and above room temperature were carried out in two different set-ups. An APD cryogenic closed cycle helium cryostat was used for the ac susceptibility measurement in the temperature range 15–300 K. High temperature (300-673 K) measurements were carried out in a home made quartz assembly. All the measurements were carried out in an ac field of 2 Oe at a frequency of 210 hz. The output of the secondary coil was analyzed using a PAR EG&G 5210 lock-in-amplifier. The susceptibility χ was calculated from the in-phase (real, χ') and the out-of-phase (imaginary, χ'') components of the resulting ac signal in the secondary coil as,

$$\chi = \sqrt{\chi'^2 + \chi''^2} \tag{2.9}$$

The lock-in-amplifier and a temperature controller was programmed through a computer and data were continuously collected as a function of temperature.

2.3.11 Initial Permeability

A *HP* 4342A Q-meter was used to determine the Q value (quality factor), initial permeability (μ_i) and relative loss factor ($\tan\delta/\mu_i$) of the NiZn ferrites and the nanocomposites. The Q-meter consists of a stable, continuously variable oscillator, whose controlled output level is connected into a resonance circuit by a transformer. A stable solid state voltmeter with a high input impedance (L) is connected across the internal variable capacitor to measure the reactive voltage in terms of circuit Q. The coil portion of the tuned circuit is connected externally and represents the unknown to be measured. By inserting low impedance in series with the coil and high impedance in parallel with the capacitor (C), different parameters (Q, μ_i, L, C, etc) of the unknown circuits or components can be measured in terms of their effect on circuit Q and resonant frequency. The unknown circuit or component of the NiZn ferrites or nanocomposites was taken in the form of toroids of

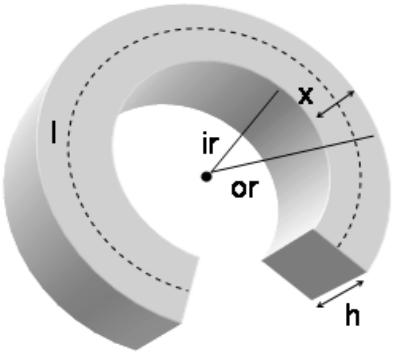

l = average magnetic path length,
lr = inner radius, or = outer radius,
h = thickness, x = or - ir

Figure 2.1: Cross section of toroid and its various parameters.

known inner and outer radii, and thickness. A test coil was wound over the toroid and the terminals of the coil were connected to the Q-meter. First the frequency was set at a desired value and then the capacitor in the Q-meter was tuned to get maximum Q value. Then, from the tuning capacitance, the inductance of the coil was calculated using the formula

$$L = \frac{1}{\omega^2 C} = \frac{1}{4\pi^2 f^2 C} \tag{2.10}$$

where ω is the angular frequency and f is the resonant frequency at which inductance was measured. The initial permeability and loss factor of the toroidal sample is calculated as follows:

A cross section of the toroidal shape is shown in Figure 2.1, where l = average length of magnetic path in the core (cm), ir = inner radius (cm), or = outer radius (cm) and h = thickness of the toroid. The circumference (l) is obtained as $l = 2\pi r = 2\pi(ir + x)$, where $x = or - ir$, and the cross sectional area of the toroidal core, A, is given by $A = xh$. Now, using the values of L, l and A, the initial permeability (μ_i) can be calculated as

$$\mu_i = \frac{L}{4\pi N^2}.\frac{l}{A}.10^9 \tag{2.11}$$

where N is the number of coil turns [286]. Moreover, the relative loss factor or loss tangent, tanδ/μ_i, is calculated as

$$tan\delta/\mu_i = \frac{1/Q}{\mu_i} \tag{2.12}$$

The temperature dependance of permeability was carried out by keeping the wound sample in a small furnace. In this case, the resonant frequency was adjusted at a fixed value (2.51 MHz in present study) and measured the inductance by varying temperature from 30-350 °C. The Curie point in such measurements is defined as 'under the condition of rising temperature, the temperature value at which the initial permeability becomes one third of the original value' [286].

2.3.12 Electrical Resistivity

Due to the high resistivity of the samples studied, the electrical resistivity measurements were carried out by the two probe method. The resistivity of various samples were obtained using an electrometer (Keithley 6517A electrometer/high resistance meter). First the samples were pelletized, sintered and then silver paste was coated on the polished surfaces of the pellets to provide electrical contacts. A single pellet was sandwiched between two electrodes of a sample holder. The resistance was then measured using the electrometer. The resistivity (ρ) of the sample is then calculated from the resistance (R), surface area (A) and thickness (h) of the pellet, using the following equation

$$\rho = \frac{RA}{h} \tag{2.13}$$

2.3.13 Dielectric Measurements

Dielectric constant of ferrite and composite samples was measured using an impedance bridge (General Radio 1608–A Impedance Bridge). It is a self-contained impedance-measuring system, which includes six bridges for the measurement of capacitance, conductance, resistance, impedance etc. in two different modes, namely parallel and series.

First the samples were pelletized, sintered and then silver paste was coated on the polished surfaces of the pellets to provide electrical contacts. A single pellet was sandwiched between two electrodes of a sample holder. The parallel capacitance was then measured in the LCR bridge as a function of frequency. The value of the dielectric constant ($\epsilon^{'}$) is calculated using the Eq. 1.23.

Chapter 3

ZnO Based Diluted Magnetic Semiconductors

3.1 Introduction

Studies on ZnO based diluted magnetic semiconductors (DMSs) received much attention in the recent years after it was first predicted by Sato *et al.*, from *ab initio* calculations, that ZnO doped with 3d transition metal (TM) ions such as V, Cr, Fe, Co and Ni may exhibit ferromagnetism [126]. Dietl *et al.* also predicted in the same period, based on the Zener model, that Mn doped p-type ZnO should be ferromagnetic above room temperature [128]. Based on these predictions, several experimental investigations have been carried out by different researchers on the ZnO based DMSs .

Most of the studies on ZnO based DMSs have been performed on thin film samples made by different techniques. It is generally believed that the origin of ferromagnetism in the transition metal (TM) doped ZnO is carrier induced. However, few research groups believe that secondary phases are responsible for ferromagnetism as the results are not always reproducible. No ferromagnetic ordering has been observed for Cr to Cu doped ZnO thin films, down to 3 K, by Jin *et al.* [144].

There are not many reports on the studies on polycrystalline samples of transition metal doped ZnO, as compared to the number of studies reported on thin film samples. Kolesnik *et al.* first synthesized Mn doped ZnO by the standard solid state method and observed antiferromagnetic nature for the doped samples [287]. After this report, efforts

have been made to synthesize *TM* doped polycrystalline ZnO where *TM* = Co, Mn, Ni, Fe, V, Cu, Cr, etc. There are reports which claim ferromagnetism in polycrystalline samples of (ZnCo)O [81,288–295], (ZnNi)O [81,141,142,296,297], (ZnMn)O [82,134,290,298–303] and (ZnFe)O [293,304–307]. Yoon *et al.* from studies on ZnO doped with Mn, Co and Fe, synthesized by the usual ceramic method as well as a soft chemistry method, found that the metal-metal interaction is dominated by antiferromagnetic coupling [153]. Very recent studies on (ZnMn)O and (ZnCo)O showed that Mn doped ZnO is paramagnetic at room temperature whereas (ZnCo)O is superparamagnetic due to clustering [150]. MCD studies showed that $Zn_{1-x}TM_xO$ (*TM* = Mn, Fe, Co, Ni or Cu) are paramagnetic DMSs [308].

Ferromagnetism with $T_C > 350$ K is reported by Schwartz *et al.* [81] in Co^{2+} doped ZnO (4% doping) colloidal quantum dots. Many studies have shown that Co^{2+} can be substituted for Zn^{2+} in ZnO upto 20% without any modification of the structure and all compositions either show ferromagnetism or absence of ferromagnetism [151,309–315]. Direct or indirect evidence for Co metal clusters and secondary phases as the origin of ferromagnetism in thin film samples of Co doped ZnO is reported [143, 155, 157, 316]. Kim *et al.* reported the antiferromagnetic superexchange interactions at high temperatures and spin-glass type transition at low temperatures in $Zn_{1-x}Co_xO$ [146]. Similarly, recent studies by Risbud *et al.* [145], Lawes *et al.* [147] and Rao *et al.* [148] showed that ferromagnetism is not observed in the Co substituted polycrystalline samples of ZnO synthesized by the acetate and oxalate routes. Recently Spaldin showed that additional *p*-type carriers are required to obtain ferromagnetic ordering in $Zn_{1-x}Co_xO$ and predicted that the magnetic moment should be 3.1 μ_B per impurity atom [317].

Though there are many reports on the observation of ferromagnetism in Co doped ZnO, there are not many studies on Ni doped ZnO. From the studies on different 3d transition metal doped ZnO films, Ueda *et al.* found that their Ni doped ZnO is not ferromagnetic [131]. Wakano *et al.* reported the observation of ferromagnetism at 2 K for the same system, which become superparamagnetic at 30 K and maintains it upto 300 K [318]. On the other hand, ferromagnetism is observed at room temperature in Ni/ZnO nanorods [319], and ZnO:Ni thin films [116, 140]. There are further reports that $Zn_{1-x}Ni_xO$ quantum dots may be a good DMS material as it is ferromagnetic upto 350 K [296,320]. However, from the observed saturation moments, it has been concluded that

only a small fraction of the doped Ni^{2+} ions gives rise to ferromagnetism and the majority of the material is paramagnetic or superparamagnetic. Magnetic measurements by Ando showed that some of the $Zn_{1-x}Ni_xO$ thin films are paramagnetic and others are ferromagnetic [321]. However, from magneto-optical studies, it has been shown that occurrence of ferromagnetic precipitations/secondary phases are responsible for the observed ferromagnetism in the films. Since small amounts of impurities cannot be detected by structural and magnetic studies, the author concluded that these measurements are not reliable for the characterization of DMS.

Mn doped polycrystalline ZnO system has been studied extensively and observation of ferromagnetism is reported in some of the cases [82, 134, 290, 298–303]. Few reports are on the observation of ferromagnetism at or above room temperature, whereas others reported the observation of ferromagnetism at low temperature. In a recent report, lattice defect was shown to be responsible for high temperature ($T_C > 350$ K) ferromagnetism in (ZnMn)O nanoparticles [322]. Kundaliya *et al.* reported that the secondary phase $Mn_{2-x}Zn_xO_{3-\delta}$ is the origin of ferromagnetism in Mn doped ZnO [156], which was initially thought to be intrinsic [298]. From the studies on thin film samples, Fukumura *et al.* showed 36% solubility of Mn in ZnO with strong antiferromagnetic ordering [323]. $Zn_{0.95}Mn_{0.05}O$ when synthesized by the solid state reaction at 1170 K is found to be ferromagnetic where as annealing the sample at 1370 K destroys ferromagnetism [324]. The observed ferromagnetism is depicted to a secondary phase (Mn,Zn)Mn_2O_4. From the studies on polycrystalline $Zn_{1-x}Mn_xO$ system with different x value ranges, it has been shown that the samples are either paramagnetic or antiferromagnetic [147, 148, 309, 325–328].

Fe doped ZnO is also shown to be an important diluted magnetic semiconductor system. Theoretically it has been predicted that (ZnFe)O should be ferromagnetic at room temperature without any kind of co-doping or hole doping [126]. But there are not much research work reported on the Fe doped ZnO system. Jin *et al.* first investigated the optical properties of Fe doped ZnO thin films and found a red shift of the absorption edge [329]. In an another interesting report, both Fe^{2+} and Fe^{3+} are shown to be substituted for Zn^{2+} in the ZnO lattice [330]. Han *et al.* successfully synthesized room temperature ferromagnetic polycrystalline $Zn_{1-x}Fe_xO$ co-doped with Cu [304]. Saturation magnetization of $0.75\mu_B$ per Fe and a T_C of 550 K are obtained for the samples.

There are also other reports where room temperature ferromagnetism is observed for Fe doped thin film or bulk samples [140, 293, 331–333].Enhanced ferromagnetism was obtained when $Zn_{0.95}Fe_{0.05}O$ powder was treated with hydrogen [307]. On the other hand, Jin *et al.* did not observe any ferromagnetism for the Fe doped ZnO thin film samples down to 3 K [144]. In a very recent article, Potzger *et al.* claimed that ferromagnetism in Fe doped ZnO solely depends on synthesis routes [334] and Shim *et al.* showed that a secondary phase of superparamagnetic $ZnFe_2O_4$ is responsible for the observed magnetism in (Fe Cu) doped ZnO [149].

Thus, the origin of ferromagnetism in the transition metal doped ZnO based DMSs is still under controversy [335]. The aim of the present work is to understand why ferromagnetism is obtained in certain cases and why the results are not reproducible when polycrystalline transition metal doped ZnO is synthesized by different methods as reported. $Zn_{1-x}TM_xO$ have been synthesized by an autocombustion method of synthesis, since this method is known to produce single phase oxide compositions, due to the atomic level mixing of the starting components in solution [257].

3.2 Synthesis of $Zn_{1-x}TM_xO$

Nanocrystalline $Zn_{1-x}TM_xO$, (where TM = Co, Ni, Mn, and Fe and $0 \leq x \leq 0.25$) powder samples were synthesized by an autocombustion method as described in *section 2.2*. High purity Zn (99.9%) metal powder was dissolved in dilute nitric acid and mixed with a water solution of the corresponding metal nitrate ($Co(NO_3)_2.6H_2O$, $Ni(NO_3)_2.6H_2O$, $Fe(NO_3)_3.9H_2O$ or $Mn(NO_3)_2$ obtained by dissolving Mn metal powder in dil. HNO_3) taken in the appropriate molar ratio of Zn and TM in $Zn_{1-x}TM_xO$. To the mixed solution of the metal nitrates, a water solution of glycine was added, taking 2 moles of glycine per mole of metal ion. The final mixed solution was evaporated on a hot plate and a thick mass formed subsequently underwent autocombustion to give a fine powder. The as-synthesized powders were characterized for their properties.

3.3 $Zn_{1-x}Co_xO$ ($0 \leq x \leq 0.25$)

All the studies on ferromagnetic $Zn_{1-x}Co_xO$ thin films and powders are performed at very low doping concentrations ($x \leq 0.1$) where it is difficult to trace the presence of any impurities, if formed, in very small amounts. Therefore, the present approach is to compare the properties of the doped samples with incorporation of smaller and larger amounts of Co ($0 \leq x \leq 0.25$) in ZnO and to see if metal clusters or secondary phases are responsible for ferromagnetism in the polycrystalline materials also at low-doping levels. It was expected that it would be easier to trace the presence of impurities, present if any, in heavily doped samples.

3.3.1 Ferromagnetic $Zn_{1-x}Co_xO$

Figure 3.1 shows the powder XRD patterns of the as-synthesized samples obtained with different amounts of Co in $Zn_{1-x}Co_xO$ ($0 \leq x \leq 0.25$). For $x = 0$, all the reflections correspond to the wurtzite structure of ZnO (JCPDS #5-664), whose simulated XRD pattern is shown as ZnO in Figure 3.1. The XRD patterns of the $x > 0$ samples show that the ZnO structure is not disturbed on substitution. All the reflections for different compositions are somewhat broad and this is due to the smaller crystallite sizes of the compositions synthesized by the low-temperature method. The average crystallite size is calculated from X-ray line broadening using the Scherrer formula and is obtained as ∼60 nm for the undoped sample and as ∼40 nm for all other compositions. Though no additional peaks due to any impurities are identified for $x \leq 0.10$, additional weak reflections are observed for $x > 0.10$ and the intensities of these additional reflections increase with increasing x.

Transmission electron micrographs of the pure ZnO and $Zn_{0.9}Co_{0.1}O$ are shown in Figure 3.2. Well dispersed nanoparticles are seen in the case of ZnO (Figures 3.2(a) and (b)), with particles of size in the range of ∼50-70nm. On the other hand, Figures 3.2(c) and (d) indicate that most of the individual plate-like particles of $Zn_{0.9}Co_{0.1}O$ are of the size 10-20 nm. The larger average particle size obtained from XRD studies may be due to the presence of bigger clusters, as seen in the TEM images.

The additional reflections in the XRD patterns shown in Figure 3.2 for $x > 0.1$ are identified as from impurities such as Co (JCPDS #15-806), CoO (JCPDS #9-402) and

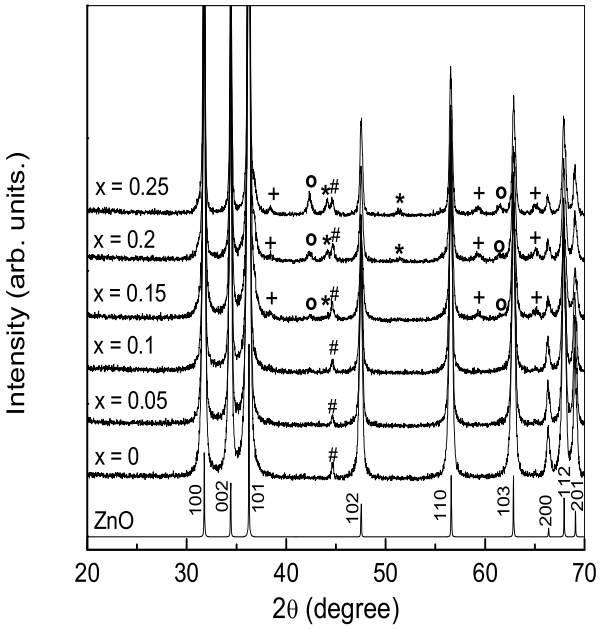

Figure 3.1: Powder XRD patterns of different compositions in $Zn_{1-x}Co_xO$ ($0 \leq x \leq 0.25$) and the simulated pattern for wurtzite ZnO. $\star$ Co; o CoO; + Co_3O_4; # contribution from sample holder.

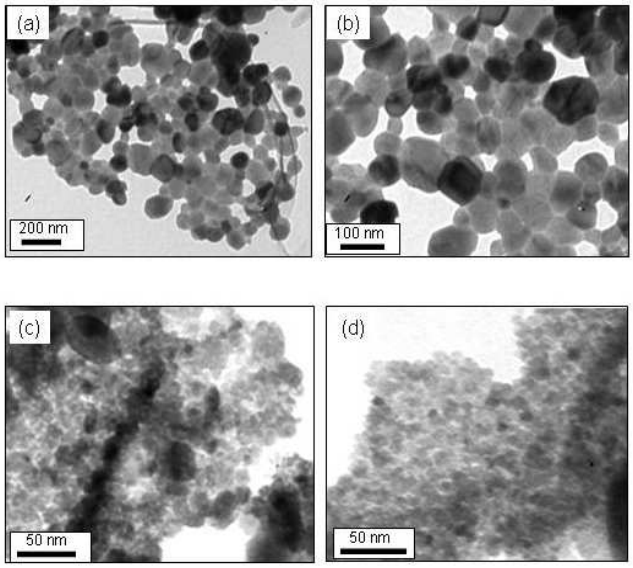

Figure 3.2: Transmission electron micrographs of pure ZnO (a, b) and $Zn_{0.9}Co_{0.1}O$ (c, d) from two different regions.

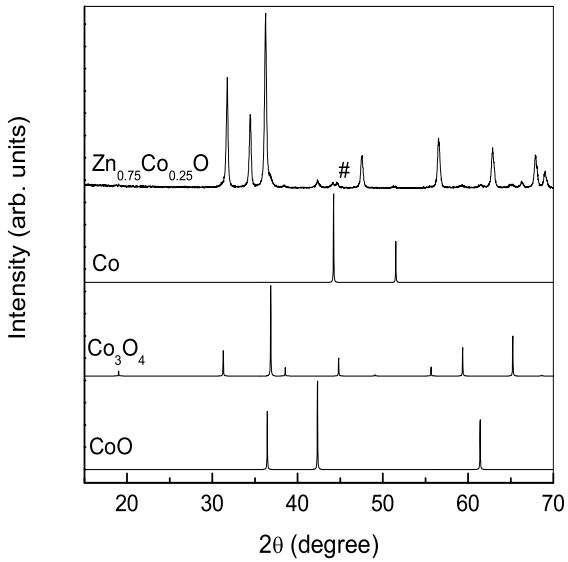

Figure 3.3: Comparison of the powder XRD pattern of $Zn_{0.75}Co_{0.25}O$ with that of simulated XRD patterns of Co, CoO and Co_3O_4. # contribution from sample holder.

Co_3O_4 (JCPDS #9-418), as indicated. Among the Co doped ZnO samples, $Zn_{0.75}Co_{0.25}O$ shows maximum number of impurity peaks. For a direct comparison, XRD pattern of $Zn_{0.75}Co_{0.25}O$ is compared with that of the simulated XRD patterns of Co, CoO and Co_3O_4, in Figure 3.3. It may be seen that all additional weak reflections are due to these three phases, indicating the presence of three impurity phases in the $Zn_{0.75}Co_{0.25}O$ sample. Figure 3.4 shows a comparison of the reflections in different 2θ regions, where the impurity peaks are clearly visible for the highly doped compositions. A close examination of the reflections in the XRD patterns of the different compositions, as shown in Figure 3.4, reveals that the presence of impurities such as CoO and Co_3O_4 can be detected in the $x = 0.1$ composition also when the reflections are compared with those of the $x > 0.1$ compositions. For example, the most intense (200) reflection of CoO and (440) reflection from Co_3O_4 are observed as very weak and broad reflections in the case of $x = 0.1$. Similarly, the presence of Co metal is detected for $x = 0.15$ and above.

The observation of reflections in the XRD patterns due to impurities such as CoO and Co_3O_4 in $x \geq 0.1$ and Co metal in $x \geq 0.15$ indicate that, either Co^{2+} is not substituted for Zn^{2+} in the ZnO lattice or only very small amounts of Co^{2+} are substituted and the

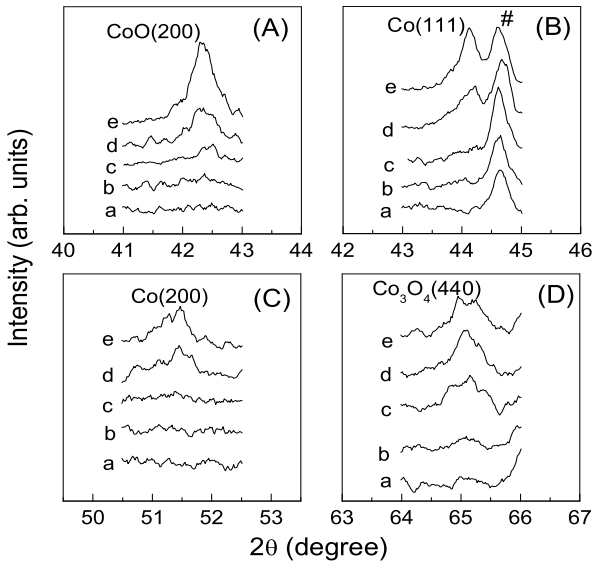

Figure 3.4: Comparison of the expanded powder XRD patterns of different compositions in $Zn_{1-x}Co_xO$ ($0 < x \leq 0.25$) in different 2θ regions where the reflections of individual impurity phases are clearly seen. a, b, c, d, and e represent the Co concentration x = 0.05, 0.1, 0.15, 0.2 and 0.25, respectively. # contribution from sample holder.

rest of the cobalt is converted to CoO and Co_3O_4 and partly to Co metal clusters in the heavily doped samples. Because of the reducing gases formed during the combustion reaction [336], it is possible that part of the cobalt is reduced to Co metal. However, since the color of all the Co added samples is pale green, the first assumption can be ruled out. It is possible that Co metal particles, in minor amounts, may be formed for x < 0.15 also and it is not detected in the XRD patterns due to very low concentrations. The weight percentages of different components in the $x = 0.25$ sample were calculated from fitting the powder XRD pattern and found to be approximately 84% of ZnO, 11% of Co_3O_4, 3% of CoO and 2% of Co. These observations imply that Co added during the synthesis of $Zn_{1-x}Co_xO$ is converted partly to CoO, Co_3O_4 and to metallic Co also at higher concentrations.

In a recent report, Lee *et al.* [316] have shown that neutron diffraction experiments are very useful to detect secondary phases in polycrystalline Co doped ZnO samples synthesized by a sol-gel method. Presence of impurities such as CoO and Co_3O_4 is detected for above 5 mol% Co-doping and Co metal phase is observed for 30 mol% Co doped ZnO

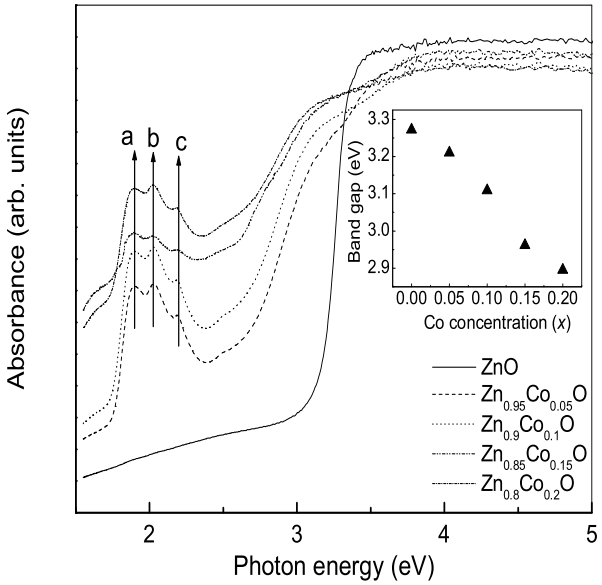

Figure 3.5: Optical absorption spectra of the as-synthesized samples of different compositions in $Zn_{1-x}Co_xO$. Inset: Variation of band gap of the different compositions with x, based on the optical spectra.

from the neutron diffraction studies. However, presence of impurities such as CoO and Co_3O_4 are detected for above 5% Co doping and Co metal is detected for 15% Co doping from powder XRD studies in the present work. Prellier *et al.* have earlier shown that lattice parameter variation is observed up to 9% Co doping in ZnO thin film samples and ferromagnetism is observed at room temperature for 5% doped film [135]. On the other hand, Ueda *et al.* [131] observed lattice parameter variation up to 25% Co doping, with ferromagnetism at room temperature, but the Curie temperature is found to be independent of the degree of doping. Different research groups have also reported similar variations of the lattice parameter of ZnO, below 25% Co doping [152, 337].

Though the present XRD studies show that Co and its oxides are present as separate phases in the doped $Zn_{1-x}Co_xO$ samples, the color of the Co doped samples was found to be greenish. The change in the color of the as-synthesized samples from colorless (slightly grayish due to residual carbon content) for $x = 0$ to pale green (for $x = 0.05$, 0.1 and 0.15) to blackish green (for $x = 0.2$ and 0.25) is an indication for the incorporation of increasing amounts of Co^{2+} in the ZnO lattice. Further evidence for this is obtained from

the optical absorption studies. The room temperature optical absorption spectra of some of the as-synthesized samples including that of ZnO ($x = 0$) are shown in Figure 3.5. Band gap transitions are seen for all the compositions. Apart from this, additional absorption features are observed in the case of $Zn_{1-x}Co_xO$, for $x \geq 0$. These absorption bands, marked as a, b and c, are at 660, 610 and 567 nm (1.89, 2.03, and 2.18 eV, respectively). These absorption bands are due to the $^4A_2(F) \rightarrow {}^2E(G)$, $^4A_2(F) \rightarrow {}^4T_1(P)$ and $^4A_2(F) \rightarrow {}^2A_1(G)$, crystal field transitions in the high spin state of Co^{2+} ($3d^7$) in the tetrahedral coordination [132,136,138,146,148]. The band gap transition for the undoped compound is observed at ~380 nm (3.272 eV), comparable to the value reported in the literature [128]. The band gap of the different Co doped samples is obtained as the energy at which the derivative of the absorption as a function of energy is maximum. The variation of the band gap as a function of x is shown in the inset of Figure 3.5. The band gap decreases with increasing Co concentration. This is a direct evidence for the incorporation of Co^{2+} ions in the ZnO lattice. The reduction of the band gap is ascribed to the increased *sp-d* exchange interaction of ZnO and Co^{2+} electrons [338]. Such type of redshift in the band gap has already been observed in the case of polycrystalline (ZnCo)O and (ZnMn)O [339]. Since Zn^{2+} in ZnO is situated in tetrahedral coordination, these observations clearly indicate that cobalt is substituted for Zn in ZnO and that the oxidation state of Co ions in the polycrystalline ferromagnetic $Zn_{1-x}Co_xO$ is Co^{2+}, which are tetrahedrally coordinated.

Figure 3.6 shows the magnetization (M) of the different compositions, as a function of magnetic field, measured at room temperature. Very weak ferromagnetism, 0.08 and 0.28 emu/g at 10 kOe, is observed for $x = 0.05$ and 0.1, respectively. On the other hand, relatively larger magnetization is observed for $x = 0.15$, 0.2 and 0.25, with saturation magnetization of 0.8, 1.56 and 3.55 emu/g at 10 kOe, respectively. Magnetization of the different compositions, measured at 10 kOe, is shown in the inset (B) of Figure 3.6, as a function of x. The larger values of M for $x \geq 0.15$ can be explained as due to the contribution from Co metal present in these samples, as evidenced from powder XRD studies. However, as no indication for the presence of metallic Co is observed in the powder XRD of $x < 0.15$ and weak ferromagnetism is observed for smaller Co concentrations in $Zn_{1-x}Co_xO$ also, it may be assumed that, at least, for $x < 0.15$, ferromagnetism originates on doping Co^{2+} at the Zn sites in ZnO.

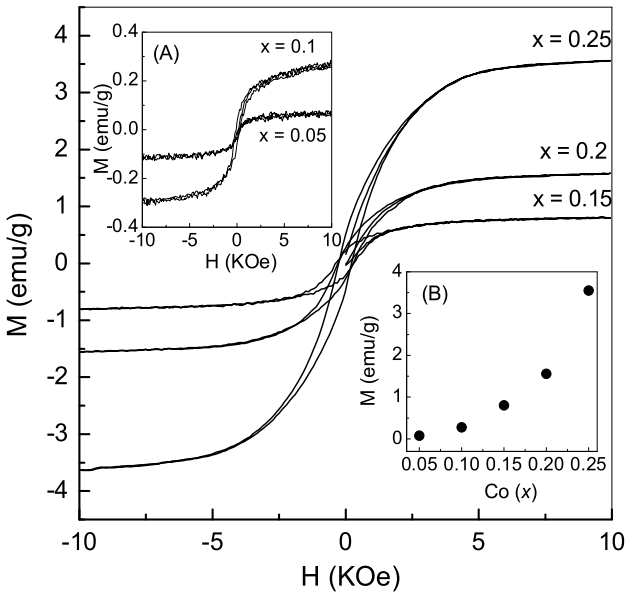

Figure 3.6: Magnetization as a function of magnetic field, measured at room temperature for different compositions in $Zn_{1-x}Co_xO$ ($0.15 \leq x \leq 0.25$). Insets: (A) M versus H curves of $x = 0.05$ and 0.1; (B) M at 10 kOe, as a function of x

However, based on the observation of smaller amounts of CoO and Co_3O_4 in $x = 0.10$ also, which could be detected from XRD data, it is possible that very small amount of Co, much less than 1%, which is beyond the detection limit of powder XRD, is present in these samples. Therefore, it may be assumed that the weak ferromagnetism observed in the lightly doped compositions also arise from Co metal particles. The fraction of Co metal formed in $x \leq 0.10$ may be very small, as the added Co during the synthesis is converted to Co, CoO and Co_3O_4 so that the small fraction of Co formed cannot be detected even by the powder XRD method. Based on the room temperature saturation magnetization of Co metal, 157.8 emu/g [179], and assuming that Co metal impurity is formed in $x < 0.15$ compositions also which is responsible for the observed ferromagnetism, the weight percentage of Co metal present in the different compositions is obtained as 0.05, 0.18, 0.51, 0.98, and 2.25, respectively, for $x = 0.05$, 0.1, 0.15, 0.2 and 0.25. From powder XRD data, the fraction of Co metal present in the $x = 0.20$ and 0.25 samples is calculated as approximately 1 and 2%, respectively, and these values are comparable to that deduced from the magnetization data, indicating that the ferromagnetic contribution is from the

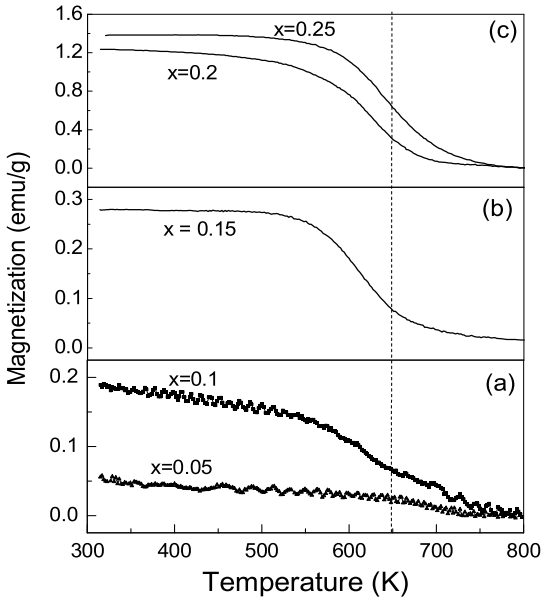

Figure 3.7: Temperature variation of the magnetization of different compositions in $Zn_{1-x}Co_xO$ ($0.05 \leq x \leq 0.25$), where the applied magnetic field is (a) 5000 Oe, (b) 500 Oe and (c) 50 Oe.

Co metal impurities.

Figure 3.7 shows the temperature dependence of magnetization of the different compositions. For $x = 0.2$ and 0.25, a magnetic transition is observed between 600 and 700 K, when measured using an external magnetic field of 50 Oe. Since the saturation magnetization of $x = 0.05$ and 0.1 are very small at room temperature (see Figure 3.6), temperature variation of the magnetization of these two compositions were measured using a field of 5000 Oe. It may be noted that, even for these compositions also, magnetic transitions are observed in the same temperature region, as observed for higher Co-containing compositions ($x \geq 0.15$). It may be argued that, since the Curie temperature of Co metal is 1388 K [179], the magnetic transition observed between 600 and 700 K, in the present case, is due to ferromagnetism in $Zn_{1-x}Co_xO$ and not due to the Co metal particles present as impurities. If this is true, it is not clear why the material is not ferromagnetic above 700 K when Co metal impurities are present (for $x > 0.1$) and why the magnetic transition temperature is independent of the Co-doping level.

Normally, the magnetic measurements for oxide samples are performed in air at-

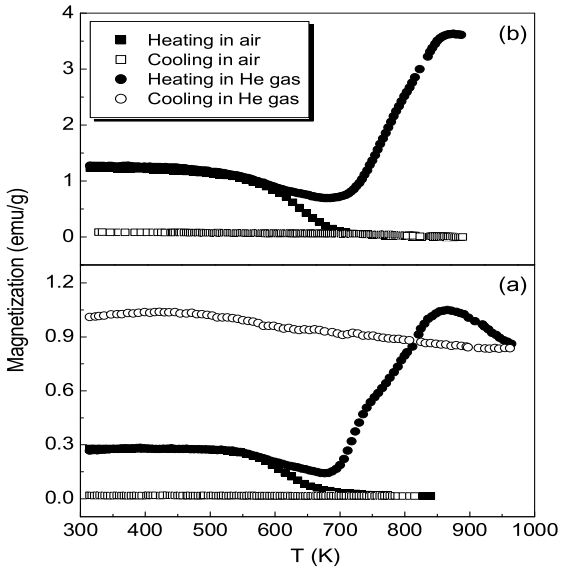

Figure 3.8: Comparison of the temperature variation of the magnetization behavior of the $x = 0.15$ and 0.2 samples when measured in air and in an inert atmosphere during the heating and cooling runs, H = 500 Oe and 50 Oe for (a) $Zn_{0.85}Co_{0.15}O$ and (b) $Zn_{0.8}Co_{0.2}O$, respectively.

mosphere. To see if the sharp decrease in the magnetization above 600 K is really due to any magnetic transition or not, the measurements were made during the heating as well as the cooling runs. Also, the measurements have been performed in air and in an inert gas (He) atmosphere. Figure 3.8 shows the temperature variation of the magnetization of the $x = 0.15$ and 0.2 samples measured under different conditions. The following observations are made during and after the measurements:

i) The magnetic transition, observed between 600 and 700 K, is not reversible when measured in air. When the samples are cooled in the same magnetic field, after recording the heating run, no magnetic transition is observed and the magnetization is close to 0.

ii) The samples cooled back to room temperature are not ferromagnetic.

iii) Ferromagnetism is retained upto 973 K (measurements are not made above this temperature), when the measurements are made in He atmosphere and ferromagnetism is retained while and after cooling the samples.

iv) There is a large increase in the magnetization between 700 and 850 K for the measurements in He atmosphere.

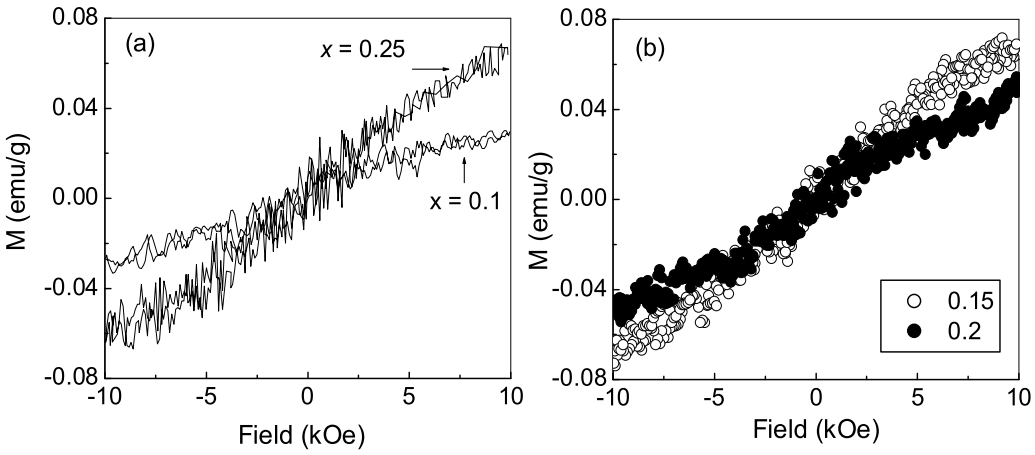

Figure 3.9: Magnetization as a function of magnetic field at room temperature for the heated samples of (a) $Zn_{0.9}Co_{0.1}O$ and $Zn_{0.75}Co_{0.25}O$; and (b) $Zn_{0.85}Co_{0.15}O$ and $Zn_{0.8}Co_{0.2}O$

Based on the above observations, all the samples were heated in air at 800 K, externally in a furnace, and magnetic measurements were performed on the cooled samples. It was found that these samples are not ferromagnetic, including the $x = 0.05$ and 0.1 samples. The M–H curves of the air annealed samples are shown in Figure 3.9. All the samples were found to be paramagnetic, with the magnetic susceptibility increasing with increasing x. These results indicate that ferromagnetism is destroyed after heating in air above the magnetic transition temperature and preserved if heated in an inert atmosphere. Therefore, it can be concluded that the observed decrease in the magnetization above 600 K, for all samples, is not a true ferromagnetic to paramagnetic transition. This is possible if some phase change or oxidation is involved in the heating process in air. If it is assumed that Co metal clusters are present in all the samples, it is possible that the metal is oxidized to the corresponding oxide and the apparent magnetic transition is coming from the loss of ferromagnetism due to the conversion of Co, which is ferromagnetic, to its oxide, which is not ferromagnetic at or above room temperature.

The increase in the magnetization above 700 K and further decrease at higher temperatures, when measured in He, is similar to the behavior reported for Co metal [340]. The hcp-fcc phase transition of Co metal takes place above 700 K, and this is associated

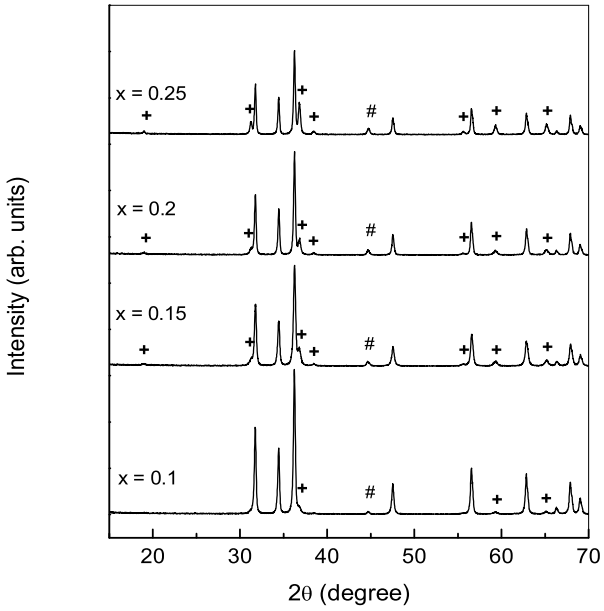

Figure 3.10: Powder XRD patterns of the samples heated to 800 K in air, for different compositions in $Zn_{1-x}Co_xO$ ($0.1 \leq x \leq 0.25$). + Co_3O_4 and # contribution from sample holder.

with a small increase in the magnetization due to the structural change. This transition is reversible but highly hysteretic so that the jump in the magnetization is observed at a lower temperature (below 600 K) while cooling. In fact, a similar behavior is observed in the present case also; a small increase in the magnetization is observed during the cooling run in He atmosphere. These observations further confirm that Co metal impurity is responsible for the ferromagnetism of the doped samples.

The above conclusions are further corroborated by powder XRD studies on the air-heated samples. Figure 3.10 shows the powder XRD patterns of some of the $Zn_{1-x}Co_xO$ samples (x = 0.1, 0.15, 0.2 and 0.25) heated in air at 800 K and cooled to room temperature. All reflections from ZnO and Co_3O_4 are observed for all the heated samples and there are no indications for the presence of Co and CoO as observed in the as-synthesized samples (see Figures 3.2 and 3.4). The fractions of ZnO and Co_3O_4 phases in x = 0.25 composition are found to be approximately 66% and 34%, respectively. Similarly, for x = 0.1 also, weak reflections from Co_3O_4 are clearly observed after heating at 800 K.

Figure 3.11 compares the XRD patterns of the x = 0.15 and 0.20 samples, before and

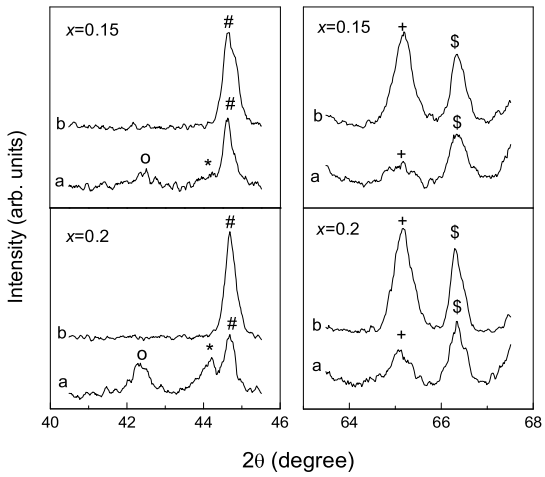

Figure 3.11: Comparison of the expanded powder XRD patterns of two different compositions (a - as-synthesized sample, b - heated sample) in $Zn_{1-x}Co_xO$ (x = 0.15, 0.2) in different 2θ regions where the presence and absence of reflections of individual impurity phases are clearly seen. * Co(111); o CoO(200); + Co3O4(440); $ ZnO(200) and # contribution from Co_3O_4(400) and sample holder.

after heating, in specific 2θ regions where the reflections from Co, CoO and Co_3O_4 are observed. For both samples, the reflections from Co and CoO are disappeared and the intensities of the reflections from Co_3O_4 are enhanced after heating at 800 K. The reflection from ZnO lattice is unaffected after heating. The disappearance of the reflections from Co and CoO and the enhancement in the intensities of the reflections of Co_3O_4 indicate the oxidation of Co clusters and CoO to Co_3O_4. At low temperatures ($<$ 800 K) oxidation of Co and CoO gives Co_3O_4 only, whereas CoO forms only above 1100 K [341, 342]. As x is increased from 0.1 to 0.25, the amount of Co_3O_4 formed is also increased. Thus, the initially observed ferromagnetism is disappeared, due to the oxidation of Co metal clusters to Co_3O_4. Since ferromagnetism is not observed in the case of the air-annealed samples, it can be interpreted that the observed broad magnetic transition is due to the slow conversion of the ferromagnetic Co metal clusters to paramagnetic Co_3O_4.

If an oxidation step is involved coinciding with the decrease in the magnetization above 600 K, it is expected that there will be a corresponding increase in the weight of the samples due to oxidation of Co and CoO to Co_3O_4. Thermogravimetric analysis

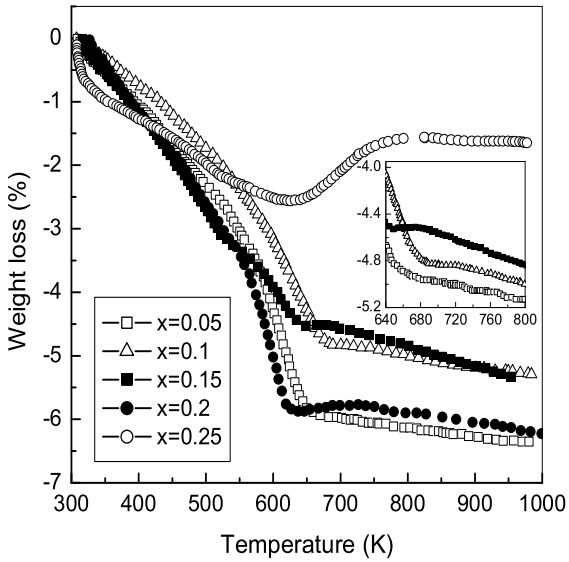

Figure 3.12: TGA curves of the as synthesized samples of different compositions in $Zn_{1-x}Co_xO$.

(TGA) was performed on all the as-synthesized samples to confirm this assumption. Figure 3.12 shows the TGA curves of all the as-synthesized samples, recording in flowing air atmosphere. For all samples, there is a continuous decrease in the weight above room temperature upto 650 K. Except for $x = 0.05$ sample, there is an increase in the weight of the sample above 650 K. There is a large weight gain for the $x = 0.25$ sample. The initial weight loss upto 650 K is most likely to be due to the removal of the adsorbed water and conversion of residual carbon as CO_2. These carbon contents remain after the autocombustion reaction, due to the partial decomposition of the glycine molecules, since glycine has been used as the fuel [263].

The temperature region in which the weight gain in the TGA curves is observed coincides almost with the magnetic transition temperature observed for all the samples, which is independent of the Co content. This is the temperature region where oxidation of Co metal to its oxide, Co_3O_4, takes place [341, 342]. It is clearly seen that, the percentage weight gain is also increased as x is increased in $Zn_{1-x}Co_xO$. Thus, it can be concluded from the powder XRD and TGA data that the weight gain for all the samples is due to the oxidation of cobalt metal to Co_3O_4. This is clear evidence for the fact that with

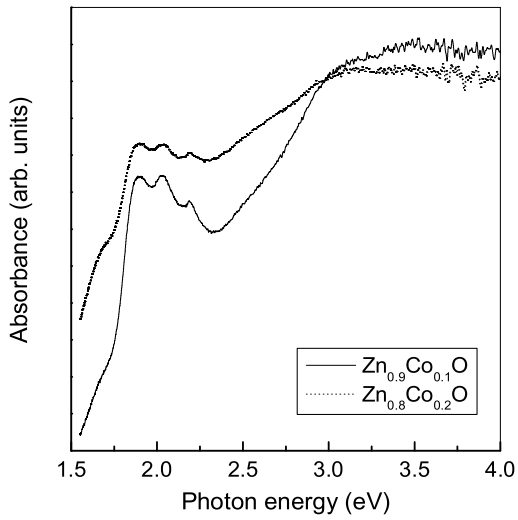

Figure 3.13: Electronic spectra of the heated samples of two different compositions.

increasing x, there is more cobalt metal content in the samples. The fact that the temperature regions where a magnetic transition in the M–T curves and the weight gain in the thermogravimetric curves are the same, indicate that the magnetic transition from the ferromagnetic to the paramagnetic state is not a true magnetic transition but because of the oxidation of the ferromagnetic Co metal to its paramagnetic oxide. Both CoO and Co_3O_4 are paramagnetic at and above room temperature (T_N of CoO and Co_3O_4 are 291 K [94] and 40 K [343], respectively).

The above analyzes reveal that a small fraction of the added Co is incorporated inside the ZnO lattice and impurity phases are formed from the remaining part. Now it is important to find out whether the incorporated Co ions are affected by heating or not. Interestingly, the color of the samples was found to be preserved after heating at 800 K, indicating that Co^{2+} is indeed incorporated in the ZnO lattice and that the (ZnCo)O lattice is preserved even after heating. Same features, including optical absorptions and band edge transition, are observed in the optical spectra of the heated samples as found for the as-synthesized samples, as shown in Figure 3.13. Thus, it is clear that heating does not affect the structure of $Zn_{1-x}Co_xO$ and the incorporated Co^{2+} ions remain inside the ZnO lattice.

X-ray photoelectron spectroscopy (XPS) measurements have been used in different

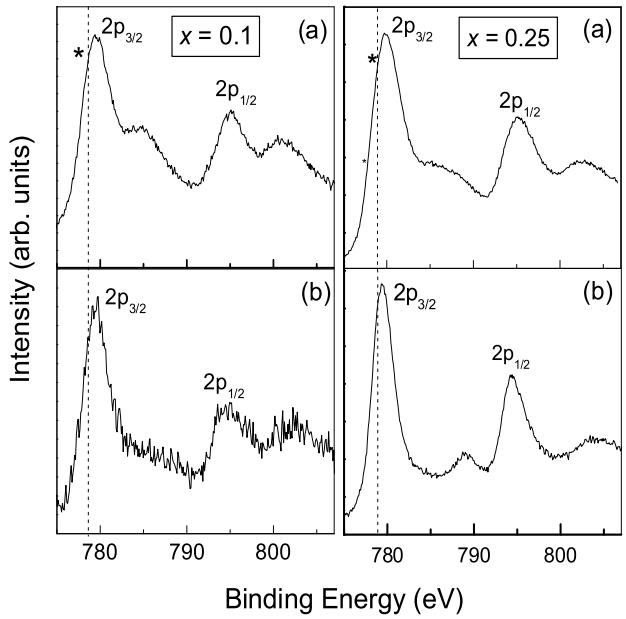

Figure 3.14: Co 2p XPS of $Zn_{0.9}Co_{0.1}O$ ($x = 0.1$) and $Zn_{0.75}Co_{0.25}O$ ($x = 0.25$) powders. (a) as-synthesized sample, (b) heated sample. * Expected Co $2p_{3/2}$ peak of Co metal [349].

reports to confirm the valence state of doped Co as well as the absence of Co metal impurities in Co doped ZnO [132, 344, 345]. The absence of Co metal clusters in the lightly doped samples was also confirmed from these studies. In the present study, it has been already found from powder XRD studies that Co metal is present as an impurity phase in samples with $x > 0.1$. More over, magnetic measurements and thermogravimetric studies indicated that even for $x \leq 0.1$, the apparent magnetic transition, which is not reversible, occurs in the same temperature range accompanied by a weight gain on heating above this temperature. To corroborate the results obtained from the optical absorption studies and to ascertain whether the presence of Co metal clusters in small amounts in the highly doped samples can be really detected, room temperature XPS analysis have been performed on the as-synthesized and the heated powders of $Zn_{0.9}Co_{0.1}O$ and $Zn_{0.75}Co_{0.25}O$. These two compositions were studied because the $x = 0.25$ sample showed the presence of approximately 2% Co metal in the XRD pattern whereas no such impurity phase was detected for the $x = 0.1$ sample. The Co 2p XPS of the two samples, before and after heating at 800 K, are shown in Figure 3.14.

All the XPS spectra show four clear peaks, the Co $2p_{3/2}$ and $2p_{1/2}$ spin-orbit components and the shake-up resonance transitions (satellite) of these two peaks at higher binding energies (BE). The Co $2p_{3/2}$ and $2p_{1/2}$ binding energies of the as-synthesized samples are obtained as 779.8 and 795.1 eV, respectively, for both samples. For the heated samples, Co $2p_{3/2}$ and $2p_{1/2}$ binding energies are at 779.5 and 794.4 eV, respectively. The difference in the $2p_{3/2}$ and $2p_{1/2}$ binding energies is 15.3 eV for the as-synthesized sample and 14.9 eV for the heated sample. The energy difference between the BEs of Co $2p_{3/2}$ and Co $2p_{1/2}$ is reported as 15.47 eV, by Lee *et al.* [132], for thin film samples of Co doped ZnO.

The observed Co $2p_{3/2}$ and Co $2p_{1/2}$ binding energies and the difference in the binding energies for the as-synthesized samples are comparable to that of the binding energies of the corresponding photoelectrons of Co^{2+} in CoO [281, 346–348]. On the other hand, for the heated samples the values are comparable to that of Co_3O_4 [281]. Similarly, the satellite peaks of the spin-orbit components are observed at a higher binding energy of 5.3 eV for the as-synthesized samples. These observations are comparable to the characteristics of high-spin Co^{2+} in CoO and these comparisons strongly suggest that the cobalt in the as-synthesized $Zn_{0.9}Co_{0.1}O$ and $Zn_{0.75}Co_{0.25}O$ samples is present in the +2 oxidized state, as confirmed from the optical absorption studies. However, if both CoO and Co_3O_4 are present in the samples as impurities, as evidenced from powder XRD studies, their presence cannot be differentiated from the XPS results. There is a large difference in the binding energies of the satellite peaks before and after heating. For the as-synthesized sample, broad satellite peaks are observed. The maximum of the Co $2p_{3/2}$ satellite peak is shifted from 785.2 eV to 789.2 eV after heating and a corresponding shift to higher binding energies is observed for the Co $2p_{1/2}$ satellite peak also. Such large difference of 9 eV for the Co $2p_{3/2}$ main and satellites peaks is observed in the case of Co_3O_4 [347]. Already the powder XRD studies have indicated the presence of large amounts of Co_3O_4 in the heated samples of $Zn_{0.75}Co_{0.25}O$ and the XPS results are in line.

As stated, there is no evidence for the presence of Co metal in the XPS spectrum of the as-synthesized $x = 0.25$ sample, as evidenced by the absence of any feature at 778 eV where the Co $2p_{3/2}$ peak of Co metal is expected [349]. This is shown as an evidence for the absence of Co metal nanoclusters in the thin film samples of Co doped ZnO [132].

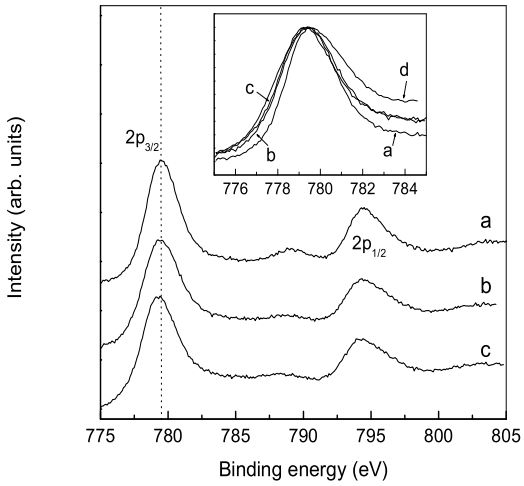

Figure 3.15: Co $2p$ XPS of a) heated sample of $Zn_{0.75}Co_{0.25}O$, b) with 2.5% weight of Co metal powder added and c) 12.5% weight of Co metal powder added. Inset: normalized Co $2p_{3/2}$ peak of the as-synthesized (curve d) and the heated sample before and after adding Co (the binding energy of the as-synthesized sample is corrected to that of the heated sample)

However, magnetic and powder XRD studies already indicated the presence of Co metal in the present $x = 0.25$ sample and therefore it is possible that since the amount of cobalt metal clusters formed is very small, the Co $2p_{3/2}$ peak of Co-metal is merged with the peak of Co^{2+}. To confirm this, extra cobalt metal powder has been added in the heated $x = 0.25$ sample and the XPS was recorded. This is shown in Figure 3.15. When about 2.5% by weight of Co is added (corresponding to the amount of Co metal present in the as-synthesized sample, as deduced from XRD data) the feature due to Co metal is not observed at 778 eV as expected. On the other hand, when a large amount of Co is added (12.5 weight%) the Co $2p_{3/2}$ peak is shifted to lower binding energies by 0.5 eV. Still no clear feature at 778 eV due to Co metal is observed. Inset of Figure 3.15 compares the normalized Co $2p_{3/2}$ peak of the as-synthesized (curve d) and the heated sample before and after adding Co (the binding energy of the as-synthesized sample is corrected to that of the heated sample). It may be seen that the peak is broader for the as-synthesized sample compared to that of the heated sample. Similarly, the peak is broadened after the addition of cobalt metal powder in the heated sample. Thus, the broad peak of the as-

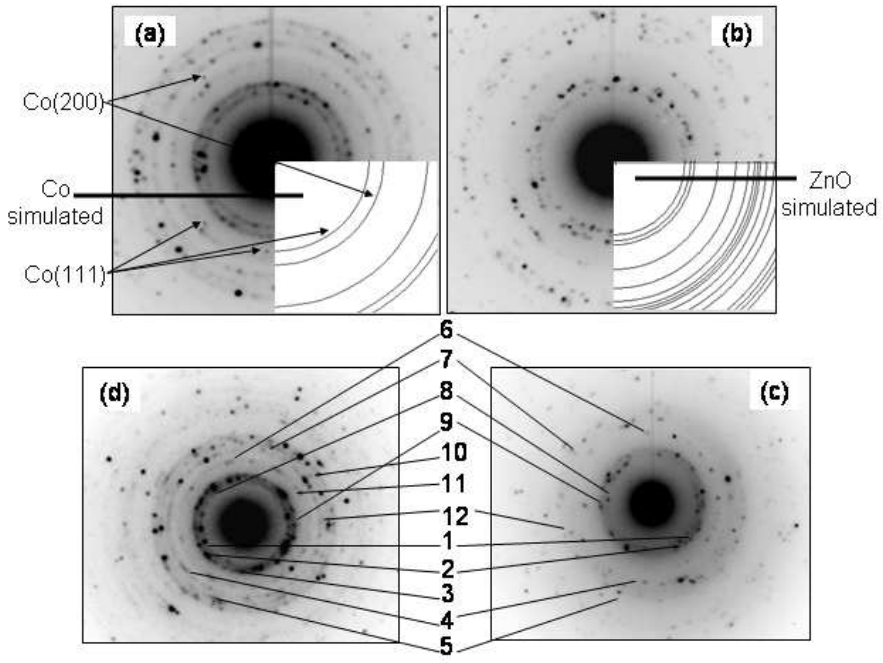

Figure 3.16: Comparison of SAED of (a) $Zn_{0.9}Co_{0.1}O$ and (b) ZnO, with the simulated patterns of Co and ZnO. SAED of (c) $Zn_{0.95}Co_{0.05}O$, and (d) $Zn_{0.9}Co_{0.1}O$. The indexing of the rings and spots corresponding to the numbers shown in the figures (c and d) are given in Table 3.1.

synthesized sample is likely to be due to the contribution from Co metal impurity. These results clearly show that it is very difficult to detect the presence of Co metal clusters, if present in small amounts, from XPS data, due to the overlapping of the peak from Co metal at the base of the broad peak from Co^{2+}. The impurity phases such as CoO and Co_3O_4 can also contribute to the Co^{2+} peaks along with the contribution from the doped fraction of Co^{2+}.

Although there is no direct evidence for the presence for Co or its oxides in the lightly doped ($x < 0.1$) samples, from any of the studies discussed so far (powder XRD studies showed the presence of CoO and Co_3O_4 in the $x = 0.1$ sample, only on comparison with the highly doped samples), clear evidence for the presence of Co metal and its oxides in $x \leq 0.1$ compositions is obtained from electron diffraction studies. Figure 3.16 shows the selected area electron diffraction (SAED) patterns of the as-synthesized samples of $x =$ 0, 0.05 and 0.1. The SAED patterns of $Zn_{0.9}Co_{0.1}O$ and ZnO are compared with that

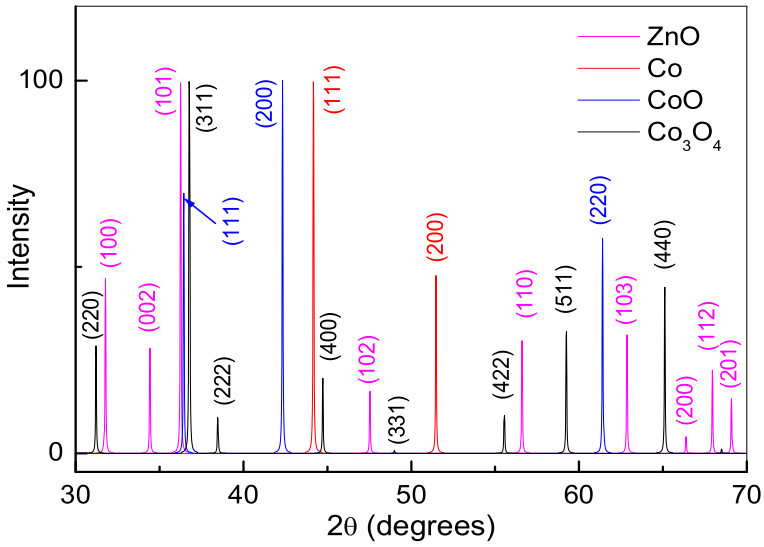

Figure 3.17: Simulated XRD patterns of ZnO, Co, CoO and Co_3O_4.

Table 3.1: Indexing of different rings and spots in the electron diffraction patterns corresponding to the numbers shown in Figure 3.16 for ZnO, $Zn_{0.95}Co_{0.05}O$ and $Zn_{0.9}Co_{0.1}O$.

Identification	Phase	hkl plane
1	ZnO	(100)
2	ZnO	(002)
3	ZnO	(101)
4	ZnO	(110)
5	ZnO	(103)
6	Co	(111)
7	Co	(200)
8	Co_3O_4	(200)
9	Co_3O_4	(311)
10	Co_3O_4	(400)
11	CoO	(200)
12	CoO	(220)

of the simulated electron diffraction patterns of Co and ZnO in Figure 3.16(a) and (b). The simulated powder XRD patterns of ZnO, Co, CoO, and Co_3O_4 (for Cu Kα radiation) are shown in the Figure 3.17 for a direct comparison of the positions of the diffraction spots/rings from the impurities with respect to that from ZnO. Many additional diffraction spots, apart from those from the ZnO lattice, are observed in the SAED patterns of the $x = 0.05$ and 0.1 samples. The additional spots in the electron diffraction patterns are identified as those from Co metal, CoO and Co_3O_4. The indexing of the different spots and rings is given in Table 3.1. The presence of these impurities in the lightly doped samples could not be detected from powder XRD studies, probably because of their very low concentrations, although some indication for the presence CoO and Co_3O_4 were obtained (see Figure 3.4). This indicates that $Zn_{0.95}Co_{0.05}O$ and $Zn_{0.9}Co_{0.1}O$ contain other impurity phases and the different impurity phases are not homogeneously distributed in the sample. The most intense (311) reflection of Co_3O_4 is very close to the intense (101) reflection of ZnO (see Figure 3.17) and is seen almost merged with that of ZnO in the electron diffraction pattern (Figure 3.16(c) and (d)). However, the two most intense reflections of Co metal, which are well separated from the reflections of ZnO, are visible as very weak spots in the electron diffraction pattern of the doped samples (Figure 3.16 (a),(c), and (d)), indicating the presence of Co metal impurities in the sample. Since information for the presence of Co metal in the $x = 0.05$ and 0.1 samples is obtained now, it can be concluded that the observed ferromagnetism of these samples also is coming from Co metal impurities. Park *et al.* have recently reported the presence of nanometer sized Co metal clusters in thin film samples of $Zn_{1-x}Co_xO$ for $x > 0.12$, as evidenced from electron diffraction studies and field emission scanning microscopic image [157]. Thus, the present experimental findings support the idea of extrinsic ferromagnetism in polycrystalline ZnO diluted magnetic semiconductors, as presented in a very recent review by Seshadri, where the author claimed that intrinsic ferromagnetism is not possible in bulk ZnO based DMSs [335].

3.3.2 Paramagnetic $Zn_{1-x}Co_xO$

Since the synthesis procedures mentioned in *section 3.2* did not give single phase compositions, and as there are some reports on the absence of ferromagnetism in Co doped

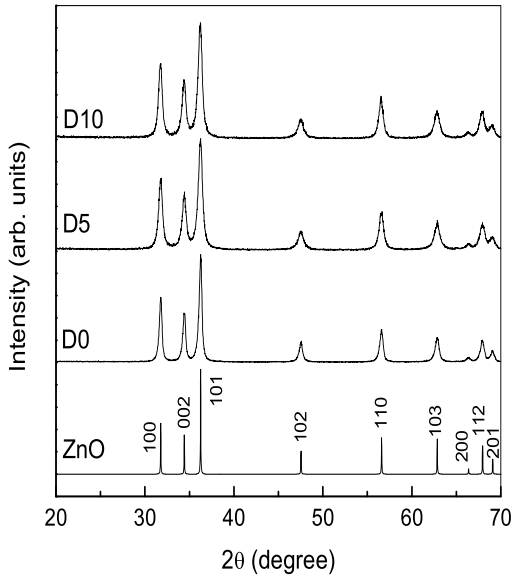

Figure 3.18: Powder XRD patterns of the as-synthesized $Zn_{1-x}Co_xO$ powder samples synthesized by the modified GNP. ZnO is the simulated XRD pattern.

ZnO synthesized by other routes, it is essential to synthesize similar non-magnetic compositions and to compare the properties of magnetic and non-magnetic compositions. In some reports, it has been stated that ferromagnetism solely depends on the synthesis conditions [152, 154]. Therefore, the GNP procedure is modified to obtain single phase compositions. Dextrose was added as an extra fuel along with glycine during the synthesis. Studies on the structural, magnetic and optical properties of $Zn_{1-x}Co_xO$ ($x = 0$, 0.05 and 0.1) synthesized by the modified GNP method are discussed in this section.

Nanoparticles of $Zn_{1-x}Co_xO$ ($x = 0$, 0.05 and 0.1) were synthesized by modifying the autocombustion method mentioned in *section 3.2*. Metal nitrates and glycine (2 moles of glycine per mole of metal ion) were taken in the stoichiometric ratio as described in *section 3.2* and dissolved in distilled water and mixed thoroughly. To the above solution a water solution of 1 M of dextrose was added as an extra fuel and carried out the synthesis as described in *section 3.2*. The 0%, 5% and 10% Co doped ZnO samples, synthesized by the modified method are coded as D0, D5 and D10, respectively. For convenience during comparison of the properties, the 0%, 5% and 10% Co doped samples synthesized by the GNP procedure, as discussed in the previous section, are coded as G0, G5 and

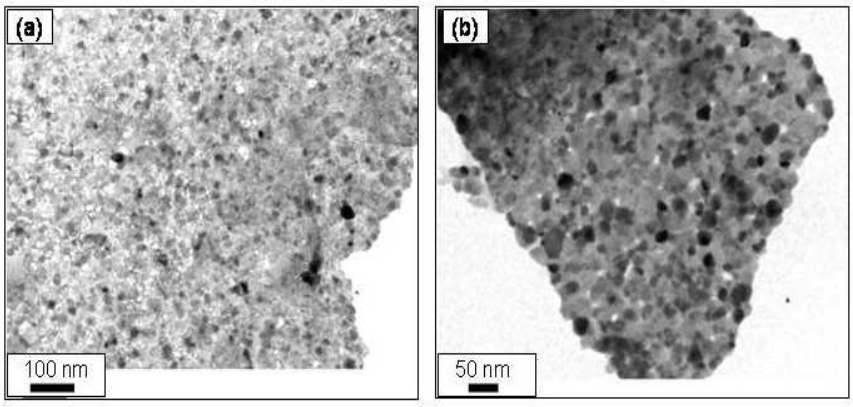

Figure 3.19: TEM images of D10 from two different regions.

G10, respectively. All the as-synthesized Co doped samples (G5, G10, D5 and D10) were green in color.

The powder XRD patterns of the as-synthesized samples of DX series (X = 0, 5 and 10) are shown in Figure 3.18. The XRD patterns for $x > 0$ show that the ZnO structure is not disturbed on substitution. All the reflections for different compositions are some what broad and this is due to the smaller crystallite sizes of the samples. The average crystallite size is obtained as ∼15 nm for all DX compositions (x = 0, 5 and 10) and is smaller than the corresponding samples obtained by the GNP method. The fact that no additional peaks due to any impurities are observed for $x > 0$ indicates that the modified method of synthesis gives single phase $Zn_{1-x}Co_xO$ nanoparticles. Transmission electron micrographs of D10 are shown in Figure 3.19. The average particle size is found be nearly matching with that of obtained from the XRD analysis.

Room temperature magnetization measurements indicated that the DX series show paramagnetic behavior, as shown in inset of Figure 3.20. No magnetic ordering is observed in the case of D5 and D10, down to 12 K, as shown in Figure 3.20. The magnetization is measured under zero field cooled (ZFC) conditions, in an applied field of 1 kOe. Magnetization decreases with increasing temperature and reaches a minimum value at 300 K. Magnetization measurements of the two samples at 12 K were carried out as a function of the magnetic field. The M–H curves of D5 and D10 at 12 K are shown in the inset of

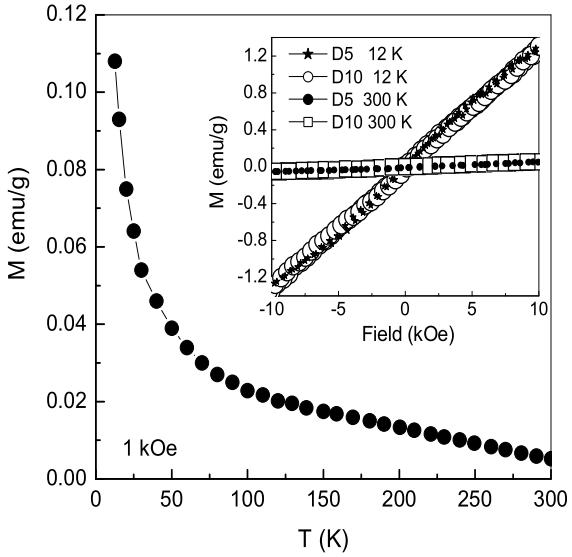

Figure 3.20: Temperature variation of magnetization for D10, measured using a magnetic field as indicated. Inset: *M–H* curves of D5 and D10 at the indicated temperatures

Figure 3.20. The magnetization measurements show that both the samples remain paramagnetic at this temperature. Thus, the results on the DX samples are in agreement with that reported in the literature for polycrystalline non-magnetic Co doped ZnO [145, 148].

To determine whether Co ions are substituted in the ZnO lattice or not and to ascertain the site of substitution and the oxidation state of Co, optical absorption studies are made on all samples. The optical absorption spectra are shown in Figure 3.21(a) along with that of pure ZnO ($x = 0$). Additional absorption features are observed in the case of the doped samples (D5 and D10) and these bands, marked as a, b, and c, at 1.89, 2.03 and 2.18 eV, respectively, are similar to the GX samples as described earlier. Hence the optical absorption studies prove the incorporation of Co^{2+} in ZnO in the non-magnetic samples. There is a linear decrease in the band gap on increase in the Co content, as shown in Figure 3.21(b). This redshift has been explained in terms of increasing *sp-d* exchange interactions with increasing Co content [338]. The values of the band gap for the DX samples are comparable to that reported recently for nonmagnetic samples [339]. However, the decrease in the band gap for the ferromagnetic GX samples is less than that observed for the DX samples, indicating that there is a difference in the extent of doping

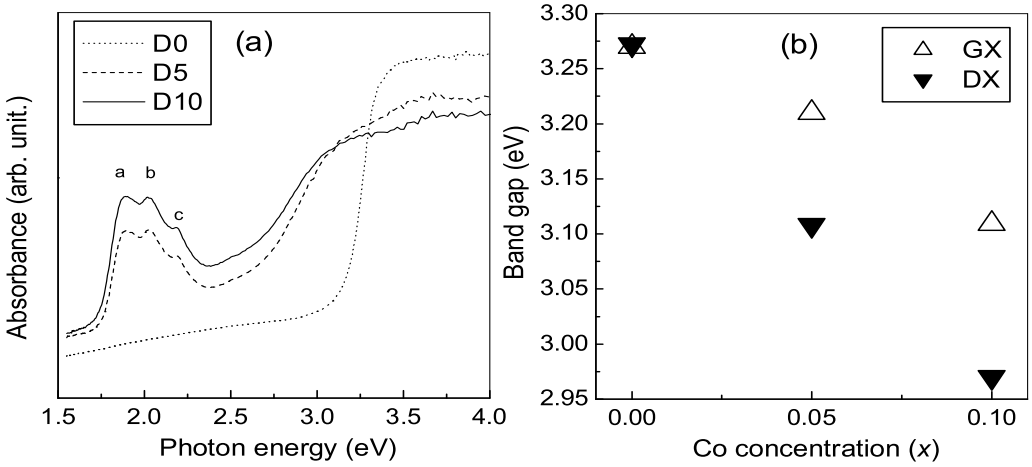

Figure 3.21: (a) Room temperature optical absorption spectra of D0, D5 and D10; (b) Comparision of variation of band gap of the GNP samples (G0, G5 and G10) with GNP+dextrose samples (D0, D5 and D10).

in the two series of samples. For example, the band gap of G10 is comparable to that of D5, indicating that only 50% of Co added is likely to be substituted for Zn. These results imply that less number of Co^{2+} ions are doped in the ferromagnetic samples.

The Co 2*p* XPS of G10 and D10 are compared in Figure 3.22. The Co $2p_{3/2}$ and $2p_{1/2}$ binding energies are obtained as 780.55 and 796.0 eV, respectively. These binding energies are in agreement with the Co^{2+} photoelectron binding energis of CoO and Co_3O_4, but around 2 eV higher that that of metallic cobalt [281, 347] as already discussed in *section 3.3.1.* The energy difference between the BEs of Co $2p_{3/2}$ and Co $2p_{1/2}$ is 15.45 eV, comparable to that reported by Lee *et al.* for thin film samples [132]. These comparisons strongly suggest that the cobalt in D10 is present in the oxidized state and the oxidation number is +2.

Thus, XRD, XPS and optical studies give evidences for the incorporation of Co^{2+} ions in the ZnO lattice. However, the difference in the magnetic behavior of the two series of samples cannot be explained based on these observations. Studies on GNP synthesized $Zn_{1-x}Co_xO$ samples showed evidence for the presence of Co metal impurities in the Co doped samples. In this case powder XRD and electron diffraction studies gave direct evidence for small amounts of Co metal impurities. Hence selected area electron

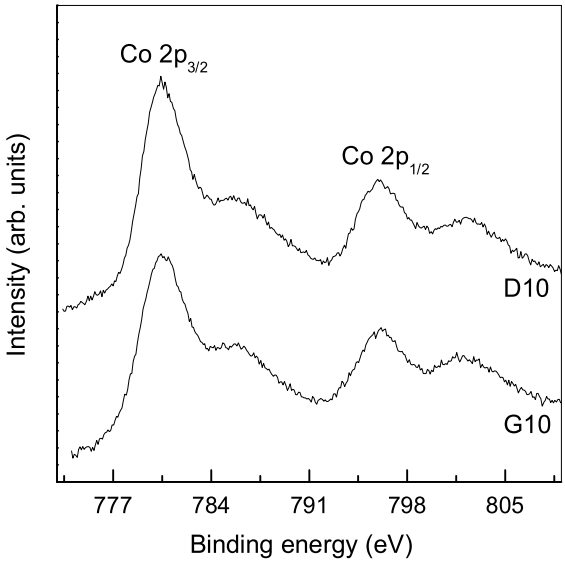

Figure 3.22: Comparison of room temperature X-ray photoelectron spectra of G10 and D10.

diffraction (SAED) studies were performed on the nonmagnetic samples also (D5 and D10) to look for the presence of Co metal or any other impurities. The SAED pattern of D10 is compared with the simulated electron diffraction ring pattern of ZnO in Figure 3.23. The SAED pattern of D10 is exactly matching with that of ZnO. There are no extra rings or spots are detected in the SAED pattern of D10. Thus Figure 3.23 establishes that (ZnCo)O synthesized by the modified route is free from any impurities free.

Because of the absence of Co metal impurities in D5 and D10, these samples remain paramagnetic down to 12 K. These results explain why the decrease in the band gap is less for the ferromagnetic samples (G5 and G10) when compared to the values for D5 and D10. In the case of G5 and G10, only part of the Co^{2+} ions are incorporated in the ZnO lattice and the rest are converted into Co, CoO and Co_3O_4, due to the particular synthesis conditions. From the studies and direct comparison of the characteristics of magnetic and nonmagnetic samples of polycrystalline $Zn_{1-x}Co_xO$, synthesized under almost identical conditions, it is shown that without ferromagnetic impurity phase, intrinsic ferromagnetism is not possible in Co doped ZnO.

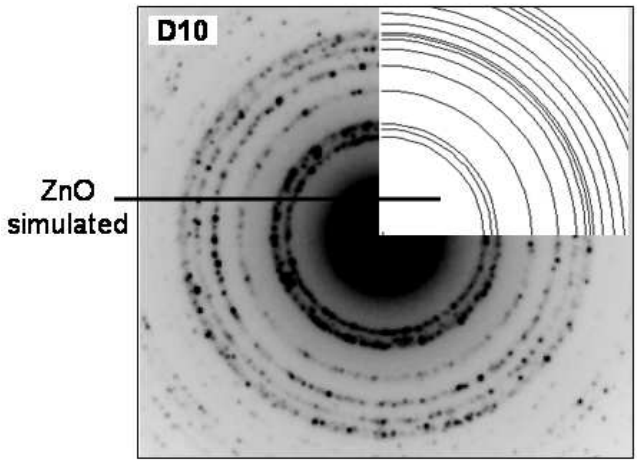

Figure 3.23: Comparison of the selected area electron diffraction pattern of D10 with the simulated pattern of ZnO.

3.3.3 Hydrogen treatment of paramagnetic $Zn_{0.95}Co_{0.05}O$

In a very recent report, Lee *et al.* showed that ZnCo(9.1%)O and ZnCo(5%)O thin films become ferromagnetic when hydrogenated with Ar-H_2 mixed-gas, due to the enhanced ferromagnetic spin-spin interaction in the H-Co coupling [158]. Though Co metallic peak is observed in the XPS spectra of the reduced samples, ferromagnetic contribution from Co metal has not been detected in the magnetic circular dichroism (MCD) studies. Therefore, for a comparison of the results with that reported in the literature, one of the paramagnetic $Zn_{1-x}Co_xO$ sample discussed in the previous section has been treated with hydrogen and studied different properties of the reduced sample.

The paramagnetic D5 sample from the above section is taken for the hydrogen treatment analysis. The $Zn_{0.95}Co_{0.05}O$ (D5) powder sample was hydrogenated in an argon-hydrogen mixed-gas (96.5%Ar+3.5%H_2) flow at 1125 K for 2 h. Another part of the sample was annealed in air at the same temperature and duration. For convenience, the as-synthesized $Zn_{0.95}Co_{0.05}O$ is referred as ZnCoO, air annealed sample as ZnCoO-A and hydrogenated sample as ZnCoO-H.

It is already established that ZnCoO (D5) is paramagnetic down to 12 K (see Figure 3.20). But, surprisingly, as shown in Figure. 3.24(a), ZnCoO-H has a very high value of magnetization at room temperature and the magnetization is saturated above 5 kOe.

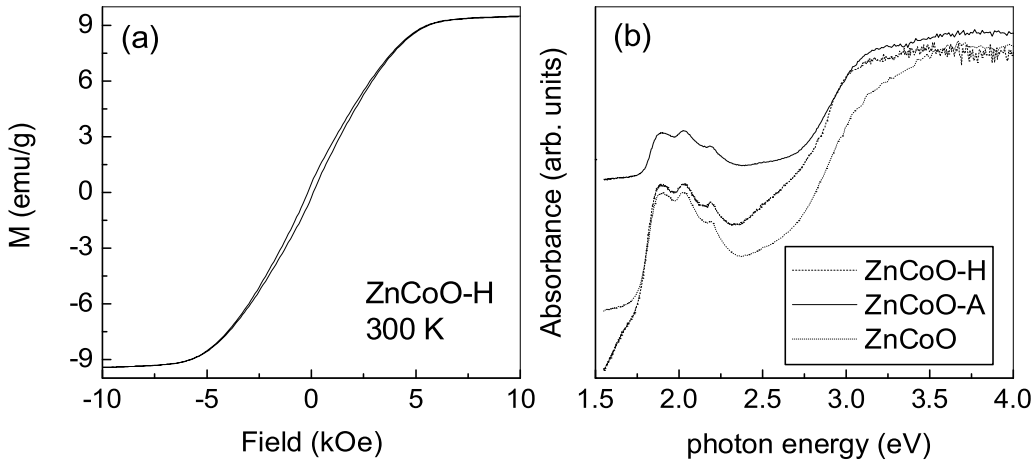

Figure 3.24: (a) Magnetization curve of ZnCoO-H at 300 K and (b) comparison of the optical absorption spectra of ZnCoO, ZnCoO-A and ZnCoO-H.

The room temperature saturation magnetization is found to be 9.5 emu/g. Though it is predicted that hydrogen can induce ferromagnetism, such a high value of magnetization is not be possible in the case of 5% Co-doping. Lee *et al.* saw very weak MCD signal when the doping was with 9.1% and 5% Co ions [158]. Thus, the origin of the ferromagnetism in the present hydrogenated sample might be from some other sources. The optical absorption spectra of ZnCoO-H is compared with that of ZnCoO and ZnCoO-A in Figure 3.24(b). It is seen clearly that ZnCoO-H and ZnCoO-A have same absorption characteristics as ZnCoO. Therefore, the substituted Co^{2+} ions have not been disturbed after annealing (in hydrogen and air environments) and remain in the high spin (d^7) state at the tetrahedral site of ZnO.

The XRD pattern of the hydrogenated sample (ZnCoO-H) is shown in Figure 3.25. Interestingly, additional reflections due to the fcc phase of Co metal [Co(111) and Co(200)] are observed in the XRD pattern. Thus, it is likely that this Co metal impurity phase is responsible for the room temperature ferromagnetism and high magnetization of the hydrogenated sample. However, optical studies showed that Co^{2+} ions are present in the hydrogenated sample and the powder XRD studies reveal that the wurtzite structure is not disturbed after hydrogenation. Hence, the additional Co phase is likely to be derived

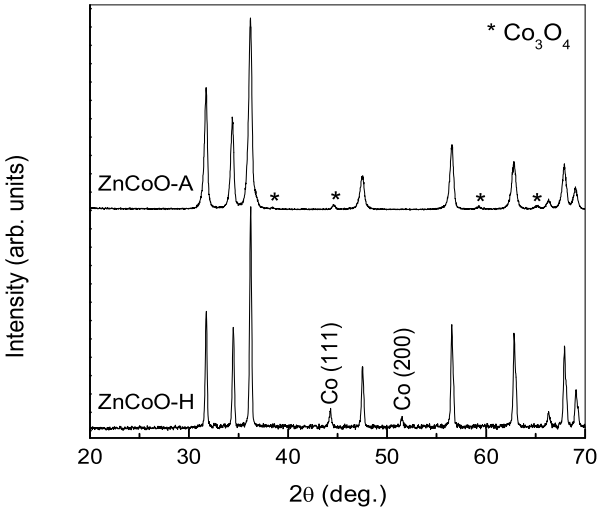

Figure 3.25: Comparison of the powder XRD patterns of ZnCoO-H and ZnCoO-A.

from some other impurity phase which was not detected in the XRD pattern of ZnCoO. The possibilities are some amorphous forms of CoO or Co_3O_4. The powder XRD pattern of the air annealed sample shows many additional reflections (Figure 3.25) which are due to Co_3O_4. However, still this sample shows optical transitions due to Co^{2+} in the tetrahedral site of the ZnO lattice as shown in Figure 3.24(b). Thus, it is possible that the as-synthesized ZnCoO sample contains some Co_3O_4 in the amorphous form which becomes more crystalline when annealed in air or is reduced to Co metal when heated in hydrogen. Therefore, the hydrogen induced ferromagnetism in ZnCoO in the present studies is coming from ferromagnetic Co metal impurities and not due to any enhanced exchange interactions.

3.4 $\mathbf{Zn_{1-x}Ni_xO}$ $\mathbf{(0 \leq x \leq 0.05)}$

Studies of the structural, optical and magnetic properties of nanocrystalline powder samples of Ni doped ZnO synthesized by the glycine-nitrate autocombustion method is reported in this section. The samples are synthesized by taking 2 moles of glycine per mole of metal ion, as discussed in *section 2.2*.

The powder XRD patterns of the as-synthesized samples of $Zn_{1-x}Ni_xO$ (x = 0, 0.025

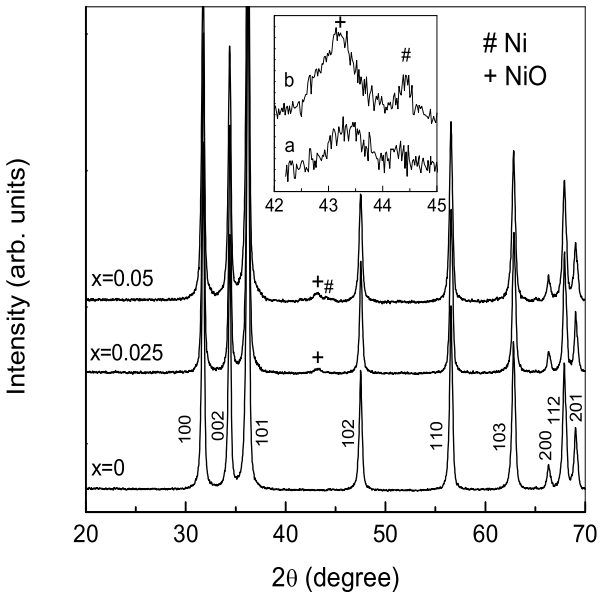

Figure 3.26: The Powder XRD patterns of $Zn_{1-x}Ni_xO$. Inset: normal scan data of $x = 0.05$ (curve a) and slow scan data of $x = 0.025$ (curve b) in the region where most intense reflection from NiO and Ni metal is expected.

and 0.05) are shown in Figure 3.26. Comparison with the XRD pattern of $x = 0$ shows that for $x > 0$ the ZnO structure is not disturbed on substitution. The average crystallite size, calculated from X-ray line broadening using the Scherrer formula, is obtained as ∼30 nm for the Ni doped compositions. An additional very low intense peak is observed at $2\theta = 43.2°$ for $x = 0.025$. This has been identified as the most intense reflection from NiO. Very recently, similar observation was reported in the 10% Ni doped ZnO powder by Pei *et al.* [141]. Apart from this peak with enhanced intensity, an additional weak reflection is observed for $x = 0.05$, close to the reflection from NiO. This weak extra peak in the XRD pattern is found to be due to Ni metal. Since Ni metal peak is detectable in the 5% doped sample, the XRD pattern of $x = 0.025$ sample is closely examined by recording the XRD pattern at a very slow scan rate, in the specific 2θ range where the most intense peak of Ni metal is expected. This procedure is known to be highly efficient in detecting very small quantities of impurity phases [350]. A weak reflection at $2\theta = 44.3°$ corresponding to Ni is obtained apart from that due to NiO, by this procedure. The normal scan data of the 5% doped sample (curve a) and the slow scan data of the 2.5% doped sample (curve

b) in the two theta region 42-45° are compared in the inset of Figure 3.26. Reflections from NiO and Ni metal can be clearly seen in both the samples. The approximate weight percentages of Ni and NiO were calculated from the least-squares refinement of the XRD patterns using the Powder Cell program [272]. The fraction of NiO is obtained as 0.3% and 2.7% and that of Ni is calculated as 0.15% and 0.3%, respectively, in the $x = 0.025$ and 0.05 samples. Based on the amounts of Ni and NiO in the $x = 0.025$ and 0.05 samples, the fractions of Ni^{2+} substituted for Zn^{2+} in the ZnO lattice are calculated as ∼2.1% and ∼2.6%, respectively.

Thus the powder XRD studies directly indicate the presence of Ni metal, apart from NiO, in the doped polycrystalline samples. Wakano *et al.* have observed the formation of NiO impurities when the substrate temperature is above 773 K during the fabrication of Ni doped ZnO films [318]. To investigate the effect of heating, both Ni doped samples have been annealed at 673 K (above the T_C of Ni metal which is 627 K [94]) for 2 hours in air in a furnace and the properties are measured after cooling the samples to room temperature. No Ni-metal peak is observed in the XRD pattern of the air annealed samples. The amounts of NiO in the 673 K annealed $x = 0.025$ and 0.05 samples is calculated from the XRD data as 0.4% and 2.7%, respectively.

Figure 3.27 shows the optical absorption spectra, near the band edge, for different samples. The band edge (band edge is obtained from the position of the maximum in the derivative of the absorption curve) is shifted to lower energy side for the Ni doped samples, as shown in the inset (A of Figure 3.27. However, for both the $x = 0.025$ and 0.05 samples, the band edge is obtained as 3.242 eV. The decrease in the band edge is a clear indication for the incorporation of Ni inside the ZnO lattice. There is not much variation in the band edge after annealing the Ni doped samples. It has been reported that the band edge becomes constant for the mole percentages of Ni >2% for $Zn_{1-x}Ni_xO$ [339], and the present results are in agreement with the reported values. Inset B in Figure 3.27 shows the spin-orbit split $^3T_1(F) \rightarrow {}^3T_1(P)$ ligand field transitions of Ni^{2+} in tetrahedral symmetry, for the as-synthesized and annealed samples of $x = 0.025$ and 0.05. The electronic transitions are observed in all cases (the absorptions are partially masked in the as-synthesized samples, due to the residual carbon present), indicating that Ni^{2+} is substituted in the tetrahedral Zn^{2+} site and is in a stable environment [296, 320, 351].

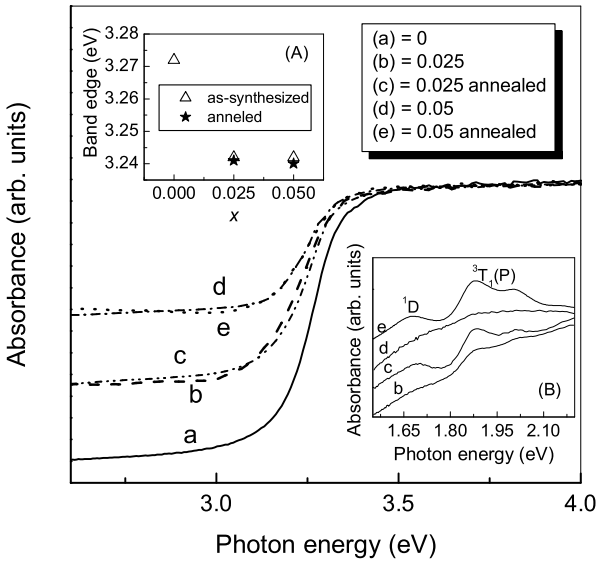

Figure 3.27: Room temperature optical absorption spectra of the as-synthesized and annealed $Zn_{1-x}Ni_xO$ powders, near the band edge. Insets: (A) band edge as a function of x; (B) the ligand field transitions of Ni^{2+} in tetrahedral symmetry for the as-synthesized and annealed samples of $x = 0.025$ and 0.05.

The decrease in the band edge and the observation of the electronic transition of Ni^{2+} are clear indications for the incorporation of Ni^{2+} inside the ZnO lattice, as observed in the case of Co doped ZnO as discussed earlier. This shows that a small fraction of Zn is substituted by Ni in the ZnO lattice. Since the band edge remains the same for both the doped samples, the degree of substitution of Ni for Zn is likely to be the same in both samples.

The Ni doped samples are found to be ferromagnetic at room temperature. Variation of the magnetization in the Ni doped samples as a function of magnetic field, measured at room temperature, is shown in Figure 3.28. Weak ferromagnetism, 0.1 and 0.15 emu/g for $x = 0.025$ and 0.05, respectively, which is saturated just above 1 kOe, is observed at 300 K. For the $x = 0.05$ sample, the magnetization measured at 12 K is also shown in the figure. There is not much variation in the magnetization at 12 K, when compared to the room temperature values. For $x = 0.025$ and 0.05, magnetization at 12 K is obtained as 0.12 and 0.19 emu/g, respectively. Since Ni metal and NiO are observed as impurities in the as-synthesized samples, it can be assumed that magnetic contribution comes mainly from the

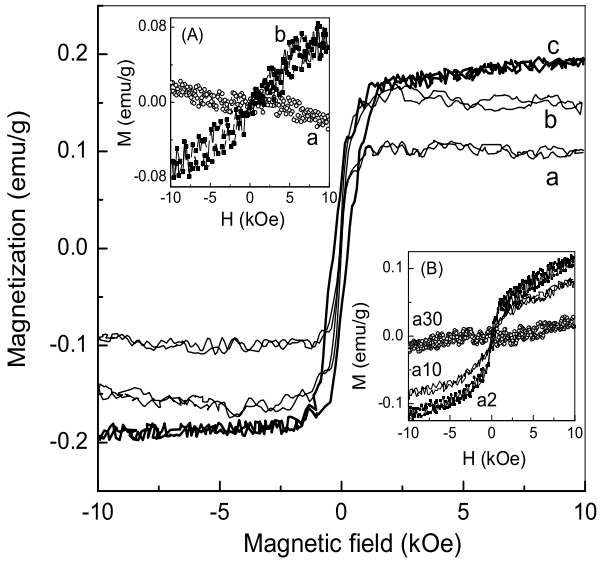

Figure 3.28: Magnetization as a function of field, measured at 300 K, for $Zn_{1-x}Ni_xO$; a) $x = 0.025$ and b) $x = 0.05$; c) $x = 0.05$ measured at 12 K. Insets: (A) M–H curves of the samples annealed at 673 K for 2 hours; (B) M–H curves of the $x = 0.025$ sample annealed at 800 K for 2 minutes (a2), 10 minutes (a10), and 30 minutes (a30).

Ni phase which is ferromagnetic. Bulk NiO is antiferromagnetic with a Neel temperature of 520 K [94]. However, in the nanocrystalline form, NiO shows weak ferromagnetic or superparamagnetic behavior at low temperatures [352, 353]. The fraction of NiO in the $x = 0.025$ sample is very small and is not likely to contribute much towards the observed ferromagnetism. For the $x = 0.05$ sample also, the antiferromagnetic (linear M–H variation) or weak ferromagnetic contribution will be much less than that expected from Ni metal. Assuming that the contribution to ferromagnetism comes from the Ni metal impurities only, the weight percentage of Ni metal present in the two different compositions is calculated based on the low-temperature saturation magnetization of Ni metal, 57.65 emu/g [179]. The calculated values are 0.21 and 0.33%, respectively, for $x = 0.025$ and 0.05. The weight percentages of Ni metal impurity calculated from the magnetization data are almost comparable to that obtained from XRD data (0.15 and 0.3%) indicating that ferromagnetic contributions are mainly coming from the Ni secondary phase present in the samples.

Further evidence for the presence of Ni metal and its oxides in the doped samples is

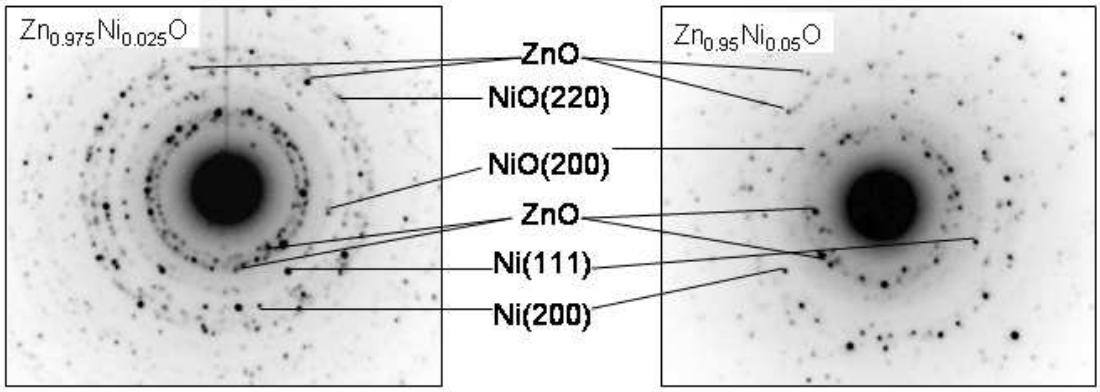

Figure 3.29: Comparison of selected area electron diffraction patterns of $Zn_{0.975}Ni_{0.025}O$ and $Zn_{0.95}Ni_{0.05}O$.

obtained from electron diffraction studies. The selected area electron diffraction patterns of the $x = 0.025$ and 0.05 samples are compared in Figure 3.29. Many additional diffraction spots and rings, apart from those from the ZnO lattice are observed in both the patterns. The additional spots and rings in the electron diffraction patterns are identified as those from fcc Ni and cubic NiO.

The next question is, if a small fraction of Ni is substituted for Zn as evidenced from the optical studies, is there a contribution to ferromagnetism from the doped sample. Since Ni metal will be oxidized to NiO at elevated temperatures when heated in air, it is expected that annealing of the samples in air will lead to complete conversion of ferromagnetic Ni metal impurities to antiferromagnetic NiO. If there is a contribution to ferromagnetism from the doped material also, this is expected to be retained after such heat treatment. The *M–H* curves of the annealed $x = 0.025$ and 0.05 samples are shown in the inset A of Figure 3.28 (magnetization values corrected by subtracting the contribution from diamagnetic ZnO). Both the compositions are found to be non-ferromagnetic after annealing at 673 K. The negligible magnetization of the $x = 0.025$ sample and the linear variation of magnetization for the $x = 0.05$ sample after annealing is likely to be due to the antiferromagnetic nature of the NiO impurity (the Neel temperature of NiO is 520 K [94], much above room temperature so that only a small linear variation is expected).

Schwartz *et al.* had annealed their thin film samples at 800 K for 2 minutes and still the film showed ferromagnetic behavior at 350 K [320]. The ferromagnetic $x = 0.025$ sample also is annealed under these conditions and found that ferromagnetism at 300 K is almost retained when annealed for 2 minutes (inset B of Figure 3.28). On increasing the annealing time, it was found that magnetization decreases and no ferromagnetism was observed after annealing for 30 minutes. It is already known that the oxidation of Ni in air is a very slow process, and therefore long annealing time is required for the complete oxidation of Ni metal impurities if present. The presence of Ni^{2+} in the ZnO lattice, as evidenced by the optical studies, and the absence of ferromagnetism in the annealed samples give evidence to the fact that the observed ferromagnetism is not intrinsic in the case of Ni doped ZnO.

In the case of Co doped ZnO, it was found that the samples synthesized by a modified GNP process are not ferromagnetic. A similar synthesis procedure using dextrose as additional fuel was repeated in the case of the Ni doped samples also, for $x = 0.025$ and 0.05, as described in *section 3.3.2*. Powder XRD studies of the new samples indicated the formation of single phase of $Zn_{1-x}Ni_xO$ without any secondary phase. Interestingly, both the samples were found to be paramagnetic down to 12 K. Optical absorption studies revealed the incorporation of Ni^{2+} inside the ZnO lattice in the tetrahedral site. Due to the absence of magnetism in these two samples, further analyzes have not been carried out.

3.5 $Zn_{1-x}Mn_xO$ ($0 \leq x \leq 0.25$)

The results on the studies of the structural, optical and magnetic properties of nanocrystalline Mn doped ZnO, synthesized by the GNP autocombustion method, are discussed in this section.

The powder XRD patterns of $Zn_{1-x}Mn_xO$ ($0 \leq x \leq 0.25$) samples are shown in Figure 3.30. The XRD patterns for $x > 0$ show that the ZnO structure is not disturbed on substitution. No reflections due to any secondary phase is detected in the XRD patterns. The average particle sizes of Mn doped ZnO, calculated from X-ray line broadening using the Scherrer formula are shown in Table 3.2. A decrease in the average particle size with increasing Mn content is observed and similar results are reported in the literature [325].

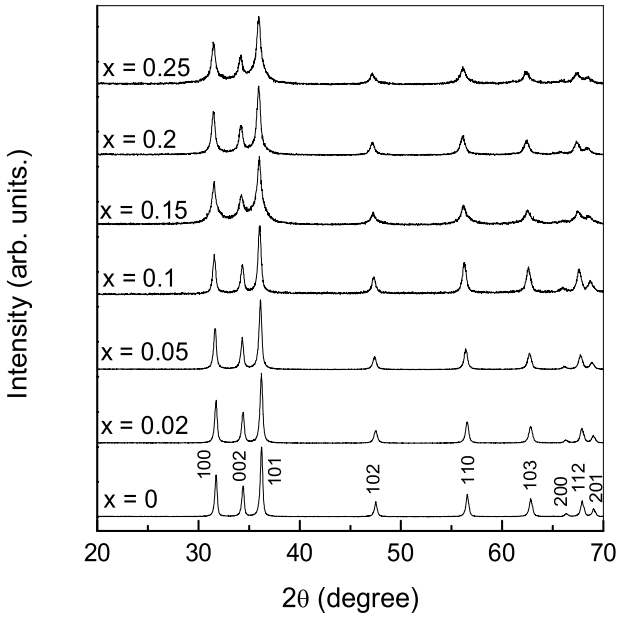

Figure 3.30: Powder X-ray diffraction patterns of different compositions of $Zn_{1-x}Mn_xO$ ($0 \leq x \leq 0.25$).

Unlike the Co doped and Ni doped compositions, all Mn doped ZnO compositions are found to be single phase up to 25% Mn-doping. Thus, from the powder XRD analysis it becomes clear that Mn is highly soluble in ZnO. Fukumura *et al.* already showed that up to 36% Mn can be incorporated inside the ZnO lattice [323],However, Jin *et al.* showed that segregation of a secondary phase starts after 20% Mn doping [144].

The expanded region XRD pattern in the 30–38° 2θ region is shown in Figure 3.31. From Figure 3.31 it can be clearly seen that the XRD reflections are shifted to lower 2θ values with increasing concentration of Mn. The positions of reflections of $Zn_{0.98}Mn_{0.02}O$ are almost identical to that of ZnO, whereas the reflections start shifting to left side with increasing x. Maximum shifting is observed for the $Zn_{0.75}Mn_{0.25}O$ sample. This is a clear proof for the incorporation of Mn ions inside the ZnO crystal lattice. The ionic radii of Zn^{2+} is 0.60 Å, and that of Mn^{2+} is 0.74 Å [144, 354]. Hence, Mn incorporation will lead to expansion of the ZnO lattice. The hexagonal lattice parameters for the different compositions are given in Table 3.2. Figure 3.32 shows the variation of the calculated lattice parameters with Mn concentration (x). The lattice parameter 'c' increases almost

Table 3.2: Mn concentration (x), particle size (t), lattice parameters (a and c) of $Zn_{1-x}Mn_xO$ nanoparticles.

x	t (nm)	a (Å)	c (Å)
0	40	3.250	5.205
0.02	26	3.251	5.208
0.05	27	3.256	5.211
0.1	21	3.264	5.214
0.15	15	3.267	5.222
0.2	18	3.271	5.228
0.25	15	3.271	5.232

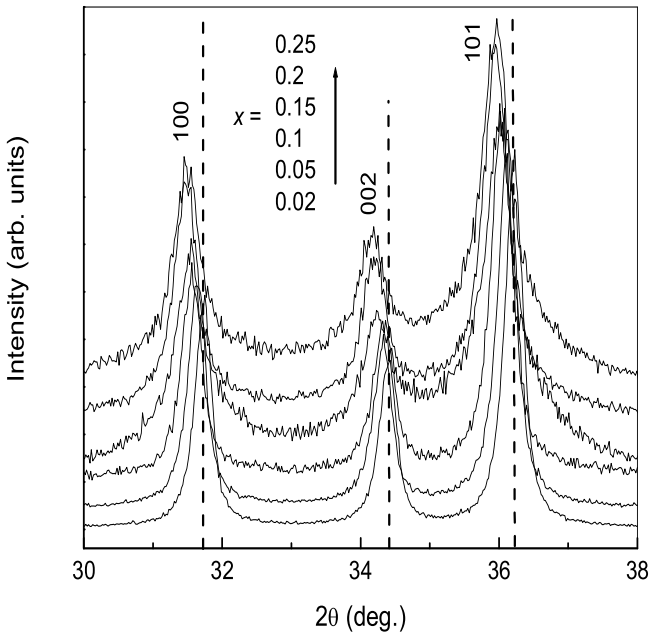

Figure 3.31: Comparison of the expanded powder XRD patterns of different compositions in $Zn_{1-x}Mn_xO$ ($0 < x \leq 0.25$) in 30–38° 2θ regions.

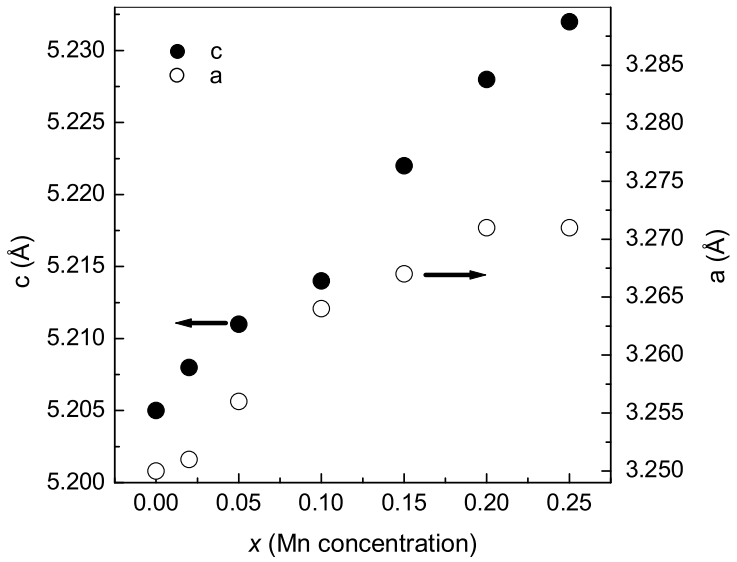

Figure 3.32: Variation of lattice parameters (a and c) with Mn concentration for $Zn_{1-x}Mn_xO$ powder samples.

linearly with x following Vegard's law, whereas 'a' increases up to 20% doping and becomes almost constant. Similar increase in the lattice parameters has been reported for (ZnMn)O by various researchers [324, 355–357].

The optical absorption spectra of the various compositions in (ZnMn)O, recorded at room temperature, are shown in Figure 3.33(a). Apart from the band gap transition, other optical absorption features are clearly seen for the doped samples at lower energies. A strong absorption is seen at 2.94 eV (marked as 'p' in Figure 3.33(a)). This is due to the spin forbidden $^6A_1(S) \rightarrow {}^4T_2(G)$ transition of Mn^{2+} in tetrahedral environment. Such type of strong spin forbidden transition is already reported for (ZnMn)O. This is explained in terms of the lattice distortion due to the incorporation of the larger Mn^{2+} ion inside the ZnO lattice [82, 329, 357, 358]. Moreover, increase in the absorption intensity is observed with increasing in x, and the intensity is found to be maximum for $x = 0.2$. A very weak absorption is seen around 1.81 eV (marked as 'q'). This feature is not much clear for the low doping concentrations, whereas slightly visible for the highly Mn doped samples. This absorption band is depicted to the spin-forbidden $^6A_1(S) \rightarrow {}^4T_1(G)$ ($\sim$15200 cm^{-1}) transition [358]. Thus, optical absorption studies confirm the

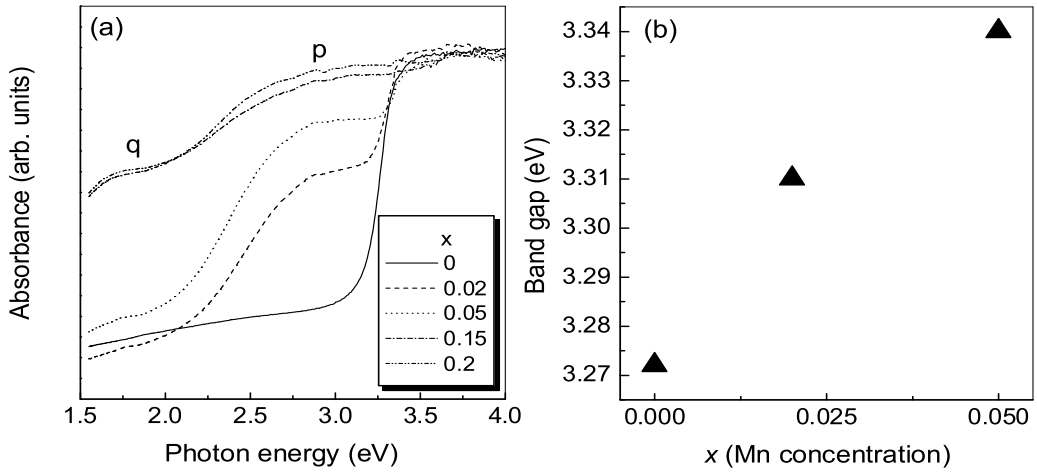

Figure 3.33: (a) Optical absorption spectra for $Zn_{1-x}Mn_xO$ (x = 0, 0.02, 0.05, 0.15 and 0.2) powder samples, recorded at room temperature. (b) Variation of band gap of $Zn_{1-x}Mn_xO$ for x = 0, 0.02 and 0.05.

incorporation of Mn ions inside the ZnO lattice in the tetrahedral sites and the oxidation state of Mn is 2+. Furthermore, blue shift of the band edge is observed as a supporting evidence for the incorporation of Mn ions inside the ZnO lattice. The band gap for x = 0, 0.02 and 0.05 are shown in Figure 3.33(b). The band gap values for the doped samples are obtained as 3.311 and 3.340 eV for $Zn_{0.98}Mn_{0.02}O$ and $Zn_{0.95}Mn_{0.05}O$, respectively. A increase in the band gap of the doped samples reveals the incorporation of Mn ions inside the ZnO lattice. Similar enhancement of the band gap, with increasing Mn concentration, have been observed earlier [329, 355–357].

Magnetization of the different samples is measured as a function of field at room temperature and as a function of temperature at a fixed field strength. All the Mn doped samples are found to be paramagnetic at room temperature. Therefore, magnetic measurements were carried out at low temperatures to examine the possibilities of any magnetic ordering at low temperatures. The temperature variation of the magnetization of $Zn_{0.9}Mn_{0.1}O$, $Zn_{0.8}Mn_{0.2}O$ and $Zn_{0.75}Mn_{0.25}O$ are shown in Figure 3.34. The applied magnetic field in each case is 5000 Oe. All the three samples show similar features. No signature of any ferromagnetic transition could be detected for any of the samples, down to 12 K. Magnetization increases with decreasing temperature, similar to that expected

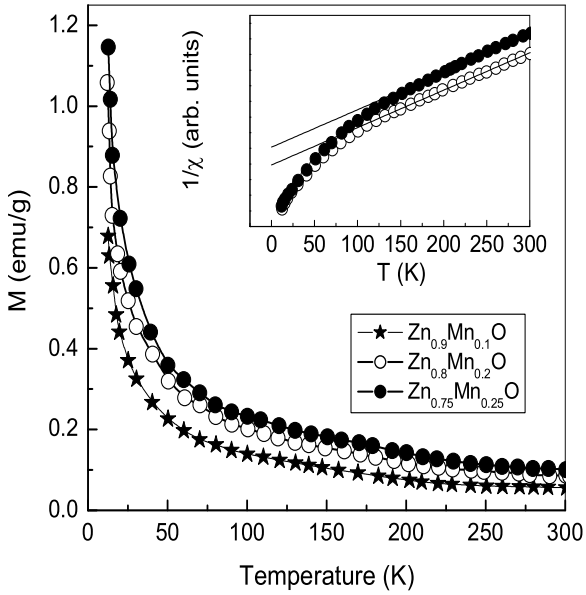

Figure 3.34: Temperature variation of magnetization of $Zn_{1-x}Mn_xO$ (x = 0.1, 0.2 and 0.25) powder samples. Inset: Reciprocal susceptibility vs. temperature of $Zn_{0.8}Mn_{0.2}O$ and $Zn_{0.75}Mn_{0.25}O$.

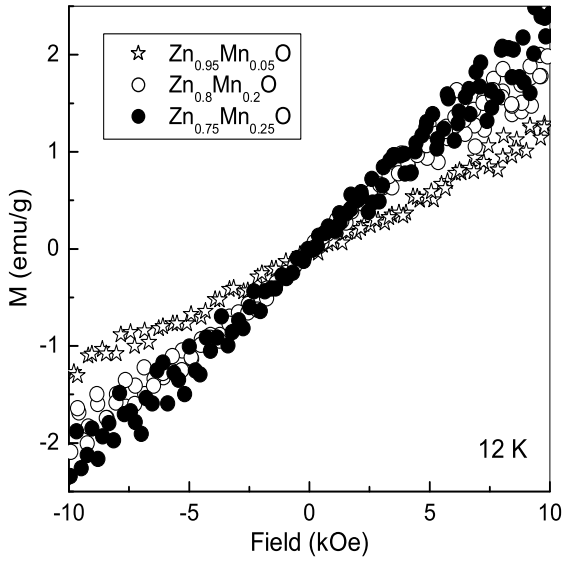

Figure 3.35: Magnetization of the Mn substituted compositions as a function of field, measured at 12 K.

for paramagnetic samples. *M–H* measurements carried out at 12 K (Figure 3.35) show paramagnetic behavior of $Zn_{1-x}Mn_xO$ (x = 0.05, 0.2 and 0.25). Thus the studies show that Mn doped polycrystalline ZnO samples are nonmagnetic at room temperature and paramagnetic down to 12 K. This is in contradiction to the theoretical predictions of Dietl *et al.* [128]. The present findings from magnetic measurements supports the idea of nonmagnetic (ZnMn)O as reported earlier [148, 150, 156, 323, 335].

The inverse of the magnetic susceptibility of two different samples are shown in the inset of Figure 3.34. A typical Curie-Weiss behavior is observed above 100 K. Least squares fit of the linear protion of the curves above 100 K gave negative Weiss temperature (Θ) for both samples. The value of Θ is obtained as –164.4 and –212 K for $Zn_{0.8}Mn_{0.2}O$ and $Zn_{0.75}Mn_{0.25}O$, respectively. The high negative values of Θ are indicating strong antiferromagnetic interactions in the Mn doped samples. Moreover, the effective paramagnetic moments (μ_{eff}) per Mn, derived for these two samples, are found to be $\sim 5.8\mu_B$ which is close to $5.9\mu_B$ for Mn^{2+} [147, 356]. The μ_{eff} value clearly indicates that the oxidation state of Mn is 2+. The results from the magnetic measurements are in agreement with that reported in the literature for $Zn_{1-x}Mn_xO$ samples [148, 323, 325, 328]. Therefore, it can be predicted that, without co-doping or hole doping, polycrystalline (ZnMn)O is not ferromagnetic in nature.

3.6 $Zn_{1-x}Fe_xO$ ($0 \leq x \leq 0.2$)

The results of the detailed investigations on the structural and magnetic properties of nanocrystalline powder samples of Fe doped ZnO, synthesized by the GNP autocombustion method, are discussed in this section.

The powder XRD patterns of the as-synthesized $Zn_{1-x}Fe_xO$ ($0 \leq x \leq 0.20$) are shown in Figure 3.36. The XRD patterns for $x > 0$ show that the ZnO structure is not disturbed on substitution. For all the cases the hexagonal lattice parameters are found to be matching with that of pure ZnO. The reflections in all the XRD patterns are found to be broadened due to the fine particle nature of the doped powder samples. The average crystallite sizes of different Fe doped ZnO samples were calculated from X-ray line broadening using the Scherrer formula. The obtained crystallite sizes are in the range of 15–20 nm for the doped samples. There are no additional reflections observed, other than those

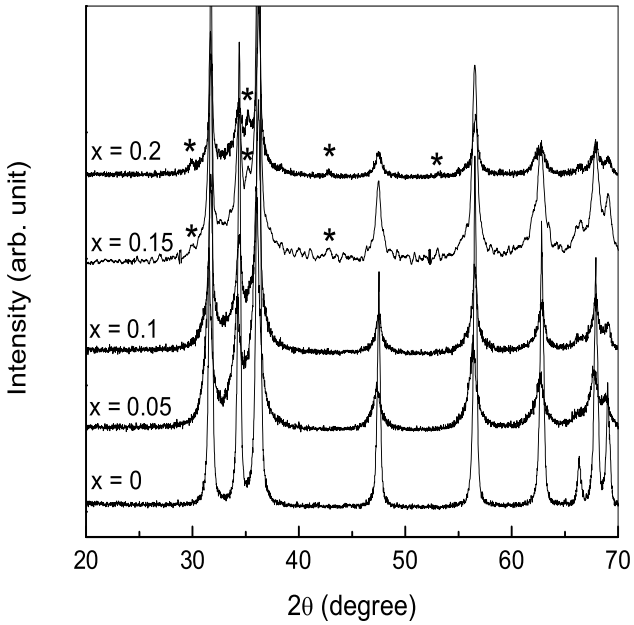

Figure 3.36: Powder X-ray diffraction patterns of different compositions of $Zn_{1-x}Fe_xO$ ($0 \leq x \leq 0.2$). * spinel-ferrite impurity.

of ZnO, for $x = 0.05$ and 0.1. However, some extra peaks are observed when $x = 0.15$, and these reflections become more distinguishable for $x = 0.2$ (marked as * in Figure 3.36). The positions of the secondary peaks are at $2\theta = 29.94$, 35.27, 42.87 and 53.14°. From the refinement of the XRD patterns, it is found that, these additional reflections correspond to a spinel phase. The crystallite size of this impurity phase is found to be 10-12 nm. Although no additional reflections are found for $x = 0.05$ and 0.1, some broad feature is observed in the patterns of these two samples around $2\theta = 35.3$, where the most intense reflection from the spinel phase is observed for the other two samples. Since Zn and Fe ions are used as the reactants, the possible impurity phase formed in little amounts may be either γ-Fe_2O_3 or Fe_3O_4 or $ZnFe_2O_4$ or a mixture of all three.

The d_{hkl} and the lattice parameter a of the impurity spinel phase in the $x = 0.15$ sample are compared with the d_{hkl} and 'a' values of the three possible ferrite impurities, in Table 3.3. From Table 3.3 it is very clear that, the 'd' values of the impurity phase are comparable to those of $ZnFe_2O_4$. Moreover, the lattice parameter 'a' is also close to the lattice parameter of $ZnFe_2O_4$. However, the d-spacings and the lattice parameter

Table 3.3: Comparison of d_{hkl} and a of the spinel impurity phase in $Zn_{0.85}Fe_{0.15}O$ with that of $ZnFe_2O_4$, Fe_3O_4 and γ-Fe_2O_3.

	impurity phase	$ZnFe_2O_4$	Fe_3O_4	γ-Fe_2O_3
d_{hkl}	2.9814	2.9838	2.9677	2.9528
	2.5425	2.5446	2.5308	2.5182
	2.1081	2.1099	2.0985	2.0880
	1.7213	1.7227	1.7134	1.7048
a (Å)	8.4327	8.4410	8.3940	8.3520

are not 100% correlated to that of $ZnFe_2O_4$. Therefore, it may be predicted that the impurity phase composition is in between that of $ZnFe_2O_4$ and Fe_3O_4. The possible formula of this spinel ferrite phase can be written as $Zn_xFe_{3-x}O_4$, where x is close to 1. The as-synthesized $Zn_{0.85}Fe_{0.15}O$ powder sample was annealed at 873 K for 2 h in air atmosphere. The X-ray diffraction pattern of the annealed sample is compared with that of the as-synthesized sample in Figure 3.37. It is seen from the figure that, all the reflections become sharper after heating. All the impurity peaks, which were not clear in the as-synthesized sample become more clearer. The average crystallite sizes of the two different phases were calculated and found to be 30 and 16 nm, for $Zn_{0.85}Fe_{0.15}O$ and the ferrite phase, respectively. Refinement of the XRD pattern of the annealed sample showed that the lattice parameter of the impurity phase in the annealed sample is more closer to $ZnFe_2O_4$. All 'd' values and the lattice parameter of the impurity ferrite phase compares with that of zinc ferrite phase. The formation of γ-Fe_2O_3 in the as-synthesized sample as a secondary phase can be ruled out from the annealing studies. It is well known that γ-Fe_2O_3 is less stable in air, and it is converted to stable α-Fe_2O_3 phase if heat treated in air atmosphere. Since no reflection of α-Fe_2O_3 is seen in the air annealed sample, it is clear that there is no trace of γ-Fe_2O_3 present in the as-synthesized sample.

Apart from the XRD line broadening, the particle sizes of the (ZnFe)O samples have been confirmed from TEM. The TEM pictures of $Zn_{0.9}Fe_{0.1}O$, taken at two different regions are shown in Figure 3.38. No specific shape has been observed for the particles. It is seen that the particle size distribution is very wide (8–30 nm). Therefore, the average crystallite size obtained from XRD line broadening is almost comparable to the particle size obtained from TEM measurement.

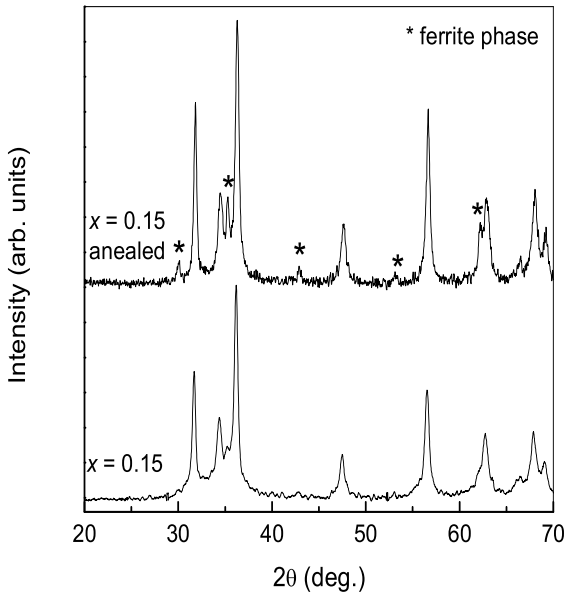

Figure 3.37: Comparison of XRD patterns of as-synthesized and annealed samples of $Zn_{0.85}Fe_{0.15}O$.

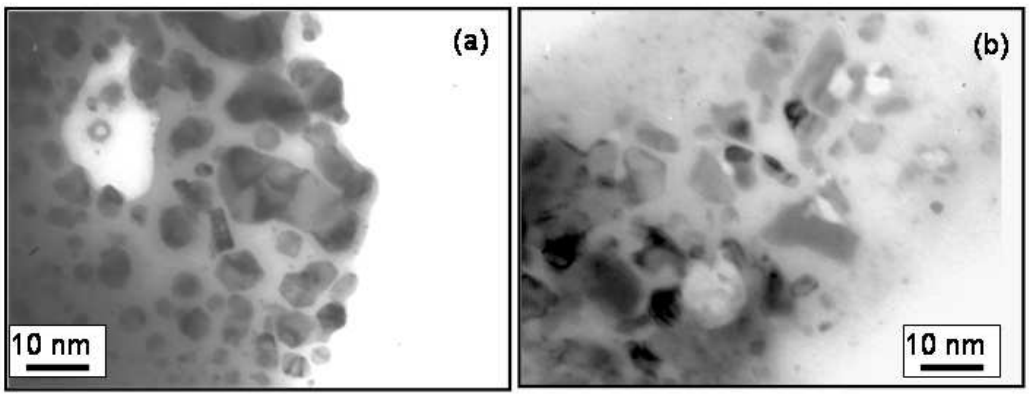

Figure 3.38: Transmission electron micrographs of $Zn_{0.9}Fe_{0.1}O$ nanoparticles.

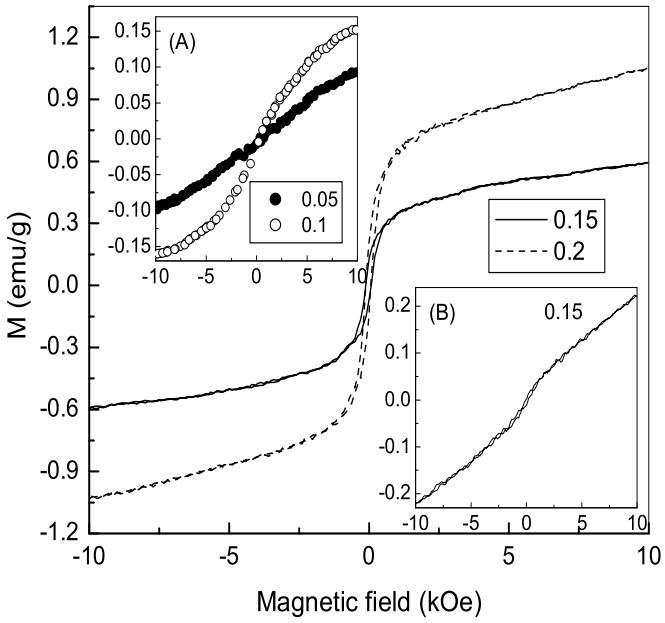

Figure 3.39: Room temperature magnetization curves of $Zn_{0.85}Fe_{0.15}O$ and $Zn_{0.8}Fe_{0.2}O$. Inset: *M–H* curves of (A) $Zn_{0.95}Fe_{0.05}O$ and $Zn_{0.9}Fe_{0.1}O$, (B) annealed sample $Zn_{0.85}Fe_{0.15}O$.

Results of the magnetization measurements of the Fe doped ZnO samples at room temperature are shown in Figure 3.39. $Zn_{0.85}Fe_{0.15}O$ and $Zn_{0.8}Fe_{0.2}O$ are found to be ferromagnetic at room temperature with well defined hysteresis loops. The observed magnetization (M) is 0.6 and 1.0 emu/g at 10 kOe and the coercivity (H_c) is 93 and 88 Oe for $x = 0.15$ and 0.2, respectively. Inset (A) of Figure 3.39 shows the magnetization curves of $Zn_{0.95}Fe_{0.05}O$ and $Zn_{0.9}Fe_{0.1}O$. Both the samples are found to be very weakly magnetic. $Zn_{0.95}Fe_{0.05}O$ is almost paramagnetic whereas $Zn_{0.9}Fe_{0.1}O$ is superparamagnetic with $M = 0.15$ emu/g in an applied field 10 kOe. Thus, from these results it can be concluded that the as-synthesized $Zn_{1-x}Fe_xO$ samples are magnetic at room temperature. Out of the four Fe doped samples, (ZnFe)O with $x = 0.15$ and 0.2 are ferromagnetic with comparatively larger magnetization. Magnetization measurements were performed on the annealed samples and is shown in the inset (B) of Figure 3.39 for $x = 0.15$. The magnetization is decreased to 0.21 emu/g at 10 kOe and the coercivity is almost negligible. Thus, $Zn_{0.85}Fe_{0.15}O$ becomes nearly paramagnetic with a negligible hysteresis loop.

Since the observed ferromagnetism is disappeared on annealing, it can be concluded

that the Fe doped samples are not true DMSs. This ferromagnetism is extrinsic, due to the ferrite phase formed in the samples. Similar results are reported for Fe doped ZnO [149, 334] and Fe doped TiO_2 [359]. The observed room temperature ferromagnetic contribution is coming from a different source which may be $ZnFe_2O_4$, Fe_3O_4 or $Zn_xFe_{3-x}O_4$. Shim *et al.* reported that superparamagnetic zinc ferrite with partially inverted cation distribution is the origin of magnetism in their sample [149]. There are several reports, where superparamagnetic zinc ferrite has been synthesized by reducing the particle size using different methods [213,217,218,220]. Either due to the low temperature of synthesis or ball milling, cation distribution of zinc ferrite is changed from normal to partial inversion. This leads to superparamagnetic $ZnFe_2O_4$ with lower magnetization and no coercivity. Since nonzero coercivity is observed in the present study, formation of superparamagnetic $ZnFe_2O_4$ with unusual cation distribution can be ruled out. If we consider Fe_3O_4 as the ferromagnetic impurity, ferromagnetism should be retained even after heating at high temperatures. Moreover, enhanced crystallinity of the ZnO and the impurity phases in the annealed sample should enhances the magnetization also. However, from inset (B) of Figure 3.39, it is seen that annealing destroys the ferromagnetism in (ZnFe)O nanoparticles. Therefore, Fe_3O_4 is not likely to be the ferrite phase impurity in the as-synthesized sample. Hence, the ferromagnetic impurity phase is likely to be $Zn_xFe_{3-x}O_4$ where is closer to 1. The room temperature magnetization of x close to 1 in $Zn_xFe_{3-x}O_4$ is known to be very low [360]. It is very difficult to determine the value of x from the present results. Thus, a $Zn_xFe_{3-x}O_4$ spinel phase is found to be responsible for the observed ferromagnetism in the Fe doped ZnO polycrystalline samples.

3.7 Conclusions

Transition metal ion (Co, Ni, Mn and Fe) doped ZnO nanoparticles have been synthesized by a simple solution combustion method. Particle size of the products depend on the conditions of synthesis and the doped metal ions. Detailed structural investigations reveal that the wurtzite structure of ZnO is not disturbed on doping. Optical studies showed that divalent metal ions are incorporated inside the ZnO lattice in the tetrahedral site. Furthermore, evidence for substitution of Co^{2+} in place of Zn^{2+} in the ZnO tetrahedral site is found from XPS studies. Interesting magnetic properties are observed for the doped

ZnO with different metal ions. Co doped ZnO shows ferromagnetism at room temperature, when synthesized by the sinple GNP method. On the other hand, the same compositions, when synthesized by a slightly modified, does not show ferromagnetic ordering down to 12 K. Different characterization techniques like XRD, TGA, VSM, SAED, etc. together showed that Co metal cluster is responsible for ferromagnetism in the Co doped powder samples. Similar results are observed for Ni doped ZnO nanoparticles. (ZnNi)O powder samples are found to be ferromagnetic at room temperature, when synthesized by GNP. The origin of ferromagnetism is proved to be from Ni metal impurities. On the other hand higher solubility of Mn (up to 25%) in ZnO observed. All Mn doped samples are found to be paramagnetic down to 12 K. In the case of Fe doped compositions, all samples are found to be magnetic at room temperature. The observed ferromagnetism is originating from a secondary spinel phase, $Zn_xFe_{3-x}O_4$. Thus, from the overall findings, it can be concluded that the changes in the optical (electronic) properties or the properties associated with the charge of the electron in $Zn_{1-x}TM_xO$ is due to the doped TM^{2+} in the ZnO lattice and the changes in the magnetic properties or the properties associated with the spin of the electron is originating from ferromagnetic impurities.

Chapter 4

Nanocrystalline $Ni_{0.5}Zn_{0.5}Fe_2O_4$

4.1 Introduction

Ferrites are one of the important magnetic materials responsible for many technological revolutions. Among the different ferrites, nickel-zinc (NiZn) ferrite is one of the most important ferrite and it is mainly used in high frequency applications [188]. The high electrical resistance of this ferrite makes eddy current losses extremely low at high frequencies and therefore, can be used as frequency or noise filters where low loss, magnetic stability and high permeability are required. This ferrite is useful for common mode chokes in the high frequency range. For signal transformers, high saturation flux density and high permeability are basic requirements. The materials for different applications are produced in cores of various shapes. For specific applications, the composition, microstructure, density, grain size, etc. are very important in determining the performance of the ferrite. Therefore, the ferrite is fabricated into different shapes and sintered with or without suitable sintering aids and additives, by controlled heating and cooling, etc. according to the requirements.

For various applications, NiZn ferrite powders are synthesized by the usual solid state method. The densification of bulk NiZn ferrite powders, to a reasonably high density, is difficult because of the relatively high melting point of the material and low bulk diffusivity. Typical NiZn ferrites sinter satisfactorily only above 1673 K, so that their microstructure and hence the performance parameters are difficult to control because of the volatility of Zn at such high temperatures. As a result, it is very difficult to obtain a sintered body with density comparable to the theoretical value, by the solid state method. However, nanosized ferrite particles have more sinterability due to their fine

particle nature as well as high surface to volume ratio [197, 361]. Therefore, for many applications, the use of nanosized ferrites offers many advantages such as possible sintering at relatively low temperatures for a short duration which saves time, cost and other factors such as reduction in the volatility of Zn at high sintering temperatures. Nanosized ferrites are more advantageous to obtain higher sintered density at relatively lower sintering temperatures, without considerable grain growth [362]. Several conventional and unconventional methods are used for the synthesis of nanosized NiZn ferrites viz. hydrothermal [205],microwave hydrothermal [216], coprecipitation [363], sol-gel [364], reverse micelle synthesis [365], high energy ball milling [366], citrate precursor method [367], etc.

We have synthesized the NiZn ferrite $Ni_{0.5}Zn_{0.5}Fe_2O_4$ in nanocrystalline form by the glycine nitrate combustion method and studied the properties of the powders as well as sintered materials to study the effect of using nanosized ferrite in determining the performance parameters such as permeability and loss factor.

4.2 Synthesis

For the synthesis of $Ni_{0.5}Zn_{0.5}Fe_2O_4$ nanoparticles, both the GNP and the modified form of the GNP method, where dextrose is added as an extra fuel along with glycine, was followed. Stoichiometric quantities of reagent grade $Fe(NO_3)_3.9H_2O$ and $Ni(NO_3)_2.6H_2O$ were dissolved in minimum amount of distilled water. The required amount of Zn metal was dissolved in minimum volume of 4 N HNO_3 to get zinc nitrate. Glycine solution was made in distilled water corresponding to 1.48 and 2 moles of glycine per mole of metal ion. The amount of dextrose was varied from 1–6 moles per 3 moles of metal ions and dissolved in distilled water. All the individual solutions were mixed together in a large crystallizing dish and the mixed solution in the dish was kept on a hot plate for evaporation and autocombustion at a temperature of 473 K. A gel of thick layer was formed at the bottom of the dish after the complete evaporation of water. During the final steps of reaction, the honey-like gel began to swell, forming a viscous foam. Spontaneous combustion started with the burning of the precursor, and the burning was found to be slow when dextrose was added along with glycine. The burning was completed within few seconds producing a fluffy and voluminous product (as-synthesized NiZn ferrite).

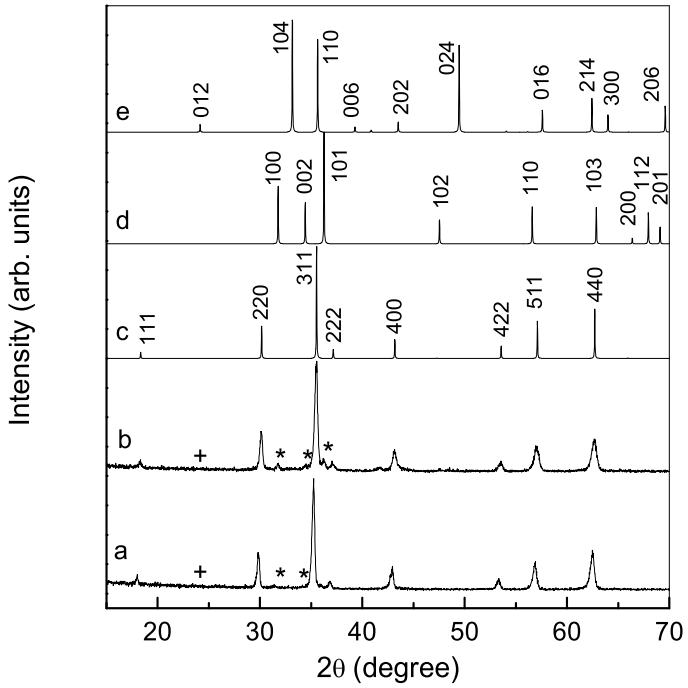

Figure 4.1: Powder XRD patterns of the as-synthesized NiZn ferrite powders using a) 1.48 moles and b) 2 moles of glycine. Simulated XRD patterns of c) $Ni_{0.5}Zn_{0.5}Fe_2O_4$, d) ZnO, and e) α-Fe_2O_3 are shown for comparison. * ZnO, + α-Fe_2O_3.

For the comparison of various properties of nanoparticles of NiZn ferrite to its bulk counterpart, bulk $Ni_{0.5}Zn_{0.5}Fe_2O_4$ is also synthesized using the solid state method of synthesis. Stoichiometric quantities of reagent grade NiO, ZnO and Fe_2O_3 were taken and followed the ceramic method as described in *section 2.2.2*. The bulk sample is referred as NZF.

4.3 Results and Discussions

4.3.1 Structure, particle size and morphology

Figure 4.1 shows the powder XRD patterns of the as-synthesized samples using a G/N ratio of 0.55 and 0.75 (1.48 and 2 moles of glycine per mole of metal, respectively). Unlike in the earlier reports [264–266], presence of small amounts of impurity phases are observed, for a G/N ratio of 0.55, which corresponds to the stoichiometric ratio.

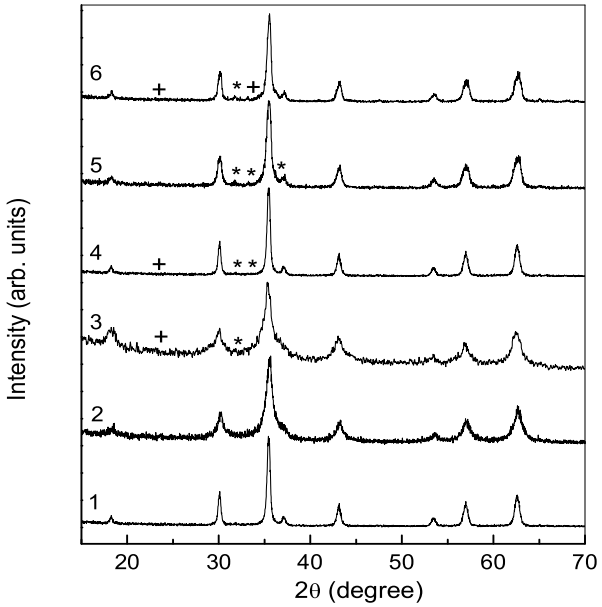

Figure 4.2: Powder XRD patterns of the as-synthesized $Ni_{0.5}Zn_{0.5}Fe_2O_4$ powders synthesized using 6 moles of glycine and 1–6 moles of dextrose. The numbers above indicate the number of moles of dextrose used. (* ZnO, + α-Fe_2O_3).

The impurity phases are identified as ZnO and α-Fe_2O_3. Thus, the preliminary studies using only glycine shows that single phase $Ni_{0.5}Zn_{0.5}Fe_2O_4$ nanoparticles are not obtained. When G/N ratio is increased, the amount of the impurity phase is increased whereas the particle size is decreased from 45 nm to 40 nm. It was observed that when only dextrose is used as the fuel, smaller particles are obtained without any impurities. However, it was found that the particle size distribution is very wide.

Hence, the effect of both glycine and dextrose as fuels in the combustion reaction was studied. The samples were prepared with increasing amounts of dextrose while keeping the ratio of metal to glycine as 1:2. Figure 4.2 shows the XRD patterns of samples synthesized with different amounts of dextrose (varied from 1 to 6 moles, for 6 moles of glycine and 3 moles of metal ions). Figure 4.2 shows that, with the addition of dextrose, initially the particle size decreases as evidenced by the increased width of the reflections, and then increases after lowest particle size for the sample synthesized with 2 moles of dextrose (particle size remains almost constant for higher amounts of dextrose). The formation of ZnO and α-Fe_2O_3 as impurities is observed on increasing the amount of

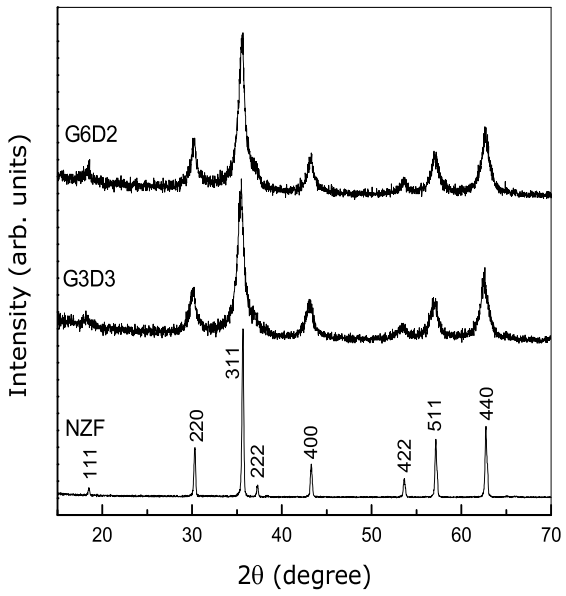

Figure 4.3: Comparison of the powder XRD patterns of G3D3 and G6D2 with that of bulk $Ni_{0.5}Zn_{0.5}Fe_2O_4$ powder synthesized by the ceramic method (NZF).

dextrose beyond 3 moles.

It was found that when 6 moles of glycine and 2 moles of dextrose are used, the reaction is reproducible without the formation of any impurity phases. For checking the reproducibility, both the XRD and magnetization at room temperature were tested. To study the role of glycine and dextrose, another combination was also tested. In this case, 3 moles of glycine and 3 moles of dextrose (for 3 moles of metal ions) were used. However, when 3 moles of glycine and 3 moles of dextrose are used, the ferrite formed was with slightly larger average particle size and the reaction is again found to be highly reproducible. The nanosized ferrite synthesized using 6 moles of glycine and 2 moles of dextrose is coded as G6D2 and the other one from 3 moles of glycine and 3 moles of dextrose is coded as G3D3 for convenience. The XRD patterns of the as-synthesized G3D3 and G6D2 are compared against the pattern of the sample synthesized by the ceramic method in Figure 4.3. The average particle size obtained from XRD patterns is 8 nm and 9 nm for G3D3 and G6D2, respectively. The lattice parameter obtained for both samples is 8.392Å, which is comparable to the reported values [368, 369].

The transmission electron micrographs of the as-synthesized G3D3 sample are shown

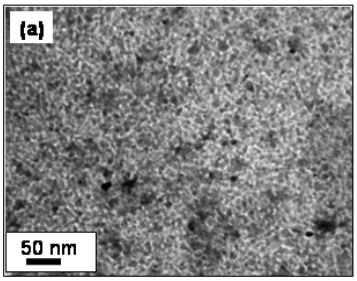

No.	d (Å)	(hkl)
1	4.8340	111
2	2.9601	220
3	2.5238	311
4	2.101	400
5	1.7121	422
6	1.6112	511
7	1.483	440

Figure 4.4: (a and b) TEM images of the as-synthesized powder (G3D3) from different regions, and (c) SAED pattern G3D3. The table shows the corresponding 'd' values with respect to *hkl* planes according to ring numbers.

in Figure 4.4 (a) and (b). The micrographs show that the particle size distribution is narrow in the range of 6-10 nm. The average crystallize size obtained from XRD analysis correlates well with the particle size obtained from TEM measurements and the particles are almost spherical in nature. The as-synthesized nanosized ferrite particles are crystalline, as evidenced by the selected area electron diffraction (SAED) pattern shown in Figure 4.4(c). The indexing of the SAED pattern (as shown in the table of Figure 4.4) reveals that the modified autocombustion method gives rise to single phase $Ni_{0.5}Zn_{0.5}Fe_2O_4$. For the as-synthesized G6D2, the average particle size is obtained as 9 nm (Figure 4.5), which correlates with the particle size obtained from XRD measurements. The particle size distribution from the TEM measurement was found to be 8-12 nm. Moreover, the SAED pattern of G6D2 reveal the formation of single phase $Ni_{0.5}Zn_{0.5}Fe_2O_4$. The cubic lattice parameter is obtained for both the as-synthesized products as $a = 8.392$ Å.

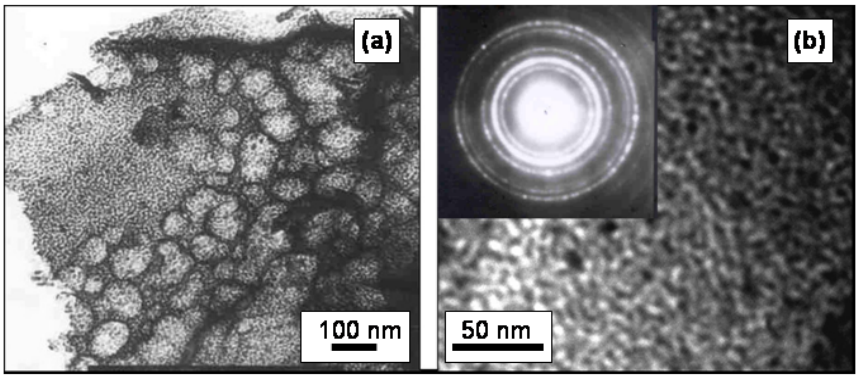

Figure 4.5: TEM images of the as-synthesized G6D2 sample from two different regions and the SAED pattern.

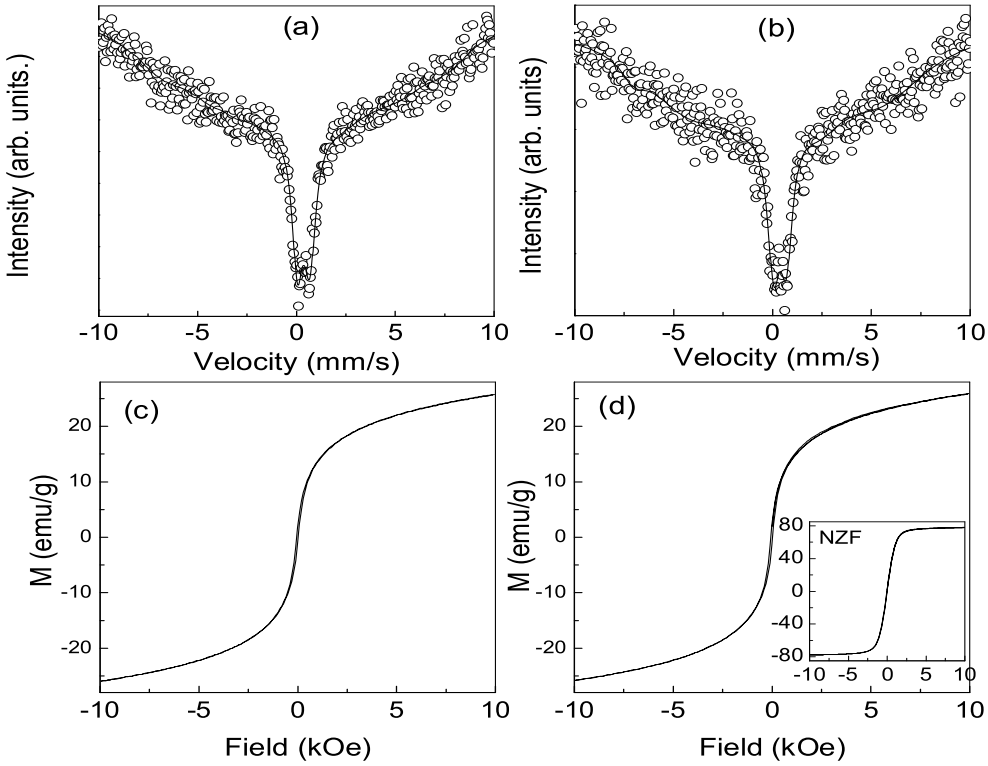

Figure 4.6: Mössbauer spectra of the as-synthesized (a) G3D3 and (b) G6D2, measured at room temperature. Room temperature M–H curve of the as-synthesized (c) G3D3 and (d) G6D2. Inset of (d) shows M–H curve of the bulk sample.

4.3.2 Magnetic properties

The ^{57}Fe Mössbauer spectra of the as-synthesized samples G3D3 and G6D2, measured at room temperature, are compared in Figure 4.6 (a) and (b). A typical doublet is observed for both the samples. The observed doublet is due the presence of superparamagnetic particles. When magnetic particles become too small (nanometer range), the magnetic anisotropy barrier (KV) is smaller than the average thermal energy (kT) of the particles. Due to the very small relaxation time (τ), the magnetic moment flips rapidly so that the effective moment during the time of measurement becomes zero ($KV \ll kT$). This causes the collapse of a multiplet for larger particles to a superparamagnetic doublet for the nanoparticles, which is observed for the as-synthesized samples in the present case. The *IS* of the doublets are found to be 0.363 and 0.360 ±0.02 mm/s, for G3D3 and G6D2, respectively. However, the observed quadruple splitting (*QS*) 0.519 ±0.02 mm/s (G3D3) and 0.520 ±0.02 mm/s (G6D2) is found to be high due to some kind of disorderness exists in the very fine 8 and 10 nm particles [370]. Comparable values of *IS* and *QS* are reported for nanosized NiZn ferrite [200, 205, 371]. The U-shaped feature of the base line and the broadening is likely to be the contribution from some ferrimagnetic particles. It is likely that there are some particles present whose sizes are larger than 8 nm, for which magnetic anisotropy barrier is larger than the average thermal energy. These particles will behave as ferrimagnetic in nature. The overall Mössbauer results show that all irons in the spinel are in Fe^{3+} state. The hyperfine magnetic field (*HMF*) could not be calculated due to its reduction to a very small value. The reduction in the *HMF* for the nanoparticles is explained by Mørup [372] in terms of collective magnetic excitation. In this case, the thermal energy is not enough to flip the magnetic moment around the easy axis and hence causes the moments to oscillate around the easy axis giving rise to a reduced effective *HMF*.

The room temperature magnetization curves of G3D3 and G6D2 are shown in Figure 4.6 (c) and (d). For both samples, the magnetization continuously increases at high fields and a very small hysteresis loop is observed. This implies that both the as-synthesized NiZn ferrite powders are mixtures of both ferrimagnetic and superparamagnetic particles. To determine the superparamagnetic blocking temperature (T_B) and the magnetic behavior of the as-synthesized samples below room temperature, low tem-

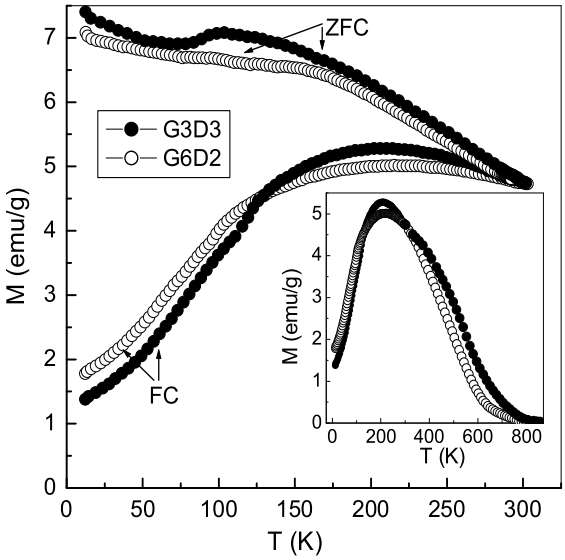

Figure 4.7: ZFC and FC magnetization curves of G3D3 and G6D2, measured in an applied field of 100 Oe. Inset: Combined low- and high-temperature ZFC curves of G3D3 and G6D2.

perature magnetic measurements have been carried out on both samples. Figure 4.7 shows the zero field cooled (ZFC) and field cooled (FC) magnetization curves measured in a field of 100 Oe. From the ZFC curves, it is clearly observed that the blocking temperature of the superparamagnetic particles is around 225 K. The deviation between FC and ZFC curves starts immediately below room temperature. This implies that there are some ferrite particles with very small size, which are believed to be superparamagnetic at room temperature whereas, other particles are ferrimagnetic at room temperature. Magnetization measurements at higher temperatures showed that the magnetic transition is very broad and broadening is observed up to 673 K. For bulk particles, a sharp magnetic transition is expected at 560 K (see detailed discussion in *section 3.3.5*).

Variation of the magnetization of G3D3 with applied field, measured at different low temperatures, are shown in Figure 4.8. From the *M–H* curves it is seen that, with lowering of the temperature both magnetization and coercivity increases. Highest magnetization as well as coercivity are obtained at 13 K. At room temperature the as-synthesized powder gives a magnetization of 26 emu/g and this is increased to 45 emu/g at 13 K. There is no magnetic saturation down to 13 K. Such type of magnetic behavior is generally

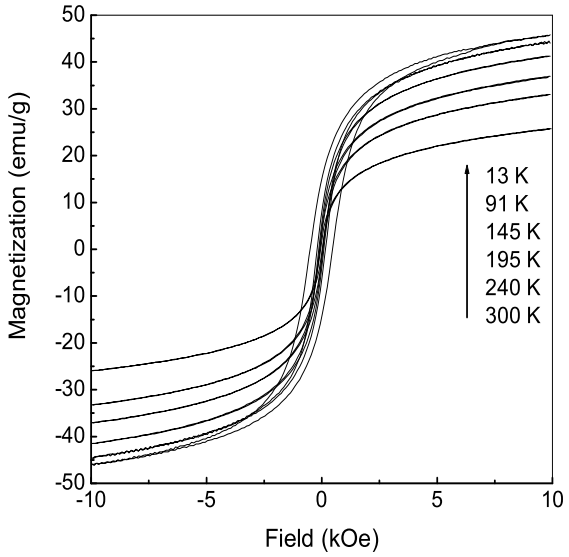

Figure 4.8: Magnetization as a function of magnetic field for the as-synthesized G3D3 powder, measured at different low temperatures.

observed for superparamagnetic particles. A similar behavior is observed for G6D2 also. Therefore, in the present case, from the M–H and M–T studies it can be concluded that the as-synthesized sample is composed of both superparamagnetic and ferrimagnetic particles.

Thus, from a comparison of the properties of the as-synthesized NiZn ferrite samples G6D2 and G3D3, it has been found that both the samples show similar behavior. Hence further studies are made only on G6D2.

4.3.3 Effect of high-temperature annealing

It is known that when the ferrite nanoparticles synthesized at low temperatures are heated at higher temperatures, particle size growth takes place due to the Ostwald ripening mechanism [373,374]. To study the effect of heating on the properties of the NiZn nanoparticles, the as-synthesized G6D2 powder is annealed in the temperature range 673-1273 K in air. Two sets of samples were annealed for two different durations, one for 6 h and another one for 12 h each, at different temperatures. The annealed samples are characterized using powder X-ray diffraction and TEM measurements. The X-ray diffraction patterns of some

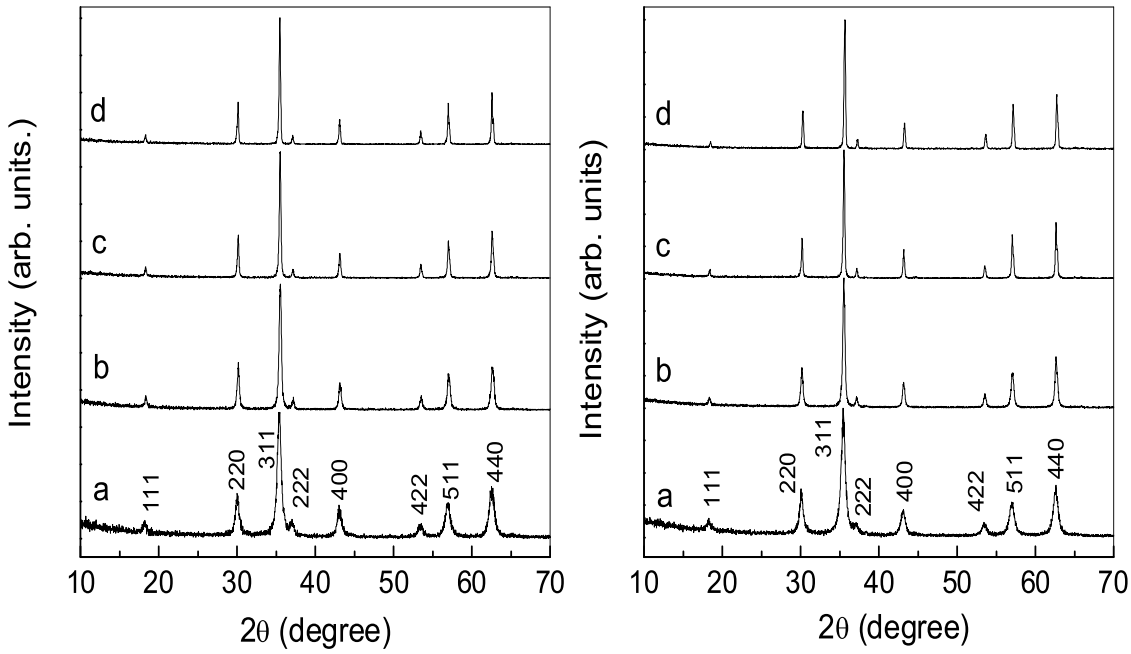

Figure 4.9: Powder X-ray diffraction patterns of G6D2, annealed at a) 673, b) 873, c) 1073, and d) 1273 K for 6 hours (left) and 12 hours (right) each.

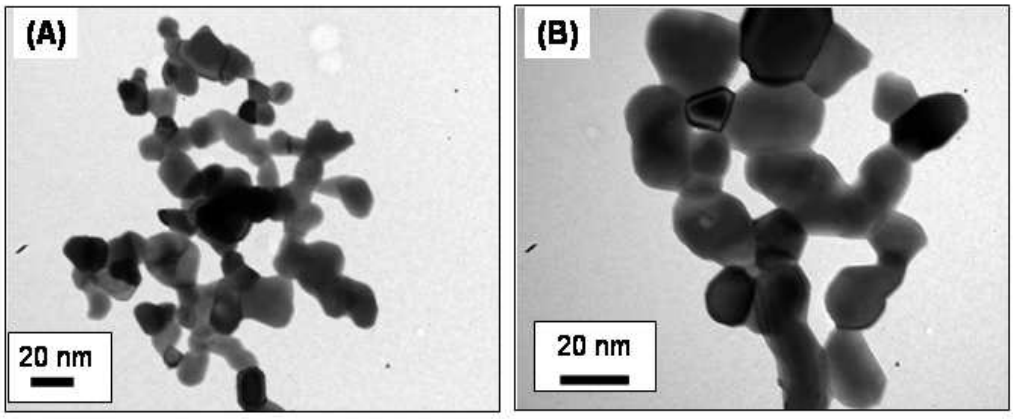

Figure 4.10: TEM images of the G6D2 sample annealed at 973 K for 6 hours.

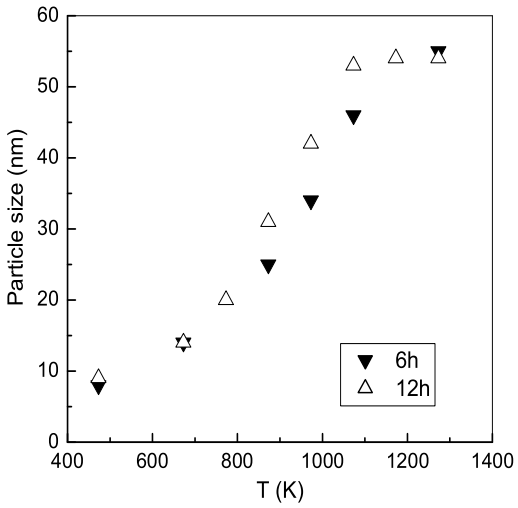

Figure 4.11: Variation of the average particle size with annealing temperature for the annealed samples, annealed for 6 h and 12 h each.

of the annealed samples are compared in Figure 4.9. It can be observed from the figure that the XRD reflections become sharp with increasing annealing temperature. This is because of the increase in the particle/crystallite size which increases with increasing annealing temperature. The TEM picture of the sample annealed at 973 K for 6 h is shown in Figure 4.10. Clear particles are observed for the annealed sample with average particle size of ∼25 nm. This is comparable to the average crystallite size of 30 nm calculated from the XRD pattern of the sample. Hence the average crystallite size calculated from XRD data can be considered as the average particle size. The variation of the particle size with annealing temperature for samples annealed for 6 h and 12 h are compared in Figure 4.11. For both series of annealed samples, the trend is almost the same, except for the fact that for the 6 h annealed samples, the growth rate is relatively low and higher temperatures are required to get larger particles. It is known that annealing at higher temperatures lead to grain growth, which affects the particle size as well as ionic distribution [205, 206], and finally bulk particles are formed with a different site distribution after annealing at higher temperatures. The particle size was found to increase to a constant value of ∼54 nm after annealing at and above 1073 K for 12 h. Thus, annealing helps in the particle size growth without affecting the crystal structure.

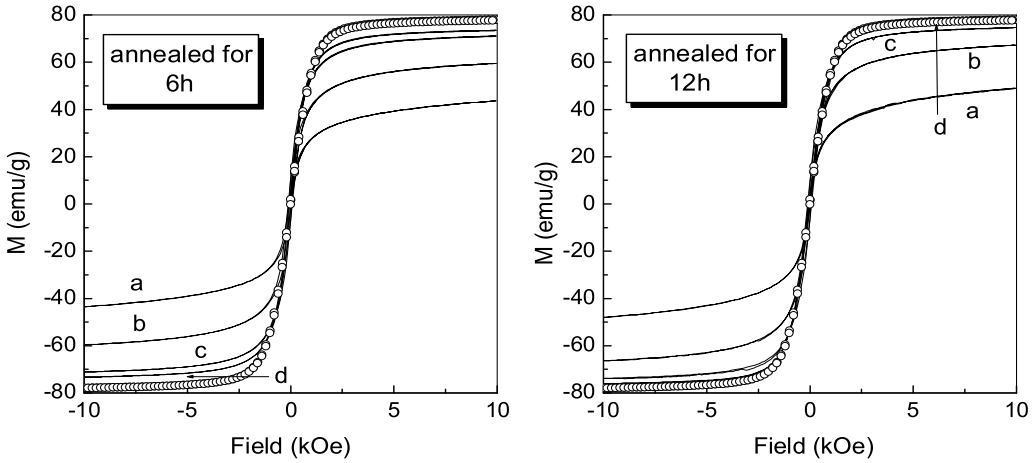

Figure 4.12: Room temperature magnetization of G6D2, annealed at a) 673, b) 873, c) 1073 and d) 1273 K for 6 h and 12 h. The open symbols correspond to the bulk 'NZF' sample.

4.3.4 Magnetic properties of the annealed samples

Figure 4.12 shows the magnetization curves of the two sets of the annealed samples. The magnetization of the as-synthesized samples is found to be 26 emu/g at 10 kOe, which is not saturated. Superparamagnetic behavior in the M–H curve has been observed with negligible hysteresis (see Figure 4.6). The magnetization is saturated for samples annealed above 873 K for 12 h and above 1273 K for 6 h. The obtained saturation magnetization of 74 emu/g at 300 K is comparable to that obtained for the bulk sample NZF. The saturation magnetization obtained for the sample annealed at 1073 K for 12 h is comparable to those reported for low-temperature synthesized samples annealed above 1273 K [365,375] as well as for the commercial bulk samples, sintered at 1673 K [368, 371, 376]. Thus, this direct comparison of magnetization values reveal that saturation magnetization can be obtained for G6D2 by annealing the powder sample at comparatively lower temperatures.

The variation of the magnetization (at 10 kOe) as a function of the particle size is compared in Figure 4.13. The lower magnetizations of the smaller particles can be due to two reasons; the effect of the particle size as generally observed for all magnetic materials and the effect of cation distribution. For the ferrite particles, both factors can

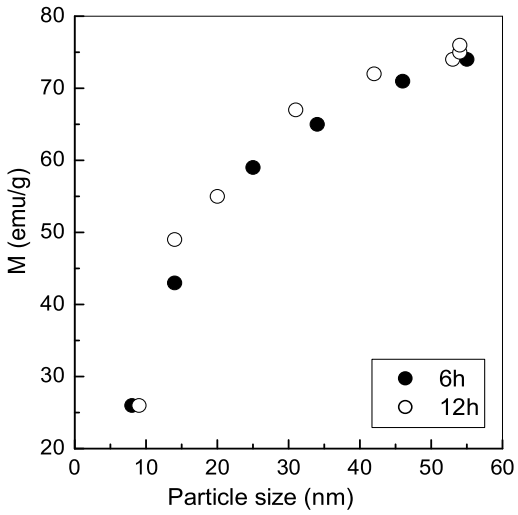

Figure 4.13: Variation of the magnetization at 10 kOe with average particle size, for the samples annealed for 6 h and 12 h.

contribute to the decreased magnetization. The coercivity of the NiZn ferrite is also governed by the particle size. Generally, the coercive force of a ferro- or ferrimagnetic material increases with decreasing particle size and exhibits a maximum coercivity in the cross over region from multi-domain to single-domain size. If the particle size is further reduced below an optimum value, the coercive force decreases and finally disappear because of superparamagnetism. From technical point of view, the coercive force is a crucial parameter, and therefore the control of particle size and shape is very important.

To study the effect of particle size on the magnetization, the best way is to compare the saturation magnetization M_s as a function of the particle size. This is because, for smaller particles, because of the increased anisotropy, larger magnetic fields will be required to attain saturation. Hence a comparison of the magnetization measured at a particular field is not sufficient. Since the as-synthesized and some of the annealed samples are not saturated even at 10 kOe, it is required to know their M_s values at the specific particle size. The saturation magnetization is obtained by extrapolating the M versus $1/H$ plot to $1/H = 0$. It is known that the saturation magnetization decreases with decreasing particle size following the relationship [377],

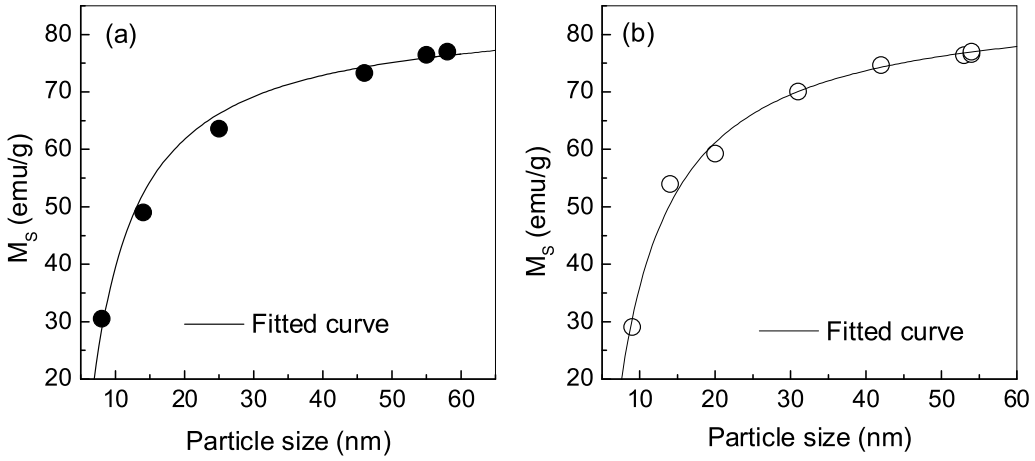

Figure 4.14: Variation of the saturation magnetization as a function of average particle size for the annealed samples, annealed for (a) 6 h and (b) 12 h.

$$M_s(t) = M_s(bulk)\,(1 - \beta/t) \tag{4.1}$$

where M_s(t) is the saturation magnetization of the particles of diameter t, M_s(bulk) is the saturation magnetization of the bulk ferrite and β is a constant. Least squares fit to the data shown in Figure 4.14 using the above relationship gives a value of M_s(bulk) as 80 and 86 emu/g for 6 h and 12 h annealed samples, respectively, which are comparable to that expected for the bulk material. The value of β is obtained as 5.8 nm for both the samples. The fitted curve is shown as solid line for both the annealed samples in Figure 4.14.

For the nanosized magnetic materials, the decrease in the saturation magnetization is due to the increasing surface area to volume ratio. It is assumed that a magnetically dead layer is formed at the surface of the particles due to the uncompensated exchange interactions in a surface layer of thickness t [206, 378, 379]. This dead layer thickness is related to β as $\beta = 6t$ [206] from which the value of t is obtained as 0.96 nm. This value is comparable to the unit cell parameter of NiZn ferrite (0.84 nm) and also comparable to the values reported in the literature for different ferrites [206, 380]. This indicates that at least one unit cell on the surface layer of the nanoparticles is magnetically inactive.

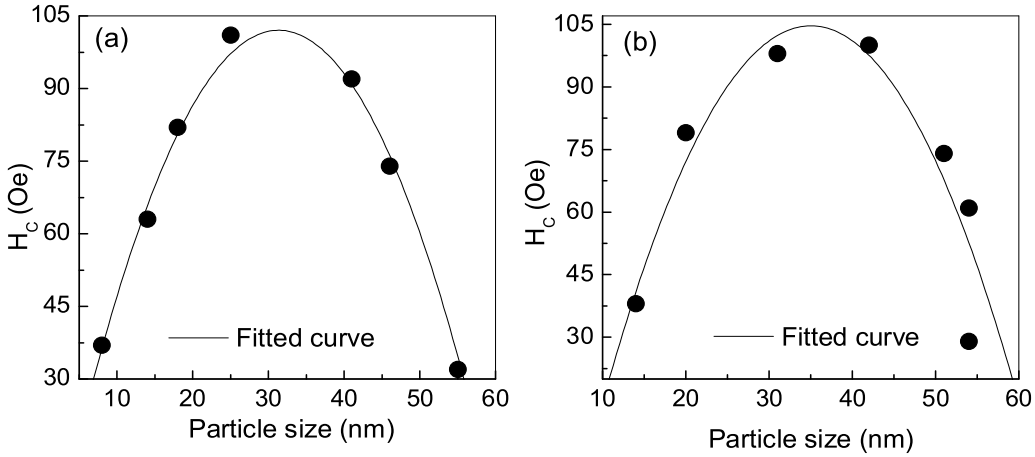

Figure 4.15: Variation of the coercivity as a function of average particle size for the annealed samples, annealed for (a) 6 h and (b) 12 h.

To examine the effect of particle size on the coercivity of the annealed samples, the observed coercivity of the as-synthesized as well as the annealed samples measured at room temperature are shown as a function of the particle size in Figure 4.15. A maximum value of the coercivity close to 100 Oe is observed for both annealed samples. The least squares fitted curves show a maximum coercivity for the particles with size ∼35 nm. This is the critical particle size below which single domain behavior is expected [371, 381].

The temperature variation of the magnetization above room temperature has been measured to study the effect of varying particle size on the Curie temperature of the samples. The measurement has been carried out in a magnetic field of 50 Oe. The M–T curves of the as-synthesized and the annealed samples are shown in Figure 4.16. For comparison, the M–T curve of $Ni_{0.5}Zn_{0.5}Fe_2O_4$ synthesized by the solid state method (bulk) is also shown in the figure. The Curie temperature is determined as the temperature at which the dM/dT versus temperature shows a maximum, shown in Figure 4.17. For the bulk sample, the derivative curve is very narrow and the Curie temperature (T_c) is obtained as 540 K. This is comparable to the values reported in the literature [368, 369]. However, for the powder sample annealed at 1000 K, whose saturation magnetization is comparable to that of the bulk material, the sharp magnetic transition is at 563 K which

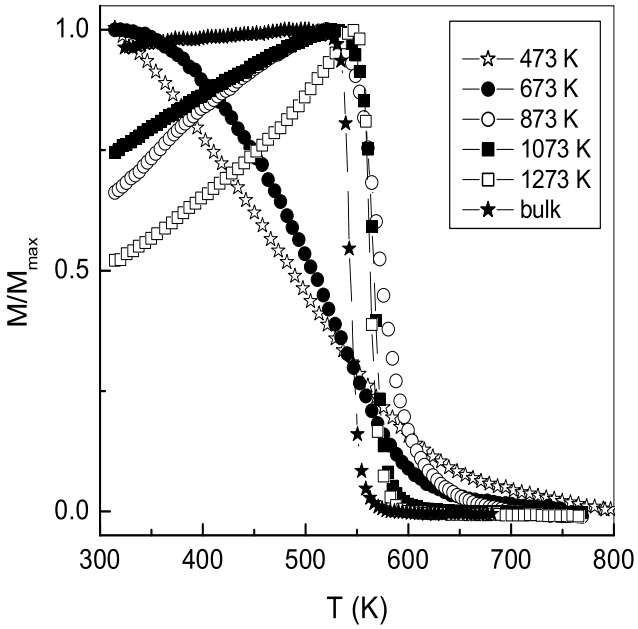

Figure 4.16: Variation of the magnetization with temperature for polycrystalline $Ni_{0.5}Zn_{0.5}Fe_2O_4$ as-synthesized and annealed samples.

is a slightly higher T_C than that of the bulk material. The magnetic transition is very broad for the as-synthesized and ∼673 K annealed samples, as shown in Figure 4.16 and Figure 4.17. In the case of the as-decomposed sample, the T_C cannot be defined as there is no maximum. However, it may be seen that the temperature below which the derivative curve deviates from the base line decreases as the particle size is increased. For the as-synthesized sample, the deviation starts below 673 K and this temperature is decreased to 643 K for the sample annealed at 673 K. For this sample, a very broad maximum is observed at 523 K. The width of the derivative curve decreases and the maximum is shifted to lower temperatures, as the particle size is increased. Thus, the transition temperatures are obtained as 573, 568, 564, and 562 K, for the samples annealed at 873, 973, 1073, and 1273 K, respectively.

Broadening of the magnetic transition and changes in the Curie temperature can be due to various reasons. It is possible that the distribution of the different cations in the tetrahedral and octahedral sites of the ferrite lattice in the nanoparticles synthesized under non-equilibrium conditions is much different than that in the bulk counterpart. Other

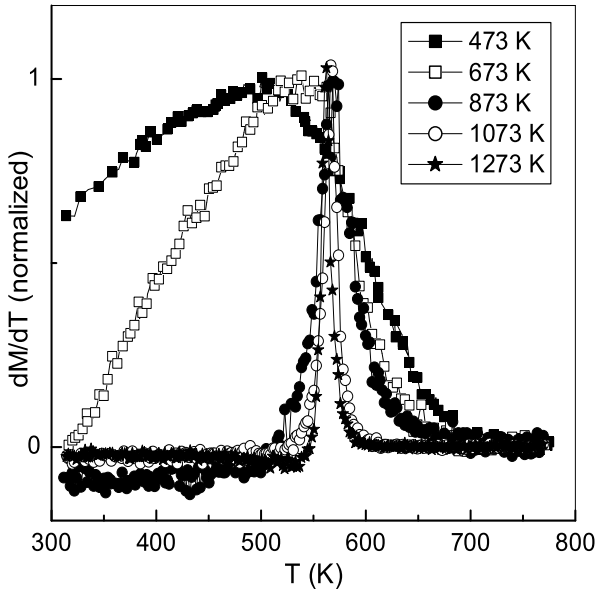

Figure 4.17: Normalized dM/dT curves of the as-synthesized and the air annealed $Ni_{0.5}Zn_{0.5}Fe_2O_4$ samples.

possibilities are the different degrees of the distribution in the individual particles and the variation of the composition from particle to particle. In both these cases, one can expect higher T_Cs for some particles and lower T_Cs for other particles. The over all broad magnetic transition can be either due to the contribution from the magnetic transition of the individual particles having either a different degree of distribution where x is different in $(Zn_{0.5-x}Fe_{0.5+x})[Ni_{0.5}Zn_xFe_{1.5-x}]O_4$ for different particles or different compositions where x is different in $Ni_{1-x}Zn_xFe_2O_4$ for different particles so that the T_C of the individual particles will vary between that of $NiFe_2O_4$ and $ZnFe_2O_4$. Enhancement in the Curie temperature has been reported for nanoparticles of $MnFe_2O_4$ [206], $NiFe_2O_4$ [209], and NiZn ferrite [200, 382]. This has been interpreted in terms of the enhanced A-O-B superexchange interactions due to the different cation distribution in the nanoparticles than that present in the bulk. Therefore, the higher T_Cs of the present nanocrystalline samples suggest that the cation distribution should be different from that of the bulk in such a way as to increase the strength of the superexchange (A-O-B) interactions. The increase in the strength of the superexchange interactions can be mainly due to two reasons: (a) partial replacement of diamagnetic Zn^{2+} ions by Fe^{3+} and/or Ni^{2+} ions from the A–sites

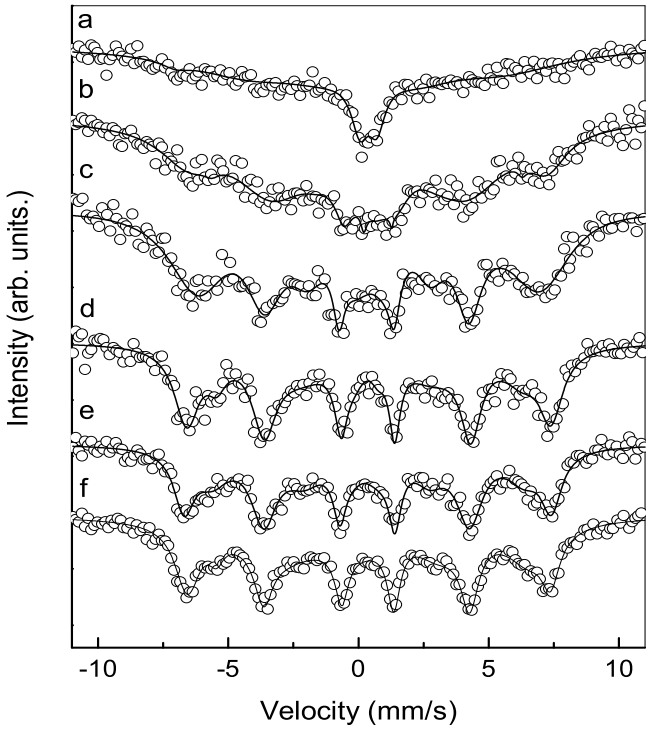

Figure 4.18: Room temperature Mössbauer spectra of $Ni_{0.5}Zn_{0.5}Fe_2O_4$. a) as-synthesized and annealed at b) 673 K, c) 873 K, d) 1073 K, e) 1273 K and (f) bulk sample.

to the *B*–sites and (b) increase in the A-O-B superexchange bond angle and decrease in the metal-oxygen bond length due to this redistribution.

4.3.5 Mössbauer studies

In order to study whether there is a difference in the cation distribution in different samples as well as the oxidation state and coordination environment of iron in the nanosized $Ni_{0.5}Zn_{0.5}Fe_2O_4$ particles, ^{57}Fe Mössbauer spectra of all the samples have been recorded at room temperature. Figure 4.18 shows the Mössbauer spectra of the as-synthesized as well as the annealed G6D2 samples. The Mössbauer spectrum of the bulk sample is also shown for comparison. The Mössbauer parameters obtained after fitting the spectra are given in Table 4.1. A very strong superparamagnetic doublet is found for the as-synthesized sample (curve a in Figure 4.18). The observed isomer shift (*IS*) value is comparable to that of Fe^{3+} in NiZn ferrite as reported earlier [200, 205]. In the case of

Table 4.1: Room temperature Mössbauer parameters for $Ni_{0.5}Zn_{0.5}Fe_2O_4$. Isomer shift (*IS*) with respect to natural iron, quadrupole splitting (*QS*), hyperfine magnetic field (*HMF*) and relative area ratio (*A*:*B*).

Sample	Site	*IS* (mm/s±0.02)	*QS* (mm/s±0.02)	*HMF* (kOe±5)	*A*:*B*
As-synthesized powder	...	0.36	0.52	...	...
Powder annealed	A	0.50	-0.03	370	1:2.1
at 673 K	B	0.37	-0.02	426	
Doublet	...	0.42	0.44	...	...
Powder annealed	A	0.51	0.02	447	1:2.5
at 873 K	B	0.41	0.04	468	
Powder annealed	A	0.39	0.06	498	1:2.7
at 1073 K	B	0.38	0.02	503	
Powder annealed	A	0.34	0.04	500	1:2.9
at 1273 K	B	0.33	0.02	516	
Bulk sample	A	0.29	0.02	502	1:3.0
	B	0.36	0.03	518	

the 673 K annealed sample, the Mössbauer spectrum could be fitted with two sextets and a doublet. The V-shaped spectrum of this sample can be the result from several effects such as reduction in magnetocrystalline anisotropy, the large distribution of hyperfine magnetic field (*HMF*) due to the nanosized particles, etc. Since 673 K is a very low temperature, not enough to increase the particle size, as evidenced from the value of saturation magnetization, it is possible that still small superparamagnetic contribution is present in this sample and as a result, the weak doublet appears. For the remaining samples, the doublet is completely disappeared and the spectra could be fitted with two sextets, due to the Fe^{3+} at the *A* and *B*–sites of the spinel structure. In all the cases the *IS* and *QS* values are as for Fe^{3+} in the *A* and *B*-sites of ferrites, as indicated in Table 4.1. Comparable values of *IS* and *QS* have already been reported for nanosized and bulk $Ni_{0.5}Zn_{0.5}Fe_2O_4$ samples [200, 205, 371, 383].

The hyperfine magnetic fields (*HMF*) at room temperature for the nanosized particles of $Ni_{0.5}Zn_{0.5}Fe_2O_4$ are found to be smaller than those from the bulk counterpart, as reported previously [384]. The calculated *HMF* values are given in Table 4.1. This difference is more for the sample annealed at 673 K and 873 K, slightly lower for the 1073 K annealed sample and almost comparable to that of the bulk for the sample annealed at

1273 K. The reduction in the *HMF* for the nanoparticles is explained by Mørup [372] in terms of collective magnetic excitation. The presence of the doublet indicates that, after heating at 673 K, still some superparamagnetic particles are present, for which effective *HMF* will disappear. The results are in agreement with that reported in the literature for high temperature annealed $Ni_{0.5}Zn_{0.5}Fe_2O_4$ nanoparticles [385].

The relative area corresponding to the two sextets for the annealed samples are shown in Table 4.1, which offer interesting observations. The ratio of the relative area due to the Fe^{3+} at the tetrahedral A site to octahedral B site for the 673 K annealed sample is found to be 1:2.1. For the bulk sample, the ideal distribution is $(Zn^{2+}_{0.5}Fe^{3+}_{0.5})_A[Ni^{2+}_{0.5}Fe^{3+}_{1.5}]_BO_4$, for which the ratio is 1:3. This observation clearly indicates that more Fe^{3+} ions are present in the A-site than in the ideal distribution and therefore equal number of Zn^{2+} ions will go to the octahedral (B) sites making the composition as $(Zn_{0.5-x}Fe_{0.5+x})[Ni_{0.5}Zn_xFe_{1.5-x}]O_4$. The increasing amount of Fe^{3+} in the A-site will strengthen the superexchange interaction between the A and the B sites (A-O-B exchange) and this accounts for the enhanced Curie temperature of this sample. Similar behavior and enhancement of T_C have been reported for the nanosized $Ni_{0.5}Zn_{0.5}Fe_2O_4$ by Ponpandian *et al.* [200]. Same explanation can be extended to the case of the as-synthesized sample also, where the relative areas could not be calculated from the room temperature Mössbauer measurement. Moreover, any increase in the A-O-B superexchange bond angle, as evidenced by a small increase in the lattice parameter for the as-synthesized sample (8.392 Å, compared to the bulk value of 8.374 Å) [368, 369], will also contribute to the enhancement of the Curie temperature. Increase in the lattice parameter (up to 8.4 Å) has already been observed when the T_C increases to 558 K for $Ni_{0.5}Zn_{0.5}Fe_2O_4$ fine particles [382]. From Table 4.1, it is seen that with the increase in the annealing temperature, the ratio of the relative area becomes almost close to that of the bulk ferrite. These observations indicate that by heating at higher temperatures the thermal energy helps the redistribution of the Fe^{3+} ions, i.e. as the annealing temperature increases, the extra Fe^{3+} ions in the A sites start distributing at the B sites and hence the relative area of the sextet from the A site Fe^{3+} is reduced. Thus, the Curie temperatures of the samples annealed at 873, 1073 and 1273 K are lower than that of the as-synthesized sample and the sample heated at 673 K, but still higher than that of the bulk $Ni_{0.5}Zn_{0.5}Fe_2O_4$.

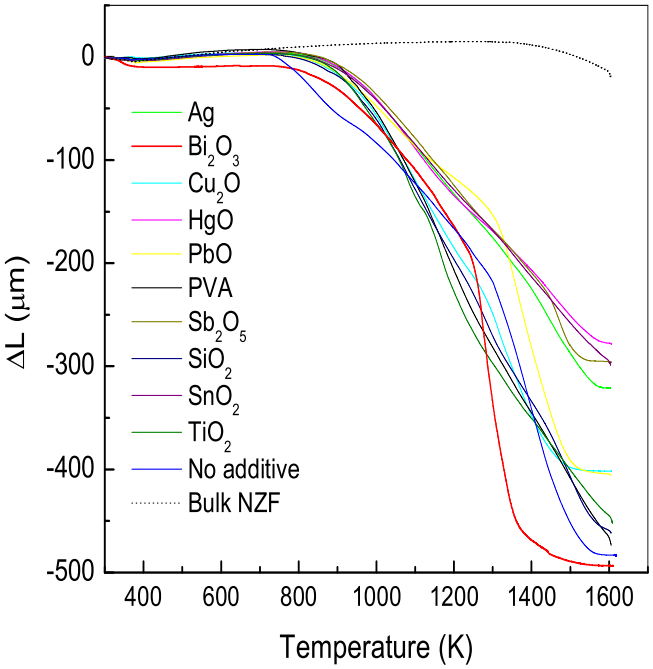

Figure 4.19: TMA signal as a function of temperature for $Ni_{0.5}Zn_{0.5}Fe_2O_4$ pellets with different additives.

4.3.6 Studies on sintered samples

The advantages of nanosized ferrites are that it is possible to sinter them at relatively low temperatures for a short duration because nanosized ferrite particles have more sinterability due to their fine particle nature as well as the high surface to volume ratio [197, 259, 361, 386, 387]. Recently, Verma and Dube showed that NiZn ferrite synthesized by a citrate method and sintered at 1473 K is suitable for high frequency applications [388]. Similarly, Hu *et al.* showed that milled NiZn ferrite sintered with CuO and V_2O_5, below 1273 K, shows very large initial permeability at low frequencies [389], due to the formation of NiZnCu ferrite [390].

The sintering behavior of the as-synthesized powder sample was studied using a thermomechanical analyzer. The studies were made on the virgin sample as well as with 1 wt% of different additives [188] added separately to the as-synthesized powder sample. To compare the sintering behavior, the virgin bulk sample is also analyzed. The shrinkage behavior of the pellets with temperature are shown in Figure 4.19. The heating rate was

kept constant for all samples as 10 K/min. For the bulk sample (bulk NZF), there is no shrinkage up to 1300 K and very little shrinkage is observed above this temperature. On the other hand, for the nanosized ferrite samples, the shrinkage starts above 973 K and the sample with Bi_2O_3 as additive shows better sintering behavior. The shrinkage in this case becomes almost constant above 1373 K.

To study the effect of sintering of the nanosized ferrite powders at a relatively lower temperature of 1473 K (compared to a temperature of 1673 K required for the bulk samples) on the performance parameters, permeability, dielectric constant and electrical resistivity measurements were made on toroids and pellets with or without any additives during sintering. In the present study, we have considered Bi_2O_3 and Ag as the additives and studied different performance parameters on the sintered samples. The samples were sintered for two different durations to compare the effect of sintering time on the microstructure as well as on the properties. Table 4.2 shows a comparison of the various parameters of the samples sintered under different conditions. Three different batches have been sintered at 1473 K, for two different durations (30 and 60 minutes). The purpose of the two additives, Ag and Bi_2O_3, is to study the effect of these liquid phase sintering additives as well as the smaller difference in the sintering time with the additives on the performance parameters. Since the ionic radii of Ag and Bi are larger than that of the transition metal ions (Ni, Zn and Fe), they are expected to go to the grain boundaries [188]. Ag added samples are expected to give lower resistivity whereas Bi_2O_3 addition should give a higher resistivity. For permeability and dielectric measurements, toroids and pellets were made in three different batches and 2% of PVA is used as the binder. The first batch is without any additive, second one is with 1 wt% of Ag powder and last one is with 1 wt% of Bi_2O_3. The toroids and pellets were sintered at 1473 K for two different durations, 30 m and 60 m. For comparison, same type of studies were performed on the bulk sample (toroid and pellet) also.

Microstructure, density and electrical resistance

The samples sintered with Bi_2O_3 as the additive shows comparatively larger density due to the higher diffusion rate with a lower activation energy for grain growth in the presence of the liquid phase sintering aid having a lower melting temperature (1100 K [391]). In

this case, the sintered densities are comparable for the 30 m and 60 m sintered samples. The sintered densities are comparable for the 30 and 60 m sintered samples. Table 4.2 shows a comparison of the various parameters of the samples sintered under different conditions.

Figure 4.20 shows the typical microstructure of the sintered NiZn ferrites. Proper grain growth has occurred when the samples are sintered at 1473 K with Bi_2O_3 (samples QN3 and QN6). Well defined, almost spherical and uniform grains with average size of 1 μm are formed after 30 m sintering. On the other hand, for the virgin sample (QN1), plate shaped grains are observed. There is no proper grain growth when Ag powder was added as the additive and sintered at 1473 K for 30 minutes (QN2). Further grain growth takes place after 60 m sintering, in all three cases. Higher sintered densities are obtained for the virgin and Ag added samples, but still no well defined grains are formed. However, with Bi_2O_3 as the additive, well-defined, irregularly shaped grains are formed. The average grain size is increased to 2-3 μm and the material is not much porous. The observed grain size values are much lower than those reported for samples prepared by the conventional ceramic method [391, 392].

The dc electrical resistivity, at room temperature, reflects the changes in the sintering conditions and additives. The Ag added samples (QN2 and QN5) show lower resistivity, as expected, and the Bi_2O_3 added samples show the highest resistivity. It is found that all the sintered samples have slightly lower resistivities than the conventionally [186] and unconventionally [393] synthesized $Ni_{0.5}Zn_{0.5}Fe_2O_4$. Among the six sintered samples QN5 has lower resistivity than all the others. This can be explained in terms of the high conductivity of Ag in the grain boundary region [387]. On the other hand QN3 and QN6 show the highest resistivities. This is due to the insulating Bi_2O_3 in the grain boundary. The resistivity of the virgin samples, QN1 and QN4, lies in between the other two category. Here also no proper grain growth occurs, and as a result there are more contact area between the grains, and the resistivity is decreased.

Generally, the changes in the resistivity of the sintered ferrites have been explained in terms of the presence of localized states in the forbidden energy gap which arises due to lattice imperfection and the electron hopping between ions of the same element existing in different valence states on equivalent lattice sites [393]. It is possible that lattice defects

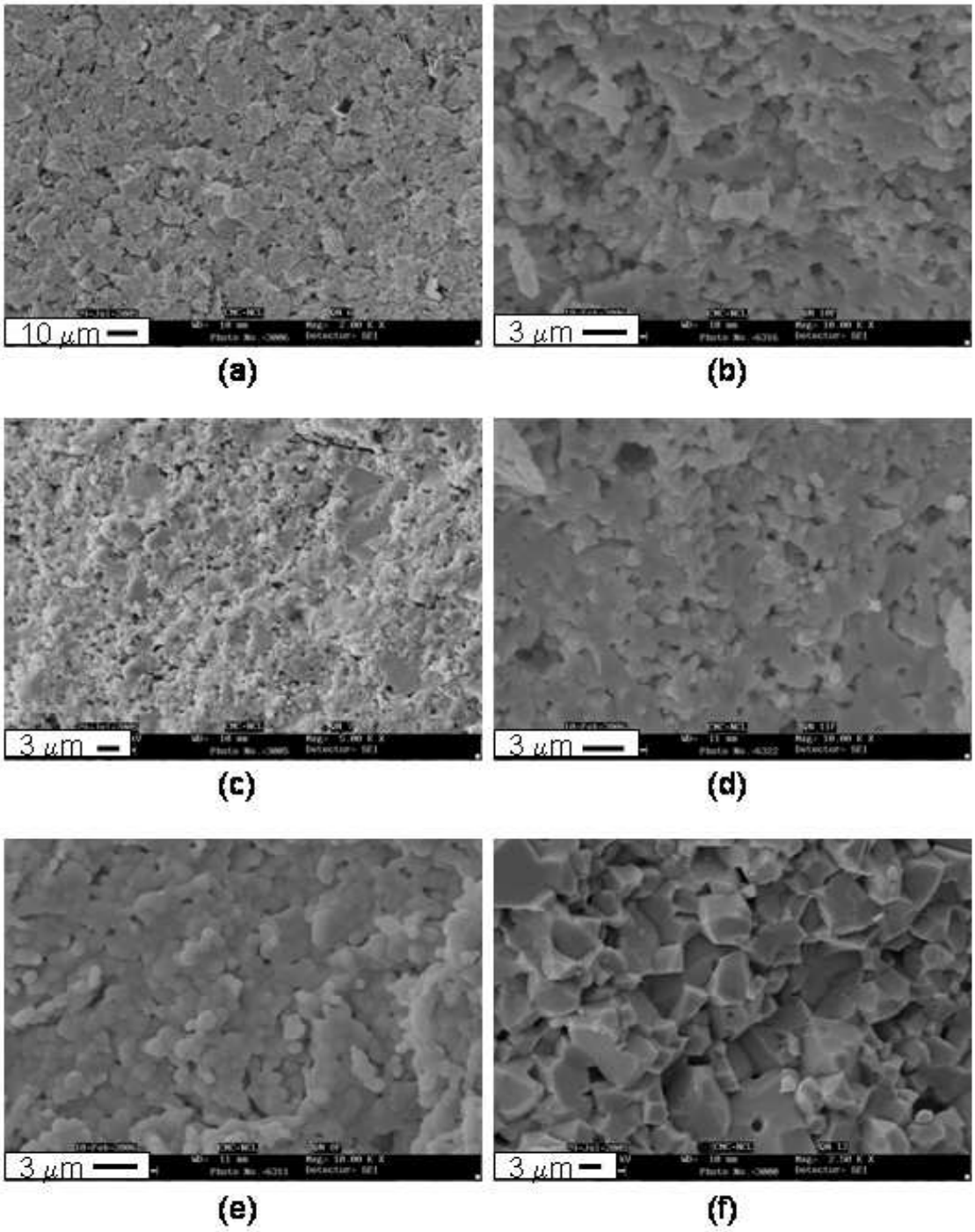

Figure 4.20: SEM photographs of Ni-Zn ferrite sintered at 1473 K under different conditions. (a) with PVA for 30 min, QN1; (b) with PVA for 60 min, QN4; (c) with Ag for 30 min, QN2; (d) with Ag for 60 min, QN5; (e) with Bi_2O_3 for 30 min, QN3; and (f) with Bi_2O_3 for 60 min, QN6.

Table 4.2: Sample codes and various measured properties of the $Ni_{0.5}Zn_{0.5}Fe_2O_4$ sintered at 1473 K.

Sample code	QN1	QN2	QN3	QN4	QN5	QN6
Sintering time	30 min	30 min	30 min	60 min	60 min	60 min
Additive	-	1wt% Ag	1wt% Bi_2O_3	-	1wt% Ag	1wt% Bi_2O_3
ρ ($\times 10^7$ ohm-cm)	4.78	1.89	17.10	1.13	0.75	8.44
$\mu_i^{'}$ at 6 MHz	374	359	754	365	335	720
rlf ($\times 10^{-4}$) at 6 MHz	1.7	1.35	2.65	1.01	0.96	2.8
$\epsilon^{'}$ at 1 kHz	5817	27389	1611	14432	38140	2905
$\tan\delta_\epsilon$ at 1 kHz	1.9	2	2	2	1.8	2
Density (%)	85	83	89	88	88	90
M_s (emu/g)	74.6	72.4	76.8	76.1	74.1	76.2

may be present in the sintered samples, as the sintering temperature, 1473 K, is relatively low. The presence of these defects effectively lower the energy barrier (activation energy) to the flow of electrons [393], thus lowering the resistivity. However, in the case of the samples sintered for 1 hour, slightly lower resistivities are observed when compared to the samples sintered for 30 minutes. Such type of decrease in the resistivity with increasing sintering time is explained on the basis of decreasing activation energy, increasing effective area of grain to grain contact, and decreasing effective area of grain boundaries [394]. Hence the conductivity will be large. At the same time, electron hopping as one of the causes of lower resistivity for $Ni_{0.5}Zn_{0.5}Fe_2O_4$, is also well accepted [393–395]. As the samples are sintered at 1473 K, Zn loss is possible as evaporation, which results in cation vacancies and unsaturated oxygen ions. The excess electron on oxygen ion then bond with neighboring Fe^{3+} ions due to the electrostatic interaction giving rise to formation of Fe^{2+} ions. Creation of Fe^{2+} ions gives rise to electron hopping between the Fe^{3+} and Fe^{2+} ions.

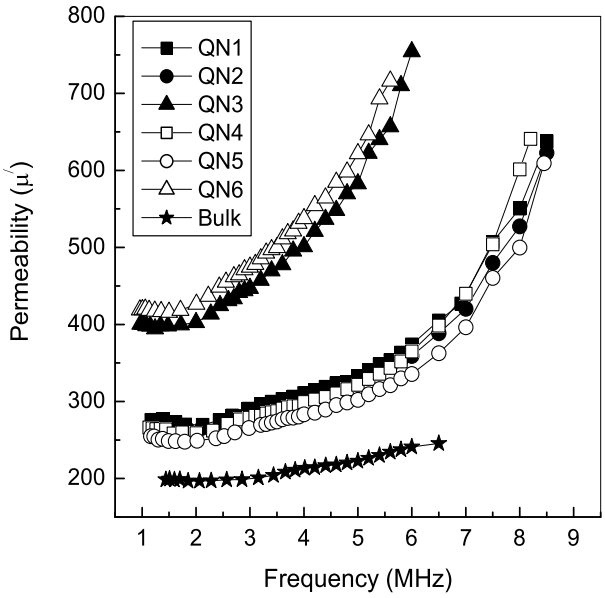

Figure 4.21: Variation of permeability with frequency for the samples sintered under different conditions.

Initial permeability

High initial permeability and low loss are important parameters to evaluate the quality of soft ferrites. The complex permeability ($\mu = \mu_i^{'} - j\mu_i^{''}$) of the ferrites is influenced by chemical composition, crystal structure, grain size, temperature and porosity. Here $\mu_i^{'}$ the real part is the initial permeability, and the imaginary part $\mu_i^{''}$ (90 ° out of phase) is the permeability loss. $\mu_i^{''}$ arises due to the lagging of the motion of the domain walls with the applied alternating magnetic field. The variation of the permeability as a function of frequency in the frequency range of 1–10 MHz has been studied for the samples sintered at two different sintering times and with or without additives.

Figure 4.21 shows the permeability spectra of the different samples sintered at 1473 K for 30 min (QN1, QN2, QN3) and 1 hour (QN4, QN5, QN6). The data for the bulk sample, sintered at the same temperature for 1h, without any additives, is also shown for comparison. Large values of the permeability (> 600) are obtained at higher frequencies. These values are very high as compared to the reported maximum values for $Ni_{0.5}Zn_{0.5}Fe_2O_4$ synthesized by the low temperature methods and sintered between 1473

and 1673 K [259, 396] or that for the bulk material [186]. At all frequencies, the permeability values are much larger for samples sintered with Bi_2O_3. Also, for all samples, the permeability values are larger than the values reported for the samples synthesized by the citrate method and sintered at 1473 K [396]. QN3 and QN6 show the highest $\mu_i^{'}$ at the specific frequency range, ever reported for any $Ni_{0.5}Zn_{0.5}Fe_2O_4$ processed from nano-sized particles. Here, it can be interpreted that the addition of Bi_2O_3 helps for uniform grain growth, with less porosity. Thus reversible displacement of domain walls, which are pinned to grain boundary, becomes easier when subjected to a small magnetic field. As Bi_2O_3 addition increases the grain size, the number of domains inside the grain also increases, resulting in the increase of $\mu_i^{'}$.

For most of the reported cases, maximum $\mu_i^{'}$ is observed when the grain size is larger than 5 μm [392]. In all cases, the permeability increases to higher values above 4 MHz, with a tendency to reach towards a maximum at the resonance frequency. When the frequency of the applied magnetic field equals the Larmor precession of the electron spin, resonance occurs and the energy is transferred from the field to the system helping in orienting the magnetic dipoles. At this point permeability will attain a highest possible value [396]. At frequencies above this value, there will be a lag between the applied field frequency and the movement of the domain spins. Thus $\mu_i^{'}$ will be decreased rapidly or $\mu_i^{''}$ will increase [397]. The resonance frequency is the limiting frequency of a magnetic material below which the material can be used. In the present work, it was, however not possible to observe the complete resonance peak due to the instrumental limitation (the Q-meter HP4342-A has maximum L scale up to 25 only, which corresponds to the maximum frequency limit as shown in figure 4.21).

The variation of the relative loss factor, *rlf*, with frequency, measured at room temperature, is shown in figure 4.22 for all the sintered samples. The *rlf* is the ratio of the magnetic loss tangent to the initial permeability, which is calculated using Eq. (3). High $\mu_i^{'}$ and low *rlf* are required for high frequency magnetic applications. The values of the loss factors found in the present work are in the range of 10^{-4}–10^{-5}, which are almost equal to the *rlf* values reported for $Ni_{0.5}Zn_{0.5}Fe_2O_4$ synthesized by the solid state and a low temperature methods [398, 399].

The observed higher permeability and low loss are not likely to be due to the smaller

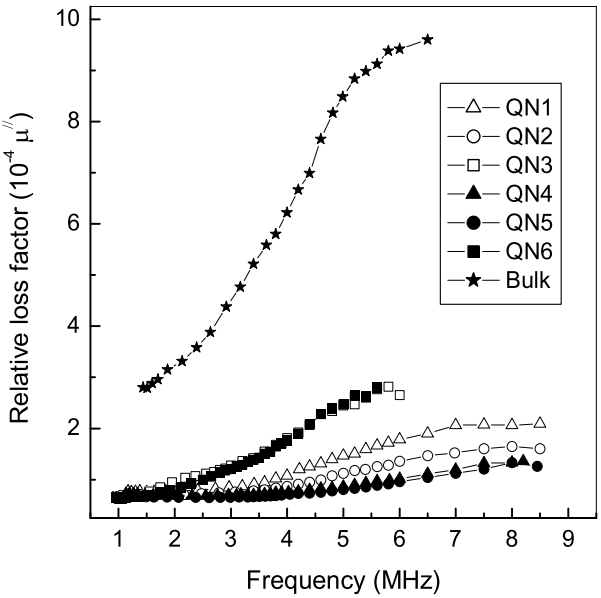

Figure 4.22: Variation of relative loss factor with frequency for the samples sintered under different conditions.

grain sizes. It is known that the permeability increases with increasing grain size, following the relation, $\mu \propto D^{1/3}$, where D is the diameter of a grain [188, 231]. However, for the ferrite materials, there are different factors which influence the permeability. These are the intrinsic factors such as saturation magnetization, magnetostriction and anisotropy as well as the extrinsic factors such as microstructure, grain size, porosity, stress, etc. For reversible rotational processes, the permeability is given by [188],

$$(\mu - 1) = CM_S^2 Sin^2\theta / K_1 \tag{4.2}$$

and for reversible wall processes,

$$(\mu - 1) = CM_S^2 S\alpha \tag{4.3}$$

where C is a constant, M_s is the saturation magnetization, θ is the angle between M and H, K_1 is the anisotropy constant, S is the surface area of the domain wall and α is the second derivative of the wall energy with respect to wall displacement [188]. Thus, in both cases, higher saturation magnetization helps higher permeability and increasing

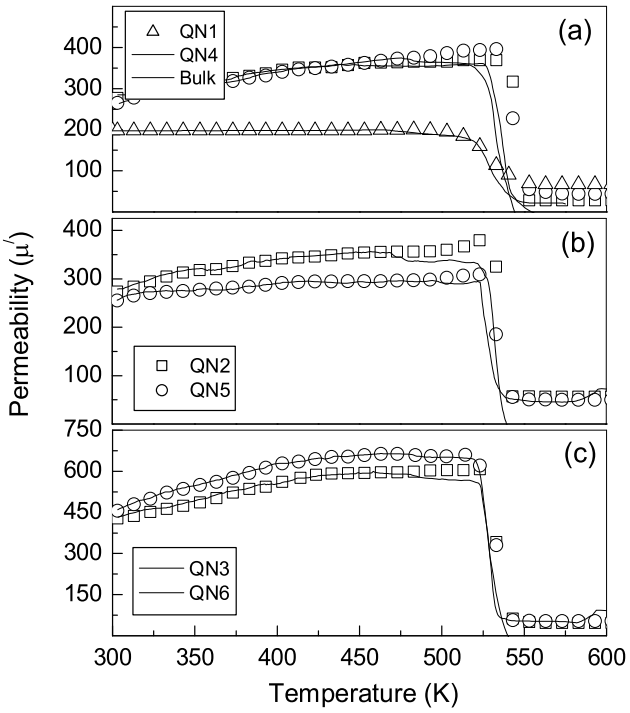

Figure 4.23: Variation of the permeability (symbols) and ac susceptibility (solid lines) with temperature for the samples sintered under different conditions. (a) with PVA, (b) with Ag, and (c) with Bi_2O_3.

anisotropy decreases the permeability. Larger grains with less number of grain boundaries give rise to larger permeability. Along with this, porosity and inclusions affect the movement of domain walls and therefore affect the permeability directly. Another factor which contributes to the magnitude of the permeability is the chemical homogeneity. It is known that lower grain sizes lead to formation of Fe^{2+} which enhances the magnetocrystalline anisotropy of the compound, as well as helps in the precipitation of secondary phases which hinder domain wall motions. However, in general, initial permeability and loss factor do not fully depend on the grain size. Such type of prediction has been made by Visser *et al.* [397]. It has been pointed out that $\mu_i^{'}$ and *rlf* may be independent of the grain size.

The study on the dependence of permeability on temperature is essential from the view point of applications. The variation of the permeability with temperature was measured for the sintered ferrites at a constant frequency 2.51 MHz in the temperature range from

300 to 625 K. Figure. 4.23 shows the variation of the real part of the permeability $\mu_i^{'}$ with temperature for all the sintered NiZn ferrite samples. The ac susceptibility curves of the corresponding samples, are also measured to compare the Curie temperature, and shown in the figure. The measurements were made at a frequency of 210 Hz in a field of 0.5 Oe. The ac susceptibility values are normalized with respect to the maximum value of the permeability at the respective temperatures. The Curie temperatures obtained from the permeability and the ac susceptibility data are identical and the curve shapes are also identical. The Curie temperature is slightly larger (538 K) for the virgin sintered samples (QN1, QN4) when compared to the slightly lower Curie temperatures (529 K) for the samples with additives (QN2, QN3, QN5, and QN6). The Curie temperature obtained for the low-temperature synthesized samples is comparable to that for the bulk material. Both the samples sintered with Bi_2O_3 show higher permeabilities at all temperatures. It is found that $\mu_i^{'}$ increases with increasing temperature. The variation in the permeability is as expected because the increase of $\mu_i^{'}$ with temperature can be related to the competition between the variation of K_1 and M_s [400].

The observed permeabilities of the different sintered samples are likely to be determined by a combination of the different factors discussed above. For example, the microstructures are different for different samples (see Figure. 4.20). Although the permeabilities of QN3 and QN6 are comparable, their microstructures are different. Similarly, the Curie temperature is slightly larger for the sample sintered without any additives. The difference in the Curie temperature is an indication for the difference in the chemical homogeneity. Also, slight changes in the distribution of the ions in the tetrahedral and octahedral sites will affect the T_C as well as the magnetization. In fact, as shown in Table 4.2, among the six samples, the saturation magnetizations are larger for QN3 and QN6 showing the highest permeabilities and lowest for QN2 and QN5 showing lower permeabilities. However, though QN4 shows saturation magnetization comparable to that of QN6, its permeability is low and comparable to that of QN2. Hence it is not possible to point out to a single factor which give higher permeabilities for the present samples.

Dielectric constant

The dielectric behavior of NiZn ferrite has been extensively studied on bulk samples [401, 402], on nonconventional samples [403] and on nanocomposites [404]. The dielectric property is one of the most important property of ferrites, which depends on the processing conditions, sintering conditions, chemical compositions and the type of additives.

The variation of the room temperature dielectric constant $\epsilon^{'}$ of $Ni_{0.5}Zn_{0.5}Fe_2O_4$, as a function of the ac frequency, is shown in Figure 4.24. Variation of the dielectric loss tangent, tanδ with frequency is shown as inset in Figure 4.24 and the value of $\epsilon^{'}$ and tanδ measured at 1 kHz are compared in Table 4.2. The observed values of $\epsilon^{'}$ at low frequencies for the samples sintered at 1473 K for 1 hour are very high as compared to the reported values [186, 402]. The dielectric constants are comparatively low for the samples sintered for 30 minutes. The observed values of $\epsilon^{'}$ can be directly correlated with the resistivity values as shown in Table 4.2. It is seen that, the sample with lowest resistivity shows the highest dielectric constant, whereas one with highest resistivity shows minimum dielectric constant. The dielectric mechanism in ferrites solely depend on the amount and presence of divalent ions, which is similar to that of the conduction process [394, 405]. The dielectric exchange between Fe^{3+} and Fe^{2+} results in local displacements determining the polarization of the ferrites. Polarization in ferrites has largely been attributed to the presence of Fe^{2+} ions which gives rise to heterogenous spinel structure up to some extent. Since Fe^{2+} ions are easily polarizable, the larger the number of ferrous ions, more will be the electron hopping between Fe^{3+} and Fe^{2+} and higher would be the dielectric constant.

It is seen form Figure 4.24 that the $\epsilon^{'}$ decreases with increasing frequency. The decrease of dielectric constant with increase of frequency as observed in the case of NiZn ferrite is a normal dielectric behavior of spinel ferrites. Such type of behavior has been already reported for $Ni_{0.5}Zn_{0.5}Fe_2O_4$ [403, 406]. Above some certain frequencies, the value of $\epsilon^{'}$ become much lower, approaching the intrinsic value. Although same number of ferrous ions are present over different frequency ranges, QN2 shows a $\epsilon^{'}$ value of 27390 at 1 kHz, whereas it is decreased to 5 when the applied frequency is increased to 1 MHz. This dispersion occurs because beyond a certain frequency of the externally applied electric field, the electron hopping or electron exchange between Fe^{3+} and Fe^{2+} can not follow the alternating field. Thus a reduction in $\epsilon^{'}$ is observed at higher frequencies for all the

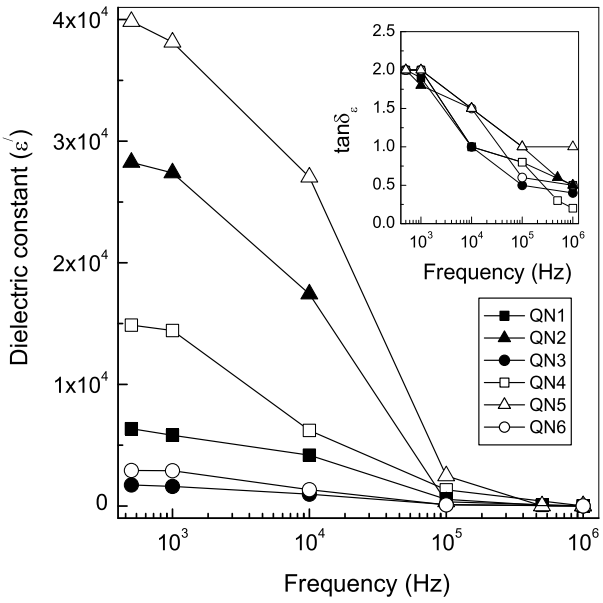

Figure 4.24: Variation of dielectric constant with frequency for samples sintered under different conditions. Inset: Dielectric loss vs. frequency.

samples.

Inset of Figure 4.24 shows the variation of dielectric loss tangent with frequency, measured at room temperature. It is seen that at lower frequencies, tanδ_ϵ becomes maximum, and with increasing frequency, it is reduced to a minimum value. The maximum tanδ_ϵ value observed in all the cases is 2, which indicates that the ferrite samples in the present work have moderate dielectric loss. These values are comparable to that reported [406] and higher than that reported by Mangalaraja *et al.* [403]. As mentioned, there is a strong correlation between conduction mechanism and dielectric behavior of ferrites; dielectric loss is also related to the electron exchange mechanism in ferrites. The dielectric loss arises due to the lag of the polarization behind the applied ac-electric field and is caused by the impurities and imperfections in the crystal lattice.

4.4 Conclusions

Nanocrystalline NiZn ferrite, $Ni_{0.5}Zn_{0.5}Fe_2O_4$ synthesized by an autocombustion method show promising results for applications. Dextrose along with glycine is found to be very

useful as a fuel to obtain single phase NiZn nanoparticles. This is because the addition of dextrose reduces the reaction rate and hence gives ferrite nanoparticles. There is not much increase in the particle size when powder samples are annealed at high temperatures and saturation magnetization comparable to that of the bulk ferrite is achieved after heating at 1073 K. Higher Curie temperatures are obtained for the nanosized powders due to the difference in the distribution of the cations, when compared to that in the bulk, in the tetrahedral and octahedral sites of the spinel lattice. The powders sintered at a temperature of 1473 K for 30-60 minutes show very high magnetic initial permeability and dielectric constant with negligible loss, due to the smaller grain size of 1-3 μm. Thus, NiZn ferrite synthesized by the present method will be more useful for device applications, as it requires low sintering temperatures and gives higher dielectric constant and magnetic permeability with low loss.

Chapter 5

Nanocrystalline $ZnFe_2O_4$ and γ-Fe_2O_3

5.1 $ZnFe_2O_4$

5.1.1 Introduction

Zinc ferrite, $ZnFe_2O_4$, is a normal ferrite and is paramagnetic at room temperature. The Zn^{2+} ions occupy the tetrahedral A-site and the Fe^{3+} ions occupy the octahedral B-site in the spinel structure of AB_2O_4. If it is possible to synthesize $ZnFe_2O_4$ with inverted or partially inverted structure, symbolized by $Zn_{1-x}Fe_x[Zn_xFe_{2-x}]O_4$ where $x = 1$ for inverted and $0 < x < 1$ for partially inverted structure, then $ZnFe_2O_4$ is also expected to show ferrimagnetic properties at or above room temperature. This is similar to $MgFe_2O_4$, which shows ferrimagnetic properties at room temperature due to the partially inverted structure in which part of Mg^{2+} ions are in the octahedral sites and corresponding amounts of Fe^{3+} are moved to the tetrahedral sites. However, it is not possible to make ferrimagnetic $ZnFe_2O_4$ by the usual solid state method of synthesis and the inversion parameter usually obtained is less than 0.05 [211]. One way to overcome this draw back is to make the material in nanocrystalline form, either by following low-temperature methods of synthesis or by reducing the size of the bulk samples to nanometer scales by mechanical milling. In the first case, as the synthesis is usually carried out at relatively low temperatures, it is possible to obtain materials with different degrees of distributions of Zn^{2+} and Fe^{3+} ions in the tetrahedral and octahedral sites [213, 407–416]. Similarly, mechanical milling can also rearrange the distribution of the Zn^{2+} and Fe^{3+} ions in the two different sites of the spinel structure [220, 417–420]. A third method is to quench the sample from high temperatures during the synthesis which also is expected to produce materials with different metal ion distributions [222, 223]. $ZnFe_2O_4$ nanoparticles with superparamagnetic properties and

with the degree of inversion of 20-50%, with a magnetization in the range 10-30 emu/g at magnetic field strengths of 1-2 T, have been reported in the literature for samples synthesized by the different methods. Superparamagnetic behavior has also been observed in thin film samples of $ZnFe_2O_4$ [212,215]. Yu *et al.* recently reported a very high value of magnetization of 54.6 emu/g at 300 K, with a high value of coercivity (52 Oe), in ultrafine $ZnFe_2O_4$ samples synthesized by the hydrothermal method [421].

In most of the studies on nanoparticles of zinc ferrite, formation of impurity phases such as ZnO and α-Fe_2O_3 has been reported [421]. Also, exceptionally large magnetization is observd in some cases. Kundu *et al.* reported that though their nanocrystalline zinc ferrite was crystallographically single phase in nature, the cation distribution was not the same throughout the sample [218]. In some parts of their sample, there was no change in the inversion whereas there was high degree of inversion in other parts of the sample. In this work we have attempted to synthesize single phase zinc ferrite nanoparticles by the autocombustion method using the glycine nitrate process and study their magnetic properties. One of the objectives is to explore the high magnetization values reported when some impurity phases are observed along with zinc ferrite.

5.1.2 Synthesis

$ZnFe_2O_4$ powder samples have been synthesized by the same GNP method as described in *section 2.2*, but by varying the glycine to nitrate ratio. 1 mole of zinc nitrate and 2 moles of ferric nitrate were dissolved in minimum amount of distilled water, and the solutions were mixed together and a water solution of glycine was added to the above mixture in a crystallizing dish. The amount of glycine was varied from 1 to 8 moles. In the present work, the glycine to nitrate ratio has been varied to reduce the flame temperature and hence to reduced the particle size. For convenience, the as-decomposed powder samples are denoted as ZNFn where n corresponds to the number of moles of glycine used for the synthesis. A bulk sample of $ZnFe_2O_4$ was also synthesized from ZnO and Fe_2O_3 by the solid state method (denoted as ZNF0), to compare the various results. ZnO and Fe_2O_3 taken in the stoichiometric ratio were mixed together and heated at 1273 K and 1373 K for 12 h each with intermediate grinding.

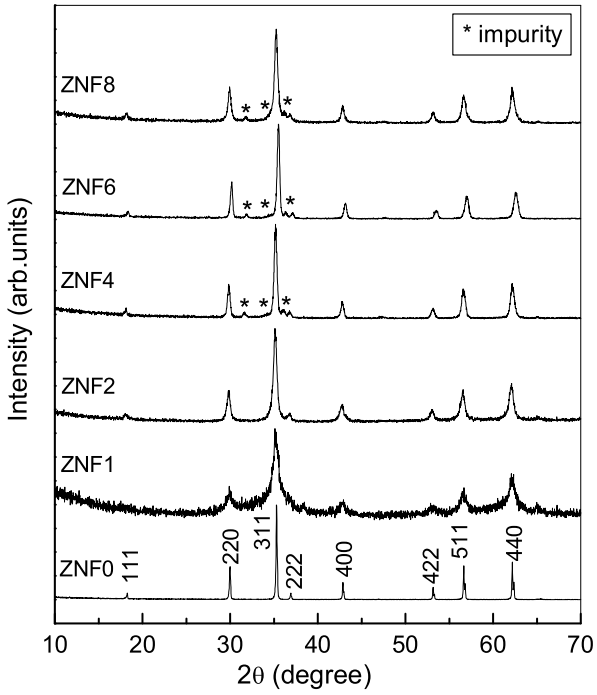

Figure 5.1: Powder X-ray diffraction patterns of $ZnFe_2O_4$, synthesized by the autocombustion method. The XRD pattern of the bulk sample synthesized by the solid state method is shown at the bottom (ZNF0) for comparison.

5.1.3 Results and discussions

Figure 5.1 shows the powder X-ray diffraction patterns of the as-synthesized samples obtained with different amounts of glycine and from the solid state method. The XRD patterns show the formation of $ZnFe_2O_4$ and the positions of all the reflections are matching with that of the pattern shown for the bulk sample, ZNF0. However, additional small peaks are observed in the XRD patterns when more than 2 moles of glycine was used for the synthesis and these additional reflections correspond to those from ZnO for ZNF3 to ZNF8. No other impurity peaks, other than those from ZnO, are observed. The presence of ZnO and/or α-Fe_2O_3 has been observed in some of the reports where the particle sizes of $ZnFe_2O_4$ are relatively large [213, 222, 407, 417, 419].

For ZNF1 and ZNF2, where no impurity peaks are observed in the XRD patterns, the cubic lattice parameter is found to be close to that obtained for the bulk sample and comparable to the literature value reported for zinc ferrite (8.441 Å, JCPDS #22-1012).

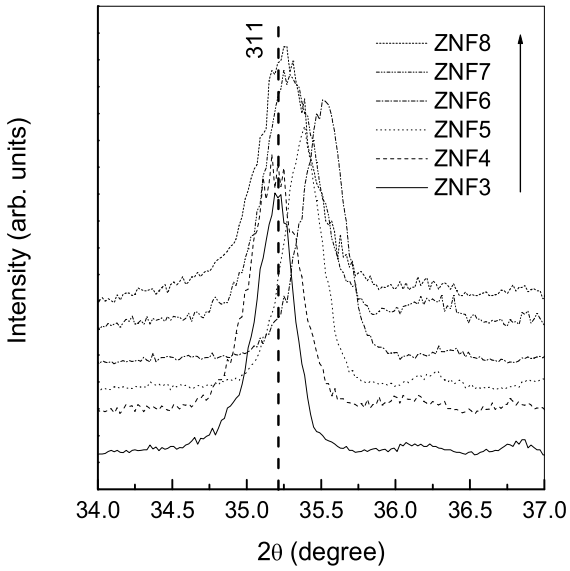

Figure 5.2: Comparison of the expanded powder XRD patterns for ZNF3 to ZNF8.

The reflections in the XRD patterns are broad and the average particle sizes, calculated using the Scherrer formula, are 8 nm and 17 nm for ZNF1 and ZNF2, respectively. The degree of crystallinity and therefore the average crystallite size increased with further increase in the amount of glycine used, as evidenced by the decreasing broadness and increasing sharpness of the reflections for ZNF3 to ZNF8. The average crystallite size vary from 25 to 45 nm for these samples. A closer look at the XRD patterns of ZNF3 to ZNF8 shows (Figure 5.2) a gradual shift of the XRD peaks to higher angles, indicating a change in the lattice parameter.

It is observed that the lattice parameter decreases from that of zinc ferrite as the number of moles of glycine used is increased from 3 to 6 and increases further with increasing the amount of glycine. The lowest value of the lattice parameter is obtained as 8.406 Å, when 6 moles of glycine is used. The variation of the cubic lattice parameter, with the number of moles of glycine used is shown in Figure 5.3. The corresponding values for the bulk sample is also shown in the figure for comparison ($n = 0$). The lattice parameter remains almost constant for ZNF1 and ZNF2 and the value is comparable to that of the bulk, ZNF0. It is further decreased as n is increased, from 8.437 to 8.406 Å, for ZNF3 to ZNF6 and then again increased to 8.438 Å, for ZNF8. Such a decrease in the

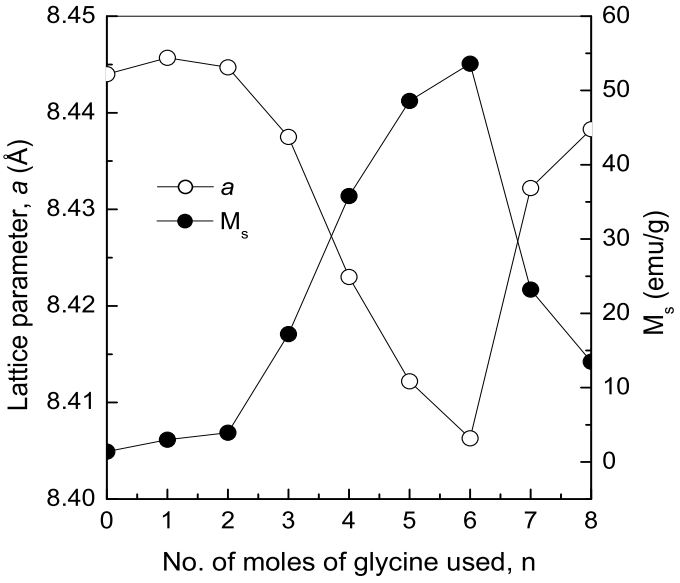

Figure 5.3: Variation of the cubic lattice parameter and saturation magnetization at 10 kOe, as a function of the number of moles of glycine, n, used for the synthesis. The values at $n = 0$ are for the bulk sample, ZNF0.

lattice parameter has been observed for decreasing particle size of zinc ferrite obtained by mechanical milling [418]. In this case, the lattice parameter decreases and the degree of inversion increases with decreasing particle size. Moreover, an increase in the ferrimagnetic transition temperature is observed with decreasing particle size. Similarly, an increase in the magnetization is observed with decreasing lattice parameter [215].

The magnetization as a function of field strength, recorded at room temperature, for the different ZNFn samples are shown in Figure 5.4 and Figure 5.5. For samples prepared with 1 and 2 moles of glycine (ZNF1 and ZNF2), superparamagnetic behavior is observed. There is no magnetic saturation and the coercivity is zero for both samples. The temperature variation of the ac magnetic susceptibility of ZNF1, measured at 2 Oe and 210 Hz, is shown in the inset (A) of Figure 5.4. The ac susceptibility curve indicates a superparamagnetic blocking temperature of 65 K. The magnetization of ZNF2 is slightly larger than that of ZNF1, where the magnetization at 10 kOe is found to be 3 and 4 emu/g for ZNF1 and ZNF2, respectively. The enhanced magnetization of ZNF2 is likely to be due to the larger particle size of ZNF2. Since bulk $ZnFe_2O_4$ is antiferromagnetic at room

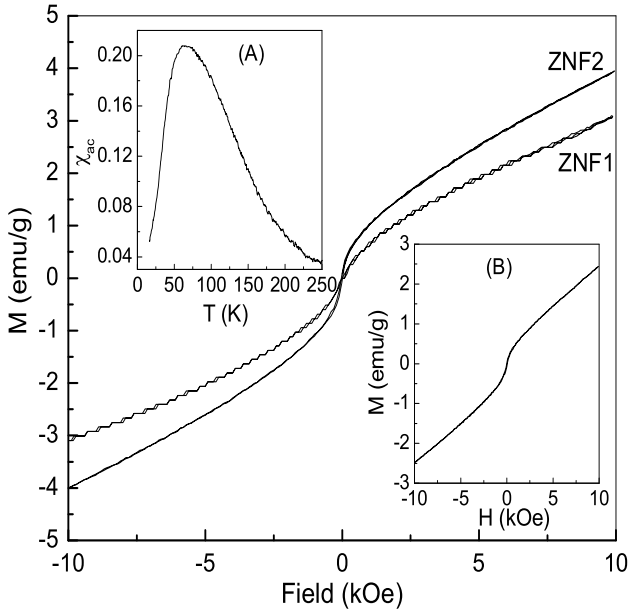

Figure 5.4: Magnetization as a function of magnetic field, measured at room temperature, for ZNF1 and ZNF2. Insets: (A) ac susceptibility curve of ZNF1 and (B) M–H curve of ZNF2a at room temperature.

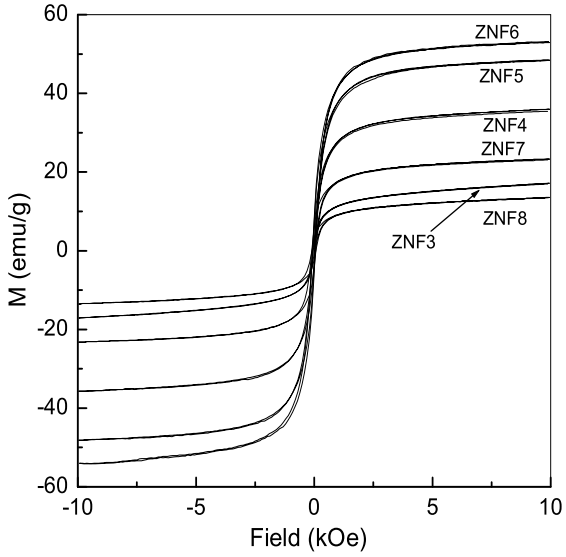

Figure 5.5: Magnetization as a function of magnetic field, measured at room temperature, for ZNF3 to ZNF8.

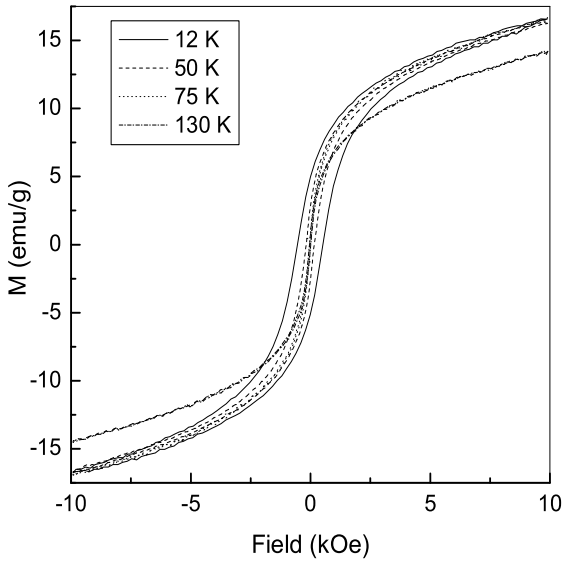

Figure 5.6: Magnetization curves of the as-synthesized ZNF1 powder sample, as a function of magnetic field, measured at different temperatures.

temperature, the observed superparamagnetism is likely to be coming from the different cation distributions in $ZnFe_2O_4$ nanoparticles. Superparamagnetism or ferrimagnetism is already observed at room temperature for nanosized $ZnFe_2O_4$ and this is ascribed to the unusual occupancy of the magnetic ferric ions in the tetrahedral sites [220, 222, 410, 413, 414, 422, 423]. In a recent report, Choi *et al.* showed very high occupancy of Fe^{3+} in the *A*-site, from the Mössbauer spectroscopic studies. The authors found the cation distribution of zinc ferrite as $(Zn_{0.39}Fe_{0.61})^A[Zn_{0.61}Fe_{1.39}]^BO_4$, where *A* and *B* are the tetrahedral and octahedral sites, respectively [424]. Moreover, Li *et al.* reported that, for zinc ferrite nanoparticles of same size, the T_N can be very much different, depending on the preparation conditions [425].

Figure 5.6 and Figure 5.7 show the magnetization curves of ZNF1 and ZNF2 measured at different temperatures (< 300 K). Magnetic hysteresis is observed below the blocking temperature and the coercivity increases with decreasing temperature. A very high value of M, 16.5 emu/g and H_c, 533 Oe, is obtained at 12 K for ZNF1. Such high values of magnetization and coercivity above 10 K are possible only if the cation distribution is different in the as-synthesized zinc ferrite nanoparticles from that of the normal $ZnFe_2O_4$.

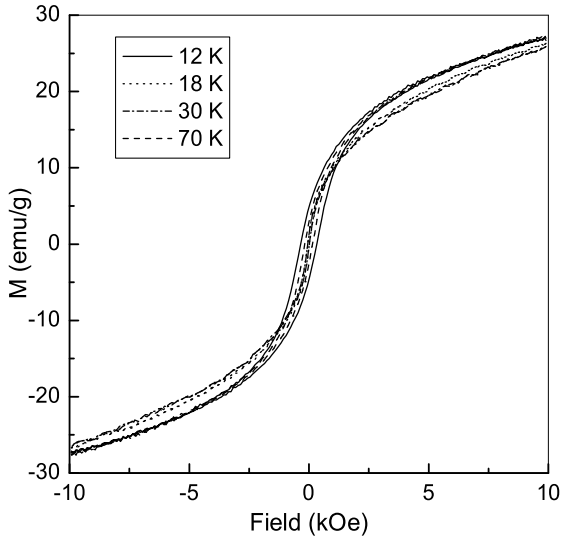

Figure 5.7: Magnetization curves of the as-synthesized ZNF2 powder sample, as a function of magnetic field, measured at different temperatures.

Same kind of magnetic characteristics are observed for ZNF2 powder sample also. However, the coercivity value, 325 Oe, at 12 K is lower than that of ZNF1. Comparable values of magnetizations and increasing trend of coercivity with decreasing temperature, for the nanosized zinc ferrite has been reported [415]. The role of the amount of glycine used for the synthesis on the phase purity and the observed magnetic characteristics of ZNF1 and ZNF2 can be explained as in the similar manner, as described for NiZn ferrite in *section 4.3.5*. Lower amount of fuel (glycine) leads to low reaction temperature and thus results in smaller particle sizes and hence to superparamagnetism.

A large increase in the magnetization, with almost saturation above 5 kOe (0.5 T) is observed for samples prepared using larger amounts of glycine, as shown in Figure 5.5. Maximum saturation magnetization of 53.6 emu/g is obtained for ZNF6. This is comparable to the high value of saturation magnetization reported by Yu *et al.* for nanoparticles of zinc ferrite synthesized by the hydrothermal method [421]. The variation of the saturation magnetization at room temperature and the cubic lattice parameter of the ferrite formed, as a function of the number of moles of glycine used, are compared in Figure 5.3. An interesting aspect is that the magnetization follows exactly a reverse trend; maximum magnetization is obtained when the lattice parameter is minimum. Superparamagnetic

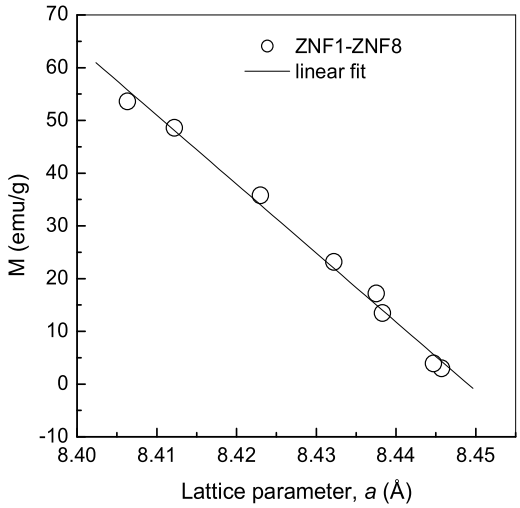

Figure 5.8: Variation of the saturation magnetization as a function of the cubic lattice parameter. The straight line is the least squares fitted curve.

behavior is observed for those samples (ZNF1 and ZNF2) whose lattice parameter is comparable to that of the bulk sample. On the other hand, magnetic saturation is obtained for those samples whose cubic lattice parameter is slightly smaller than that of the bulk and saturation magnetization increases with decreasing lattice parameter.

The variation of the magnetization as a function of the cubic lattice parameter is seen clearly in Figure 5.8. The magnetization increases almost linearly with decreasing lattice parameter. This observation indicates that the onset of ferrimagnetism, in the otherwise normal zinc ferrite which is paramagnetic at room temperature and antiferromagnetic below 10 K, is associated with lattice contraction. A decrease in the lattice parameter with increasing inversion is generally observed for ferrites [426] and therefore, the present results point to the increasing magnetization as due to increasing degree of inversion of zinc ferrite. The degree of inversion, i.e. the distribution of cations in the tetrahedral and octahedral sites, can be generally calculated approximately from the intensity ratio of a pair of diffraction lines [427]. However, in the present case, this method could not be used, as the diffraction lines were very broad due to the fine particle nature of the powders and the average particle sizes were found to vary between 10 to 45 nm for ZNF1 to ZNF8.

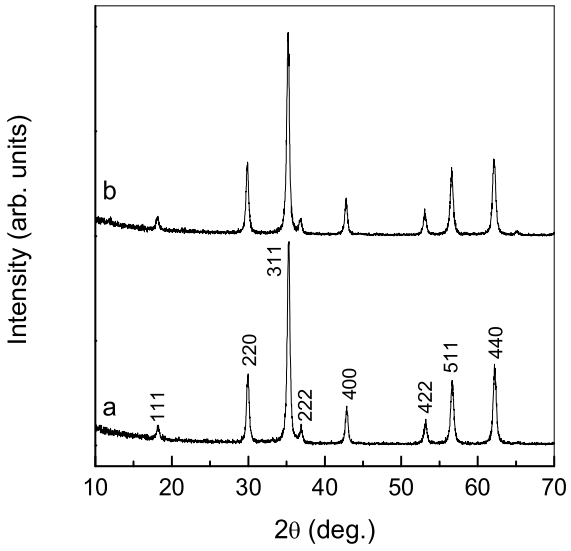

Figure 5.9: Powder X-ray diffraction patterns of $ZnFe_2O_4$ annealed samples. a) ZNF1a and b) ZNF2a.

Since the presence of impurity phase as ZnO has been detected in the XRD patterns of ZNFn with $n \geq 3$, it is reasonable to assume that impurity phases may be present in the amorphous state in ZNF1 and ZNF2 samples also, which are not detected due to their very fine particle size nature. In many of the reports, ZnO and α-Fe_2O_3 are already observed as impurity phases in nanocrystalline form [213, 222, 407, 417, 419]. To clarify this issue, the as-synthesized ZNF1 and ZNF2 powder samples were annealed in air at 873 K for 6 hours and cooled down to room temperature. The annealed samples are now named as ZNF1a and ZNF2a, respectively. It was expected that if any impurity phases were present in ZNF1 and/or ZNF2 in the amorphous form, annealing would help the particles to grow to become crystalline at higher temperatures. Powder X-ray diffraction measurements have been carried out on these annealed samples. The XRD patterns of the annealed samples are shown in Figure 5.9. It can be observed from Figure 5.9 that the XRD reflections of the zinc ferrite phase become sharp with annealing. The average particle size is found to increase to $\sim$25 nm when the samples are annealed at 873 K. There are no impurity peaks observed in the XRD patterns of the annealed samples indicating that ZNF1 and ZNF2 are single phase $ZnFe_2O_4$ nanoparticles obtained by the present combustion method.

Since no ZnO impurity is detected in the superparamagnetic samples (ZNF1 and

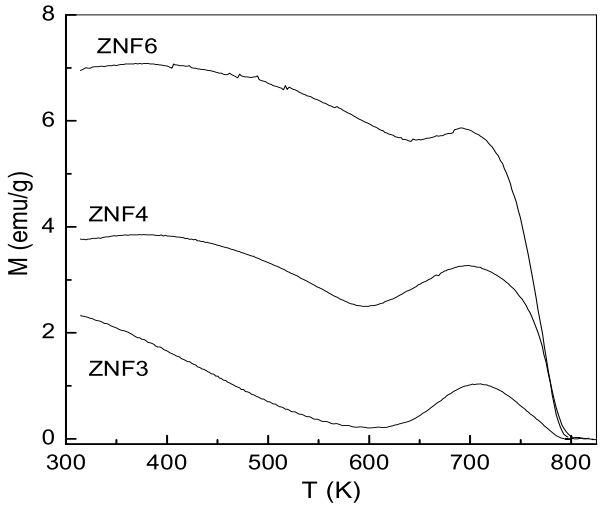

Figure 5.10: Temperature variation of magnetization of ZNF3, ZNF4 and ZNF6, measured in a field of 50 Oe.

ZNF2), having lattice parameter comparable to that of the bulk (ZNF0), and ZnO impurity is detected in the samples showing magnetic saturation at room temperature and smaller lattice parameters, it is possible that the magnetic zinc ferrite formed is deficient in zinc. Chen *et al.* [212] have earlier reported the formation of zinc ferrite films which are rich in iron and deficient in zinc. However, in the present studies, it is found that the amount of ZnO formed is very small and almost in constant amounts. Among the samples from ZNF3 to ZNF8, it was found that the amount of ZnO phase was lowest in ZNF6, which shows the highest saturation magnetization. This suggests that the compositions of the samples with varying M_s may be identical and the only difference may be in the degree of distribution of Zn^{2+} and Fe^{3+} ions in the tetrahedral and octahedral sites.

There are no reports in the literature on the studies on the magnetic measurements of the nanocrystalline zinc ferrite at high temperatures. All the reported studies are performed at or below 300 K. Figure 5.10 shows the temperature variation of the magnetization of some of the samples, measured above room temperature. For ZNF3, ZNF4, and ZNF6, a magnetic transition is observed at ∼775 K. The magnetic transition temperature is independent of the number of moles of glycine used for the synthesis. If it is assumed that the decreasing lattice parameter is due to the changes in the degree of

inversion, a change in the magnetic transition temperature would have been observed. The identical transition temperature implies the contribution from a same phase having identical distribution of the different ions in the lattice. It is likely that this is an impurity phase in all the samples, not detected by XRD. The increasing room temperature magnetization indicates increasing amount of this impurity phase. An important aspect is that the observed transition temperature is almost identical but slightly less than that of Fe_3O_4 [186]. This indicates the presence of this phase, in increasing amounts, in the samples. For all the samples, the initial decrease in the magnetization and further increase above 625 K is likely to be due to the growth of the particles during the heating run. Similar features have already been observed for other ferrites [380]. It is also possible that small amounts of γ-Fe_2O_3 is also present as an impurity phase and the initial decrease in the magnetization below 675 K is due to the conversion of γ-Fe_2O_3 to α-Fe_2O_3 which is expected at 673 K [228, 229] and the second magnetic transition is that of Fe_3O_4. If this is true, the samples are likely to contain $ZnFe_2O_4$, γ-Fe_2O_3 and Fe_3O_4, apart from ZnO.

Up to this point, it is found that, the as-synthesized $ZnFe_2O_4$ samples ZNF1 and ZNF2 are single phase and superparamagnetic at room temperature and the T_B lies far below room temperature. But the question is, are there any other impurity phases formed along with normal $ZnFe_2O_4$, which are superparamagnetic in nature and could not be detected from XRD analyzes? Due to the smaller particle size nature, these impurity phases also may show superparamagnetic behavior. The two main possible magnetic impurities are Fe_3O_4 and γ-Fe_2O_3. The presence of γ-Fe_2O_3, which is a room temperature ferrimagnetic material can be ruled out as there is no other peak, other than that of $ZnFe_2O_4$ as seen in the XRD spectra of the annealed samples in Figure 5.9, since γ-Fe_2O_3 should be converted to α-Fe_2O_3 at around 675 K [228,229]. Moreover, the magnetization also should disappear if γ-Fe_2O_3 is converted to α-Fe_2O_3. To confirm this, *M–H* measurement has been carried out at room temperature on the annealed ZNF2a sample. The magnetization curve of ZNF2a is shown in inset (B) of Figure 5.4. The considerable value of M of the annealed sample clearly indicates the absence of γ-Fe_2O_3 impurity phase along with $ZnFe_2O_4$ in ZNF2, since α-Fe_2O_3 is antiferromagnetic at room temperature [94]. On the other hand, Liu *et al.* reported the enhancement of magnetization of $ZnFe_2O_4$ nanowires, when annealed at elevated temperatures in air atmosphere [416].

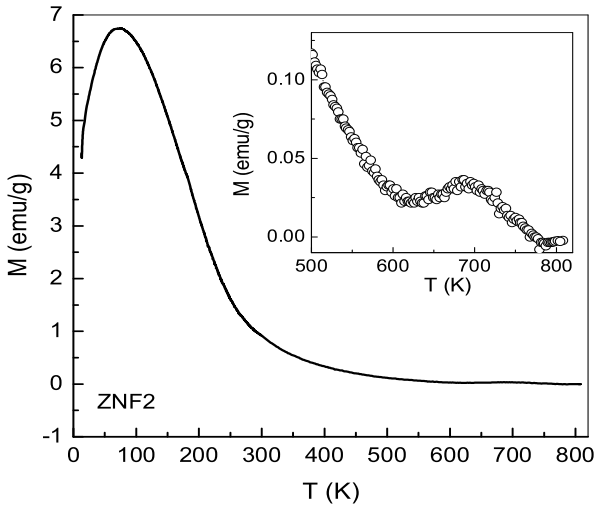

Figure 5.11: Variation of the ZFC magnetization of ZNF2 in the 10 to 800 K range. Inset: temperature variation of magnetization of ZNF2 in the region 500–800 K.

Figure 5.11 shows the variation of the ZFC magnetization of ZNF2 in the 10 to 800 K region. The characteristics are similar to that of reported for zinc ferrite nanoparticles. However, as shown in the inset of Figure 5.11, even for ZNF2, a very week magnetic transition is observed at the same temperature as that observed for ZNF3 to ZNF8, indicating the presence of very small amounts of Fe_3O_4 impurity in this sample. Hence the superparamagnetism observed for $ZnFe_2O_4$ is likely to be from the Fe_3O_4 impurity phase. This sample is likely to show a large degree of inversion from Mössbauer studies if it is assumed that the sample is single phase $ZnFe_2O_4$. No measurements at or below room temperature can give information on the small amount of the impurity phase.

Figure 5.12 compares the Mössbauer spectra of ZNF2 and ZNF6, recorded at room temperature. ZNF2 shows a doublet as expected for superparamagnetic zinc ferrite whereas a six finger pattern apart from the central doublet is obtained for ZNF6. The spectra of ZNF6 could be fitted to two sextets and a doublet. For ZNF2, apart from the doublet, a sextet also could be fitted, indicating the presence of some ferrimagnetic component in this sample. Already the high temperature magnetization measurements point to the presence of some impurity phase, likely to be Fe_3O_4, in this sample. Similar room temperature Mössbauer spectra are reported for nanocrystalline zinc ferrite samples

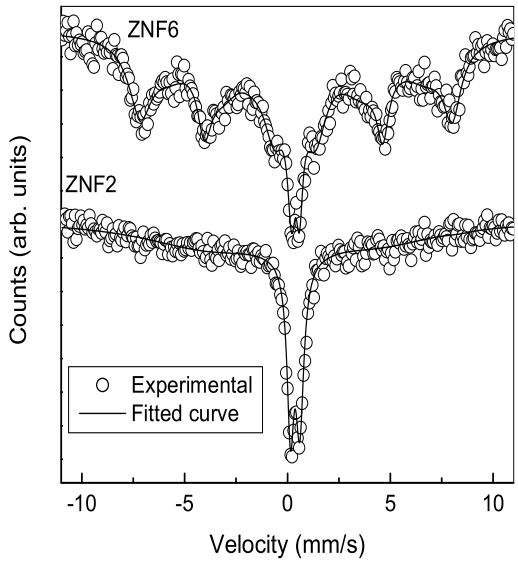

Figure 5.12: Room temperature Mössbauer spectra of ZNF2 and ZNF6.

obtained by mechanical milling of bulk zinc ferrite or those synthesized by low temperature methods [213, 218, 223, 417, 418, 423, 428]. In most of the reported studies, either only Mössbauer studies at low temperatures are used to get information on the distribution of the Fe^{3+} in the lattice or the magnetic measurements are made only below room temperature to show the superparamagnetic nature of the samples. The present results show that the interpretation of the data on nanocrystalline zinc ferrite samples could lead to wrong conclusions from such studies.

The higher magnetization and smaller lattice parameter obtained for samples synthesized using larger amounts of glycine needs further consideration. The lowest lattice parameter obtained (8.406 Å) is closer to that of Fe_3O_4 (∼8.394 Å). Then the question arises whether the samples are mixtures of $ZnFe_2O_4$ and Fe_3O_4 or not? It is also possible that the samples are $Zn_xFe_{3-x}O_4$ where the lattice parameter is known to vary with the Zn content [360]. However, in this case the magnetic transition temperature also varies with the Zn content. In the present case, the identical T_Cs obtained for the different samples is an indication for the presence of a single composition in all the samples. There are no detailed structural analysis reported in the literature on the nanocrystalline zinc ferrite showing higher room temperature magnetizations. If $ZnFe_2O_4$ and Fe_3O_4 are formed and

present in nanocrystalline forms, both phases are expected to show broad XRD peaks. In such a case, it may be difficult to distinguish the presence of both phases from the XRD pattern, as the difference between the lattice parameters is very small and the position of the most intense (311) reflections differs only by 0.2 degrees in the 2θ scale (for Cu Kα radiation).

It was found that the powder XRD patterns of ZNF3 to ZNF8, showing magnetic saturation at room temperature, could be fitted with two ferrite phases, with the lattice parameters of $ZnFe_2O_4$ and Fe_3O_4, with varying amounts. With decreasing overall lattice parameter, as shown in Figure 5.8, the contribution of Fe_3O_4 increases. This is in accordance with the variation of the saturation magnetization at room temperature. Hence it is possible that the zinc ferrite samples showing large room temperature magnetization are a mixture of $ZnFe_2O_4$ and Fe_3O_4, apart from small amounts of ZnO, where the large magnetization is the contribution from Fe_3O_4. Similarly, even in the zinc ferrite samples showing superparamagnetic behavior, presence of Fe_3O_4 could be envisaged. However, more detailed studies are required to confirm these arguments.

5.1.4 Conclusions

Nanocrystalline $ZnFe_2O_4$ has been synthesized in the 10–40 nm particle size range by the autocombustion method using glycine. When small amounts of glycine is used for the synthesis, the ferrite samples are found to be superparamagnetic at room temperature, whereas its bulk counterpart is paramagnetic at room temperature. The room temperature magnetization values obtained is 3 and 4 emu/g, for 8 nm and 17 nm particles, respectively, when 1 and 2 moles of glycine is used per 3 moles of the metal ions. The superparamagnetic blocking temperature is found to be 65 and K 75 for the corresponding samples. The observed magnetism is thought to be due to the unusual cation distribution, since the nanoparticles are synthesized by a low temperature method. However, presence of Fe_3O_4 as impurity is observed, from high temperature magnetization studies in one of the samples, implying that the observed superparamagnetic behavior could be that of the impurity phase which is otherwise ferrimagnetic in the bulk form. High values of saturation magnetization is observed when larger amounts of glycine is used for synthesis. In this case, the lattice parameter of $ZnFe_2O_4$ decreases and reaches towards that of Fe_3O_4.

5.2 γ-Fe_2O_3

5.2.1 Introduction

Maghemite (γ-Fe_2O_3) has been widely used as a material for recording devices because it has good magnetic properties and it is rather inexpensive. Usually, commercial γ-Fe_2O_3 acicular particles are synthesized from elongated α-FeOOH particles, which are first dehydrated and converted to α-Fe_2O_3. The latter is then converted into magnetite (Fe_3O_4) by partial reduction with hydrogen at elevated temperatures and, finally, reoxidized to γ-Fe_2O_3 in air [429]. A single step synthesis of γ-Fe_2O_3 in the nanometer range is very important for various applications such as high density data storage, magneto-optical devices, biocompatible ferro-fluids, magnetic ink, etc. Various methods have been reported for the synthesis of γ-Fe_2O_3 nanoparticles, such as wet chemical [229, 430, 431], electrochemical [432], pyrolysis techniques [433,434], combustion method [435,436] and chemical oxidation in micellar media [437] or in polymer [227] or mineral matrices [438, 439]. In general, all of these methods do not yield pure maghemite phase, and good control of particles size and achieving monodispersity are still the challenges in all these techniques.

When maghemite nanoparticles are synthesized by various low temperature techniques, in most of the cases, hematite (α-Fe_2O_3) is formed as a secondary phase. γ-Fe_2O_3 is converted to α-Fe_2O_3 at high temperatures above ~673 K. There are some efforts to enhance the transformation temperature by suitable doping of part of Fe by other ions. In an important experimental investigation, Lai *et al.* showed that the transition of γ-Fe_2O_3 to α-Fe_2O_3 phase can be suppressed by doping Mn^{3+} for Fe^{3+} [230]. The phase transformation temperature is enhanced up to 873 K by this method. We have attempted to synthesize γ-Fe_2O_3 nanoparticles by doping Zn^{2+} and investigated the role of Zn^{2+} on the formation and transition temperature of γ-Fe_2O_3.

5.2.2 Synthesis

The usual GNP has been used to synthesize γ-Fe_2O_3 nanoparticles. $Fe(NO_3)_3.9H_2O$ was dissolved in minimum amount of distilled water and a water solution of 2 moles of glycine was mixed to the metal nitrate solution. Zinc nitrate solution was added in different molar amounts (0, 0.025, 0.05, 0.075, 0.1, 0.125, 0.15, 0.175 and 0.2 mole for 2 moles of

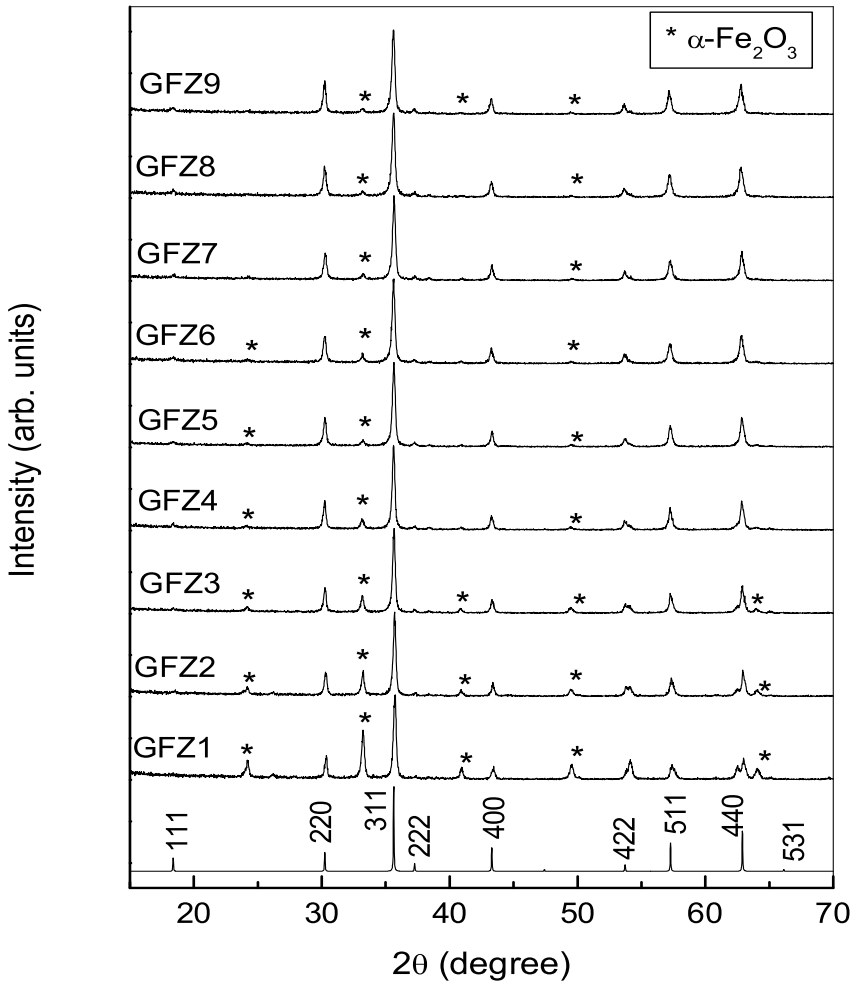

Figure 5.13: Powder X-ray diffraction patterns of different γ-Fe_2O_3 samples. The simulated XRD pattern of γ-Fe_2O_3 is shown for comparison.

Fe) and the combustion reaction was carried out on a hot plate at 473 K as described in *section 2.2*. The as-decomposed powder samples were characterized by XRD and magnetic measurements. The as-synthesized powders are coded as GFZ1, GFZ2, GFZ3, GFZ4, GFZ5, GFZ6, GFZ7, GFZ8, and GFZ9, for increasing concentration of Zn from 0 to 0.2 moles.

5.2.3 Results and discussions

The powder X-ray diffraction patterns of the as-synthesized samples are shown in Figure 5.13. The simulated XRD pattern of γ-Fe_2O_3 is also compared with the experimental

Table 5.1: Sample codes, doped amount of Zn (mole), magnetization (emu/g), coercivity (Oe), wt% of γ-Fe_2O_3 calculated from XRD and magnetization data, particle size (t) and lattice parameter (a) of different synthesis.

Sample code	Zn (mole)	M (emu/g)	H_c (Oe)	wt% γ-Fe_2O_3 from XRD	wt% γ-Fe_2O_3 from M–H	t (nm)	a (Å)
GFZ1	0	34	200	45	47	39	8.348
GFZ2	0.025	47	146	70	65	42	8.348
GFZ3	0.05	56	132	76	76	42	8.352
GFZ4	0.075	61	118	83	82	37	8.355
GFZ5	0.1	63	115	90	85	37	8.358
GFZ6	0.125	67	116	92	91	37	8.358
GFZ7	0.15	68	121	94	92	36	8.360
GFZ8	0.175	68	174	94	92	32	8.366
GFZ9	0.2	65	105	90	88	36	8.371

patterns. It is observed that α-Fe_2O_3 is formed along with γ-Fe_2O_3 in all cases and the amount of α-Fe_2O_3 decreases with increasing amounts of Zn. No other phases such as ZnO is observed, which may originate from Zn ions. The γ-Fe_2O_3 phase formed is cubic in structure and the space group is *Fd3m*. The lattice parameter 'a' of the γ-Fe_2O_3 phase formed when no zinc is added (8.348 Å) is comparable to the value reported for single phase material (a = 8.352Å, JCPDS #39-1346). When the concentration of Zn is increased from 0.025 to 0.2, a small increase in the lattice parameter is observed and the value varies between 8.35 to 8.37 Å. The weight percentages of the α-Fe_2O_3 and the ferrite phases were calculated from least squares refinement of the XRD patterns using PCW [272]. When Zn is not added, the major phase is obtained as α-Fe_2O_3 (55%). The γ-Fe_2O_3 phase content increases with increasing Zn concentration and become the dominant phase at higher Zn concentrations. Only 6% of α-Fe_2O_3 phase is observed when 0.15 and 0.175 moles of Zn is used. Thus the XRD studies show that doping of Zn suppresses the formation of the α-Fe_2O_3 phase. It is found that the peaks in the XRD patterns are broad and the average particle size is calculated using Scherrer formula for each sample. The particle sizes are found to be in the range of 32-42 nm. The calculated wt% of the ferrite phase, particle size and lattice parameter for the different samples are given in Table 5.1.

Since no ZnO phase is formed and the lattice parameter is only slightly larger than

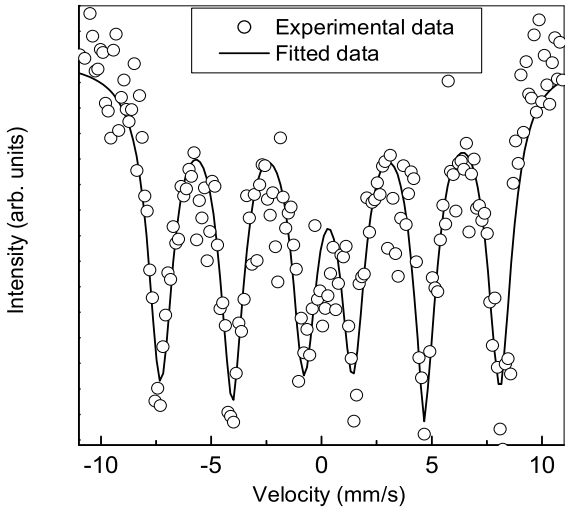

Figure 5.14: Room temperature Mössbauer spectrum of GFZ7.

that of maghemite when 0.15 and 0.175 moles of Zn is added, it can be assumed that Zn is incorporated in the vacant sites of the γ-Fe_2O_3 structure. Lai *et al.* have reported the formation of γ-Fe_2O_3, doped with Mn(III) [230]. In this investigation, formation of α-Fe_2O_3 in minor amounts along with γ-Fe_2O_3 is also reported. Mn(III), which is believed to be doped in the *B*-site of the spinel lattice, suppresses the transformation of γ-Fe_2O_3 to α-Fe_2O_3 on heating, by enhancing the phase transformation activation energy. But in the present case, the site occupancy of Zn^{2+} is not clear. In ferrites, Zn^{2+} always prefers the tetrahedral *A*-site. But may be due to the synthesis condition, unusual cation distribution occurs and Zn^{2+} occupy some of the octahedral sites as in $ZnFe_2O_4$ nanoparticles synthesized at low temperatures. It is also possible that Fe^{3+} is displaced from the tetrahedral sites to the octahedral sites and Zn ions occupy the tetrahedral sites. Assuming the spinel formula, γ-Fe_2O_3 contains a vacancy concentration of 0.33 and therefore the largest amount of Zn^{2+} that can be doped in the structure is 0.33, corresponding to $Zn_{0.33}Fe_{2.67}O_4$.

From the analysis of the XRD data it is found that, GFZ7 and GFZ8 are composed of mostly γ-Fe_2O_3 phase with very little amount of hematite phase. Thus, Mössbauer measurement was carried out at room temperature on one of these samples. The experimental and the fitted Mössbauer spectrum of GFZ7 is shown in Figure 5.14. The spectrum is

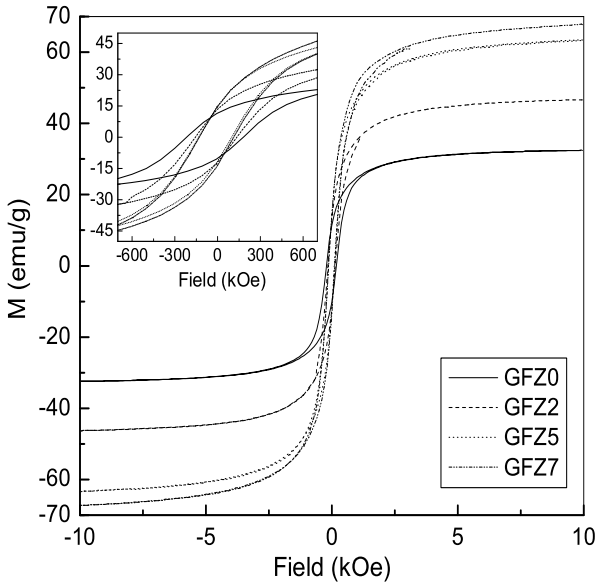

Figure 5.15: Room temperature magnetization curves of four different γ-Fe_2O_3 samples. The inset shows the enlarged hysteresis loops.

similar to that reported by different groups [432,440]. The experimental spectrum is fitted into a sextet. The corresponding hyperfine parameters are $IS = 0.352$ mm/s, and $QS = 0.041$ mm/s, which are typical of iron(III) [282,283,432,440]. The hyperfine magnetic field (HMF) at room temperature for the nanosized particles of maghemite is found to be 476 kOe, which smaller than that for the bulk counterpart, as found previously [282,283,368]. The reduction in the HMF for the nanoparticles is already explained in terms of collective magnetic excitation in *section 4.3.5*. The Mössbauer data suggests the presence of only Fe^{3+} ions in the as-synthesized sample, whereas Fe_3O_4 contains Fe^{2+} ions, whose hyperfine parameters differ from that of maghemite [282, 283, 441].

Magnetization as a function of field has been measured at room temperature for all the samples. Some of the selected *M–H* curves are shown in Figure 5.15 and the expanded hysteresis loops of these samples in the region ±600 Oe, are shown in the inset. The room temperature magnetization and coercivity of all the samples are listed in Table 5.1. Except GFZ1, all samples are found to be highly magnetic and the magnetization values are higher than that of the M_s values reported in the literature for nanostructured γ-Fe_2O_3 [227,230,435,436,442]. Magnetization increases with Zn-doping and reaches max-

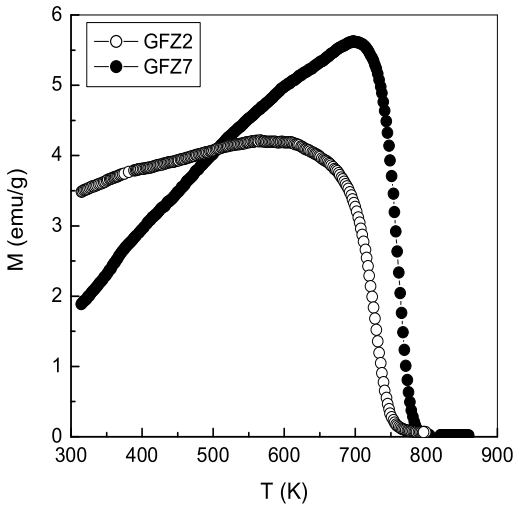

Figure 5.16: Variation of magnetization with temperature for GFZ2 and GFZ7 at an applied field of 50 Oe.

imum values for GFZ7 and GFZ8 and then starts decreasing. Magnetization values for the different samples can be correlated to the presence of α-Fe_2O_3. GFZ1 has maximum amount of impurity, thus lower M value. On the other hand, GFZ7 and GFZ8 have maximum γ-Fe_2O_3 phase as derived from XRD and hence higher magnetization. Moreover, magnetization values of these two samples are near to the saturation magnetization value (74 emu/g [368]) of γ-Fe_2O_3. The amount of the ferrimagnetic phase present in each sample is calculated from the magnetization data assuming 74 emu/g as the saturation magnetization and the calculated values are almost comparable to the amount calculated from XRD patterns, as shown in Table 5.1. It is observed that, in all cases, the wt% of γ-Fe_2O_3 phase obtained from magnetic measurements is slightly lower than that obtained from XRD. This may be due to the nanocrystalline nature of the ferrite phase. Interestingly, coercivity of all the samples are found to be relatively larger.

Fe_3O_4 and γ-Fe_2O_3 are difficult to distinguish from XRD and magnetization data, especially if they are in the nanoparticle forms. Therefore, the possibility of the formation of Fe_3O_4 instead of γ-Fe_2O_3 can not be ruled out from the XRD and magnetization measurements on the as-synthesized samples. However, it is well known that γ-Fe_2O_3 is thermally unstable, and convert irreversibly to the more stable hexagonal α-Fe_2O_3

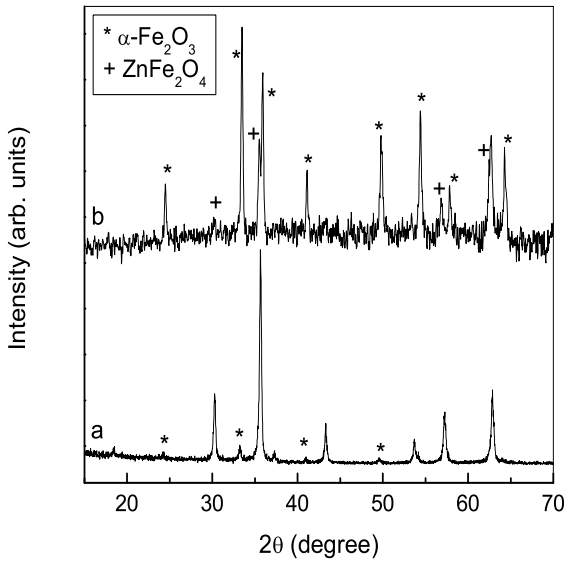

Figure 5.17: Powder XRD patterns of a) GFZ7 and b) its air annealed powder.

structure when heated in air atmosphere. The γ-Fe_2O_3 to α-Fe_2O_3 phase transformation temperature is 673 K. When the magnetization is measured as a function of temperature, a magnetic transition is similarly observed at this temperature which is due to the conversion from ferromagnetic γ-Fe_2O_3 to antiferromagnetic α-Fe_2O_3. On the other hand, Fe_3O_4 is highly stable and will not be converted to α-Fe_2O_3 at this temperature and magnetization will be retained up to its T_C (858 K [186]). If Zn is incorporated in the lattice of γ-Fe_2O_3, it is expected that the phase transformation temperature will be increased with respect to that of the undoped sample. To verify this, magnetization of two different samples has been measured as a function of temperature at a constant magnetic field (50 Oe). The M–T curves are shown in Figure 5.16. It may be seen that for the 2.5% doped sample, the magnetic transition is observed at 723 K, larger than that for γ-Fe_2O_3 and the transition temperature increases with increasing Zn concentration. For GFZ7, the magnetic transition is observed at 773 K, an increase of 100 K from that of the undoped sample.

To clarify whether there is a conversion of the γ-Fe_2O_3 phase to α-Fe_2O_3, the sample GFZ7 was heated in a furnace at 873 K for 2h in air atmosphere. The XRD patterns of GFZ7 before and after annealing are compared in Figure 5.17. It may be seen that

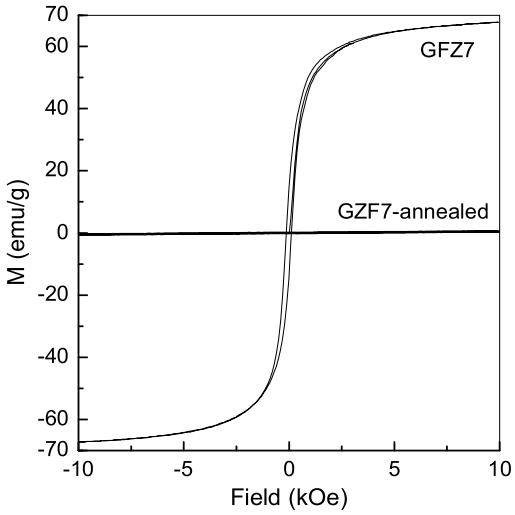

Figure 5.18: Variation of magnetization with applied field for GFZ7 and its air annealed powder sample.

the annealed sample shows the reflections from α-Fe_2O_3 and a ferrite phase. Detailed structural analysis revealed that the ferrite phase is $ZnFe_2O_4$. No trace of ZnO phase is seen in the pattern. Annealing destroys the maghemite phase and is converted to the hematite phase. The doped Zn ions form $ZnFe_2O_4$ instead of ZnO. It was found that the wt% of the two phases obtained from XRD analysis are comparable to the wt% of $ZnFe_2O_4$ and Fe_2O_3 formed from $Zn_{0.15}Fe_2O_3$. The room temperature magnetization data of the as-synthesized and annealed samples are compared in Figure 5.18. The annealed sample shows a paramagnetic like behavior. α-Fe_2O_3 is a very weak ferromagnet and shows almost antiferromagnetic behavior. Moreover, $ZnFe_2O_4$ is paramagnetic at room temperature. Thus the structural and magnetization data of the annealed samples reveal that the magnetic phase of the present samples synthesized by the GNP and doped with Zn is γ-Fe_2O_3, which is thermally more stable as compared to pure maghemite.

5.2.4 Conclusions

It is possible to synthesize Zn-doped γ-Fe_2O_3 nanoparticles using the solution combustion method. Doping of Zn suppresses the formation of antiferromagnetic α-Fe_2O_3 phase. With the increased amount of the dopant, the amount of the impurity phase formed is

reduced and becomes constant for more than 15 mole percent of Zn. Comparatively larger magnetization is observed for all the samples with higher coercivity, which are generally not observed for γ-Fe_2O_3 nanoparticles as reported earlier. Addition of Zn increases the phase transformation temperature of γ-Fe_2O_3 to α-Fe_2O_3, from 673 K to >773 K. Thus, the present method is useful for the synthesis of γ-Fe_2O_3 nanoparticles with negligible amount of impurity phase and higher transformation temperatures.

Chapter 6

Magnetic Nanocomposites

6.1 Polymer/Metal/Ferrite Nanocomposites

Polymer based magnetic composites with high magnetic permeabilities and high dielectric constants have drawn much attention recently because of their flexibility, compatibility with printed wiring boards, and their easy fabrication into various shapes. The main advantages of magneto-polymer composites are the ability to tailor materials for special purposes, low cost of production, availability to develop totally new material morphologies and device geometries, etc [236]. Most of the research work carried out on these composite materials are on bulk metals and ferrite particles and only few reports are available on the polymer based magnetic nanocomposite systems. In the three phase polymer/metal/magnetic-oxide composites, metal and metal oxide particles are added separately to the polymer matrix and is followed by hot molding or mixing [240, 245, 246, 443–446]. Several properties such as magnetic, dielectric, ferroelectric, conductivity, mechanical properties, etc. have been investigated on ferrite/polymer [238, 447–452], metal-metal oxide core-shell/polymer [453–455], and metal/polymer [456–459] composites. Out of these, some of the studies on the composites are related to nanosized metal particles and ferrite particles with polymers. In the polymer based magnetic composites, usually polypyrole, polyaniline, polymethylmethacrylate, polystyrene, teflon, poly (vinylidene fluoride), polyvinylchloride or polyvinyl alcohol is used as the polymer matrix.

There is a disadvantage in the processing methods of polymer/metal/ferrite nanocomposites if the metal and ferrite particles are added separately to the polymer matrix during the processing. In such cases, nonuniform mixing of metal and ferrite particles may occur and this may give rise to defective properties. To recover from this problem, in the present

study, metal/ferrite nanocomposites have been synthesized under *in situ* conditions and dispersed in the poly (vinylidene fluoride) (PVDF) polymer matrix. From our studies on ZnO based DMS systems synthesized by the glycine nitrate process, it was observed that metal nanoparticles are formed along with the oxides, as impurity phases. Based on these observations, we have used one of the component metal in excess than that required for the formation of the corresponding ferrite phase to get the metal/ferrite nanocomposite.

6.1.1 Synthesis

$Co/CoFe_2O_4$ and $Ni/NiFe_2O_4$ nanocomposites were synthesized by using the GNP method. 2 moles of $Co(NO_3)_2.6H_2O$ (or $Ni(NO_3)_2.6H_2O$) and 2 moles of $Fe(NO_3)_3.9H_2O$ were dissolved in minimum amount of distilled water and mixed thoroughly in a crystallizing dish. To the mixed solution of the metal nitrates, a water solution of glycine was added, taking 2 moles of glycine per mole of metal ion. The final mixed solution was evaporated on a hot plate till it forms a thick mass, which subsequently underwent autocombustion to give a fine powder. The as-synthesized powders were characterized for their different properties. For comparison of various properties of $Co/CoFe_2O_4$ and $Ni/NiFe_2O_4$ nanocomposites, single phase of $CoFe_2O_4$ and $NiFe_2O_4$ nanoparticles were also synthesized by the same procedure. For convenience, the as-synthesized $CoFe_2O_4$ and $NiFe_2O_4$ are coded as CFO and NFO and the composites $Co/CoFe_2O_4$ and $Ni/NiFe_2O_4$ are named as C-CFO and N-NFO, respectively.

Poly (vinylidene fluoride) (PVDF) was used as the polymer matrix in the present study, whose dielectric constant is around 10 [246]. PVDF is a better polymer, having melting point of 444 K, upper service temperature of 402 K and very low thermal conductivity (3.0 x 10^{-4} K/cm). The PVDF powder was ground thoroughly with the $CoFe_2O_4$ (CFO), $Co/CoFe_2O_4$ (C-CFO), $NiFe_2O_4$ (NFO) and $Ni/NiFe_2O_4$ (N-NFO) nanocomposites separately and then blended. The mixture was poured into a toroidal mold (toroids for the permeability measurements) and into a disk mold (pellets for dielectric measurements), and hot pressed at 473 K for 20 min. Silver electrodes were painted on both sides of the pellets for the dielectric measurements. Composites were made with different polymer to magnetic nanocomposites ratio. The compositions and ratios of polymer and metal/ferrite nanocomposites are given in Table 6.1 along with their various properties.

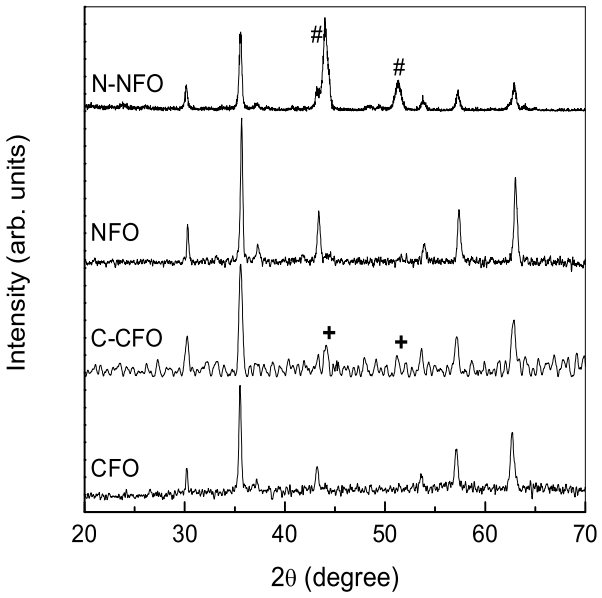

Figure 6.1: Powder XRD patterns of CFO, C-CFO, NFO and N-NFO. (+ Co and # Ni)

6.1.2 Results and discussions

The powder XRD patterns of CFO, C-CFO, NFO and N-NFO are shown in Figure 6.1. For CFO and NFO, all the reflections correspond to the spinel ferrites $CoFe_2O_4$ (JCPDS #22-1086) and $NiFe_2O_4$ (JCPDS #10-325), respectively. On the other hand, along with $CoFe_2O_4$, reflections from Co metal are seen in case of C-CFO (marked by + in the XRD pattern) in Figure 6.1. Similarly, along with $NiFe_2O_4$, reflections from Ni metal (marked by # in the XRD pattern) are seen in N-NFO. The average particle size of each phase is calculated from X-ray line broadening using the Scherrer formula, and is obtained as 34 nm for $CoFe_2O_4$ in CFO, 36 nm for $NiFe_2O_4$ in NFO, 29 nm and 35 nm for $CoFe_2O_4$ and Co phases in C-CFO, 35 nm and 59 nm for $NiFe_2O_4$ and Ni phases in N-NFO, respectively. Thus, X-ray diffraction studies make it clear that, the present GNP synthesis procedure gives metal/ferrite nanocomposites when the metal nitrates are taken in proper amounts during the combustion reaction.

Figure 6.2 shows the room temperature M–H curves of the different Co based nanocomposites. The as-synthesized samples are found to be highly magnetic. The magnetization of CFO indicates that the nanoparticles do not get saturated at 10 kOe and the observed

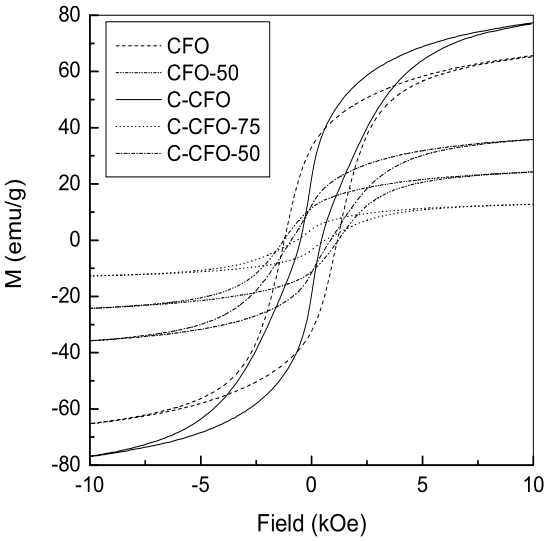

Figure 6.2: Magnetization as a function of magnetic field for the as-synthesized $CoFe_2O_4$ and $Co/CoFe_2O_4$, and their polymer composites, measured at room temperature. The numbers correspond to the wt% of the polymer in the composites.

M, 66 emu/g, is slightly less than the saturation magnetization of bulk $CoFe_2O_4$ [186]. This observation is due to the nanoparticle nature of CFO. Though the nanoparticles not saturated at 10 kOe, C-CFO has relatively higher magnetization than that of CFO. This is due to the presence of Co metal particles along with $CoFe_2O_4$, which is having higher saturation magnetization than that of cobalt ferrite. Magnetization decreases for the polymer based nanocomposites. This is expected because of the non-magnetic nature of the polymer. Higher coercivities are obtained for both polymer based composites. Out of the two compositions studied, CFO-50 shows the maximum coercivity, which is larger than that of CFO. Similar behavior of magnetization and enhanced coercivity has also been observed for the PVDF/Ni/$NiFe_2O_4$ nanocomposites. The M–H curves of the different PVDF/Ni/$NiFe_2O_4$ nanocomposites are shown in Figure 6.3. In this case also, relatively higher magnetization is observed for the as-synthesized Ni/$NiFe_2O_4$ nanocomposite as compared to that of $NiFe_2O_4$, due to the presence of Ni metal in the composite.

The M and H_c values of the different compositions are compared in Table 6.1. Figure 6.4 shows the variation of the magnetization and coercivity as a function of the polymer concentration. For both C-CFO and N-NFO composites, the variation in the

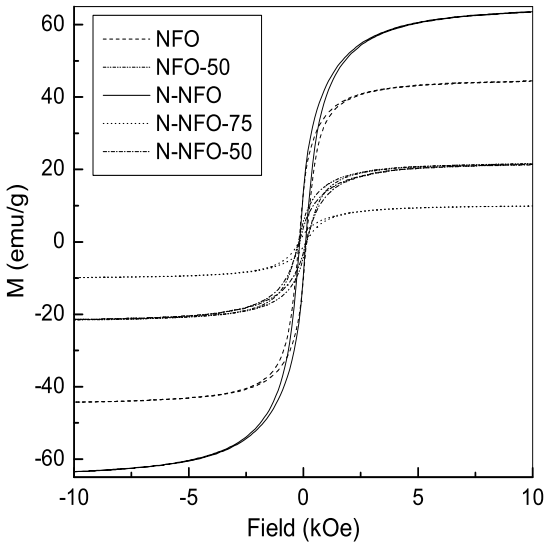

Figure 6.3: Magnetization as a function of magnetic field for the as-synthesized $NiFe_2O_4$ and $Ni/NiFe_2O_4$, and their polymer composites, measured at room temperature. The numbers correspond to the wt% of the polymer in the composites.

magnetization is almost linear, indicating that the metal/ferrite composite is uniformly mixed in the polymer matrix. In the case of simple ferrites (CFO and NFO), only one composition is studied. However, in this case also, enhanced coercivity is observed for both cobalt ferrite and nickel ferrite composites.

Similar observations as in the present work have been reported for iron-iron oxide-polymer composites [453] and Fe_3O_4-polymer composite [460]. Matutes-Aquino *et al.* observed the enhancement of coercivity for the strontium hexaferrite-polyvinyl chloride composites system, with increasing amount of polymer [461]. These observations have been interpreted in terms of a magnetizing-like effect due to the increasing magnetic interaction between the metal-ferrite particles as the mean interparticle distance decreases. Similar behavior observed for nickel ferrite-polymer composite has been explained in terms of the increased dipolar interactions between the particles causing a slower decay of the remanence and coercivity [462].

Typical microstructures of the polymer/metal/ferrite nanocomposites are shown in Figure 6.5. The $Co/CoFe_2O_4$ and $Ni/NiFe_2O_4$ nanocomposites are dispersed almost homogeneously in the polymer matrix. In all cases, the metal/ferrite nanocomposites are

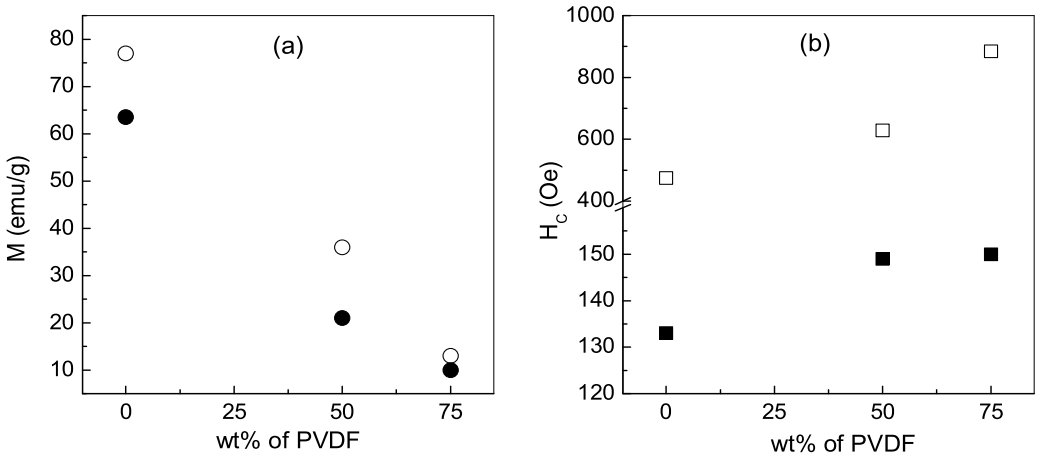

Figure 6.4: (a) Variation of the magnetization and (b) variation of the coercivity as a function of the polymer concentration for the magneto-polymer composites. Open symbols: C-CFO series and filled symbols: N-NFO series.

embedded inside the pores of the polymer matrices. Therefore, there is no direct link or connectivity between the nanocomposite clusters inside the polymer matrix. Shen *et al.* found an increase in the permeability of Ni/NiZn-ferrite/PVDF composite when the concentration of Ni metal is increased and this has been explained in terms of a double percolation effect [246].

Magnetic permeability

Figure 6.6 shows the permeability spectra of different polymer based nanocomposites along with the permeability spectra of C-CFO and N-NFO. There is a overall decrease in the permeability for the polymer based composites when compared to that of the metal composites. For all samples, permeability ($\mu_i^{'}$) increases with increasing frequency. The values of $\mu_i^{'}$ measured at 35 MHz are compared in Table 6.1. Higher values of permeability are obtained for C-CFO, as shown in Figure 6.6(a). Interestingly, $\mu_i^{'}$ is found to decrease with polymer loading. The decrease in the permeability with polymer loading for both $Co/CoFe_2O_4$ and $Ni/NiFe_2O_4$ composites can be explained in terms of the increased coercivity. It can be seen from Figure 6.4(b) that, these samples have higher coercivities (H_c) where H_c increases with increasing polymer content. Since higher

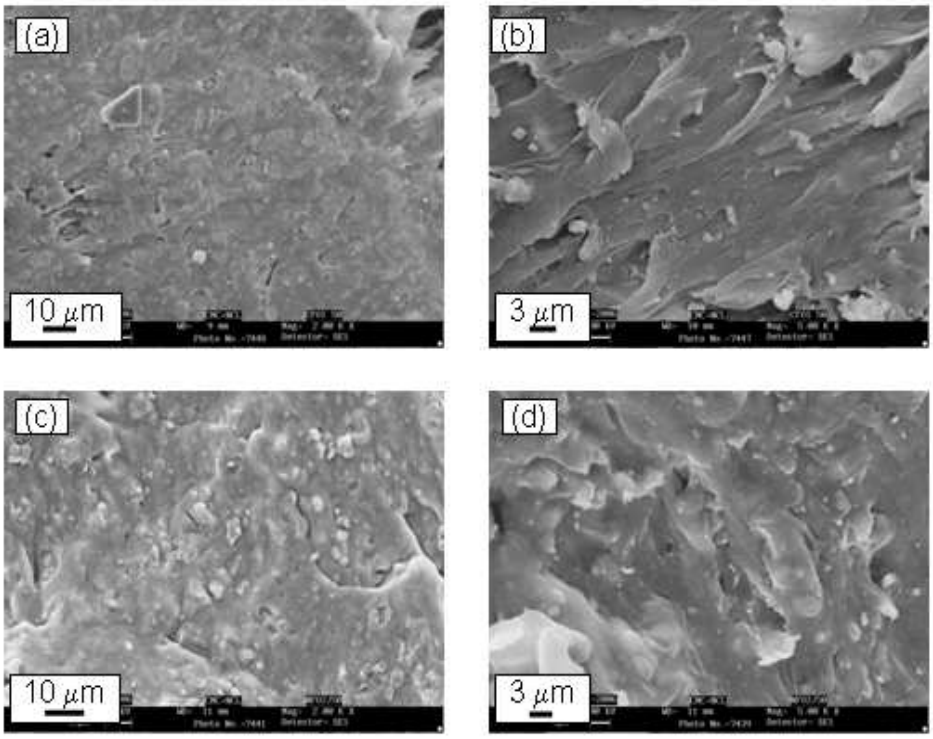

Figure 6.5: Cross sectional micrographs of C-CFO-50 (a,b) and NFO-50 (c,d) under two different magnifications.

Table 6.1: Summary of the properties of the samples produced in this (polymer/metal/ferrite nanocomposite) study.

Sample code	wt% of polymer	M (emu/g)	H_c (Oe)	$\mu^{'}$ at 35 MHz	$\epsilon^{'}$ at 1kHz
CFO	0	66	1195	–	–
CFO-50	50	24	1228	6.2	42
C-CFO	0	77	475	15.7	–
C-CFO-75	75	13	885	7.7	53
C-CFO-50	50	36	629	6.3	45
NFO	0	44.5	164	–	–
NFO-50	50	21	188	6.7	58
N-NFO	0	63.5	133	25	–
N-NFO-75	75	10	150	5	58
N-NFO-50	50	21	149	6.7	51

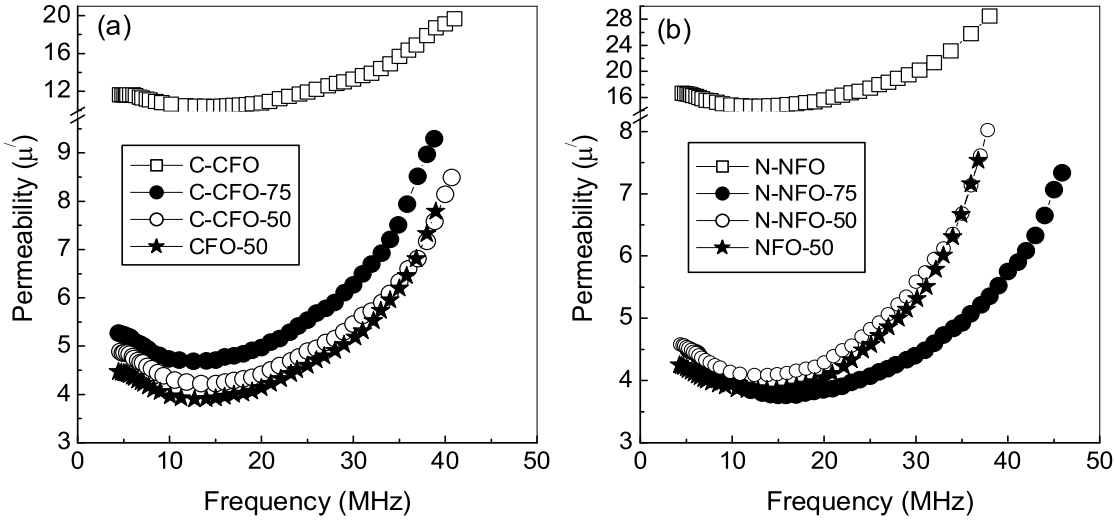

Figure 6.6: Variation of permeability with frequency for the samples (a) $Co/CoFe_2O_4$ and its polymer nanocomposites and (b) $Ni/NiFe_2O_4$ and its polymer nanocomposites.

coercivity means higher magnetocrystalline anisotropy energy of the system and the later is inversely proportional to $\mu_i^{'}$. Therefore, in the present case permeability reduces as the polymer content is increased.

Dielectric constant

The variation of the room temperature dielectric constant ($\epsilon^{'}$) of $PVDF/Co/CoFe_2O_4$ and $PVDF/Ni/NiFe_2O_4$ nanocomposites, as a function of the ac frequency, is shown in Figure 6.7. All the samples show almost identical behavior and similar trend. $\epsilon^{'}$ decreases with increasing ac frequency. Maximum $\epsilon^{'}$ is seen for all samples at the lowest frequency studied (200 Hz). $\epsilon^{'}$ values decreases with increasing frequency and reaches a minimum non-zero value at 2 MHz. The values of $\epsilon^{'}$ measured at 1 kHz are compared in Table 6.1. Similar trend of decreasing dielectric constant with increasing frequency have been observed for several polymer based magnetic composite systems [240, 245, 246, 446, 458].

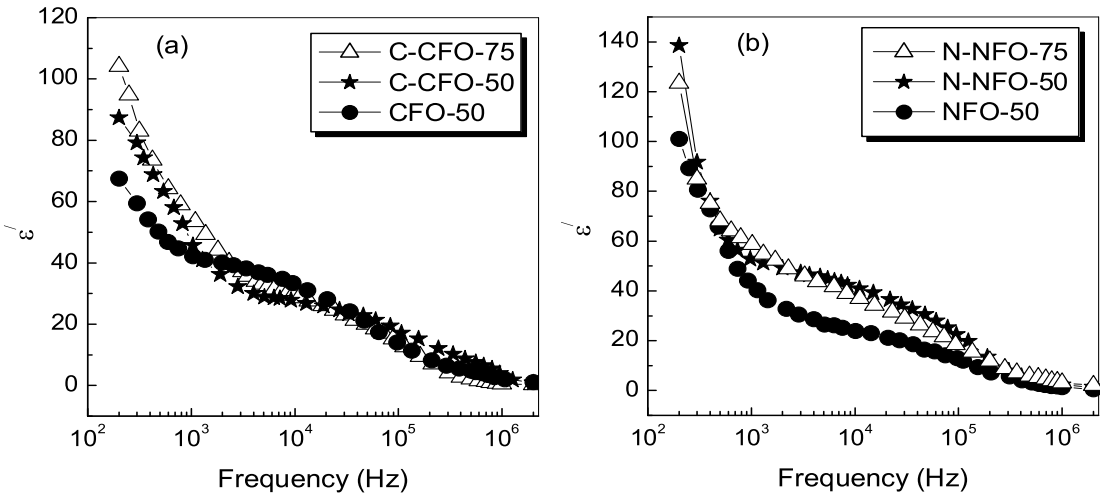

Figure 6.7: Variation of dielectric constant with frequency for samples (a) PVDF/Co/$CoFe_2O_4$ nanocomposites and (b) PVDF/Ni/$NiFe_2O_4$ nanocomposites.

6.1.3 Conclusions

Two phase nanocomposite, consisting of nanoparticles of a metal (Co or Ni) and a ferrite ($CoFe_2O_4$ or Ni_2O_4) could be synthesized by a simple single step process by the glycine nitrate autocombustion reaction. The metal/ferrite nanocomposite embedded in a PVDF matrix has been prepared by a simple hot-pressing method. The performance parameters obtained for these three-phase nanocomposite systems are comparable to the values reported in the literature for other similar systems. However, more studies are required to come to a specific conclusion on the results obtained, as studies on similar systems have not been reported. The objective of the present study was only to look at the feasibility of the synthesis of metal/ferrite nanocomposites and an initial evaluation of the properties of such composites.

6.2 Co/CoO/Co_3O_4 Nanocomposites

Co/CoO bilayer or composite system, consisting of ferromagnetic (FM) Co and antiferromagnetic (AFM) CoO, is known to exhibit exchange bias (EB) phenomenon. The exchange anisotropy in such systems originates from the interface coupling between the

ferromagnetic and the antiferromagnetic materials. In an external magnetic field, H, the magnetic moment of the FM component does not easily align along H, because the AFM layers do not well respond to H. This is manifested by a shift in the hysteresis loop (H_{eb}, exchange bias) along the field axis and an increased coercivity when the FM/AFM system is cooled in a magnetic field through the Neel temperature T_N of the AFM component [463]. This phenomenon, discovered in 1957 by Meiklejohn and Bean [464], has presently attracted extensive research interest because of the potential applications of such exchange biased materials in recording media, read heads, magnetic sensors and magnetoelectronic switching devices [465–468]. Several theoretical models have been proposed to explain the possible mechanisms of exchange bias [469–472]. Many phenomena related to EB have been investigated experimentally, such as the relationship between EB and the material's transport properties, the size dependence of the FM and AFM components on such properties, temperature dependence of exchange anisotropy, magnetoresistance, etc. Almost all of the materials studied for this purpose are in the form of thin film bilayers [248–252]. There are very few studies reported on Co/CoO nanoparticles or clusters [463, 473, 474]. Sumiyama *et al.* recently reported the observation of H_{eb} as high as 8.1×10^5 A/m at 5 K for Co/CoO coreshell cluster assemblies with the mean cluster size of 6 nm [475].

In the present study, we have extended our attempts to synthesize Co/CoO nanocomposite in the polycrystalline form, following the glycine nitrate process of autocombustion, based on the results obtained on the DMS materials.

6.2.1 Synthesis

The GNP is used to synthesized Co/CoO nanocomposite system. 1 mole of $Co(NO_3)_2.6H_2O$ was dissolved in minimum amount of distilled water. To the solution of the metal nitrate, a water solution of glycine was added, taking 2 moles of glycine per mole of metal ion. The autocombustion reaction was carried out as described in *section 2.2.* Further samples were made by adding excess nitrate ions in the solution, to study the effect of varying the glycine to nitrate ratio on the properties of the product. Therefore, varying amounts of dilute nitric acid (0–7 ml of 4 N HNO_3) was added to the mixed solution of cobalt nitrate and glycine and the autocombustion reaction was carried out. For convenience,

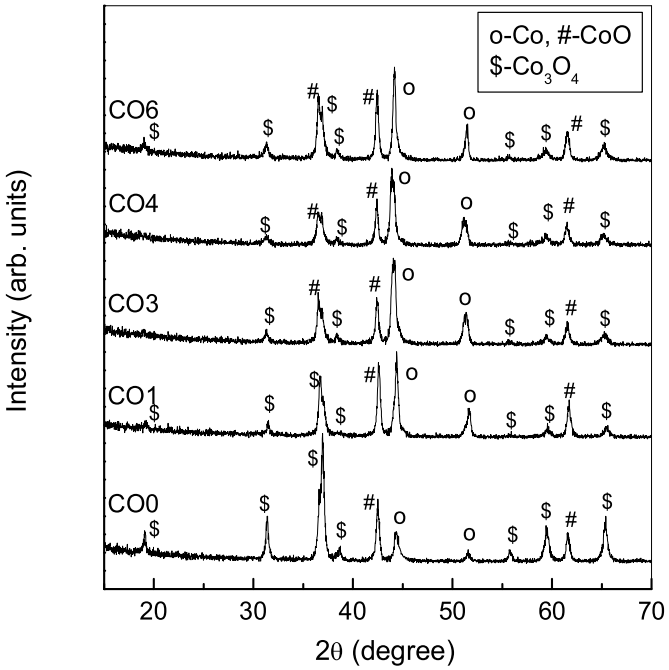

Figure 6.8: Powder XRD patterns of CO0, CO1, CO3, CO4, and CO6.

the samples are named as COn where n stands for the volume of nitric acid used and varies from 0 ml to 7 ml.

6.2.2 Results and discussions

Figure 6.8 shows the powder XRD patterns of some of the as-synthesized samples. As expected, Co and CoO are obtained from the autocombustion reaction. However, reflections from Co_3O_4 are also observed in the XRD pattern of CO0. Interestingly more intense peaks of Co are observed when nitric acid is added before the synthesis and the intensities of the reflections from Co_3O_4 are decreased. The amount of Co formed is found to increase with increasing amount of added HNO_3. Highest amount of Co content is obtained when 3 ml of 4N nitric acid was used. Addition of excess HNO_3 leads to the formation of more CoO and Co_3O_4 and less Co metal as seen for CO6 in Figure 6.8. The fractions and the average particle sizes of all the three components calculated from the XRD patterns are given in Table 6.2.

Some annealing studies were carried out on sample CO4 to look at the changes in the

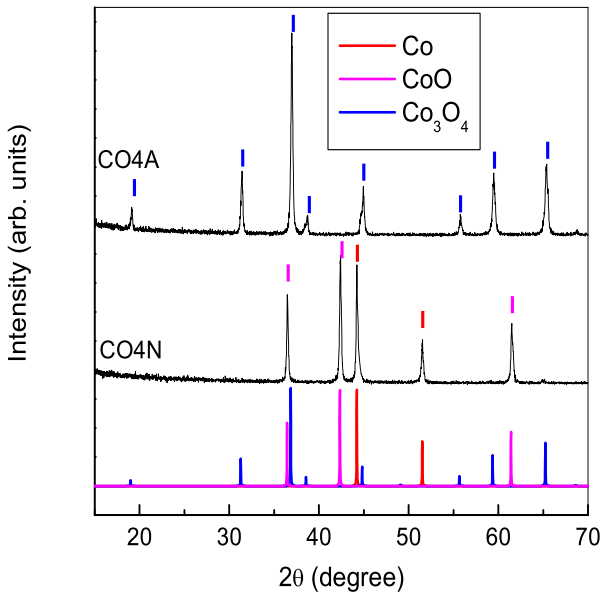

Figure 6.9: Comparison of powder XRD patterns of CO4N and CO4A with that of simulated XRD patterns of Co, CoO and Co_3O_4.

structural, compositional and magnetic properties of this sample. A part of CO4 powder was annealed in a N_2 atmosphere at 773 K for 6 h (sample code CO4N) and another part of the sample was annealed in air (sample code CO4A) at the same temperature and duration. The powder XRD patterns of the air and nitrogen annealed samples are compared in Figure 6.9, along with the simulated XRD patterns of Co, CoO and Co_3O_4. It may be seen that the air annealed sample is completely converted to Co_3O_4, whereas, the nitrogen annealed sample contains only *fcc* Co and *fcc* CoO [130]. The Co_3O_4 present in CO4 is reduced and completely transformed to CoO when the sample was annealed for 6 h in a N_2 atmosphere. The average particle size of Co and CoO in the reduced sample is found to be 68 and 54 nm, respectively.

Figure 6.10 shows the magnetization (M) of the different nanocomposites, as a function of magnetic field, measured at room temperature. The magnetization at 10 kOe and the coercivity values are given in Table 6.2. Magnetization increases with increasing Co content, as expected, as both CoO and Co_3O_4 are paramagnetic at and above room temperature (T_N of CoO and Co_3O_4 are 291 K [94] and 40 K [343], respectively). Therefore, the highest M is obtained for the sample CO3, where the wt% of Co nanoparticles is

Table 6.2: Summary of the properties of the samples produced in this ($Co/CoO/Co_3O_4$ nanocomposite) study.

Sample	M	H_c	particle size (nm)			wt% from XRD		
code	(emu/g)	(Oe)	Co	CoO	Co_3O_4	Co	CoO	Co_3O_4
CO0	17	185	24	27	35	7	27	66
CO1	56	137	32	28	32	25	45	30
CO2	58	132	22	27	38	30	30	40
CO3	69	119	16	27	24	39	28	33
CO4	68	116	18	27	32	38	30	32
CO5	56	120	23	28	33	26	32	42
CO6	45	127	28	22	29	24	36	40
CO7	22	151	30	30	36	10	35	55

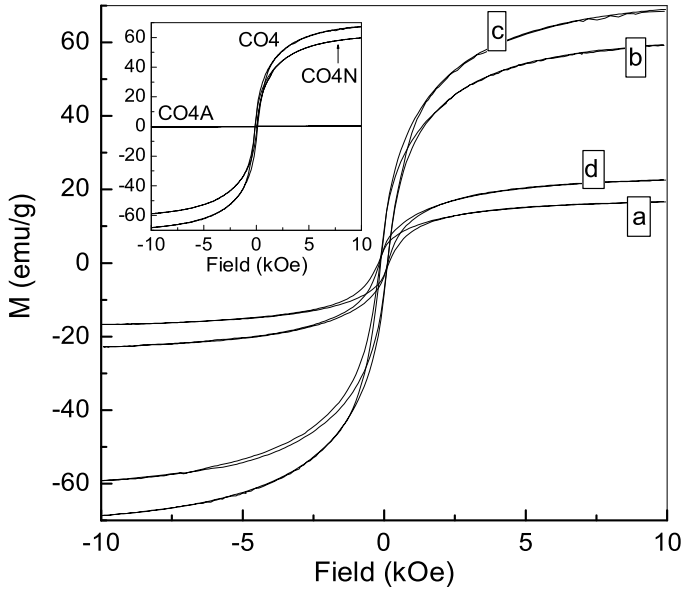

Figure 6.10: Magnetization curves, measured at room temperature for the samples a) CO0, b) CO2, c) CO3 and d) CO7. Inset: M–H curves of CO4, CO4A and CO4N at room temperature.

maximum. The M–H curves of CO4, CO4N and CO4A, measured at room temperature, are compared in the inset of Figure 6.10. CO4A shows only paramagnetic behaviour, as Co_3O_4 is paramagnetic at or above room temperature [343]. CO4N remains ferromagnetic, and the magnetization and coercivity values are found to decrease slightly as compared to that of CO4. The M and H_c of CO4N are found to be 60 emu/g and 86 Oe, respectively. The decrease in H_c is likely to be due to the increased particle size of Co (from 18 nm to 68 nm) and the decrease in M is likely to be due to the oxidation of minor amount of Co due to the oxygen impurities in the N_2 gas used.

6.2.3 Conclusions

Preliminary studies showed that Co/CoO/Co_3O_4 nanocomposites with varying amounts of the components can be synthesized by the glycine nitrate process and by controlling the glycine to nitrate ratio. Also, Co/CoO nanocomposite can be obtained by the partial reduction of the as-synthesized composite containing Co_3O_4. More studies are required to understand the mechanism of formation of the nanocomposites and detailed magnetic studies are required to see whether the composites show exchange bias or not.

Bibliography

[1] *Nanoscale Materials in Chemistry*, Ed. by K. J. Klabunde, (Wiley-Interscience, New york, 2001).

[2] P. M. Ajayan, L. S. Schadler and P. V. Braun, *Nanocomposite Science and Technology*, (Wiley-VCH GmbH & Co. KGaA, Weinheim, 2003).

[3] *Nanoparticles: Building Blocks for Nanotechnology*, Ed. by V. Rotello, *Nanostructure Science and Technology Series*, (Springer, New York, 2004).

[4] G. Cao, *Nanostructures & Nanomaterials: Synthesis, Properties and Applications*, (Imperial College Press, London, 2004).

[5] *Nanoscale Science and Technology*, Ed. by R. Kelsall, I. Hamley and M. Geoghegan, (John Wiley & Sons, Ltd, West Sussex, 2005).

[6] G. Fasol, *Science* 280 (1998) 545.

[7] A. Thiaville and J. Miltat, *Science* 284 (1999) 1939.

[8] H. Gleiter, *Adv. Mater.* 4, (1992) 474.

[9] G. A. Ozin, *Adv. Mater.* 4, (1992) 612.

[10] M. N. Rittner and T. Abraham, *Am. Ceram. Soc. Bul.* 76 (1997) 51.

[11] H. Verweij, *Adv. Mater.* 10 (1998) 1483.

[12] U. Simon, *Adv. Mater.* 10 (1998) 1487.

[13] F. J. Himpsel, J. E. Ortega, G. J. Mankey and R. F. Willis, *Adv. Phys.* 47 (1998) 511.

[14] M. E. McHenry, M. A. Willard and D. E. Laughlin, *Prog. Mater. Sci.* 44 (1999) 291.

[15] P. Moriarty, *Rep. Prog. Phys.* 64 (2001) 297.

[16] M. L. Cohen, *Mater. Sci. Eng. C* 15 (2001) 1.

[17] K. L. Kelly, E. Coronado, L. L. Zhao and G. C. Schatz, *J. Phys. Chem. B* 107 (2003) 668.

[18] K. Raj and R. Moskowitz, *J. Magn. Magn. Mater.* 85 (1990) 233.

[19] P. Rice and J. Moreland, *Rev. Sci. Instrum.* 62 (1991) 844.

[20] Q. A. Pankhurst and R. J. Pollard, *J. Phys.: Condens. Matter* 5 (1993) 8487.

[21] K. V. P. M. Shafi, A. Gedanken and R. Prozorov, *Adv. Mater.* 10 (1998) 590.

[22] P. Toneguzzo, G. Viau, O. Acher, F. Fievet-Vincent and F. Fievet, *Adv. Mater.* 10 (1998) 1032.

[23] N. Toshima and T. Yonezawa, *New J. Chem.* 22 (1998) 1179.

[24] S. Chen, R. S. Ingram, M. J. Hostetler, J. J. Pietron, R. W. Murray, T. G. Schaaff, J. T. Khoury, M. M. Alvarez and R. L. Whetten, *Science* 280 (1998) 2098.

[25] A. N. Shipway, E. Katz and I. Willner, *ChemPhysChem* 1 (2000) 18.

[26] P. Gomez-Romero, *Adv. Mater.* 13 (2001) 163.

[27] P. V. Kamat, *J. Phys. Chem. B* 106 (2002) 7729.

[28] I. Brigger, C. Dubernet and P. Couvreur, *Adv. Drug Delivery Rev.* 54 (2002) 631.

[29] M. C. Daniel and D. Astruc, *Chem. Rev.* 104 (2004) 293.

[30] D. Wang and H. Mohwald, *J. Mater. Chem.* 14 (2004) 459.

[31] E. Matejivic, *MRS Bull.* 14 (1989) 18.

[32] C. A. Ross, H. I. Smith, T. Savas, M. Schattenburg, M. Farhoud, M. Hwang, M. Walsh, M. C. Abraham and R. J. Ram, *J. Vac. Sci. Technol. B* 17 (1999) 3168.

[33] B. D. Terris and T. Thomson, *J. Phys. D: Appl. Phys.* 38 (2005) R199.

[34] R. D. McMichael, R. D. Shull, L. J. Swartzendruber, L. H. Bennett and R. E. Watson, *J. Magn. Magn. Mater.* 111 (1992) 29.

[35] Y. Z. Shao, J. K. L. Lai and C. H. Shek, *J. Magn. Magn. Mater.* 163 (1996) 103.

[36] D. L. Graham, H. A. Ferreira and P. P. Freitas, *Trends Biotech.* 22 (2004) 455.

[37] J. Shi, Y. Zhu, X. Zhang, W. R. G. Baeyens and A. M. Garca-Campaa, *TrAC Trends Anal. Chem.* 23 (2004) 351.

[38] K. K. Jain, *Drug Discovery Today,* 10 (2005) 1435.

[39] M. J. Toohey, *Sensors Actuators B: Chem.* 105 (2005) 232.

[40] L. Murphy, *Current Opinion Chem. Bio.* 10 (2006) 177.

[41] S. A. Agnihotri, N. N. Mallikarjuna and T. M. Aminabhavi, *J. Controlled Release,* 100 (2004) 5.

[42] T. C. Yih and M. Al-Fandi, *J. Cell. Biochem.* 97 (2006) 1184.

[43] L. E. van Vlerken and M. M. Amiji, *Expert Opin. Drug Deliv.* 3 (2006) 205.

[44] A. K. Gupta and A. S. G. Curtis, *J. Mater. Sci.: Mater. Med.* 15 (2004) 493.

[45] A. Ito, M. Shinkai, H. Honda and T. Kobayashi, *J. Biosci. Bioeng.* 100 (2005) 1.

[46] C. A. Mirkin, R. L. Letsinger, R. C. Mucic and J. J. Storhoff, *Nature* 382 (1996) 607.

[47] A. P. Alivisatos, K. P. Johnson, X. Peng, T. E. Wilson, C. J. Loweth, M. P. Bruchez and P. G. Schultz, *Nature* 382 (1996) 609.

[48] K. Keis, L. Vayssieres, S.E. Lindquist and A. Hagfeldt, *NanoStruct. Mater.* 12 (1999) 487.

[49] K. Grieve, P. Mulvaney and F. Grieser, *Curr. Opin. Colloid Interface Sci.* 5 (2000) 168.

[50] S. Barazzouk and S. Hotchandani, *J. Appl. Phys.* 96 (2004) 7744.

[51] S. M. Ponder, J. G. Darab and T. E. Mallouk, *Environ. Sci. Technol.* 34 (2000) 2564.

[52] D. W. Elliott and W.-X. Zhang, *Environ. Sci. Technol.* 35 (2001) 4922.

[53] J. Hu, G. Chen and I. M. C. Lo, *Water Res.* 39 (2005) 4528.

[54] P. Jain and T. Pradeep, *Biotechnol. Bioeng.* 90 (2005) 59.

[55] M. Kralik and A. Biffis, *J. Mol. Catal. A: Chem.* 177 (2001) 113.

[56] Y. Niu and R. M. Crooks, *Comptes Rendus Chimie* 6 (2003) 1049.

[57] Y. Shen, C. S. Friend, Y. Jiang, D. Jakubczyk, J. Swiatkiewicz and P. N. Prasad, *J. Phys. Chem. B* 104 (2000) 7577.

[58] Y. Shen and P. N. Prasad, *Appl. Phys. B: Lasers and Optics* 74 (2002) 641.

[59] P. N. Prasad, *Molecular Crys. Liquid Crys.* 466 (2006) 1.

[60] X. Zhang, B. Sun, R. H. Friend, H. Guo, D. Nau and H. Giessen *Nano Lett.* 6 (2006) 651.

[61] S. A. Majetich, J. H. Scott, E. M. Kirkpatrick, K. Chowdary, K. Gallagher and M. E. McHenry, *NanoStruct. Mater.* 9 (1997) 291.

[62] F. E. Kruis, H. Fissan and A. Peled, *J. Aerosol Sci.* 29 (1998) 511.

[63] T. Thurn-Albrecht, J. Schotter, G. A. Kastle, N. Emley, T. Shibauchi, L. Krusin-Elbaum, K. Guarini, C. T. Black, M. T. Tuominen and T. P. Russell, *Science* 290 (2000) 2126.

[64] A. E. Berkowitz, R. H. Kodama, S. A. Makhlouf, F. T. Parker, F. E. Spada, E. J. McNiff Jr. and S. Foner, *J. Magn. Magn. Mater.* 196 (1999) 591.

[65] R. H. Kodama, *J. Magn. Magn. Mater.* 200 (1999) 359.

[66] T. Bala, S. D. Bhame, P. A. Joy, B. L. V. Prasad and M. Sastry, *J. Mater. Chem.* 14 (2004) 2941.

[67] A. Kale, S. Gubbala and R. D. K. Misra, *J. Magn. Magn. Mater.* 277 (2004) 350.

[68] G. Gundiah, N. S. John, P. J. Thomas, G. U. Kulkarni, C. N. R. Rao and S. Heun, *Appl. Phys. Lett.* 84 (2004) 5341.

[69] A. Bharde, A. Wani, Y. Shouche, P. A. Joy, B. L. V. Prasad, M. Sastry, *J. Am. Chem. Soc.* 127 (2005) 9326.

[70] S. S. P. Parkin, N. More and K. P. Roche, *Phys. Rev. Lett.* 64 (1990) 2304.

[71] E. M. Chudnovsky and L. Gunther, *Phys. Rev. Lett.* 60 (1988) 661.

[72] F. T. Parker, F. E. Spada, T. J. Cox and A. E. Berkowitz, *J. Magn. Magn. Mater.* 162 (1996) 122.

[73] M. H. Sousa, F. A. Tourinho, J. Depeyrot, G. J. da Silva and M. C. F. L. Lara, *J. Phys. Chem. B* 105 (2001) 1168.

[74] D. Kechrakos, K. N. Trohidou and J. A. Blackman, *Phys. Rev. B* 63 (2001) 134422.

[75] G. A. Fiete, G. Zarand, B. I. Halperin and Y. Oreg, *Phys. Rev. B* 66 (2002) 024431.

[76] G. Shemer and G. Markovich, *J. Phys. Chem. B* 106 (2002) 9195.

[77] L. X. Tiefenauer, A. Tschirky, G. Khne and R. Y. Andres, *Magn. Res. Imag.* 14 (1996) 391.

[78] L. Josephson, J. M. Perez, R. Weissleder, *Angew. Chem. Int. Ed. Engl.* 40 (2001) 3204.

[79] O. Mykhaylyk, A. Cherchenko, A. Ilkin, N. Dudchenko, V. Ruditsa, M. Novoseletz and Yu. Zozulya, *J. Magn. Magn. Mater.* 225 (2001) 241.

[80] P. Jezzard and R. B. Buxton, *J. Magn. Res. Imag.* 23 (2006) 787.

[81] D. A. Schwartz, N. S. Norberg, Q. P. Nguyen, J. M. Parker and D. R. Gamelin, *J. Am. Chem. Soc.* 125 (2003) 13205.

[82] N. S. Norberg, K. R. Kittilstved, J. E. Amonette, R. K. Kukkadapu, D. A. Schwartz and D. R. Gamelin, *J. Am. Chem. Soc.* 126 (2004) 9387.

[83] B. D. Cullity, *Introduction to Magnetic Materials*, (Addison-Wesley Pub. Company, Massachusetts, 1972).

[84] A. R. West, *Solid State Chemistry and its Applications*, (John Wiley & Sons, Singapore, 2003).

[85] *Ferrite Materials: Science and technology*, Ed. B. Viswanathan, and V. R. K. Murthy (Narosa Publishing House, New Delhi, 1990).

[86] R. Wood, *IEEE Trans. Magnet.* 36 (2000) 36.

[87] D. E. Speliotis, *J. Magn. Magn. Mater.* 193 (1999) 29.

[88] R. Hergt, W. Andra, C. G. d'Ambly, I. Hilger, W. A. Kaiser, U. Richter and H.-G. Schmidt, *IEEE Trans. Magnet.* 34 (1998) 3745.

[89] X. Batlle and A. Labarta, *J. Phys. D: Appl. Phys.* 35 (2002) R15.

[90] A. Moser, K. Takano, D. T. Margulies, M. Albrecht, Y. Sonobe, Y. Ikeda, S. Sun and E. E. Fullerton, *J. Phys. D: Appl. Phys.* 35 (2002) R157.

[91] V. Skumryev, S. Stoyanov, Y. Zhang, G. Hadjipanayis, D. Givord and J. Nogues, *Nature* 423 (2003) 850.

[92] J. L. Dormann, D. Fiorani and E. Tronc, *J. Magn. Magn. Mater.* 202 (1999) 251.

[93] F. Pfeifer and C. Radeloff, *J. Magn. Magn. Mater.* 19 (1980) 190.

[94] J. B. Goodenough, *Magnetism and Chemical Bond* (John Wiley & Sons: New York, 1963).

[95] C. Zener, *Phys. Rev.* 82 (1951) 000403.

[96] J. K. Furdyna, *J. Appl. Phys.* 64 (1988) R29.

[97] H. Ohno, H. Munekata, T. Penney, S. von Molnar and L. L. Chang, *Phys. Rev. Lett.* 68 (1992) 2664.

[98] H. Ohno, A. Shen, F. Matsukura, A. Oiwa, A. Endo, S. Katsumoto and Y. Iye, *Appl. Phys. Lett.* 69 (1996) 363.

[99] G. A. Prinz, *Science* 282 (1998) 1660.

[100] S. J. Pearton, C. R. Abernathy, M. E. Overberg, G. T. Thaler, D. P. Norton, N. Theodoropoulou, A. F. Hebard, Y. D. Park, F. Ren, J. Kim and L. A. Boatner, *J. Appl. Phys.* 93 (2003) 1.

[101] W. Prellier, A. Fouchet and B. Mercey, *J. Phys.: Condens. Matter* 15 (2003) R1583.

[102] T. Fukumura, Y. Yamada, H. Toyosaki, T. Hasegawa, H. Koinuma and M. Kawasaki, *Appl. Surf. Sci.* 223 (2004) 62.

[103] I. Zutic, J. Fabian and S. D. Sarma, *Rev. Mod. Phys.* 76 (2004) 323.

[104] (a) R. Srinivasan, *Resonance* 10 (9), (2005) 53. (b) R. Srinivasan, *Resonance* 10 (11), (2005) 8.

[105] R. Janisch, P. Gopal and N. A. Spaldin, *J. Phys.: Condens. Matter* 17 (2005) R657.

[106] S. A. Wolf, A. Y. Chtchelkanova and D. M. Treger, *IBM J. Res. Dev.* 50 (2006) 101.

[107] A. V. Esch, L. V. Bockstal, J. D. Boeck, G. Verbanck, A. S. van Steenbergen, P. J. Wellmann, B. Grietens, R. Bogaerts, F. Herlach and G. Borghs, *Phys. Rev. B* 56 (1997) 13103.

[108] F. Matsukura, H. Ohno, A. Shen and Y. Sugawara, *Phys. Rev. B* 57 (1998) R2037.

[109] T. Hayashi, M. Tanaka, K. Seto, T. Nishinaga, H. Shimada and K. Ando, *J. Appl. Phys.* 83 (1998) 6551.

[110] T. M. Pekarek, B. C. Crooker, I. Miotkowski and A. K. Ramdas, *J. Appl. Phys.* 83 (1998) 6557.

[111] B. Beschoten, P. A. Crowell, I. Malajovich and D. D. Awschalom, *Phys. Rev. Lett.* 83 (1999) 3073.

[112] H. Ohno, *Science* 281 (1998) 951.

[113] P Kacman, *Semicond. Sci. Technol.* 16 (2001) R25.

[114] C. Liu, F. Yun and H. Morko, *Mater. Electronics* 16 (2005) 555.

[115] S. von Molnar, *J. Superconductivity* 16 (2003) 1.

[116] L. S. Dorneles, D. O'Mahony, C. B. Fitzgerald, F. McGee, M. Venkatesan, I. Stanca, J. G. Lunney and J. M. D. Coey, *Appl. Surf. Sci.* 248 (2005) 406.

[117] M. B. Haider, R. Yang, H. Al-Brithen, C. Constantin, D. C. Ingram, A. R. Smith, G. Caruntu and C. J. O'Connor, *J. Crys. Growth* 285 (2005) 300.

[118] H. Akai, *Phys. Rev. Lett.* 81 (1998) 3002.

[119] A. J. Blattner, P. L. Prabhumirashi, V. P. Dravid and B.W. Wessels, *J. Crys. Growth* 259 (2003) 8.

[120] A. Ney, R. Rajaram, R. F. C. Farrow, J. S. Harris Jr. and S. S. P. Parkin, *J. Superconductivity* 18 (2005) 41.

[121] P. P. Chen, H. Makino and T. Yao, *Solid State Commun.* 130 (2004) 25.

[122] R. Fiederling, M. Keim, G. Reuscher, W. Ossau, G. Schmidt, A. Waag and L. W. Molenkamp, *Nature* 402 (1999) 787.

[123] Y. Ohno, D. K. Young, B. Beschoten, F. Matsukura, H. Ohno and D. D. Awschalom, *Nature* 402 (1999) 790.

[124] J. Schneider, U. Kaufmann, W. Wilkening, M. Baeumler and F. Kohl, *Phys. Rev. Lett.* 59 (1987) 240.

[125] J. Okabayashi, A. Kimura, O. Rader, T. Mizokawa A. Fujimori, T. Hayashi and M. Tanaka, *Phys. Rev.* 58 (1998) R4211.

[126] K. Sato and H. Katayama-Yoshida, *Jpn. J. Appl. Phys. part 2* 39 (2000) L555.

[127] Yu. Uspenskii, E. Kulatov, H. Mariette, H. Nakayama and H. Ohta, *J. Magn. Magn. Mater.* 258-259 (2003) 248.

[128] T. Dietl, H. Ohno, F. Matsukura, J. Cibert and D. Ferrand, *Science* 287 (2000) 1019.

[129] C.-H. Chien, S. H. Chiou, G. Y. Guo and Y.-D. Yao, *J. Magn. Magn. Mater.* 282 (2004) 275.

[130] F. S. Galasso, *Structure and Properties of Inorganic Solids*, (Pergamon Press, Oxford, 1970).

[131] K. Ueda, H. Tabata and T. Kawai, *Appl. Phys. Lett.* 79 (2001) 988.

[132] H.-J. Lee, S.-Y. Jeong, C. R. Cho and C. H. Park, *Appl. Phys. Lett.* 81 (2002) 4020.

[133] H. Saeki, H. Tabata and T. Kawai, *Solid State Commun.* 120 (2001) 439.

[134] P. Sharma, A. Gupta, K. V. Rao, F. J. Owens, R. Sharma, R. Ahuja, J. M. O. Guillen, B. Johansson and G. A. Gehring, *Nature Mater.* 2 (2003) 673.

[135] W. Prellier, A. Fouchet, B. Mercey, Ch. Simon and B. Raveau, *Appl. Phys. Lett.* 82 (2003) 3490.

[136] S.-W. Lim, D.-K. Hwang and J.-M. Myoung, *Solid State Commun.* 125 (2003) 231.

[137] D. A. Schwartz and D. R. Gamelin, *Adv. Mater.* 16 (2004) 2115.

[138] S. Ramachandran, A. Tiwari and J. Narayan, *Appl. Phys. Lett.* 84 (2004) 5255.

[139] H.-Ta. Lin, T.-S. Chin, J.-C. Shih, S.-H. Lin, T.-M. Hong, R.-T. Huang, F.-R. Chen and J.-J. Kai, *Appl. Phys. Lett.* 85 (2004) 621.

[140] M. Venkatesan, C. B. Fitzgerald, J. G. Lunney and J. M. D. Coey, *Phys. Rev. Lett.* 93 (2004) 177206.

[141] G. Pei, C. Xia, S. Cao, J. Zhang, F. Wu and J. Xu, *J. Magn. Magn. Mater.* 302 (2006) 340.

[142] D. P. Joseph, S. Ayyappan and C. Venkateswaran, *J. Alloy. Comp.* 415 (2006) 225.

[143] W. H. Brumage, C. F. Dorman and C. R. Quade, *Phys. Rev. B* 63 (2001) 104411.

[144] Z. Jin, T. Fukumura, M. Kawasaki, K. Ando, H. Saito, T. Sekiguchi, Y. Z. Yoo, M. Murakami, Y. Matsumoto, T. Hasegawa and H. Koinuma, *Appl. Phys. Lett.* 78 (2001) 3824.

[145] A. S. Risbud, N. A. Spaldin, Z. Q. Chen, S. Stemmer and R. Seshadri, *Phys. Rev. B* 68 (2003) 205202.

[146] J. H. Kim, H. Kim, D. Kim, S. G. Yoon and W. K. Choo, *Solid State Commun.* 131 (2004) 677.

[147] G. Lawes, A. S. Risbud, A. P. Ramirez and R. Seshadri, *Phys. Rev. B* 71 (2005) 045201.

[148] C. N. R. Rao and F. L. Deepak, *J. Mater. Chem.* 15 (2005) 573.

[149] J. H. Shim, T. Hwang, S. Lee, J. H. Park, S.-J. Han and Y. H. Jeong, *Appl. Phys. Lett.* 86 (2005) 082503.

[150] M. H. Kane, K. Shalini, C. J. Summers, R. Varatharajan, J. Nause, C. R. Vestal, Z. J. Zhang and I. T. Ferguson, *J. Appl. Phys.* 97 (2005) 023906.

[151] J. Alaria, H. Bieber, S. Colis, G. Schmerber and A. Dinia, *Appl. Phys. Lett.* 88 (2006) 112503.

[152] K. Rode, A. Anane, R. Mattana, J.-P. Contour, O. Durand and R. LeBourgeois, *J. Appl. Phys.* 93 (2003) 7676.

[153] S. W. Yoon, S.-B. Cho, S. C. We, S. Yoon, B. J. Suh, H. K. Song and Y. J. Shin, *J. Appl. Phys.* 93 (2003) 7879.

[154] B. Martinez, F. Sandiumenge, Ll. Balcells, J. Arbiol, F. Sibieude and C. Monty, *Appl. Phys. Lett.* 86 (2005) 103113 .

[155] J. H. Kim, H. Kim, D. Kim, Y. E. Ihm and W. K. Choo, *J. Appl. Phys.* 92 (2002) 6066.

[156] D. C. Kundaliya, S. B. Ogale, S. E. Lofland, S. Dhar, C. J. Metting, S. R. Shinde, Z. Ma, B. Varughese, K. V. Ramanujachary, L. Salamanca-Riba and T. Venkatesan, *Nature Mater.* 3 (2004) 709.

[157] J. H. Park, M. G. Kim, H. M. Jang, S. Ryu and Y. M. Kim, *Appl. Phys. Lett.* 84 (2004) 1338.

[158] H.-J. Lee, C. H. Park, S.-Y. Jeong, K.-J. Yee, C. R. Cho, M.-H. Jung and D. J. Chadi, *Appl. Phys. Lett.* 88 (2006) 062504 .

[159] S. A. Chambers, S. Thevuthasan, R. F. C. Farrow, R. F. Marks, J. U. Thiele, L. Folks, M. G. Samant, A. J. Kellock, N. Ruzycki, D. L. Ederer and U. Diebold, *Appl. Phys. Lett.* 79 (2001) 3467.

[160] Y. Matsumoto, M. Murakami, T. Shono, T. Hasegawa, T. Fukumura, M. Kawasaki, P. Ahmet, T. Chikyow, S.-Y. Koshihara and H. Koinuma, *Science* 291 (2001) 854.

[161] P. A. Stampe, R. J. Kennedy, Y. Xin and J. S. Parker, *J. Appl. Phys.* 92 (2002) 7114.

[162] Z. Wang, W. Wang, J. Tang, L. D. Tung, L. Spinu and W. Zhou, *Appl. Phys. Lett.* 83 (2003) 518.

[163] Z. Wang, J. Tang, Y. Chen, L. Spinu, W. Zhou and L. D. Tung, *J. Appl. Phys.* 95 (2004) 7384.

[164] D. Wu, Y. Chen, J. Liu, X. Zhao, A. Li and N. Ming, *Appl. Phys. Lett.* 87 (2005) 112501.

[165] T. C. Kaspar, T. Droubay, C. M. Wang, S. M. Heald, A. S. Lea and S. A. Chambers, *J. Appl. Phys.* 97 (2005) 073511.

[166] R. Suryanarayanan, V. M. Naik, P. Kharel, P. Talagala and R. Naik, *Solid State Commun.* 133 (2005) 439.

[167] D. H. Kim, J. S. Yang, K. W. Lee, S. D. Bu, T. W. Noh, S.-J. Oh, Y.-W. Kim, J.-S. Chung, H. Tanaka, H. Y. Lee and T. Kawai, *Appl. Phys. Lett.* 81 (2002) 2421.

[168] S. R. Shinde, S. B. Ogale, S. Das Sarma, J. R. Simpson, H. D. Drew, S. E. Lofland, C. Lanci, J. P. Buban, N. D. Browning, V. N. Kulkarni, J. Higgins, R. P. Sharma, R. L. Greene and T. Venkatesan, *Phys. Rev. B* 67 (2003) 115211.

[169] S. A. Chambers, T. Droubay, C. M. Wang, A. S. Lea, R. F. C. Farrow, L. Folks, V. Deline and S. Anders, *Appl. Phys. Lett.* 82 (2003) 1257.

[170] J.-Y. Kim, J.-H. Park, B.-G. Park, H.-J. Noh, S.-J. Oh, J. S. Yang, D.-H. Kim, S. D. Bu, T.-W. Noh, H.-J. Lin, H.-H. Hsieh and C. T. Chen, *Phys. Rev. Lett.* 90 (2003) 017401.

[171] R. J. Kennedy, P. A. Stampe, E. Hu, P. Xiong, S. von Molnar and Y. Xin, *Appl. Phys. Lett.* 84 (2004) 2832.

[172] G. S. Chang, E. Z. Kurmaev, D. W. Boukhvalov, L. D. Finkelstein, D. H. Kim, T.-W. Noh, A. Moewes and T. A. Callcott, *J. Phys.: Condens. Matter* 18 (2006) 4243.

[173] H. Kimura, T. Fukumura, M. Kawasaki, K. Inaba, T. Hasegawa and H. Koinuma, *Appl. Phys. Lett.* 80 (2002) 94.

[174] S. B. Ogale, R. J. Choudhary, J. P. Buban, S. E. Lofland, S. R. Shinde, S. N. Kale, V. N. Kulkarni, J. Higgins, C. Lanci, J. R. Simpson, N. D. Browning, S. Das Sarma, H. D. Drew, R. L. Greene and T. Venkatesan, *Phys. Rev. Lett.* 91 (2003) 077205.

[175] L. Yan, J. S. Pan and C. K. Ong, *Mater. Sci. Eng. B* 128 (2006) 34.

[176] S. N. Kale, S. B. Ogale, S. R. Shinde, M. Sahasrabuddhe, V. N. Kulkarni, R. L. Greene and T. Venkatesan, *Appl. Phys. Lett.* 82 (2003) 2100.

[177] M. Wei, N. Braddon, D. Zhi, P. A. Midgley, S. K. Chen, M. G. Blamire and J. L. MacManus-Driscoll, *Appl. Phys. Lett.* 86 (2005) 072514.

[178] L. Pan, H. Zhu, C. Fan, W. Wang, Y. Zhang and J. Q. Xiao, *J. Appl. Phys.* 97 (2005) 10D318.

[179] C. Kittel, *Introduction to Solid State Physics*, 7th ed. (John Wiley & Sons: Singapore, 2000).

[180] J. Inoue, S. Nonoyama and H. Itoh, *Phys. Rev. Lett.* 85 (2000) 4610.

[181] M. Berciu and R. N. Bhatt, *Phys. Rev. Lett.* 87 (2001) 107203.

[182] J. Konig, H.-H. Lin and A. H. MacDonald, *Phys. Rev. Lett.* 84 (2000) 5628.

[183] T. Jungwirth, J. Sinova, J. Kucera and A. H. MacDonald, *Curr. Appl. Phys.* 3 (2003) 461.

[184] C. Timm, *J. Phys.: Condens. Matter* 15 (2003) R1865.

[185] A. B. P. Lever, *Inorganic Electronic Spectroscopy: Studies in Physical and Theoretical Chemistry*, V. 33, 2nd ed. (Elsvier Science Publishers, Amsterdam, 1984).

[186] J. Smit and H. P. J. Wijn, *Ferrites*, (Philips Technical Library, Eindhoven, 1959).

[187] I. C. Heck. *Magnetic Materials and their Applications*, (Butterworth & Co. Pub. Ltd, London, 1974).

[188] A. Goldman, *Modern Ferrite Technology*, (Van Nostrand Reinhold, New York, 1990).

[189] *Magnetism: Materials and Applications* Ed. by E. du T. de Lacheisserie, D. Gignoux and M. Schlenker, (Springer, New York, 2003).

[190] O. Muller and R. Roy, *Crystal Chemistry of Non-Metallic Materials*, (Springer-Verlag, Berlin, 1974).

[191] W. H. Bragg, *Nature* 95 (1915) 561.

[192] S. Nishikawa, P*roc. Tokyo Math. Phys. Soc.* 8 (1915) 199.

[193] R. W. G. Wyckoff, *Crystal Structures: Miscellaneous Inorganic Compounds, Silicates and basic structural information* Vol. 4, 2nd ed. (Interscience Publishers, New York, 1968), pp. 540.

[194] R. Valenzuela, *Magnetic Ceramics, Chemistry of Solid State Materials*, Series Ed. B. Dunn, J. W. Goodby, A. R. West, (Cambridge Univ. Press, Cambridge, 1994).

[195] B. Lax and K. J. Button, *Microwave Ferrites and Ferrimagnetics*, (McGraw Hill Book Company, New York, 1962).

[196] A. R. Das, V. S. Anandhan and D. C. Khan, *J. Appl. Phys.* 57 (1985) 4189.

[197] T. Nakamura, *J. Magn. Magn. Mater.* 168 (1997) 285.

[198] G. F. Dionne, *J. Appl. Phys.* 81 (1997) 5064.

[199] Z. Yue, J. Zhou, X. Wang, Z. Gui and L. Li, *J. Mater. Sci. Lett.* 20 (2001) 1327.

[200] N. Ponpandian, A. Narayanasamy, C. N. Chinnasamy, N. Sivakumar, J.-M. Greneche, K. Chattopadhyay, K. Shinoda, B. Jeyadevan and K. Tohji, *Appl. Phys. Lett.* 86 (2005) 192510.

[201] P. Papazoglou, E. Eleftheriou and V. T. Zaspalis, *J. Magn. Magn. Mater.* 296 (2006) 25.

[202] *Magnetic properties of fine particles*, Ed. J. L. Dormann, D. Fiorani, (North-Holland Delta Series, North-Holland 1992).

[203] C. C. Berry, *J. Mater. Chem.* 15 (2005) 543.

[204] G. Herzer, M. Vazquez, M. Knobel, A. Zhukov, T. Reininger, H. A. Davies, R. Grossinger and J. L. Sanchez Li, *J. Magn. Magn. Mater.* 294 (2005) 252.

[205] C. Upadhyay, H. C. Verma and S. Anand, *J. Appl. Phys.* 95 (2004) 5746.

[206] J. P. Chen, C. M. Sorensen, K. J. Klabunde, G. C. Hadjipanayis, E. Devlin and A. Kostikas, *Phys. Rev. B* 54 (1996) 9288.

[207] Z. X. Tang, C. M. Sorensen, K. J. Klabunde and G. C. Hadjipanayis, *Phys. Rev. Lett.* 25 (1991) 3602.

[208] C. N. Chinnasamy, A. Narayanasamy, N. Ponpandian, K. Chattopadhyay, K. Shinoda, B. Jeyadevan, K. Tohji, K. Nakatsuka, T. Furubayashi and I. Nakatani, *Phys. Rev. B* 63 (2001) 184108.

[209] C. N. Chinnasamy, A. Narayanasamy, N. Ponpandian, R. Justin Joseyphus, B. Jeyadevan, K. Tohji and K. Chattopadhyay, *J. Magn. Magn. Mater.* 238 (2002) 281.

[210] C. Rath, N. C. Mishra, S. Anand, R. P. Das, K. K. Sahu, C. Upadhyay and H. C. Verma, *Appl. Phys. Lett.* 76 (2000) 475.

[211] F.K. Lotgering, *J. Phys. Chem. Solids* 27 (1966) 139.

[212] J. Chen, G. Srinivasan, S. Hunter, V. S. Babu and M. S. Seehra, *J. Magn. Magn. Mater.* 146 (1995) 291.

[213] H. H. Hamdeh, J. C. Ho, S. A. Oliver, R. J. Willey, G. Oliveri and G. Busca, *J. Appl. Phys.* 81 (1997) 1851.

[214] G. F. Goya, H. R. Rechenberg, M. Chen and W. B. Yelon, *J. Appl. Phys.* 87 (2000) 8005.

[215] K. Tanaka, S. Nakashima, K. Fujita and K. Hirao, *J. Phys.: Condens. Matter* 15 (2003) L469.

[216] S. Verma, P. A. Joy, Y. B. Khollam, H. S. Potdar and S. B. Deshpande, *Mater. Lett.* 58 (2004) 1092.

[217] G. F. Goya and H. R. Rechenberg, *J. Magn. Magn. Mater.* 196 (1999) 191.

[218] A. Kundu, C. Upadhyay and H. C. Verma, *Phys. Lett. A* 311 (2003) 410.

[219] S. D. Shenoy, P. A. Joy and M. R. Anantharaman, *J. Magn. Magn. Mater.* 269 (2004) 217.

[220] C. N. Chinnasamy, A. Narayanasamy, N. Ponpandian, K. Chattopadhyay, H. Guerault and J.-M. Greneche, *Scripta Materialia* 44 (2001) 1407.

[221] H. Ehrhardt, S. J. Campbell and M. Hofmann, *Scripta Materialia* 48 (2003) 1141.

[222] K. Tanaka, M. Makita, Y. Shimizugawa, K. Hirao and N. Soga, *J. Phys. Chem. Solids* 59 (1998) 1611.

[223] F. J. Burghart, W. Potzel, G. M. Kalvius, E. Schreier, G. Grosse, D. R. Noakes, W. Schafer, W. Kockelmann, S. J. Campbell, W. A. Kaczmarek, A. Martin and M. K. Krause, *Physica B* 289-290 (2000) 286.

[224] K. Haneda and A. H. Morrish, *Solid State Commun.* 22 (1977) 779.

[225] M. P. Morales, C. Pecharroman, T. G. Carreno and C. J. Serna, *J. Solid State Chem.* 108 (1994) 158.

[226] D. Vollath, D. V. Szabo, R. D. Taylor, J. O. Willis and K. E. Sickafus, *NanoStruct. Mater.* 6 (1995) 941.

[227] (a) R. F. Ziolo, E. P. Giannelis, B. A. Weinstein, M. P. O'Horo, B. N. Ganguly, V. Mehrotra, M. W. Russell and D. R. Huffman, *Science* 257 (1992) 219. (b) B. Z. Tang, Y. Geng, J. W. Y. Lam, B. Li, X. Jing, X. Wang, F. Wang, A. B. Pakhomov and X. X. Zhang, *Chem. Mater.* 11 (1999) 1581.

[228] C. Chaneac, E. Tronc and J. P. Jolivet, *Nanostruct. Mater.* 6 (1995) 715.

[229] G. Ennas, G. Marongiu, A. Musinu, A. Falqui, P. Ballirano and R. Caminiti, *J. Mater. Res.* 14 (1999) 1570.

[230] J. Lai, K. V. P. M. Shafi, K. Loos, A. Ulman, Y. Lee, T. Vogt and C. Estournes, *J. Am. Chem. Soc.* 125 (2003) 11470.

[231] H. Igarashi and K. Okazaki, *J. Am. Cer. Soc.* 60 (1977) 51.

[232] J. B. Schutz, *Cryogenics* 38 (1998) 3.

[233] S. Ramakrishna, J. Mayer, E. Wintermantel and K. W. Leong, *Composites Sci. Tech.* 61 (2001) 1189.

[234] D. Xie, I.-D. Chung, G. Wang and J. Mays, *J. Biomater. Appl.* 20 (2006) 221.

[235] H.-L. Tasi, J. L. Schindler, C. R. Kannewurf and M. G. Kanatzidis, *Chem. Mater.* 9 (1997) 875.

[236] D. Y. Godovsky, *Adv. Poly. Sci.* 153 (2000) 163.

[237] R. Gangopadhyay and A. De, *Chem. Mater.* 12 (2000) 608.

[238] S. T. Tan, J. H. Wendorff, C. Pietzonka, Z. H. Jia and G. Q. Wang, *ChemPhysChem* 6 (2005) 1461.

[239] X.-L. Xie, Y.-W. Mai and X.-P. Zhou, *Mater. Sci. Eng. R* 49 (2005) 89.

[240] J. R. Liu, M. Itoh and K.-i Machida, *Appl. Phys. Lett.* 88 (2006) 062503.

[241] R. Skomski and J. M. D. Coey, *Phys. Rev. B* 48 (1993) 15812.

[242] K. O'Donnell, C. Kuhrt and J. M. D. Coey, *J. Appl. Phys.* 76 (1994) 7068.

[243] P. G. McCormick, W. F. Miao, P. A. I. Smith, J. Ding and R. Street, *J. Appl. Phys.* 83 (1998) 6256.

[244] H. Zeng, J. Li, J. P. Liu, Z. L. Wang and S. Sun, *Nature* 420 (2002) 395.

[245] A. C. Razzitte, W. G. Fano and S. E. Jacobo, *Physica B* 354 (2004) 228.

[246] Y. Shen, Z. Yue, M. Li and C.-W. Nan, *Adv. Funct. Mater.* 15 (2005) 1100.

[247] I. N. Krivorotov, H. Yan, E. D. Dahlberg and A. Stein, *J. Magn. Magn. Mater.* 226-230 (2001) 1800.

[248] J. A. Borchers, Y. Ijiri, S.-H. Lee, C. F. Majkrzak, G. P. Felcher, K. Takano, R. H. Kodama and A. E. Berkowitz, *J. Appl. Phys.* 83 (1998) 7219.

[249] B. Raquet, R. Mamy, J. C. Ousset, N. Negre, M. Goiran and C. Guerret-Piecourt, *J. Magn. Magn. Mater.* 184 (1998) 41.

[250] T. C. Schulthess and W. H. Butler, *J. Magn. Magn. Mater.* 198-199 (1999) 321.

[251] F. Lucari and F. D'Orazio, *J. Magn. Magn. Mater.* 272-276 (2004) e837.

[252] D. Venus, F. Hunte and E. D. Dahlberg, *J. Magn. Magn. Mater.* 286 (2005) 191.

[253] K. Suresh and K. C. Patil, *J. Solid State Chem.* 99 (1992) 12.

[254] L. A. Chick, G. D. Maupin and L. R. Pederson, *NanoStruct. Mater.* 4 (1994) 603.

[255] (a) J. J. Moore and H. J. Feng, *Prog. Mater. Sci.* 39 (1995) 243. (b) J. J. Moore and H. J. Feng, *Prog. Mater. Sci.* 39 (1995) 275.

[256] T. Mimani and K. C. Patil, *Mater. Phys. Mech.* 4 (2001) 134.

[257] K. C. Patil, S. T. Aruna and T. Mimani, *Curr. Opinion Solid State Mater. Sci.* 6 (2002) 507.

[258] E. E. Sileo, R. Rotelo and S. E. Jacobo, *Physica B* 320 (2002) 257.

[259] A. C. F. M. Costa, E. Tortella, M. R. Morelli and R. H. G. A. Kiminami, *J. Magn. Magn. Mater.* 256 (2003) 174.

[260] J. Huang, H. Zhuang and W. Li, *J. Magn. Magn. Mater.* 256 (2003) 390.

[261] J. C. Toniolo, M. D. Lima, A. S. Takimi and C. P. Bergmann, *Mater. Res. Bull.* 40 (2005) 561.

[262] L. R. Pederson, G. D. Maupin, W. J. Weber, D. J. McReady and R. W. Stephens, *Mater. Lett.* 10 (1990) 437.

[263] L. A. Chick, L. R. Pederson, G. D. Maupin, J. L. Bates, L. E. Thomas and G. J. Exarhos, *Mater. Lett.* 10 (1990) 6.

[264] C.-C. Hwang, J.-S. Tsai and T.-H. Huang, *Mater. Chem. Phys.* 93 (2005) 330.

[265] C.-H. Yan, Z.-G. Xu, F.-X. Cheng, Z.-M. Wang, L.-D. Sun, C.-S. Liao and J.-T. Jia, *Solid State Commun.* 111 (1999) 287.

[266] N. Kikukawa, M. Takemori, Y. Nagano, M. Sugasawa and S. Kobayashi, *J. Magn. Magn. Mater.* 284 (2004) 206.

[267] K. J. Standley, *Oxide Magnetic Materials, Monographs on the Physics and Chemistry of Materials*, Ed. by W. jackson, H. Frohlion, N. F. Mott and E. C. Bullard (Oxford University Press, London, 1962).

[268] M. M. Schierber, *Experimental Magnetochemistry: Nonmetallic Magnetic Materials*, (North-Holland Publishing Company, Amsterdam, 1967).

[269] C. N. R. Rao, *Chemical Approaches to the synthesis of Inorganic Materials*, (Wiley Eastern Ltd., New Delhi, 1994).

[270] B. D. Cullity, *Elements of X-Ray Diffraction* 2nd ed. (Addison-Wesley, Reading, 1978).

[271] M. Calligaris and S. Geremia, *Powder Diffraction Package program*, (International Centre for Theoretical Physics, University of Trieste, Italy).

[272] W. Kraus and G. Nolze, *PowderCell for Windows (PCW), version 2.4* (The software is freely available from http://www.ccp14.ac.uk.).

[273] G. Thomas, *Transmission Electron Microscopy of Metals*, (John Wiley & Sons, Inc, New York, 1962).

[274] D. B. Williams and C. B. Carter, *Transmission Electron Microscopy: A Textbook for Materials Science*, Vol. I-IV, (Plenum Press, New York, 1996).

[275] X. Z. Li, *Ultramicroscopy* 99 (2004) 257.

[276] J. Goldstein, D. Newbury, D. Joy, C. Lyman, P. Echlin, E. Lifshin, L. Sawyer and J. Michael, *Scanning Electron Microscopy and X-ray Microanalysis*, 3rd ed., (Kluwer Academic/Plenum Publishers, New York, 2003).

[277] W. WM. Wendlant, *Thermal Methods of Analysis*, 2nd ed. (John Wiley & Sons, New York, 1974).

[278] T. Hatakeyama, and F. X. Quinn, *Thermal Analysis: Fundamentals and Applications to Polymer Science*, (John Wiley & Sons, New York, 1995).

[279] A. Chainani, M. Mathew and D. D. Sarma, *Phys. Rev. B* 46 (1992) 9976.

[280] T. Saitoh, A. E. Bocquet, T. Mizokawa, H. Namatame, A. Fujimori, M. Abbate, Y. Takeda and M. Takano, *Phys. Rev. B* 51 (1995) 13942.

[281] D. Briggs and M. P. Seah, *Practical Surface Analysis. Vol. I: Auger and X-Ray Photoelectron Spectroscopy* (John Wiely: Reading, New York, 1990).

[282] G. M. Bancroft, *Mössbauer Spectroscopy: An Introduction for Inorganic Chemists and Geochemists*, (McGraw-Hill Book Company Ltd., London, 1973).

[283] *Applications of Mössbauer Spectroscopy* Vol. I, Ed. by R. L. Cohen, (Academic Press, New York, 1976).

[284] S. Foner, *Rev. Sci. Inst.* 30 (1959) 548.

[285] A. J. van Duyneveldt, *J. Appl. Phys.* 53 (1982) 8006.

[286] *Ferrite Cores-2 for telecommunication and industrial fields*, (TDK Electronics Co., LTD, Tokyo, 1978).

[287] S. Kolesnik, B. Dabrowski and J. Mais, *J. Superconductivity: Incorporating Novel Magnetism* 15 (2002) 251.

[288] N. A. Theodoropoulou, A. F. Hebard, D. P. Norton, J. D. Budai, L. A. Boatner, J. S. Lee, Z. G. Khim, Y. D. Park, M. E. Overberg, S. J. Pearton and R. G. Wilson, *Solid-State Electronics* 47 (2003) 2231.

[289] H.-T. Lin, T.-S. Chin, J.-C. Shih, R.-T. Huang, F.-R. Chen and J.-J. Kai, *Physica Status. Solidi (c)* 1 (2004) 3472.

[290] K. R. Kittilstved, N. S. Norberg and D. R. Gamelin, *Phys. Rev. Lett.* 94 (2005) 147209.

[291] B. Martinez, F. Sandiumenge, Ll. Balcells, J. Fontcuberta, F. Sibieude and C. Monty, *J. Magn. Magn. Mater.* 290-291 (2005) 168.

[292] B. D. Yuhas, D. O. Zitoun, P. J. Pauzauskie, R. He and P. Yang, *Angew. Chem. Int. Ed.* 45 (2006) 420.

[293] L. Q. Liu, B. Xiang, X. Z. Zhang, Y. Zhang and D. P. Yu, *Appl. Phys. Lett.* 88 (2006) 063104.

[294] Y. Q. Chang, Y. N. Wu, M. W. Wang, H. Z. Zhang, D. P. Yu, Z. Wang, Y. Long and R. C. Ye, *J. Crys. Growth* 289 (2006) 183.

[295] S. Maensiri, J. Sreesongmuang, Ch. Thomas and J. Klinkaewnarong, *J. Magn. Magn. Mater.* 301 (2006) 422.

[296] P. V. Radovanovic and D. R. Gamelin, *Phys. Rev. Lett.* 91 (2003) 157202.

[297] B. B. Li, X. Q. Xiu, R. Zhang, Z. K. Tao, L. Chen, Z. L. Xie, Y. D. Zheng and Z. Xie, *Mater. Sci. Semiconductor Process.* 9 (2006) 141.

[298] P. Sharma, A. Gupta, F. J. Owens, A. Inoue and K. V. Rao, *J. Magn. Magn. Mater.* 282 (2004) 115.

[299] H. J. Blythe, R. M. Ibrahim, G. A. Gehring, J. R. Neal and A. M. Fox, *J. Magn. Magn. Mater.* 283 (2004) 117.

[300] D. P. Joseph, G. S. Kumar and C. Venkateswaran, *Mater. Lett.* 59 (2005) 2720.

[301] J. J. Liu, M. H. Yu and W. L. Zhou, *Appl. Phys. Lett.* 87 (2005) 172505.

[302] K. R. Kittilstved and D. R. Gamelin, *J. Am. Chem. Soc.* 127 (2005) 5292.

[303] O. D. Jayakumar, H. G. Salunke, R. M. Kadam, M. Mohapatra, G. Yaswant and S. K. Kulshreshtha, *Nanotech.* 17 (2006) 1278.

[304] S-J. Han, J. W. Song, C.-H. Yang, S. H. Park, J.-H. Park Y. H. Jeong and K. W. Rhie, *Appl. Phys. Lett.* 81 (2002) 4212.

[305] A. Y. Polyakov, A. V. Govorkov, N. B. Smirnov, N. V. Pashkova, S. J. Pearton, K. Ip, R. M. Frazier, C. R. Abernathy, D. P. Norton, J. M. Zavada and R. G. Wilson, *Mater. Sci. Semiconductor Process.* 7 (2004) 77.

[306] G. Y. Ahn, S.-I. Park, I.-B. Shim and C. S. Kim, *J. Magn. Magn. Mater.* 282 (2004) 166.

[307] G. Y. Ahn, S.-I. Park and C. S. Kim, *J. Magn. Magn. Mater.* 303 (2006) e329.

[308] K. Ando, H. Saito, V. Zayets and M. C. Debnath, *J. Phys.: Condens. Matter* 16 (2004) S5541.

[309] S. Kolesnik, B. Dabrowski and J. Mais, *J. Appl. Phys.* 95 (2004) 2582.

[310] S-J. Han, B. Y. Lee, J.-S. Ku, Y. B. Kim and Y. H. Jeong, *J. Magn. Magn. Mater.* 272-276 (2004) 2008.

[311] M. Bouloudenine, N. Viart, S. Colis and A. Dinia, *Chem. Phys. Lett.* 397 (2004) 73.

[312] M. Bouloudenine, N. Viart, S. Colis, J. Kortus and A. Dinia, *Appl. Phys. Lett.* 87 (2005) 052501.

[313] P. Lommens, P. F. Smet, C. d. M. Donega, A. Meijerink, L. Piraux, S. Michotte, S. Matefi-Tempfli, D. Poelman and Z. Hens, *J. Luminescence* 118 (2006) 245.

[314] M. Bouloudenine, N. Viart, S. Colis and A. Dinia, *Cat. Today* 113 (2006) 240.

[315] S. Colis, H. Bieber, S. Begin-Colin, G. Schmerber, C. Leuvrey and A. Dinia, *Chem. Phys. Lett.* 422 (2006) 529.

[316] H.-J. Lee, G.-H. Ryu, S.-K. Kim, S. A. Kim, C.-H. Lee, S.-Y. Jeong and C. R. Cho, *phys. stat. sol. (b)* 241 (2004) 2858.

[317] N. A. Spaldin, *Phys. Rev. B* 69 (2004) 125201.

[318] T. Wakano, N. Fujimura, Y. Morinaga, N. Abe, A. Ashida and T. Ito, *Physica E* 10 (2001) 260.

[319] S. W. Jung, W. I. Park, G.-C. Yi and M. Y. Kim, *Adv. Mater.* 15 (2003) 1358.

[320] D. A. Schwartz, K. R. Kittilstved and D. R. Gamelin, *Appl. Phys. Lett.* 85 (2004) 1395.

[321] K. Ando, http://xxx.aps.org/abs/cond-mat/0208010.

[322] J. B. Wang, G. J. Huang, X. L. Zhong, L. Z. Sun, Y. C. Zhou and E. H. Liu, *Appl. Phys. Lett.* 88 (2006) 252502.

[323] T. Fukumura, Z. Jin, M. Kawasaki, T. Shono, T. Hasegawa, S. Koshihara and H. Koinuma, *Appl. Phys. Lett.* 78 (2001) 958.

[324] S-J. Han, T.-H. Jang, Y. B. Kim, B.-G. Park and Y. H. Jeong, *Appl. Phys. Lett.* 83 (2003) 920.

[325] J. Luo, J. K. Liang, Q. L. Liu, F. S. Liu, Y. Zhang, B. J. Sun and G. H. Rao, *J. Appl. Phys. 97* (2005) 086106.

[326] S. Kolesnik and B. Dabrowski, *J. Appl. Phys.* 96 (2004) 5379.

[327] W. Chen, L. F. Zhao, Y. Q. Wang, J. H. Miao, S. Liu, Z. C. Xia and S.L. Yuan, *Solid State Commun.* 134 (2005) 827.

[328] H.-W. Zhang, E.-W. Shi, Z.-Z. Chen, X.-C. Liu and B. Xiao, *Solid State Commun.* 137 (2006) 272.

[329] Z. Jin, M. Murakami, T. Fukumura, Y. Matsumoto, A. Ohtomo, M. Kawasaki and H. Koinuma, *J. Crys. Growth* 214-215 (2000) 55.

[330] K. J. Kim and Y. R. Park, *J. Appl. Phys.* 96 (2004) 4150.

[331] Y. M. Cho, W. K. Choo, H. Kim, D. Kim and Y. E. Ihm, *Appl. Phys. Lett.* 80 (2002) 3358.

[332] J. M. D. Coey, M. Venkatesan and C. B. Fitzgerald, *Nature Mater.* 4 (2005) 173.

[333] J. M. D. Coey, M. Venkatesan, C. B. Fitzgerald, L. S. Dorneles, P. Stamenov and J. G. Lunney, *J. Magn. Magn. Mater.* 290-291 (2005) 1405.

[334] K. Potzger, S. Zhou, H. Reuther, A. Mucklich, F. Eichhorn, N. Schell, W. Skorupa, M. Helm, J. Fassbender, T. Herrmannsdorfer and T. P. Papageorgiou, *Appl. Phys. Lett.* 88 (2006) 052508.

[335] R. Seshadri, *Current opinion Solid State Mater. Sci.* 9 (2005) 1.

[336] R. D. Purohit, B. P. Sharma, K. T. Pillai and A. K. Tyagi, *Mater. Res. Bull.* 36 (2001) 2711.

[337] J.-J. Wu, S.-C. Liu and M.-H. Yang, *Appl. Phys. Lett.* 85 (2004) 1027.

[338] K. J. Kim and Y. R. Park, *Appl. Phys. Lett.* 81 (2002) 1420.

[339] S. V. Bhat and F. L. Deepak, *Solid State Commun.* 135 (2005) 345.

[340] E. P. Wohlfarth, *Ferromagnetic Materials*, Vol 1 (North-Holland Publishing Company: Amsterdam, 1980) p. 21.

[341] *Comprehensive Inorganic Chemistry*, Vol 3, 1st ed. (Edited by J. P. Bailer, Pergamon Press: Oxford, 1973), p. 1056.

[342] F. A. Cotton and G. Wilkinson, *Advance Inorganic Chemistry*, 4th ed. (John Wiley & Sons: New York, 1980) p. 767.

[343] W. L. Roth, *J. Phys. Chem. Solids* 25 (1964) 1.

[344] Z.-B. Gu, C.-S. Yuan, M.-H. Lu, J. Wang, D. Wu, S.-T. Zhang, S.-N. Zhu, Y.-Y. Zhu and Y.-F. Chen, *J. Appl. Phys.* 98 (2005) 053908.

[345] Y. Z. Peng, W. D. Song, C. W. An, J. J. Qiu, J. F. Chong, B. C. Lim, M. H. Hong, T. Liew and T. C. Chong, *Appl. Phys. A: Mater. Sci. Process.* 80 (2005) 565.

[346] T. J. Chuang, C. R. Brundle and D. W. Rice, *Surf. Sci.* 59 (1976) 413.

[347] B. J. Tan, K. J. Klabunde and P. M. A. Sherwood, *J. Am. Chem. Soc.* 113 (1991) 855.

[348] D. Barreca, C. Massignan, S. Daolio, M. Fabrizio, C. Piccirillo, L. Armelao and E. Tondello, *Chem. Mater.* 13 (2001) 588.

[349] N. S. McIntyre, D. D. Johnston, L. L. Coatsworth, R. D. Davidson and J. R. Brown, *Surf. Interface Anal.* 15 (1990) 265.

[350] J. A. T. Taylor, *Am. Cer. Soc. Bull.* 74 (1995) 81.

[351] H. A. Weakliem, *J. Chem. Phys.* 36 (1962) 2117.

[352] J. T. Richardson and W. O. Milligan, *Phys. Rev.* 102 (1956) 1289.

[353] R. H. Kodama, S. A. Makhlouf and A. E. Berkowitz, *Phys. Rev. Lett.* 79 (1997) 1393.

[354] E. Huheey, E. A. Keiter and R. L. Keiter, *Inorganic Chemistry: Principles of structure and Reactivity*, 4th Ed. (Pearson Education, Delhi, 2000). p. 115-117.

[355] S. W. Jung, S.-J. An, G.-C. Yi, C. U. Jung, S.-I. Lee and S. Cho, *Appl. Phys. Lett.* 80 (2002) 4561.

[356] A. Tiwari, C. Jin, A. Kvit, D. Kumar, J. F. Muth and J. Narayan, *Solid State Commun.* 121 (2002) 371.

[357] T. Fukumura, Z. Jin, A. Ohtomo, H. Koinuma and M. Kawasaki, *Appl. Phys. Lett.* 75 (1999) 3366.

[358] C. H. Bates, W. B. White and R. Roy, *J. Inorg. Nucl. Chem.* 28 (1966) 397.

[359] Y. J. Kim, S. Thevuthasan, T. Droubay, A. S. Lea, C. M. Wang, V. Shutthanandan, S. A. Chambers, R. P. Sears, B. Taylor and B. Sinkovic, *Appl. Phys. Lett.* 84 (2004) 3531.

[360] C. M. Srivastava, S. N. Shringi, R. G. Srivastava and N. G. Nanadikar, *Phys. Rev. B* 14 (1976) 2032.

[361] S. Komarneni, E. Fregeau, E. Breval and R. Roy, *J. Am. Cer. Soc.* 71 (1988) C-26.

[362] I.-W. Chen and X.-H. Wang, *Nature* 404 (2000) 168.

[363] H. Tang, Y.-W. Du, Z.-Q. Qiu and J. C. Walker, *J. Appl. Phys.* 63 (1988) 4105.

[364] L. L. Hench and J. K. West, *Chem. Rev.* 90 (1990) 33.

[365] V. Uskokovic, M. Drofenik and I. Ban, *J. Magn. Magn. Mater.* 284 (2004) 294.

[366] J. S. Jiang, L. Gao, X. L. Yang, J. K. Guo and H. L. Shen, *J. Mater. Sci. Lett.* 18 (1999) 1781.

[367] M. Mouallem-Bahout, S. Bertrand and O. Pena, *J. Solid State Chem.* 178 (2005) 1080.

[368] *Landolt-Börnstein, Numerical Data and Functional Relationship in Science and Technology* Ed. by K.-H. Hellwege (Springer-Verlag, New York, 1980) V 12, part b.

[369] N. S. S. Murthy, M. G. Natera, R. J. Begum and S. I. Youssef, *Proc. 1st Int. Conf. on Ferrites, Kyoto, 1970* (University Park Press, Baltimore, MD, 1971), p.60.

[370] E. Lima, Jr., A. L. Brandl, A. D. Arelaro and G. F. Goya, J. Appl. Phys. 99 (2006) 083908.

[371] A. S. Albuquerque, J. D. Ardisson, W. A. A. Macedo and M. C. M. Alves, *J. Appl. Phys.* 87 (2000) 4352.

[372] S. Mørup, *J. Magn. Magn. Mater.* 37 (1983) 39.

[373] A. S. Kabalnov and E. D. Shchukin, *Adv. Colloid Interface Sci.* 38 (1992) 69.

[374] Y. Sun, B. Mayers and Y. Xia, *Nano Lett.* 3 (2003) 675.

[375] L. Yu, J. Zhang, Y. Liu, C. Jing and S. Cao, *J. Magn. Magn. Mater.* 288 (2005) 54.

[376] C. J. Chen, K. Bridger, S. R. Winzer and V. R. Paiverneker, *J. Appl. Phys.* 63 (1988) 3786.

[377] R. D. Sanchez, J. Rivas, P. Vaqueiro, M. A. Lopez-Quintela and D. Caeiro, *J. Magn. Magn. Mater.* 247 (2002) 92.

[378] Y.-H. Wang, W.-C. Chen, S.-Y. Yang, K.-H. Shen, C. Park, M.-J. Kao and M.-J. Tsai, *J. Appl. Phys.* 99 (2006) 08M307.

[379] B. Sass, S. Buschhorn, W. Felsch, D. Schmitz and P. Imperia, *J. Magn. Magn. Mater.* 303 (2006) 167.

[380] S. Verma and P. A. Joy, *J. Appl. Phys.* 98 (2005) 124312.

[381] C. Caizer, *Mater. Sci. Eng. B* 100 (2003) 63.

[382] T. Sato, C. Kuroda and M. Saito, *Proc. 1st Int. Conf. on Ferrites, Kyoto, 1970* (University Park Press, Baltimore, MD, 1971), p.72.

[383] D.-P. Yang, L. K. Lavoie, Y. Zhang, Z. Zhang and S. Ge, *J. Appl. Phys.* 93 (2003) 7492.

[384] L. K. Leung, B. J. Evans and A. H. Morrish, *Phys. Rev. B* 8 (1973) 29.

[385] A. Chatterjee, D. Das, S. K. Pradhan and D. Chakravorty, *J. Magn. Magn. Mater.* 127 (1993) 214.

[386] W.-C. Hsu, S. C. Chen, P. C. Kuo, C. T. Lie and W. S. Tsai, *Mater. Sci. Eng. B* 111 (2004) 142.

[387] S. H. Hong, J. H. Park, Y. H. Choa and J. Kim, *J. Magn. Magn. Mater.* 290-291 (2005) 1559.

[388] A. Verma and D. C. Dube, *J. Am. Ceram. Soc.* 88 (2005) 519.

[389] J. Hu, M. Yan and W. Luo, *Physica B* 368 (2005) 251.

[390] J. Hu and M. Yan, *J. Zhejiang Univ.* 6 (2005) 580.

[391] S.-I. Pyun and J. T. Baek, *Am. Cer. Soc. Bull.* 64 (1985) 602.

[392] H. L. Turk, *Proc. 1st Int. Conf. on Ferrites, Kyoto, 1970* (University Park Press, Baltimore, MD, 1971), p.99.

[393] A. Verma, T. C. Goel, R. G. Mendiratta and R. G. Gupta, *J. Magn. Magn. Mater.* 192 (1999) 271.

[394] B. P. Rao and K. H. Rao, *J. Mater. Sci.* 32 (1997) 6049.

[395] C. Prakash and J. S. Baijal, *J. Less-Common Met.* 107 (1985) 51.

[396] A. Verma, T. C. Goel and R. G. Mendiratta, *J. Magn. Magn. Mater.* 210 (2000) 274.

[397] E. G. Visser and M. T. Johnson, *J. Magn. Magn. Mater.* 101 (1991) 143.

[398] G.-L. Sun, J.-B. Li, J.-J. Sun and X.-Z. Yang, *J. Magn. Magn. Mater.* 281 (2004) 173.

[399] A. Verma, T. C. Goel, R. G. Mendiratta and P. Kishan, *J. Magn. Magn. Mater.* 208 (2000) 13.

[400] T. Tsutaoka, M. Ueshima, T. Tokunaga, T. Nakamura and K. Hatakeyama, *J. Appl. Phys.* 78 (1995) 3983.

[401] S. S. N. Murthy, V. R. K. Murthy and J. Sobhanadri, *J. Appl. Phys.* 65 (1989) 2159.

[402] A. M. Abdeen, *J. Magn. Magn. Mater.* 192 (1999) 121.

[403] R. V. Mangalaraja, S. Ananthakumar, P. Manohar and F. D. Gnanam, *Mater. Lett.* 57 (2003) 1151.

[404] K. H. Wu, W. C. Huang, C. C. Yang and J. S. Hsu, *Mater. Res. Bull.* 40 (2005) 239.

[405] C. G. Koops, *Phys. Rev.* 83 (1951) 121.

[406] G. R. Mohan, D. Ravinder, A. V. R. Reddy and B. S. Boyanov, *Mater. Lett.* 40 (1999) 39.

[407] M. Kiyama and T. Takada, *Proc. Internat. Conf. Ferrites, ICF3* (1980) 11.

[408] M. Yokoyamaa, T. Oku, T. Taniyama, T. Sato, E. Ohta, T. Sato, K. Haneda, S. Itoh, K. Kurahashi and M. Takeda, *Physica B* 213–214 (1995) 251.

[409] M. Yokoyama, E. Ohta, T. Sato, T. Komaba and T. Sato, *J. Phys. IV (France)* 7 (1997) C1-521.

[410] J. F. Hochepied, P. Bonville and M. P. Pileni, *J. Phys. Chem. B* 104 (2000) 905.

[411] F. Grasset, N. Labhsetwar, D. Li, D. C. Park, N. Saito, H. Haneda, O. Cador, T. Roisnel, S. Mornet, E. Duguet, J. Portier and J. Etourneau, *Langmuir* 18 (2002) 8209.

[412] H. H. Hamdeh, J. C. Ho, S. A. Oliver, R. J. Willey, J. Kramer, Y. Y. Chen, S. H. Lin, Y. D. Yao, M. Daturi and G. Busca, *IEEE Trans. Magn.* 31 (1995) 3808.

[413] Z. H. Zhou, J. M. Xue, H. S. O. Chan and J. Wang, *Mater. Chem. Phys.* 75 (2002) 181.

[414] M. Atif, S. K. Hasanain and M. Nadeem, *Solid State Commun.* 138 (2006) 416.

[415] H. Xue, Z. Li, X. Wang and X. Fu, *Mater. Lett.* (2006), http://doi:10.1016/j.matlet.2006.04.061.

[416] S. Liu, B. Yue, K. Jiao, Y. Zhou and H. He, *Mater. Lett.* 60 (2006) 154.

[417] G. F. Goya and H. R. Rechenberg, *J. Magn. Magn. Mater.* 203 (1999) 141.

[418] J. Z. Jiang, P. Wynn, S. Morup, T. Okada and F. J. Berry, *NanoStruct. Mater.* 12 (1999) 737.

[419] C. N. Chinnasamy, A. Narayanasamy, N. Ponpandian and K. Chattopadhyay, *Mater. Sci. Eng. A* 304-306 (2001) 983.

[420] S. Ozcan, B. Kaynar, M. M. Can and T. Firat, *Mater. Sci. Eng. B* 121 (2005) 278.

[421] S.-H. Yu, T. Fujino and M. Yoshimura, *J. Magn. Magn. Mater.* 256 (2003) 420.

[422] P. Druska, U. Steinike and V. Sepelak, *J. Solid State Chem.* 146 (1999) 13.

[423] H. Ehrhardt, S. J. Campbell and M. Hofmann, *J. Alloys. Comp.* 339 (2002) 255.

[424] E. J. Choi, Y. Ahn and K.-C. Song, *J. Magn. Magn. Mater.* 301 (2006) 171.

[425] F. S. Li, L. Wang, J. B. Wang, Q. G. Zhou, X. Z. Zhou, H. P. Kunkel and G. Williams, *J. Magn. Magn. Mater.* 268 (2004) 332

[426] T. Sato, *IEEE Trans. Magn.* 6 (1970) 795.

[427] K. Tkacova, V. Sepelak, N. Stevulova and V. V. Boldyrev, *J. Solid State Chem.* 123 (1996) 100.

[428] K. Tanaka, Y. Nakahara, K. Hirao and N. Soga, *J. Magn. Magn. Mater.* 131 (1994) 120.

[429] M. Ozaki and E. Matijevic, *J. Colloid Interface Sci.* 107 (1985) 199.

[430] Y. S. Kang, S. Risbud, J. F. Rabolt and P. Stroeve, *Chem. Mater.* 8 (1996) 2209.

[431] S. Y. An, I.-B. Shim and C. S. Kim, *J. Appl. Phys.* 97 (2005) 10Q909.

[432] C. Pascal, J. L. Pascal, F. Favier, M. L. E. Moubtassim and C. Payen, *Chem. Mater.* 11 (1999) 141.

[433] B. Martinez, A. Roig, E. Molins, T. Gonzalez-Carreno and C. J. Serna, *J. Appl. Phys.* 83 (1998) 3256.

[434] M. P. Morale, S. Veintemillas-Verdaguer and C. J. Serna, *J. Mater. Res.* 14 (1999) 3066.

[435] A. Venkataraman, V. A. Hiremath, S. K. Date and S. D. Kulkarni, *Bull. Mater. Sci.* 24 (2001) 617.

[436] K. Deshpande, M. Nersesyan, A. Mukasyan and A. Varma, *Ind. Eng. Chem. Res.* 44 (2005) 6196.

[437] N. Feltin and M. P. Pileni, *Langmuir* 13 (1997) 3927.

[438] M. Froba, R. Kohn, G. Bouffard and G. van Tendeloo *Chem. Mater.* 11 (1999) 2858.

[439] M.-P. Pileni and A.-T. Ngo, *ChemPhysChem* 6 (2005) 1027.

[440] Y. Ni, X. Ge, Z. Zhang and Q. Ye, *Chem. Mater.* 14 (2002) 1048.

[441] R. V. Kumar, Y. Koltypin, X. N. Xu, Y. Yeshurun, A. Gedanken and I. Felner, *J. Appl. Phys.* 89 (2001) 6324.

[442] K. V. P. M. Shafi, A. Ulman, A. Dyal, X. Yan, N.-L. Yang, C. Estournes, L. Fournes, A. Wattiaux, H. White and M. Rafailovich, *Chem. Mater.* 14 (2002) 1778.

[443] A. Kosturiak, J. Polavka, L. Valko, J. Slama, A. Gruskova and M. Miglierini, *J. Magn. Magn. Mater.* 153 (1996) 184.

[444] Y. Bai, Z.-Y. Cheng, V. Bharti, H. S. Xu and Q. M. Zhang, *Appl. Phys. Lett.* 76 (2000) 3804.

[445] A. Verma, A. K. Saxena and D. C. Dube, *J. Magn. Magn. Mater.* 263 (2003) 228.

[446] B.-W. Li, Y. Shen, Z.-x. Yue and C.-W. Nan, *J. Appl. Phys.* 99 (2006) 123909.

[447] S. A. Gomez-Lopera, R. C. Plaza and A. V. Delgado, *J. Colloid Interface Sci.* 240 (2001) 40.

[448] I. Gilbert, A. Millan, F. Palacio, A. Falqui, E. Snoeck and V. Serin, *Polyhedron* 22 (2003) 2457.

[449] J. Slama, R. Dosoudil, R. Vicen, A. Gruskova, V. Olah, I. Hudec and E. Usak, *J. Magn. Magn. Mater.* 254-255 (2003) 195.

[450] S. S. Nair, M. Mathews, P. A. Joy, S. D. Kulkarni and M. R. Anantharaman, *J. Magn. Magn. Mater.* 283 (2004) 344.

[451] N. Gupta, S. C. Kashyap and D. C. Dube, *J. Magn. Magn. Mater.* 288 (2005) 307.

[452] R. Dosoudil, M. Usakova, J. Franek, J. Slama and V. Olah, *J. Magn. Magn. Mater.* 304 (2006) 755.

[453] C. Baker, S. I. Shah and S. K. Hasanain, *J. Magn. Magn. Mater.* 280 (2004) 412.

[454] Y.-W. Zhao, X. K. Zhang and J. Q. Xiao, *Adv. Mater.* 17 (2005) 915.

[455] K. H. Wu, Y. M. Shin, C. C. Yang, W. D. Ho and J. S. Hsu, *J. Polym. Sci. Part A: Polym. Chem.* 44 (2006) 2657.

[456] A. Nandi, M. DuttaGupta and A. K. Banthia, *Mater. Lett.* 52 (2002) 203.

[457] M. Z. Rong, M. Q. Zhang, H. B. Wang and H. M. Zeng, *Appl. Surf. Sci.* 200 (2002) 76.

[458] Z.-M. Dang, Y.-H. Lin and C.-W. Nan, *Adv. Mater.* 15 (2003) 1625.

[459] K. Nielsch, F. J. Castano, C. A. Ross and R. Krishnan, *J. Appl. Phys.* 98 (2005) 034318.

[460] X. G. Li, S. Takahashi, K. Watanabe, Y. Kikuchi and M. Koishi, *Powder Technol.* 133 (2003) 156.

[461] J. Matutes-Aquino, D. Ros-Jara, O. Ayala-Valenzuela, P. Sifuentes Gallardo, L. F. Ramos De Valle and O. S. Rodrguez Fernndez, *Polym Composite* 21 (2000) 734.

[462] H. Nathani and R. D. K. Misra, *Mater. Sci. Eng. B* 113 (2004) 228.

[463] M. Spasova, U. Wiedwald, M. Farle, T. Radetic, U. Dahmen, M. Hilgendorff and M. Giersig, *J. Magn. Magn. Mater.* 272-276 (2004) 1508.

[464] W. H. Meiklejohn and C. P. Bean, *Phys. Rev.* 105 (1957) 904.

[465] T. Ozue, M. Kondo, Y. Soda, S. Fukuda, S. Onodera and T. Kawana, *IEEE Trans. Magn.* 38 (2002) 136.

[466] T. Gredig, I. N. Krivorotov and E. D. Dahlberg, *J. Appl. Phys.* 91 (2002) 7760.

[467] K. Ogawa, T. Miyauchi and T. Ozue, *J. Appl. Phys.* 93 (2003) 7780.

[468] J. B. Yi, J. Ding, B. H. Liu, Z. L. Dong, T. White and Y. Liu, *J. Magn. Magn. Mater.* 285 (2005) 224.

[469] D. Mauri, H. C. Siegmann, P. S. Bagus and E. Kay, *J. Appl. Phys.* 62 (1987) 3047.

[470] N. C. Koon, *Phys. Rev. Lett.* 78 (1997) 4865.

[471] H. Moradi, *J. Magn. Magn. Mater.* 278 (2004) 317.

[472] C. Binek, X. He and S. Polisetty, *Phys. Rev. B* 72 (2005) 054408.

[473] M. Verelst, T. O. Ely, C. Amiens, E. Snoeck, P. Lecante, A. Mosset, M. Respaud, J. M. Broto and B. Chaudret, *Chem. Mater.* 11 (1999) 2702.

[474] D. L. Peng, K. Sumiyama, T. Hihara, S. Yamamuro and T. J. Konno, *Phys. Rev. B.* 61 (2000) 3103.

[475] K. Sumiyama, T. Hihara, D. L. Peng and R. Katoh, *Sci. Technol. Adv. Mater.* 6 (2005) 18.

Few informations are obtained from the following websites, which are not included in the bibliography.

1. http://www.cem.msu.edu/ reusch/VirtTxtJml/Spectrpy/UV-Vis/uvspec

2. http://en.wikipedia.org

3. http://www.unl.edu/CMRAcfem

4. http://nsm1.fullerton.edu/ skarl/EM/Microscopy/IntroTEM

5. http://hyperphysics.phy-astr.gsu.edu/hbase/hph.html

List of Publications

1. "Ferromagnetism induced by hydrogen in polycrystalline nonmagnetic $Zn_{0.95}Co_{0.05}O$"
   Sasanka Deka and P. A. Joy, *Appl. Phys. Lett.* 89 (2006) 032508.

2. "Experimental comparison of the structural, magnetic, electronic, and optical properties of ferromagnetic and paramagnetic polycrystalline $Zn_{1-x}Co_xO$ (x = 0, 0.05, 0.1)"
   Sasanka Deka, R. Pasricha and P. A. Joy, *Phys. Rev. B.* 74 (2006) 033201.

3. "Size-dependent magnetic properties of nanocrystalline yttrium iron garnet powders"
   M. Rajendran, **Sasanka Deka**, P. A. Joy and A. K. Bhattacharya, *J. Magn. Magn. Mater.* 301 (2006) 212-219.

4. "Characterization of nanosized NiZn ferrite synthesized by an auto-combustion method"
   Sasanka Deka and P. A. Joy, *Mater. Chem. Phys.* in press, (2006).

5. "Direct observation of Ni metal impurities in lightly doped ferromagnetic polycrystalline (ZnNi)O"
   Sasanka Deka and P. A. Joy, *Chem. Mater.* 17 (2005) 6507-6510.

6. "Electronic structure and ferromagnetism of polycrystalline $Zn_{1-x}Co_xO$ ($0 \leq x \leq 0.15$)"
   Sasanka Deka and P. A. Joy, *Solid State Commun.* 134 (2005) 665-669.

7. "Synthesis and ferromagnetic properties of lightly doped nanocrystalline $Zn_{1-x}Co_xO$"
   Sasanka Deka, R. Pasricha and P. A. Joy, *Chem. Mater.* 16 (2004) 1168-1169.

8. "High magnetic aspects of nanosized NiZn ferrite powders synthesized by an auto combustion method"
   Sasanka Deka, S. K. Date and P. A. Joy, *Proc. of the 9th International Conference on Ferrites (ICF-9)*, p149-154, (2004).

9. "Synthesis and magnetic properties of polycrystalline Co-doped ZnO"
   Sasanka Deka, S. K. Date and P. A. Joy, *Proc. of the 9th International Conference on Ferrites (ICF-9)*, p913-918, (2004).

10. "High permeability and dielectric constant of NiZn ferrite synthesized in nanocrystalline form by a combustion method"
    Sasanka Deka and P. A. Joy, *Communicated*.

11. "Studies on polycrystalline ferromagnetic samples of cobalt doped ZnO"
    Sasanka Deka, P. A. Joy and C. S. Gopinath, *Communicated*.

Awards:

"**Best Poster Award**" in National Science Day poster presentation competition, by NCL Research Foundation 2006, National Chemical Laboratory, Pune, India.

"**Award of Senior Research Fellowship (SRF)**" for 2004-2006 yrs. by University Grants Commission, Govt. of India, New Delhi.

"**Award of Junior Research Fellowship (JRF)**" for 2002-2004 yrs. by University Grants Commission, Govt. of India, New Delhi.

Workshops:

1. National workshop on "Advanced Methods for Materials Characterization, (NWMC)" MRSI, Mumbai Chapter, Bhabha Atomic Research Centre, Mumbai, 2004.

2. SERC Summer School on "Solid State and Materials Chemistry" SSCU, Indian Institute of Science, Bangalore, 2005.

Symposia and Conferences

Oral presentation

1. "*Studies on ZnO based diluted magnetic semiconductors*" Royal Society of Chemistry, RSC-2005, NCL, Pune [2005].

2. "*Ferromagnetic and optical properties of nanocrystalline* $Zn_{1-x}Co_xO$" Raman Memorial Conference, Dept. of Physics, Pune University, Pune, [2005].

3. "*Nanosized NiZn ferrite: Synthesis and Magnetism*" National Symposium on Current Trends in Chemical Research, Deptartment of Chemistry, Gauhati University, [2004].

4. "*Nanocrystalline Zinc ferrite with high magnetization at room temperature*" MEEMA, Powder Metallurgy Association of India & Materials Society of India, Pune [2003].

Poster presentation

1. "*Studies on the origin of ferromagnetism in Co and Ni doped polycrystalline ZnO*" National Science Day Poster Presentation, NCL Research Foundation, National Chemical Laboratory, Pune, [2006].

2. "*Synthesis of nanocrystalline NiZn ferrite with high room temperature magnetization*" Materials Research Society of India, NCL, Pune, [2005].

3. "*Studies on ZnO based diluted magnetic semiconductors*" Royal Society of Chemistry, RSC-2005, NCL, Pune [2005].

4. "*Studies on the origin of room temperature ferromagnetism in Co and Ni doped polycrystalline ZnO*" National Symposium and Conference on Solid State Chemistry and Allied Areas, ISCAS-2005 , Goa University, Goa, [2005].

5. "*Ferromagnetism in polycrystalline Co-doped ZnO*" Materials for Future, MRC, Indian Institute of Science, Bangalore, [2004].